

UNIVERSITÀ DEGLI STUDI DI PADOVA
Dipartimento di Astronomia

UNIVERSITÉ PIERRE ET MARIE CURIE PARIS 6
Observatoire de Paris

UNIVERSITÀ ITALO-FRANCESE

DOTTORATO DI RICERCA IN ASTRONOMIA CICLO XX

ÉCOLE DOCTORALE D'ASTRONOMIE ET D'ASTROPHYSIQUE D'ÎLE-DE-FRANCE

DOTTORATO DI RICERCA IN CO-TUTELA ITALIA-FRANCIA

The Small Scale Physical Evolution of Molecular Gas in Nearby Galaxies

Coordinatori: Ch.mo Prof. Giampaolo Piotto
Ch.mo Prof. Pierre Encrenaz

Supervisori: Ch.mo Prof. Giuseppe Galletta
Ch.ma Prof. Françoise Combes

Dottorando: VIVIANA CASASOLA

31 Gennaio 2008



UNIVERSITÀ DEGLI STUDI DI PADOVA
Dipartimento di Astronomia

UNIVERSITÉ PIERRE ET MARIE CURIE PARIS 6
Observatoire de Paris

UNIVERSITÉ FRANCO-ITALIENNE

DOTTORATO DI RICERCA IN ASTRONOMIA CICLO XX

ÉCOLE DOCTORALE D'ASTRONOMIE ET D'ASTROPHYSIQUE D'ÎLE-DE-FRANCE

DOCTORAT EN CO-TUTELLE ITALIE-FRANCE

The Small Scale Physical Evolution of Molecular Gas in Nearby Galaxies

Responsables: Prof. Giampaolo Piotto
Prof. Pierre Encrenaz

Directeurs de thèse: Prof. Giuseppe Galletta
Prof. Françoise Combes

Doctorant: VIVIANA CASASOLA

31 Janvier 2008



UNIVERSITY OF PADOVA
Astronomy Department
PIERRE ET MARIE CURIE UNIVERSITY PARIS 6
Paris Observatory
ITALIAN-FRENCH UNIVERSITY

PhD IN ASTRONOMY COURSE XX (ITALY)

PhD IN ASTRONOMY AND ASTROPHYSICS (FRANCE)

PhD IN CO-TUTORSHIP ITALY-FRANCE

The Small Scale Physical Evolution of Molecular Gas in Nearby Galaxies

PhD Coordinators: Prof. Giampaolo Piotto
Prof. Pierre Encrenaz

Supervisors: Prof. Giuseppe Galletta
Prof. Françoise Combes

PhD Student: VIVIANA CASASOLA

January 31st, 2008

A Benito, Carmen, e Simone

Prefazione (Italian Preface)

Con il termine di Mezzo Interstellare (o ISM) ci riferiamo al gas e polvere che occupano lo spazio interstellare. L'ISM è costituito da una miscela estremamente diluita (se confrontata alle densità terrestri) di ioni, atomi, molecole, grani di polvere, raggi cosmici, e campi magnetici galattici. Il mezzo interstellare ricopre un ruolo fondamentale nell'astrofisica rappresentando il punto di congiunzione tra scale stellari e scale galattiche. Le stelle si formano all'interno delle regioni più dense del mezzo interstellare, le nubi molecolari, e lo riforniscono di materia ed energia tramite l'azione delle nebulose planetarie, dei venti stellari, e delle supernovae. Questa interazione tra stelle e mezzo interstellare ci aiuta a determinare il tasso con cui una galassia perde il suo contenuto gassoso e il tempo di vita del processo di formazione stellare attiva.

La distribuzione e la massa delle varie componenti dell'ISM (gas atomico, gas molecolare freddo e denso, gas caldo e ionizzato, ...) variano per galassie differenti per tipo morfologico, peculiarità, o proprietà dell'ambiente circostante. Poichè le differenze sui contenuti stellari tra galassie dei primi tipi e quelle di morfologia più avanzata possono essere studiate in termini di differenze delle proprietà del loro ISM, l'analisi del mezzo interstellare è fondamentale per comprendere la natura delle galassie.

Ogni intervallo dello spettro elettromagnetico ci fornisce informazioni su componenti diverse dell'ISM: le righe ottiche tracciano regioni ionizzate o regioni HII, l'intervallo infrarosso dà informazioni sulla radiazione proveniente dai grani di polvere interstellare, la riga di emissione a 2.6 mm della molecola di monossido di carbonio è un buon tracciante del gas molecolare, la riga a 21 cm traccia il gas atomico, e nell'intervallo di lunghezze d'onda dell'ordine del decimetro e metro si possono rivelare forti sorgenti della radiazione continua di sincrotrone.

Lo studio del mezzo interstellare delle galassie si sta avvicinando ad una fase di grande progresso tecnologico, soprattutto relativamente alla componente molecolare. Strumenti millimetrici sia *single-dish* (FCRAO 14 m, IRAM 30 m, NRO 45 m) che interferometri (IRAM, CARMA, NRO, SMA) sono in grado di osservare ad alta risoluzione ($<10''$) le (sotto)strutture delle nubi molecolari presenti nelle galassie. L'immediato futuro, grazie alla costruzione di nuovi strumenti - primo fra tutti l'*Atacama Millimeter Array* (ALMA) - sarà contraddistinto da una rivoluzione nel campo dell'astronomia millimetrica. ALMA, operando a lunghezze d'onda tra 0.3 e 9.6 millimetri e raggiungendo risoluzioni di $0.005''$, ricoprirà un ruolo simile a quello che l'HST ha avuto nel dominio ottico dando inizio a nuove possibilità e strategie osservative.

In questa tesi di dottorato ci siamo dedicati ad uno dei principali argomenti che ALMA si prefigge di studiare, il gas molecolare nelle galassie esterne, con l'obiettivo di non farci trovare impreparati all'arrivo di questo

strumento. Questa tesi studia la fisica di eccitazione a piccola scala, le proprietà di frammentazione, la distribuzione, e la cinematica del gas molecolare in due galassie vicine (Messier 81 e NGC 3147) con osservazioni ottenute sia con uno strumento millimetrico *single-dish* che con un radiointerferometro. Affrontiamo inoltre il problema della variazione del fattore di conversione H_2-CO in galassie esterne. Il valore assunto da questo rapporto, definito come $X = N(H_2)/I_{CO}$, è una problematica molto discussa poichè esso dipende dalle particolari condizioni fisico-chimiche del gas molecolare (e.g. temperature, densità, e metallicità). Il rapporto di riga è un altro strumento utilizzato in questa tesi per derivare le condizioni fisiche del gas, come temperatura di eccitazione e profondità ottica. In combinazione e in maniera complementare a questi due studi dettagliati sul gas molecolare in galassie specifiche, in questa tesi presentiamo anche un lavoro statistico ed interpretativo sulle relazioni esistenti tra differenti componenti dell'ISM ottenuto analizzando un campione di galassie di tutte le morfologie, attività nucleare, e tipo di interazione. Alcune relazioni, come quella già nota tra il flusso della riga CO(1-0) e quello a 100 μm per galassie ellittiche, vengono confermate ed estese analizzando un grande ed eterogeneo campione di galassie, altre invece che sembrano non valere solo per specifiche tipologie di galassie vengono interpretate con l'aiuto di modelli chimico-dinamici.

Questo duplice approccio allo studio del mezzo interstellare - analisi dettagliata della componente molecolare di singole galassie e studio statistico delle relazioni tra differenti componenti dell'ISM per un grande campione di galassie - ci ha aiutato a comprendere meglio lo scenario alquanto complesso che si prospetta studiando il mezzo interstellare. Particolare attenzione è stata rivolta alla componente molecolare nelle galassie.

La tesi è strutturata nella seguente maniera: nel primo capitolo descriviamo le principali caratteristiche delle diverse fasi del mezzo interstellare. Il secondo capitolo è interamente dedicato alla componente molecolare dell'ISM, fornendo una panoramica dettagliata delle proprietà delle principali strutture di gas molecolare (nubi molecolari, *clumps* molecolari, ...) e del loro legame con il processo di formazione stellare. Viene anche descritta la problematica legata alla variazione del fattore di conversione H_2-CO, parametro usato in tutti gli studi sul gas molecolare, e la distribuzione del gas al variare del tipo morfologico, dell'ambiente, del *redshift*, e dell'attività. Nel terzo capitolo presentiamo un'analisi sulle relazioni esistenti tra i flussi della riga CO(1-0), a 100 μm, della luminosità B, e dei raggi X per un campione di $\sim$ 3000 galassie. Il quarto capitolo è interamente dedicato allo studio della componente molecolare gassosa nella regione centrale della galassia M 81. Nel quinto capitolo analizziamo il gas molecolare della galassia Seyfert 2 NGC 3147 con l'obiettivo di studiare i meccanismi di rifornimento di gas del suo Nucleo Galattico Attivo (AGN). Nel sesto capitolo riassumiamo i risultati ottenuti e descriviamo il ruolo e l'importanza che attualmente riveste una ricerca sul gas molecolare.

Préface (French Preface)

Le Milieu Interstellaire (ou MIS) est composé du gaz et de la poussière qui occupent l'espace interstellaire. Le MIS est constitué d'un mélange extrêmement dilué (par rapport aux densités terrestres) d'ions, d'atomes, de molécules, de grains de poussière, rayons cosmiques, et champ magnétique galactique. Le milieu interstellaire joue un rôle fondamental en astrophysique, étant le point de jonction entre les échelles stellaires et galactiques. Les étoiles se forment dans les régions les plus denses du milieu interstellaire, les nuages moléculaires, et elles le réapprovisionnent en matière et énergie par l'action des nébuleuses planétaires, des vents stellaires, et des supernovae. Cette interaction entre étoiles et milieu interstellaire nous aide à déterminer le taux avec lequel une galaxie consume son contenu gazeux, et donc la durée de vie du processus de formation stellaire.

La distribution et la masse des diverses composantes du MIS (gaz atomique, gaz moléculaire froid et dense, gaz chaud et ionisé, ...) varient de galaxie à galaxie en fonction du type morphologique, de leur degré de perturbations/interactions, et en fonction de l'environnement. Puisque les différences en contenu stellaire entre galaxies des différents types morphologiques peuvent être étudiées et rapportées aux propriétés de leur MIS, l'analyse du milieu interstellaire est fondamentale pour comprendre la nature des galaxies.

Chaque intervalle du spectre électromagnétique nous fournit des informations sur des composantes différentes du MIS: les raies optiques tracent les régions ionisées ou régions HII, l'infrarouge donne des informations sur le rayonnement provenant des grains de poussière, la raie de rotation à 2.6 mm de la molécule de monoxyde de carbone est un bon traceur du gaz moléculaire, la raie à 21 cm trace le gaz atomique, et le domaine de longueurs d'onde du décimètre et du mètre révèle les sources de rayonnement continu synchrotron ou free-free (supernovae, formation d'étoiles).

L'étude du milieu interstellaire des galaxies va entrer dans une phase de grand progrès technologique, surtout relativement à sa composante moléculaire. Aujourd'hui les télescopes millimétriques à antenne unique (FCRAO 14 m, NRO 45m, IRAM 30 m) et les interféromètres (IRAM, NRO, CARMA) peuvent résoudre avec une résolution spatiale raisonnable ($< 10''$) les (sous)-structures des nuages moléculaires présentes dans les galaxies. Le futur immédiat, grâce à la construction de nouveaux instruments - essentiellement *Atacama Millimeter Array* (ALMA) - sera caractérisé par une révolution dans le champ de l'astronomie millimétrique. ALMA, en opérant aux longueurs d'onde entre 0.3 et 9.6 millimètres et en atteignant une résolution de $0.005''$, jouera un rôle similaire à celui du HST dans le domaine optique en donnant à l'astronomie des nouvelles possibilités observationnelles.

Cette thèse de doctorat est dédiée à un des principaux sujets qu'ALMA pourra approfondir, le gaz moléculaire dans les galaxies extérieures, avec

l'objectif d'être bien préparé à l'arrivée de ce instrument. Cette thèse étudie la physique de l'excitation collisionnelle à petite échelle, les propriétés de fragmentation, la distribution, et la cinématique du gaz moléculaire en deux galaxies proches (Messier 81 et NGC 3147) avec des observations obtenues soit avec un instrument millimétrique à antenne unique, soit avec un interféromètre. Nous étudions aussi le problème de la variation du facteur de conversion H_2-CO dans les galaxies extérieures. La valeur supposée de ce rapport, défini comme $X = N(H_2)/I_{CO}$, relève d'une problématique très débattue car elle dépend des conditions physico-chimiques particulières du gaz moléculaire (e.g. température, densité, et métallicité). Le rapport d'intensité des raies CO(1-0) et CO(2-1) est des moyens utilisés dans cette thèse pour déduire les conditions physiques du gaz, comme la température d'excitation et l'épaisseur optique. En complément à ces deux études détaillées du gaz moléculaire dans des galaxies spécifiques, cette thèse présente aussi un travail statistique et son interprétation sur les relations existantes entre les différentes composantes du MIS, obtenu en analysant un échantillon de galaxies de tout type morphologique, activité nucléaire, et type d'interaction. Quelques relations, comme par exemple celle déjà connue entre le flux de la raie CO(1-0) et le flux infrarouge à 100 μm, sont confirmées et étendues en analysant un grand échantillon hétérogène de galaxies; d'autres moins connues qui font intervenir des (sous)échantillons des galaxies, sont interprétées avec l'aide de modèles couplant la chimie et la dynamique.

Cette double approche à l'étude du milieu interstellaire - analyse détaillée de la composante moléculaire des galaxies individuelles et étude statistique des relations entre les différentes composantes du MIS pour un grand échantillon de galaxies - a aidé à mieux comprendre le scénario complexe qui contrôle la physique du milieu interstellaire.

La thèse est structurée de la façon suivante: dans le premier chapitre nous décrivons les principales caractéristiques des différentes phases du milieu interstellaire. Le deuxième chapitre est entièrement consacré à la composante moléculaire du MIS, en fournissant une panoramique détaillée des propriétés des principales structures du gaz (nuages moléculaires, grumeaux et sous-structures) et de leur lien avec le processus de formation stellaire. Dans ce chapitre nous décrivons aussi la problématique liée à la variation du facteur de conversion H_2-CO, paramètre utilisé dans toutes les études du gaz moléculaire, la répartition du gaz selon le type morphologique, l'environnement, le *redshift*, et l'activité de formation d'étoiles. Dans le troisième chapitre nous présentons une analyse des corrélations entre les flux de la raie CO(1-0), le flux infrarouge à 100 μm, la luminosité B, et les rayons X pour un échantillon de $\sim$3000 galaxies. Le quatrième chapitre est entièrement dédié à l'étude de la composante moléculaire dans la région centrale de la galaxie M 81. Dans le cinquième chapitre nous analysons le gaz moléculaire de la galaxie Liner 2 NGC 3147 avec l'objectif d'étudier les mécanismes de ravitaillement de gaz de son Noyau Galactique Actif (AGN). Dans le sixième chapitre nous résumons les résultats obtenus et décrivons le rôle et l'importance que revêt actuellement une thèse sur le gaz moléculaire. Grâce à la construction de nouveaux instruments, ALMA en particulier, l'astronomie millimétrique entre dans une phase de progrès considérable.

Preface

With the term of Interstellar Medium (or ISM) we refer to the gas and the dust that pervade the interstellar space. The ISM consists of an extremely dilute (by terrestrial standards) mixture of ions, atoms, molecules, dust grains, cosmic rays, and (galactic) magnetic fields. The interstellar medium plays a crucial role in astrophysics because it intermediates between stellar and galactic scales. Stars form within the densest regions of the ISM, molecular clouds, and replenish the ISM with matter and energy through planetary nebulae, stellar winds, and supernovae. This interplay between stars and the ISM helps to determine the rate at which a galaxy depletes its gaseous content, and therefore its lifespan of active star formation.

The distribution and mass of the different components of the ISM (the atomic gas, the cold dense molecular gas, the hot ionized gas, ...) change for different galaxies, according to their Hubble morphological types, peculiarities, or properties of the environment. Since differences in stellar contents and light distributions of early- and late-type galaxies can be studied as differences in their ISM, the study of the interstellar medium is fundamental for understanding the nature of the galaxies.

Observations of different energy ranges give us information on different gas components of the ISM: the optical lines trace ionized regions or HII regions, the infrared range gives information on the radiation from interstellar dust grains, the 2.6 mm emission line of the carbon monoxide molecule is a good tracer of the molecular gas, the 21 cm line traces the atomic gas, and in the meter and decimeter range we can detect strong sources of continuous synchrotron radiation.

The study of the interstellar medium in galaxies is currently in a phase of strong technical progress, especially concerning the molecular gas component of the ISM. Both millimeter-wave single-dish telescopes (FCRAO 14 m, IRAM 30 m, NRO 45 m) and interferometers (IRAM, CARMA, NRO, SMA) already perform high resolution observations ($< 10''$) resolving (sub)structures of the molecular clouds present in the galaxies. The immediate future with the construction of new instruments, the Atacama Millimeter Array (ALMA) in particular, will bring a great revolution in millimeter astronomy. ALMA, operating at wavelengths between 0.3 to 9.6 millimeters and with resolutions as fine as $0.005''$, will play a role similar to HST in the optical domain by opening a completely new range of observational possibilities.

In this PhD Thesis we focus on a important topic of the ALMA science, the molecular gas in external galaxies in order to prepare ourselves to this revolutionary instrument. We investigate the small scale excitation, fragmentation properties, distribution and kinematics of the molecular gas in two nearby galaxies (Messier 81 and NGC 3147) observed both with single-dish and interferometer instruments. We discuss the problem of the H_2-CO conversion factor variation in external galaxies. The value of this factor,

defined as $X = N(H_2)/I_{CO}$, is matter of discussion because it appears to depend on the particular physical and chemical conditions of the molecular gas (e.g. temperature, density, and metallicity). The line ratio is also used to derive the physical conditions of the gas, such as excitation temperature and optical depth. In combination and complementary to these two detailed studies on the molecular gas component in specific galaxies, in this Thesis we also present a statistical and interpretative work on the relations existing between different components of the ISM obtained considering a sample of galaxies of all the morphologies, nuclear activities, and type of interaction. Some relations, such as that known between CO and the 100 μm fluxes for early-type galaxies, are confirmed and extended considering a large and heterogeneous sample of galaxies, other relationships lacking for particular typologies of galaxies are interpreted with the help of chemo-dynamical models.

This double approach to the study of the interstellar medium - a detailed analysis of the molecular component of single galaxies and a statistical study of the relations between different components of the ISM for a large sample of galaxies - helped us to understand better the complex scenario of the ISM. Major efforts have been dedicated to the molecular gas component in the galaxies.

The Thesis is organized as follows: in the first chapter we describe the principal characteristics of the different phases of the interstellar medium. The second chapter is completely dedicated to the molecular component of the ISM, describing the properties of the principal molecular gas structures (molecular clouds, molecular clumps, ...) and their link with the star formation process. We also introduce the problem of the H_2-CO conversion factor variation, parameter always used in the studies of the molecular gas, and describe the molecular gas distribution in galaxies as a function of the morphological type, environment, redshift, and activity. In the third chapter we present a analysis of the relations existing between CO(1-0) line, 100 μm, B, and X-ray fluxes for a sample of $\sim$ 3000 galaxies. The fourth chapter is devoted to a detailed study of the molecular gas component of the M 81 galaxy center. In the fifth chapter we analyze the molecular gas of the Seyfert 2 NGC 3147 galaxy to study the mechanisms for gas fueling of its Active Galactic Nucleus (AGN). In the sixth chapter we summarize our conclusions and describe the role - at the present day - of a Thesis on the molecular gas.

Contents

List of Figures

List of Tables

Chapter 1

The Interstellar Medium

Introduction

For centuries, astronomers believed that the space between the stars was empty. It wasn't until the eighteenth century, when William Herschel observed nebulous patches of sky through his telescope, that serious consideration was given to the notion that the interstellar space was something to study. It was only in the last century that observations of interstellar material suggested that it was not even uniformly distributed through space, but that it had a unique structure. Today, we know that regions between the stars are far from to be empty, and that contain rarefied gas, dust particles, magnetic fields, relativistically moving electrons, protons and other atomic nuclei. These various components are coupled together, with the result that for many purposes they together form a single dynamical entity. The terms Interstellar Medium, Interstellar Matter, or simply the acronym ISM, are commonly used to define this composite dynamical entity.

Even if the ISM only represents a small fraction (~ 0.1) of the mass of the galaxies, the distribution, the phases and the mass of different components of the interstellar medium change for different galaxies, according to their Hubble morphological types, peculiarities, or properties of the environment. Differences in stellar contents and light distributions of early- and late-type galaxies can be studied as differences in their interstellar medium, and for this reason the study of the ISM is a prerequisite for understanding why galaxies are as we observe them.

Until the early 1980s it was thought that only spiral galaxies had a significant interstellar medium, but microwaves, optical and X-ray surveys have demonstrated that some elliptical galaxies also have a non negligible interstellar medium content. The most important difference between early- and late-type galaxies is nor so much in the quantity of the interstellar medium, as in how the ISM is structured. In spiral galaxies the major part of the ISM resides in a cold component (in form of atomic and molecular gas) and a smaller fraction in photoionized gas. The hot coronal gas has a large volume filling factor, but constitutes a small mass function. In contrast, the great majority of elliptical galaxies are much poorer in cool gas component than spirals of similar luminosity, while the most massive gaseous component is hot X-ray coronal gas, usually extending to a large galactic radius, with masses ranging between 10^8 to 10^{10} $M_\odot$ (Fabbiano, 1989).

However the presence of a cold gas component has been also inferred for elliptical galaxies from observations in the HI, far infrared (FIR) (such as Knapp et al., 1985, 1989). A growing number of elliptical galaxies are

now found to contain molecular gas component thanks to CO surveys (Lees et al., 1991; Bregman et al., 1992; Wiklind et al., 1995; Morganti et al., 2006; Combes et al., 2007) that reported the detection of several ellipticals containing molecular gas.

Then, elliptical and SO galaxies normally contain less ionized gas than spirals, but significant detections of ionized gas also exist for early-type galaxies. Spectroscopic surveys for H_α and [NII] emissions found a non negligible percentage of E and S0 galaxies with ionized gas. The mass of the ionized gas in early-type galaxies is very small, with values typically in the range from 10^3 to 10^4 $M_\odot$ (see Phillips et al., 1986; Sadler, 1987).

1.1 Components of the Interstellar Medium

The ISM has an extremely low density, lower than that of the best vacuum created on Earth. For comparison, the air that we breathe contains 3×10^{19} molecules/cm^3, while the interstellar gas around our solar system only contains one atom in 10 cm^3. The ISM is mainly made up of gas with some dust. The gas is mostly hydrogen (90%), with a small amount of helium (9%), and very small quantities of heavier elements (1%). The dust particles are extremely small, their size being about the wavelength of blue light and consist of silicates, carbon, ice, and/or iron compounds. In average, for every 10^6 atoms of hydrogen, there are 250 atoms of carbon, 500 of oxygen and 80 of nitrogen. The average density of the ISM is of 1 particle/cm^3, and regions at higher density are molecular cloud cores with density $\geq 10^6$ particles/cm^3.

The physical conditions in the ISM span from extremely hot X-ray emitting plasma with typically T $\approx 10^7$ K and $n_e \approx 10^{-3}$ cm^{-3} to the cool molecular phase with temperatures T $\approx$10 K (little above the 2.7 K cosmic background radiation) and molecular densities up to 10^3 cm^{-3}.

The phase of the interstellar medium and the transitions to other phases mainly depend on the energy quantity of the ISM. The stellar environments play the main role as source of energy: stellar winds, supernova explosions, shock heating, and cosmic ray heating enrich the ISM with heavy elements.

The principal phases of the ISM are the neutral component, the cold dense molecular component, and the hot ionized component. Most of the mass is concentrated in cool dense clouds of molecular gas, while most of volume is occupied by hot dilute ionized hydrogen. Another component of the cooler part of the ISM consists of dust grains that, although they only constitute the 1% of the total mass contained in the interstellar medium -containing $\sim$ 50% of the heavy elements of the ISM- and their effect on the dynamics of the gas is weak, they lead to efficient scattering, polarization, and absorption of starlight and thus provide important observational clues.

In addition to these thermal-gas components there is a background of high-energy particles, the cosmic-ray component, consisting mainly of relativistic electrons and ions, tied to the galaxy by its magnetic field. This is continuum radio emission (cm) and it mainly traces the high-energy processes and the structure or the intensity of the interstellar magnetic field.

Information on the physical conditions of the ISM can be obtained with observations in different energy ranges. In the optical domain emission lines are the signatures of ionized regions or HII regions, infrared observations allow to study the radiation from interstellar dust grains, and in the millimetric domain the 2.6 mm emission line of the carbon monoxide molecule

Table 1.1: Principal parameters of the different components of the ISM (Biskamp, 2003).

Component	Density (cm^{-3})	Temperature (K)	Volume fraction	Mass fraction
Coronal HII plasma	0.005	10^6	0.5	10^{-3}
Warm HII plasma	0.3	10^4	0.5	0.1
HI clouds	10	10^2	0.05	0.4
Warm HI	0.4	8×10^3	0.1-0.5	
H_2 clouds	10^3-10^6	10-100	0.005	0.5
Diffuse H_2	10^2-10^3	30-80	$\leq$0.01	
Cosmic rays	3×10^{-10}	3×10^9 eV	1	0
Cosmic rays			0.5	0.01

(CO) is a good tracer of the hydrogen molecule (H_2). In addition, most of the common molecules (e.g. HCN or CS) have lines in the mm region, making the mm-wave astronomy a powerful tool for studying the dense molecular component of the ISM. In the centimeter radio domain the thermal continuum radiation also indicates the presence of HII regions, and the 21cm line of the atomic hydrogen (HI) allows the mapping of galaxies on a large scale and at very great distances from the center, well beyond the optical radiation of the galaxy. The ISM is also a strong source of continuous synchrotron radiation, visible in the radio at meter and decimeter wavelength. This non-thermal radiation arises from the interaction of the cosmic ray electrons with the galaxy magnetic field. The main parameters of the different components coexisting in the ISM are summarized in Table 1.1.

1.2 Observation of different emissions in the ISM

As said in the previous Section, each region of the energetic spectral range traces a particular component of the ISM. To understand the physical mechanisms that characterize the whole interstellar matter it is necessary to study in detail each individual component of the interstellar medium.

1.2.1 X-ray and Extreme UV emissions

As already mentioned, there is a hot fraction of the ISM -called plasma- present in all galaxies and with temperature always $> 10^5$ K where the hydrogen and the helium are fully ionized. This component mainly emits in the extreme ultraviolet (EUV) and X-ray ranges. The energies of EUV photons are in the range 13.6-100 eV, while those of X-ray photons are usually classified as soft (0.1-1 keV), medium (1-10 keV), or hard ($>$ 10 keV).

Relatively to the EUV photons, the interstellar hydrogen atoms have a large cross-section for the absorption of photons with energies larger than 13.6 eV, energy needed for the ionization. He atoms and He^+ ions also offer cross-sections to the absorption of EUV photons (the energies necessary to eject the first and second electrons from a helium atom are 24.6 eV and

54.4 eV, respectively). Since significant column densities of HI, He and He^+ accumulate over short distances along any line of sight from the Sun, the local ISM is highly opaque to EUV photons and it is extremely difficult to probe the Milky Way and external galaxies with observations in the EUV band.

The X-rays emitted by a plasma are generated by two principal mechanisms: (i) the **bremsstrahlung** process, where a free electron scatters off an ion, and (ii) the **bound-bound** transitions of ions, in which an excited state of an ion decays to a less energetic state.

In a hot plasma the bremsstrahlung emissivity is proportional to the square of the density of the plasma (ρ^2). It happens because the electron density is proportional to ρ and the rate at which electron suffers collisions is proportional to the ion density, which is itself proportional to ρ.

In an optically thin medium the ions are excited by collisions with energetic electrons and de-excited either by collision with a second electron, or radiatively through the emission of a photon. At the typical densities of the hot plasma, collisional de-excitation is much less important than radiative decay, with the result that essentially every collisional excitation gives rise to the emission of a photon. So, the luminosity per unit volume in line radiation also is proportional to ρ^2.

In a hot plasma, the bremsstrahlung radiation is not the only emission process. At high temperatures low-mass atoms are fully ionized, but heavier highly-charged nuclei are able to hold on to some of their most tightly bound electrons. These remaining bound electrons are excited to higher levels by collisions with energetic free electrons in the hot gas. The consequent radiative decay of these excited atoms produces X-ray emission. Thus, the X-ray spectra generally contain discrete emission lines from various highly-ionized heavy elements on top of the bremsstrahlung continuum.

Analyzing a X-ray spectrum, it is possible to determine the temperature, density and metallicity of a plasma. Another parameter that alters the spectrum at low energies is the amount of absorption by cold gas along the line of sight, either in the local ISM or in any material surrounding the emitting object. All these quantities can be estimated by comparing the observed spectrum to ones simulated using the full range of plausible parameter values.

1.2.2 UV emission

The ultraviolet emission (4-400 nm), between X-rays and blue visible light, gives us useful information about the stellar content of a galaxy. For instance, the spiral arms in a spiral galaxy contain many hot blue and blue-white stars. These regions are more prominent when viewed in UV light than other regions that are dominated by older stars which have redder colours. In galaxies the UV emission is dominated by contribution from early-type stars (O, B stars).

The UV window has been less explored until the advent of space astronomy: from spatial missions we know that UV observations produce more different samples of galaxies than observations made from the ground looking at visible light. These studies have shown that UV output is proportional to the rate at which stars form, the *star formation rate* (SFR). UV is a much more sensitive energy range for tracking evolution and star formation activity within galaxies because the brightest stars are the hottest and emit a lot of UV radiation.

Thanks to UV emission detected by satellites -the most recent is the Galaxy Evolution Explorer satellite (*GALEX*)- we can investigate the *star formation history*, how star formation in galaxies evolved from the early Universe up to the present. With the *GALEX* satellite we hope to learn answers to the questions, "When and where did the stars and elements we see today have their origin?" and "What factors cause star formation in galaxies?". UV astronomy is mapping the history of star formation in the Universe 80 percent of the way back to the Big Bang.

The main problem afflicting UV SFR indicators, but also optical, is dust attenuation. We need to consider two aspects linked to this problem. One is that regions with moderate amounts of dust are obscured in a way that depends not only on the amount of dust but also on the distribution of the emitters relative to the absorbers (Calzetti et al., 2005). This problem is due to the fact that populations of different ages suffer different amounts of dust extinction (e.g. Calzetti et al., 1994; Charlot & Fall, 2000; Zaritsky et al., 2004). In addition, it has been shown that quiescently star-forming galaxies follow a dust opacity-reddening relation different by star-burst galaxies (e.g. Gordon et al., 2004; Laird et al., 2005). In particular, their IR/UV ratio, a measure of dust opacity, is on average lower than that of starbursts for the same UV colour, a measure of dust reddening, and shows a larger spread. Different ratios between current SFR and lifetime SFR, defined as "b-parameter", for star-forming and starburst galaxies have been invoked as an explanation for the observed difference (Kong et al., 2004).

A second problem is the unknown fraction of star formation that is completely obscured by dust at UV and optical wavelengths. The UV and far-infrared (FIR) emissions may, indeed, probe different regions/stages of star formation. Heavy obscuration is generally tied to the first temporal phases of star formation, roughly a few million years; as the stars age, they tend to drift off the parental cloud and diffuse in regions of lower gas/dust density or to disperse the natal gas/dust cloud (Leisawitz & Hauser, 1988). Estimates indicate that the fraction of completely obscured star formation is relatively small in the local Universe, $\sim$ 20% - 30% (Calzetti, 2001), but uncertainties are larger and their impact on the calibration of SFR indicators mostly unprobed.

Interesting results on the relation between dust extinction and SF have been also obtained by Sullivan et al. (2001). They, presenting a decimetric radio survey undertaken with the Very Large Array, have compared independent star formation diagnostics (H_α, UV continuum, and 1.4 GHz) for a UV-selected sample of nearby galaxies. Sullivan et al. (2001) have found broad correlations over several orders of magnitude between the different SF diagnostics but with a large galaxy-to-galaxy scatter and offsets/nonlinearities from relations predicted using simple dust extinction and SF scenarios. Finding evidence for luminosity dependent effects, they have shown that luminosity dependent dust corrections, or a miscalibration of the 1.4 GHz-SFR calibration, or a combination of both, can go some way to resolving this effect. They have concluded that differential extinction between galaxies cannot be solely responsible for the scatter in relations between different star formation diagnostics, and that discrepancies between different SF diagnostics can only be partly explained by simple models of dust extinction in galaxies. These models cannot by themselves explain all the observed differences, introducing the need for temporally varying SFHs and/or more complex models of extinction.

1.2.3 Optical line emission

Emission optical lines, present in the spectra of many galaxies, are generally formed in excited interstellar gas. The gas has usually been excited by ionizing radiation from either hot stars or an active galactic nucleus, or also it has been excited by the passage of a powerful shock wave. The more important case is however that of the photo-excited regions, characterized by the presence of atoms in higher states of ionization than would occur in thermodynamic equilibrium at the kinetic temperatures of the gas ($T \simeq 8000$ K).

The spectra of hot stars are generally such that the radiation from these stars ionizes all hydrogen atoms within some limiting distance from the stars, while material beyond this distance is neutral. Regions of ionized hydrogen are called **HII regions** and the volume within which they are contained are called Strömgren spheres.

Hydrogen lines

In the optical spectra of HII regions lines of the Balmer series (such as Hα at 656 nm, Hβ at 486 nm and Hγ at 434 nm) are prominent. In the thermodynamic equilibrium at the kinematic temperature of a typical HII region (∼8000 K), there would be negligible flux in these lines since they arise from states that lie more than 12 eV above hydrogen's ground state. It follows that the observed lines are produced by H atoms cascading to their ground state following capture of an electron by a proton. The relative intensities of the different lines formed by this recombination process can be accurately calculated, and depend only weakly on T and -for interstellar densities- negligibly on the density. The Hα line is caused by the recombination process passing through the stage H(n=3)→H(n=2) + $h\nu$. This emission is the conventional standard by which to gauge star formation (Kennicutt et al., 1998b). The idea of this method is quite straightforward: if the galaxy is optically thick it will absorb all the ionizing photons emitted by OB stars. Thus the total number of ionizing photons emitted and the ionizations are balanced by the total number of recombination per unit time. However, to derive the SFR of a galaxy from the observed Hα flux one needs stellar evolution and photoionization models.

Metal lines

In the spectra of the HII regions there are two most prominent lines, the N_1 at 500.7 nm and the N_2 at 495.9 nm. These lines, "forbidden" as demonstrated by Bowen (1927), are lines of the O^{2+}. In general the spectra of interstellar nebulae are dominated by forbidden and semi-forbidden lines of the ions of heavy elements such as N, O and S. These ions are over 1000 times rarer than those of H and He, and the transitions that are dominating the observed radiation are precisely the least probable transitions of these ions.

The only excited states of ions that will be significantly populated in an HII region are those whose energies lie within a few times $kT \simeq 1$ eV of the relevant ground-state energy. All such low-lying states have the same electronic "configuration" as the ground state, with the result that all transitions between them and the ground state are forbidden. The forbidden nature of these transitions prevents their giving rise to interstellar absorption, and significant interstellar absorption from ground states only occurs in the UV range.

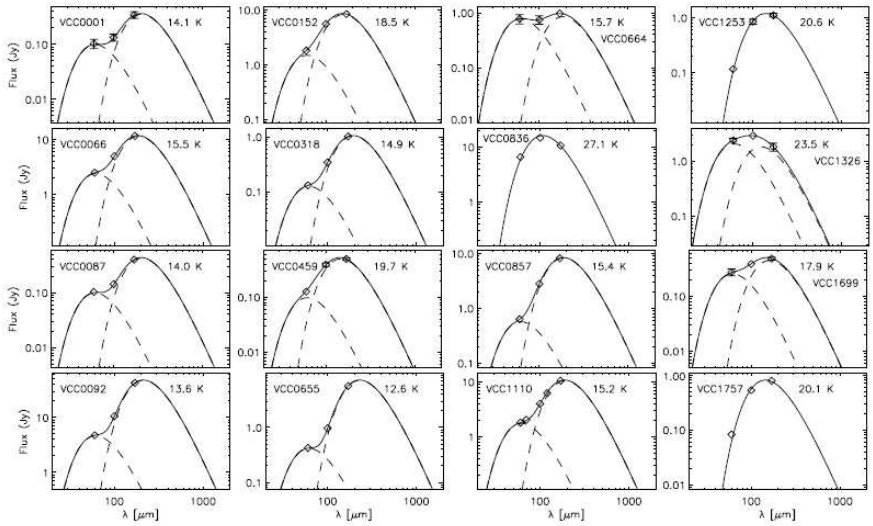

Figure 1.1: FIR SEDs for some spiral galaxies of the Virgo Cluster studied by Popescu et al. (2002). The two modified blackbody functions that fitted the data points (ISOPHOT data) are plotted with dashed lines. The temperature of the warm component is constrained to be 47 K. The fitted temperature of the cold component is marked in each plot, and the sum of the two fitting functions is plotted as the solid line. The galaxy VCC 1110 has additional measurements at 70 and 120 μm, and some galaxies do not show evidence for the two dust components (VCC 1757).

1.2.4 Infrared emission: radiation by dust

The far-infrared (FIR) luminosity ($\sim$3-300 μm) from galaxies is emitted by the interstellar dust heated by the general interstellar radiation field and the more intense radiation in star formation regions. These should produce FIR-sources at different distributions. The grains of dust, mixed with the gas in the ISM, enrich -together to stars- the interstellar gas of heavy elements.

A variety of models have been developed to describe the quasi-blackbody[1] FIR spectral energy distribution (SED) of dusty galaxies. Following the simplest SED, a single blackbody function may not accurately describe the physics of the emission of the dust. The first observations suggesting the existence of a cloud dust component in galaxies were made at submillimeter wavelengths (Chini et al., 1986). The strong millimeter emission found in all the observed galaxies could not be accounted for by dust emitting at an uniform temperature.

To explain this not uniform temperature, it was suggested that the emis-

[1]A very simple description of the FIR emission from a dusty galaxy is based on a blackbody spectrum modified by a frequency dependent emissivity function $\epsilon_\nu \propto \nu^\beta$, where β is in the range 1-2 (Hildebrand, 1983). This yields a spectral distribution function

$$f_\nu = \epsilon_\nu B_\nu \propto \frac{\nu^{3+\beta}}{e^{h\nu/kT} - 1} \tag{1.1}$$

sions at 60 μm and 100 μm observed by the *Infrared Astronomy Satellite* (IRAS) -satellite that has revolutionised the infrared astronomy- could be deconvolved in two components: a warm component with temperature of 50-60 K, and a cool component in *cirrus* at 10-20 K. Since the peak in the thermal spectrum of dust with temperature below $\sim$30 K falls longwards of 100 μm, thus outside the IRAS bands, a clear separation of the warm and cool components was only possible with the *Infrared Space Observatory* (ISO), whose spectral coverage extended up to wavelengths of $\sim$180 μm.

Popescu et al. (2002), studying the spatially integrated FIR emissions of a sample of late-type Virgo Cluster galaxies measured with the ISO centered at 60, 100 and 180 μm, have fitted the FIR spectral energy distribution with a combination of two modified blackbody functions: a localized dust emission component associated with the HII regions, whose temperature is 47 K, and a diffuse emission component of cold dust, broadly distributed, with a median temperature of 18 K (see Fig. 1.1).

The relative contribution of optical and UV photons in heating the dust is an argument that has been much studied in the literature. Popescu et al. (2000), describing a tool for the analysis from the UV to the sub-millimeter spectral energy distribution (SED) of spiral galaxies then applied to the galaxy NGC 891, have calculated which part of emitted FIR luminosity from each volume element of the galaxy is due to the optical and near-infrared (NIR) photons, and which part is due to the UV photons. Fig. 1.2 shows the factional contribution of ultraviolet light from different sources to dust heating for the galaxy NGC 891 (Tuffs & Popescu, 2003). The diffuse optical radiation field only makes a relatively small contribution to the total emitted dust luminosity.

Detailed studies of the FIR emission are now possible thanks to the *Spitzer Space Telescope*, whose high resolution capabilities are leading to new possibilities in studying the structure of nearby galaxies. Two optimum examples are the images of the galaxies M 81 (Gordon et al., 2004) and M 51 (Calzetti et al., 2005), that show the details in the spiral structure of the cold and warm dust. Fig. 1.3 shows the M 81 galaxy observed with the *Spitzer* telescope at 24, 70 and 160 μm, respectively.

Concerning the size of the dust grains, like already said in Section 1.1, there is a significant number of grains comparable in size to the wavelength of the blue light. Grains much smaller than 500 nm would scatter less the light, and this scattering would be isotropic. Grains with dimensions of a fraction of a micron radiate fairly efficiently at temperatures much in excess of tens of Kelvin: these grains are expected to be cool, T $\leq$ 20 K. A grain at 20 K will radiate most strongly near 200 μm, for instance in the sub-mm domain. With IRAS, in addition to the "classical" dust grains, with a size of 0.1 μm and containing $\geq$ 10000 atoms, we have understood that in the ISM there are dust grains extremely small containing $\leq$ 100 atoms. These small grains are detected at shorter IRAS wavebands when a UV photon is absorbed by a grain and its $\sim$10 eV heats the grain. A grain containing only N $\sim$50 atoms has the dimension of a molecule. Leger & Puget (1984) have suggested that many of these objects may be Polycyclic Aromatic Hydrocarbons (PAHs), which are fragments of graphite sheets onto which hydrogen and perhaps some other atoms have adhered here or there.

1.2.5 Radio line emission

Radio telescopes provide some of the most powerful diagnostic of interstellar gas. They can detect spectral line radiation from atomic and mole-

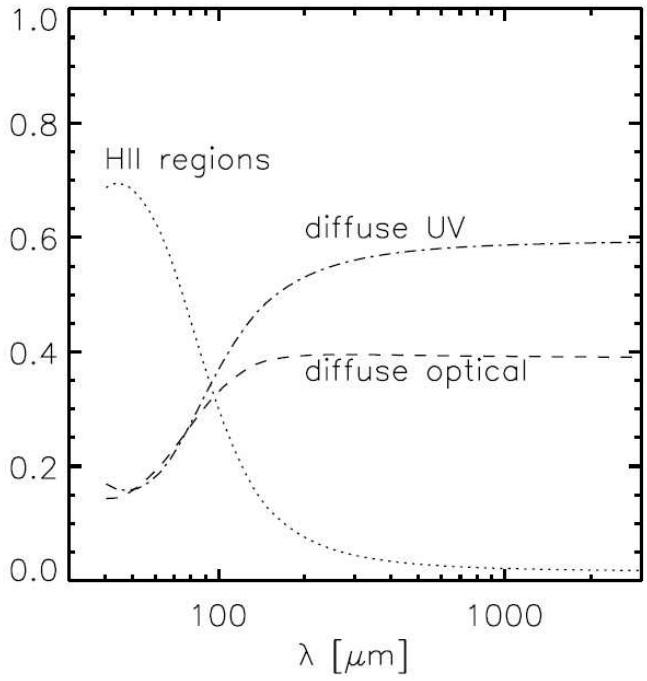

Figure 1.2: The fractional contribution of the UV light from HII regions and the diffuse old stellar component to dust heating for the spiral galaxy NGC 891, studied by Tuffs & Popescu (2003). The diffuse optical contribution is small.

cular transitions that occur in the interstellar medium or in the gaseous envelopes around stars, thermal radiation from solid bodies such as the planets, thermal, or "bremsstrahlung" radiation from hot gas in the interstellar medium, synchrotron radiation from relativistic electrons in weak magnetic fields, pulsed radiation resulting from the rapid rotation of neutron stars surrounded by an intense magnetic field and energetic electrons, and so on.

The 21cm line of atomic hydrogen

The 21cm line of atomic hydrogen, one of the best-studied spectral features in the radio domain, is used to study the distribution and velocity of the atomic gas in the Milky Way Galaxy and in other galaxies. The ground state of the structure of the atomic hydrogen is split into two hyperfine levels by the interaction between the spins of electron and proton. This line arises from the transition between $F = 1$ and $F = 0$ hyperfine structure levels of the ground state (where F is the total angular momentum). Photons with frequency of 1.4204 GHz, corresponding to a wavelengths of 21 cm, mediate transitions between these two levels.

The atomic hydrogen mass of an external galaxy can be determined following the standard way with the 21cm corrected magnitude, when possible, or else with this formula:

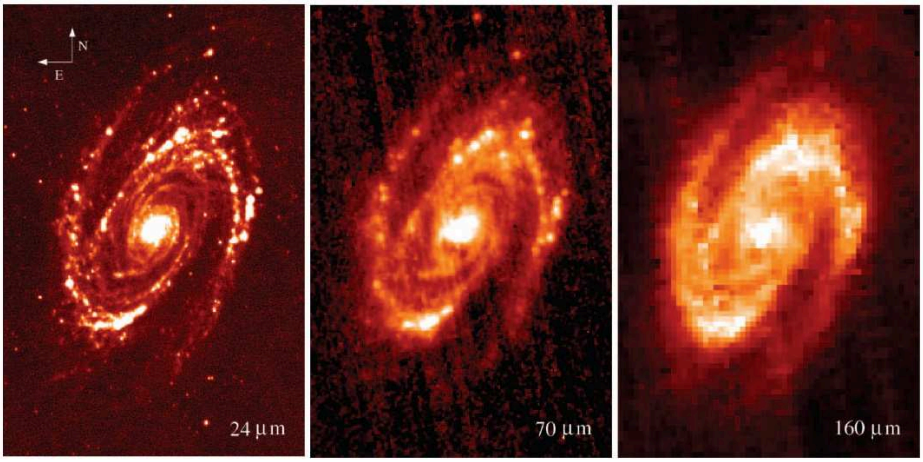

Figure 1.3: *Spitzer* images of M 81 galaxy shown at full instrumental resolution: $6''$, $18''$, and $40''$ for 24, 70, and 160 μm, respectively. The field of view of the image is $20' \times 30'$, much larger than the field covered by M 81.

$$M_{HI}(M_\odot) = 2.36 \times 10^5 \times d^2 \int_{-\infty}^{\infty} S(v)dv \tag{1.2}$$

where d is the distance of the galaxy expressed in Mpc and $S(v)$ the HI integrated flux in Jy km s^{-1} (see, for instance, Roberts et al., 1991; Horellou & Booth, 1997; Binney & Merrifield, 1998).

Molecular component

Using radio telescopes equipped with sensitive spectrometers, radio astronomers have discovered more than 100 separate molecules, including "familiar" chemical compounds like water vapor, formaldehyde, ammonia, methanol, ethanol, and carbon dioxide. These distinct molecular species have been found in a wide range of astronomical localizations. Now we know that molecules are present within our Galaxy: in the atmospheres of cool stars, in stellar envelopes, in planetary nebulae, in the jets of novae and supernovae, in diffuse and dense clouds in the ISM, and star formation regions. Molecules are present in external galaxies too, and have been identified in objects at redshift up to $\sim$6.

The major constituent of the molecular clouds is the hydrogen molecule, H_2. Unfortunately, the H_2 molecule has no permanent electric dipole moment and is only excited to vibrational states. The lowest vibrational transitions are excited at about 2000 K, therefore the emission lines of H_2 at $\lambda \approx 2\ 6\mu$m are only observed towards molecular clouds in the vicinity of HII regions where the molecular gas is heated to temperatures of about 1000 K. In star forming regions where the temperature is only 10-100 K, H_2 is excited only at low-lying rotational states which lifetime is extremely long. Since most of the molecular gas is hidden from our view, we have to rely on

the emission lines of other molecules, in combination with the knowledge of a relation between the line radiation of these molecules and the H_2.

The carbon monoxide molecule (CO), existing in the form of its different isotopes (*e.g.* ^{12}CO, ^{13}CO), is the second most abundant molecule in the cool dense phase of the ISM. The relative abundance of CO and H_2 is of order of 10^{-5} - 10^{-4} and depends on the metallicity (the abundance of C and O), and other influences like the strength of the radiation field and the efficiency of molecule formation. One of the main advantage of the ^{12}CO is that the lower rotational transitions (J=1 $\rightarrow$ J=0 and J=2 $\rightarrow$ J=1, observed at 2.6 mm and 1.3 mm, respectively) are already excited for collision (with H_2 molecules) at relatively low H_2 densities, and so the ^{12}CO is usually used to estimate indirectly the H_2 abundance in cold molecular clouds. These CO millimetric lines and those of CS and HCN constitute powerful probes of the dense and cold components of the ISM.

The H_2 - CO conversion factor

In spite of the high optical depth of the ^{12}CO line, as noted by Phillips et al. (1979), there are theoretical and empirical basis for the use of CO as a tracer of the mass of the Giant Molecular Clouds (GMCs) in luminous galaxies. There is an empirical correlation between the virial masses of molecular clouds with known sizes and linewidths, and their CO luminosities for some Local Group galaxies (see Fig. 1.4). The same measures for external galaxies are difficult because a high spatial resolution is needed. However, since the few extragalactic molecular clouds seem apparently similar to those in the Milky Way (Young & Scoville, 1991), the use of the Galactic H_2 to CO proportionality for external galaxies is, at least partially, justified.

This proportionality is defined as the conversion factor X between the H_2 column density of the molecular hydrogen $N(H_2)$ and the intensity of CO emission integrated over the line profile:

$$X = N(H_2)/I_{CO} \tag{1.3}$$

where

$$I_{CO} = \int T_{CO} dv \tag{1.4}$$

with T_{CO}, the ^{12}CO(1$\rightarrow$0) brightness temperature. Following Young & Scoville (1991), we can show the theoretical basis of the proportionality between H_2 mass and CO luminosity. Defining the CO luminosity of a cloud as

$$L_{CO} = d^2 \int I_{CO} d\Omega \tag{1.5}$$

where d is the distance of the cloud, for an uniform and spherical cloud of radius R, the CO luminosity is given by:

$$L_{CO} = \pi R^2 T_{CO} \Delta v \tag{1.6}$$

where Δv is the linewidth. Numerous studies of molecular clouds in our Galaxy have shown that they are self-graviting, and for a cloud in virial

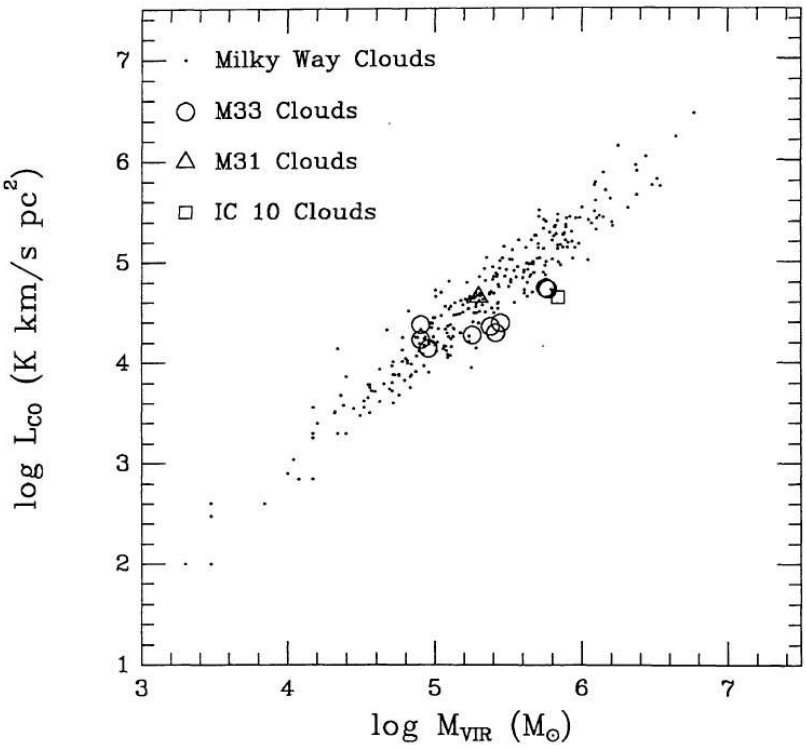

Figure 1.4: Comparison of CO luminosities and virial mass of the molecular clouds in the Milky Way, M 31, M 33, and in the low-metallicity galaxy IC 10. The linear proportionality found for these objects justifies the use of the same H_2 to CO conversion factor in external galaxies (Young & Scoville, 1991).

equilibrium $\Delta V = \sqrt{GM/R}$, and since $M_{cloud} = \frac{4}{3}\pi R^3 \rho$ we obtain:

$$M_{cloud} = L_{CO}\sqrt{\frac{4\rho}{3\pi G}}\frac{1}{T_{CO}} \tag{1.7}$$

If the ratio $\sqrt{\rho}/T_{CO}$ does not vary in the mean from galaxy to galaxy and the emission of separate clouds along each line of sight is not overlapped in velocity, the Eq. 1.7 shows that the total CO luminosity of a cloud is directly proportional to its molecular mass.

The value of the conversion factor X is still a subject of debate. Usually the *standard* value of X found for the Milky Way is universally adopted for all the galaxies and for all the regions of a same galaxy ($X = 2.3 \times 10^{20}$ mol cm^{-2} (K km s^{-1})$^{-1}$, Strong et al., 1988). This assumption turned out to be often not correct. In general the determination of H_2 column densities and CO measurements is a difficult task, and detailed analyses of the cloud conditions are needed to get reliable estimates of the molecular content in environments different from our local neighbourhood.

The delicate dependence of the X value on the small scale physical properties of the gas will be discussed in detail in the Chapter 2.

1.3 Other emissions

Even if this Thesis is dedicated to the molecular gaseous component of the interstellar medium in external galaxies and to the relations between this component and the other ones, such as UV or IR, in this section we will shortly describe also the other constituents of the ISM in order to give a complete scenario of gas and dust content of the galaxies.

1.3.1 γ-ray emission

Gamma-rays are the most energetic form of electromagnetic radiation, with over 10^4 times more energy than visible light photons, and the corresponding spectral domain extends from an energy of 0.05 MeV to 10^{11} MeV. γ-rays are difficult to observe from ground-based telescopes due to atmospheric absorption, and high-altitude balloons, sounding rockets, and orbiting observatories are therefore used, such as the Compton Gamma Ray Observatory-CGRO or the future Gamma-ray Large Area Space Telescope-GLAST.

Low-energy (or soft) γ-ray astronomy (up to a few megaelectronvolts) deals mainly with processes in dense media, such as plasmas confined close to neutron stars and black holes. It also concerns cosmic sites where monoenergetic photons are released either by deexcitation of atomic nuclei (nuclear lines) or by positron-electron annihilation (the 0.511 MeV line). γ-ray astronomy at higher energies relates to emissions induced by relativistic particles throughout the whole interstellar medium, as well as in the vicinity of some neutron stars and in the powerful jets beamed by active galactic nuclei. The penetration power of γ-ray photons enables exploration of regions that are hidden at other wavelengths, such as the galactic center region, as well as of the first stages of the Universe, since the cosmos is particularly transparent to γ-rays (with the exception of photons whose energy exceeds 10^6 MeV).

A large fraction of the cosmic γ-ray photons originates in interstellar sites: cosmic-ray-induced interstellar emission results mostly from the interaction of cosmic rays (electrons and protons) with the interstellar gas. The high-energy γ-ray sky is dominated by radiation from the galactic plane whose spatial distribution and intensity can be reliably modeled from knowledge of the interstellar gas distribution. A large fraction of the pointlike sources observed at medium galactic latitude may be related to the local interstellar medium. γ-rays have been found emanating from radio galaxies, Seyfert galaxies, and supernovae.

1.3.2 Thermal radio continuum emission

The radio continuum emission from a normal galaxy consists of two components: a non-thermal component produced via synchrotron emission and a thermal one due to a free-free emission from HII regions.

Thermal re-irradiation of starlight by dust quickly overwhelms these components above ν ~200 GHz (λ ~1.5 mm), defining a practical upper bound to the frequencies of the radio observations. Observing the spectrum of the starburst galaxy M 82 (Fig. 1.5), we can note the typical relative intensities of synchrotron radiation, free-free (bremsstrahlung) emission, and the dust re-irradiation.

The free-free emission emerges from HII regions containing ionizing stars, where the electrons in the interstellar plasma are subject to coulomb interaction with ions, and they travel on hyperbolic trajectories in which they are

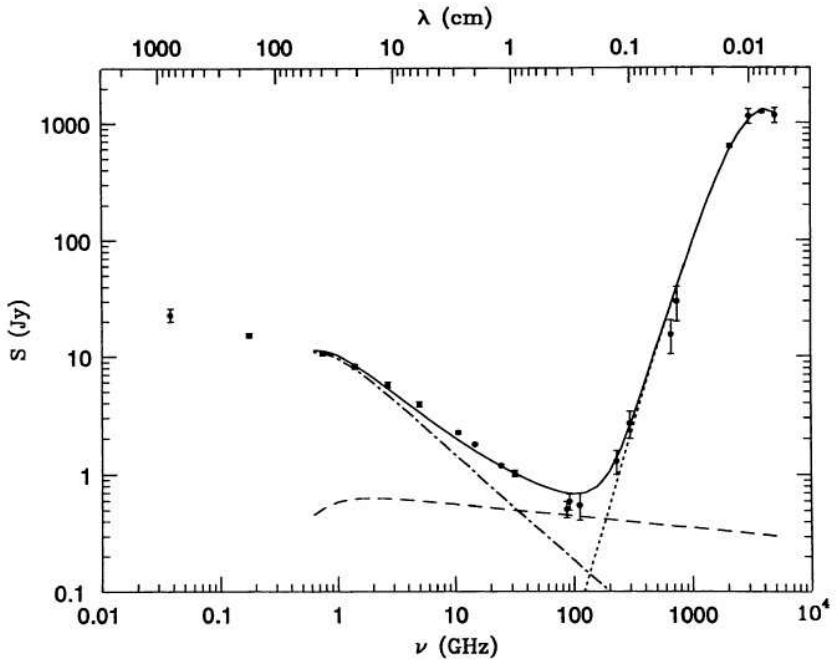

Figure 1.5: The observed radio/FIR spectrum of the galaxy M 81 (Klein et al., 1988; Carlstrom & Kronberg, 1991) is the sum of the synchrotron (*solid line*), free-free (*dot-dash line*), and dust (*dashed-line*) components (Condon, 1992).

accelerated and radiate. This emission, called "free-free" because the electron passes from an unbound state to another unbound state -though it loses energy- has an intensity proportional to the production rate of Lyman continuum photons. However, isolating the free-free component and measuring its flux density is very difficult observationally because the flat-spectrum free-free emission is usually weaker than the steep-spectrum synchrotron emission below $\nu \sim$30 GHz (see Fig. 1.5).

The specific emissivity, in c.g.s. units, at a certain temperature T (in K) for an ionized plasma of electrons with Maxwellian velocity distribution and numerical density n_e (in cm^{-3}), and a density n_i (in cm^{-3}) of ions with atomic number Z, is given by:

$$J_{br} \simeq 6.8 \times 10^{-38} T^{-1/2} e^{-h\nu/kT} n_i n_e Z^2 \bar{g}_{ff} \tag{1.8}$$

in units of erg s^{-1} Hz^{-1} cm^{-3}, and where $\bar{g}_{ff}$ is the average Gaunt factor. The $\bar{g}_{ff}$ value has been determined for a great number of different situations, and for typical radio frequencies $\bar{g}_{ff}$ varies as $T^{0.15}\nu^{-0.1}$ (Spitzer, 1978).

Using the radiative transport equation, the brightness of an object emitting via bremsstrahlung is given by:

$$B_{br} = \frac{J_{br}}{4\pi k_{br}}(1 - e^{\tau}) \tag{1.9}$$

where the k_{br} is the absorption coefficient, and τ is the optical depth. In the Rayleigh-Jeans domain, the brightness can be approximated and the Eq. (1.9) becomes:

$$B(\nu,T) = 2kT_e\frac{\nu^2}{c^2} \qquad \tau \gg 1$$
$$B(\nu,T) = 2kT_e\frac{\nu^2}{c^2}\tau \qquad \tau \ll 1 \tag{1.10}$$

where T_e is the electron temperature. From Eqs. 1.10 we can note that in the optically thick case, at low frequencies, the spectrum region emitting via bremsstrahlung grows proportionally to ν^2, while in the optically thin case the spectrum is almost constant for a large range of frequencies. Thus the temperature of the plasma is the observed brightness temperature at $\nu \ll \nu_1$, where ν_1 is the frequency at which the spectrum passes from the constant value to the Rayleigh-Jeans form $f_\nu \sim \nu^2$.

Free-free radiation is the most intense source of radiation from HII regions, and the nearby Orion nebula is one of the best studied HII region. In general, the thermal radio luminosity of a normal galaxy indicates the total photoionization rate and so the current number of the most massive short-live stars.

1.3.3 Non-Thermal synchrotron emission

The non-thermal synchrotron radiation is produced by highly relativistic electrons spiralising in a magnetic field. The radiation from a single electron, of energy $E = \gamma m_0 c^2$ with $\gamma = 1/\sqrt{1 - v^2/c^2}$ Lorentz factor, has a helicoidal trajectory, with the helix axis parallel to the magnetic lines of force and is collimated into a cone with half-opening angle $1/\gamma$, centered in the instantaneus direction of the velocity. The observer receives a short pulse each time the beam crosses the line of sight. The synchrotron power by a single electron, moving at an angle θ to the direction of the magnetic field B is:

$$-\frac{dE}{dt} \sim (Bsin\theta)^2\gamma^2 \tag{1.11}$$

and the most of its energy is emitted near the critical frequency $\nu_c \sim (Bsin\theta)\gamma^2$.

At a given frequency, the energy (or Lorentz factor) of the emitting electrons depends upon the magnetic field strength. For a typical spiral disk the order of magnitude for the magnetic filed strength is ∼1-10 μG, in the radio domain between 10 MHz and 100 GHz, the synchrotron emission is generated by electrons with Lorentz factor in the range 10^3 - 10^5.

In Astrophysics normally we deal with a gas of electrons with different energies: assuming that every particle is emitted independently from the others, that total emission can be obtained by simply adding contributions from each particle. If $N(E)dE$ is the number of particles per unit volume with energy between E and $E + dE$, and we assume a power-law energy

distribution of the electrons, such as

$$N(E) = N_0 E^{-\delta} \tag{1.12}$$

where N_0 and δ are constants, the synchrotron emissivity is:

$$J_s(\nu) \propto N_0 B^{(\delta+1)/2} \nu^{-\alpha} \qquad ergs^{-1}Hz^{-1}cm^{-3} \tag{1.13}$$

where $\alpha = \frac{\delta-1}{2}$ is the spectral index.

The spectral index of the non-thermal emission from a normal galaxy is usually $\alpha \sim 0.8$, and so $\delta \sim 2.6$.

Synchrotron polarization

The synchrotron radiation presents a high degree of linear polarization. If the magnetic field acting on the plasma is uniform, the synchrotron radiation emitted is strongly polarized perpendicular to the direction of the magnetic field. The degree of polarization may vary between 70 - 80% of the total intensity, in practice, however, the direction of the magnetic field may vary along the line of sight, and the observed value is less than these values. The total synchrotron emission traces the total field in the sky plane and the polarized synchrotron emission traces the regular field component.

To determine the field strength from the synchrotron intensity it is necessary to do an assumption on the relation between cosmic ray electrons and magnetic fields: the minimum total energy density, $\epsilon_{tot} = \epsilon_{CR} + \epsilon_B =$ min, where ϵ_{CR} is the relativistic particle energy density and ϵ_B is the magnetic field density. The total energy for a given synchrotron luminosity is minimized when $\epsilon_B = \frac{3}{4}\epsilon_{CR}$, that is very close to energy equipartition ($\epsilon_{CR} = \epsilon_B$), so minimum-energy and equipartition are often used as synonymous.

This assumption was first proposed by Burbidge (1956) and applied to the optical synchrotron emission of the jet in M 81 galaxy. The validity of this method has been discussed in the literature, and in our Galaxy the accuracy of the equipartition assumption can be tested because we have independent information about the local ray-cosmic energy density from in-situ measurements and about their radial distribution from γ-ray data. Combination with radio synchrotron data gives a local strength of the total field $\langle B_T \rangle$ of 6 μG (Strong et al., 2000), in agreement with the value derived from energy equipartition estimates (Beck, 2001). On the other hand, Chi & Wolfendale (1993) claimed significant deviation from equipartition conditions in the Magellanic Clouds.

Equipartition estimates of field strengths were determined in many spiral galaxies (Beck, 2000). The mean strength of the total field ranges from a few μG in galaxies with a low star-formation rate to $\cong$ 30 μG in grand-design galaxies like M 51. A recent equipartition and minimum energy formula have been proposed by Beck & Krause (2005). This revised estimate for the field strength gives larger values than the classical estimate for the flat radio spectra ($\alpha \sim$0.5 - 0.6) but smaller values for steep spectra.

Separating thermal and non-thermal emissions

As said before, the total radio spectrum of a galaxy consists of thermal and non-thermal component. Concerning the non-thermal component radio

emission, a division can be made between the diffuse radio emission from cosmic ray electrons spread over the galactic disk and halo, and the discrete emission from supernova remnants (SNRs)[2]. The spectrum of the diffuse synchrotron emission is shaped by the physical processes that are characterizing the cosmic rays, in particular the type of propagation (diffuse or convection), the type of energy losses, and the confinement. Gioia et al. (1982), analysing a sample of nearby spiral galaxies, have found that the distribution of integrated indices is peaked at $\alpha = 0.75$ recalling the fact that the spectra are dominated by the non-thermal component.

In principle, the relatively flat-spectrum ($\alpha \leq 0.1$) thermal radio emission should be distinguishable from the steeper-spectrum ($\alpha \sim 0.8$) non-thermal emission via total flux densities or maps obtained at two or more frequencies. In practice, most normal galaxies are not bright enough to be detected at frequencies much higher than $\nu \sim 10$ GHz, so the observed thermal fractions S_T/S, where S is the total flux density, are small and most measured S_T are uncertain by a factor of two.

Condon & Yin (1990) suggested that the ratio of non-thermal to thermal radio fluxes may be the same for the most spiral galaxies. The average value of this ratio is approximately given by:

$$\left\langle \frac{S_{NT}}{S_T} \right\rangle \sim 10 \left(\frac{\nu}{1GHz} \right)^{0.1-\alpha} \tag{1.14}$$

where $\alpha \sim 0.8$ is a typical non-thermal index. The non-thermal flux typically exceeds the thermal flux for all frequencies below $\nu \sim 30$ GHz ($\lambda \sim 1$ cm). At $\nu \sim 1.4$ GHz, on average, about only 10 % of the total flux is thermal.

To separate observationally the diffuse radio emission from the SNRs requires spatially resolved observations, but is difficult since the spectral index of these two emissions are very similar. Lisenfeld & Völk (2000) estimated that the radio emission of SNRs represents about 10% of the non-thermal emission of a galaxy. This moderate contribution has a noticeable effect on the non-thermal radio spectral index, lowering it by 0.1 for steep spectra.

[2]Stars with masses greater than ~ 8 $M_\odot$ die in a catastrophic and spectacular way: the core collapses within a second and the energy released drives infalling matter outwards in a violent explosion, producing the visible supernova. The interaction of the expanding supernova debris with the ISM produces supernova remnants.

Chapter 2

Molecular gas in galaxies

Introduction

Technical progress in millimeter-wave receiver technology made possible to map molecular clouds at high sensitivity in short time of integration. Focal plane arrays at the FCRAO 14 m (Five College Radio Astronomy Observatory) and the NRAO 12 m (National Radio Astronomy Observatory) single dish telescopes have increased the mapping speed by an order of magnitude. Up to four receivers operating at different frequencies can be used simultaneously at the IRAM 30 m (Institut de Radioastronomie Millimétrique) telescope to observe the same position on the sky. The building and improvement of the millimeter-wave interferometers (IRAM, OVRO-Owens Valley Radio Observatory, and BIMA-Berkeley Illinois Maryland Association) have dramatically increased the imaging quality and sensitivity of these instruments and have made high resolution observations ($< 10''$) of structure in molecular clouds considerably quicker and easier.

Thanks to these instruments the molecular component in Our and external galaxies has been and is now explored and it is, correctly, considered an important constituent of the ISM. In this Chapter we analyze the principal characteristics of the molecular structures in the galaxies.

2.1 Molecular Clouds

Molecular clouds are generally self-gravitating, magnetized, turbulent, and compressible fluids. The puzzle of how stars form from molecular clouds begins with understanding the physics of such objects and how individual, gravitationally unstable cores condense within them.

Most of the mass of the molecular ISM is in the form of Giant Molecular Clouds (GMCs), with masses $\sim 10^{5-6}$ $M_\odot$, diameters ~ 50 pc, and average densities $n_{H_2} \sim 10^2$ cm^{-3} (e.g. Blitz, 1993). The upper end of the molecular cloud mass distribution has a sharp cut-off at $\sim 6 \times 10^6$ $M_\odot$, indicating that cloud masses are limited by some physical process, such as the tidal field of the galaxies or the disrupting effect of massive stars within them.

Heyer & Terebey (1998), performing a high resolution survey of the CO emission on the outer Galaxy with the FCRAO telescope, have realized a detailed study of the large scale structure of the ISM. They confirmed that there are large regions with little or no CO emission (Dame et al., 1986), in agreement to earlier results that these regions have been cleared of molecular

gas by the intense radiation fields and stellar winds from massive stars. The structural imprint of the massive star formation in individual star forming regions is discussed in several observational studies, such as Carpenter et al. (1995) and Heyer et al. (1996) for our Galaxy, or Patel et al. (1995) for the IC 1396 galaxy. Carpenter et al. (1995) have suggested that massive stars can compress gas and create dense cores that give rise to the next generation of star formation as originally proposed by Elmegreen & Lada (1977).

Digel et al. (1996) and Heyer & Terebey (1998) showed that CO emission in the outer Galaxy is confined almost exclusively to the spiral arms, confirming the earlier results of Cohen et al. (1980). The ratio of emission in the arm with respect to the interarm regions is greater than 28:1. The absence of molecular gas in the interarm regions implies that molecular clouds form from a compressed atomic medium, and have lifetimes that are shorter than the arm crossing time ($\sim 10^7$ yr). These conclusions may not apply in the inner Galaxy where it has been more difficult to isolate arm emission and calculate an arm-to-interarm ratio. Solomon & Rivolo (1989) have argued that about half of the CO in the inner Galaxy is in clouds that are not actively forming stars, and that this gas is not concentrated in spiral arms. However, Loinard et al. (1996) have found an arm-to-interarm ratio $\sim$10:1 in M 31 galaxy in the south-west ring $\sim$9 kpc from the galaxy center, which suggests that similar conclusions about cloud formation and lifetimes can be draw in that galaxy too.

Studies on HI halos around molecular clouds (e.g. Williams & Maddalena, 1996; Moriarty-Schieven et al., 1997) have shown that to form a GMC of mass 10^6 $M_\odot$ out of an atomic ISM of density n_H $\sim$1 cm^{-3}, gas must be accumulated from a volume $\sim$0.4 kpc in diameter. Since such a large region encompasses many atomic clouds, the density inhomogeneities in molecular clouds may simply reflect the initial non-uniform conditions of their formation rather than the first step in the fragmentation/condensation process that leads to the creation of stars (Elmegreen, 1985). To distinguish between the remnants of the formation of a cloud and the first steps toward star formation, it is necessary to analyze and compare structures in a number of different clouds.

2.2 Cloud structure

Before to discuss the analysis of cloud structure, we can define an operational categorization into clouds, clumps, and cores. Almost all known molecular clouds in the Galaxy are detectable in CO. Giant molecular clouds have masses $\gtrsim 10^4$ $M_\odot$, are generally gravitationally bound, and may contain several sites of star formation. However, there are also small molecular clouds with masses $\lesssim 10^2$ $M_\odot$, such as the unbound high latitude clouds discovered by Blitz et al. (1984), and the small gravitational bound molecular clouds in the Galactic plane catalogated by Clemens & Barvainis (1988). A small number of low mass stars are observed to form in some of these clouds but the contribution to the total SFR in the Galaxy is negligible (Magnani et al., 1995).

Clumps are coherent regions in galactic longitude and latitude, and radial velocity space (l-b-v), generally identified from spectral line maps of molecular emission. Star-forming clumps are the massive clumps out of which stellar clusters form. Although most clusters are unbound, the gas out of which they form is bound (Williams et al., 1995).

Cores are regions out of which single stars (or multiple systems such as binaries) form and are necessarily gravitationally bound. Not all material that goes into forming a star must come from the core; some may be accreted from the surrounding clump or cloud as the protostar moves trough it (Bonnell et al., 1997).

2.2.1 The Virial Theorem for molecular clouds

The condition for a molecular cloud or a clump within it to be gravitationally bound can be inferred from the virial theorem, which can be written:

$$\frac{1}{2}\ddot{I} = 2\,(T - T_0) + E_M + W \tag{2.1}$$

where I is the moment of inertia, T is the total kinetic energy (including thermal), E_M is the net magnetic energy, and W is the gravitational energy (see McKee et al., 1993, for more details). The kinetic energy term can been expressed as:

$$T = \int_{V_{cl}} \left(\frac{3}{2}P_{th} + \frac{1}{2}\rho v^2\right) dV = \frac{3}{2}\bar{P}V_{cl} \tag{2.2}$$

that includes both the thermal and non-thermal pressure inside the cloud. The surface term can be expressed as $T_0 = 3/2 P_0 V_{cl}$, where P_0 is about equal to the total thermal plus non-thermal pressure in the ambient medium (McKee & Zweibel, 1992). Finally, the gravitational term can be written as (Bertoldi & McKee, 1992):

$$W = -3P_G V_{cl} \tag{2.3}$$

where the gravitational pressure P_G is the mean weight of the material in the cloud. With these results, the steady-state virial theorem becomes:

$$\bar{P} = P_0 + P_G\left(1 - \frac{E_M}{|W|}\right) \tag{2.4}$$

In this form, the virial theorem has an immediate intuitive meaning: the mean pressure inside the cloud is the surface pressure plus the weight of the material inside the cloud, reduced by the magnetic field.

In the absence of an external gravitational field, W is the gravitational energy of the cloud:

$$W = -\frac{3}{5}a\left(\frac{GE_M^2}{R}\right) \tag{2.5}$$

where a is a numerical factor of order unity that has been evaluated by Bertoldi & McKee (1992). The gravitational pressure is then:

$$P_G = \frac{3\pi a}{20}G\Sigma^2 \rightarrow 5540\bar{A}_V^2 \qquad \mathrm{K\,cm^{-3}} \tag{2.6}$$

where Σ is the mean surface density of the cloud and A_V is the corresponding visual extinction. The numerical evaluation is for a spherical cloud with a $1/r$ density profile.

Magnetic fields play a crucial role in the structure and evolution of molecular clouds. For poloidal fields, the relative importance of gravity and magnetic field is determining by the ratio of the mass to the *magnetic critical mass*:

$$M_\phi = \frac{c_\phi \phi}{G^{1/2}} \tag{2.7}$$

where ϕ is the magnetic flux through a clump of radius R, $\phi = \pi R^2 B$ with B magnetic field intensity, and the value of the numerical factor c_ϕ depends on the distribution of mass to flux. For $M < M_\phi$, the cloud is said to be *magnetically subcritical*: such a cloud can never undergo gravitational collapse since the magnetic force always exceeds the gravitational force. Conversely, $M > M_\phi$, the cloud is *magnetically supercritical*, and magnetic fields cannot prevent gravitational collapse.

If the cloud is supported by thermal and non-thermal pressure in addition to the magnetic stresses, then the maximum stable mass is the critical mass M_{cr}, and the cloud is subcrtitical for $M < M_{cr}$ and supercritical for $M > M_{cr}$. For an isothermal cloud, the critical mass is given by $M_{cr} \simeq M_\phi + M_{BE}$, where the Bonnor-Ebert mass $M_{BE} = 1.18 c_s^4/(G^3 P_0)^{1/2}$ is the largest gravitationally stable mass at an exterior pressure P_0 for a non magnetic sphere (McKee, 1989).

What do observations say about the importance of magnetic fields in clouds? Crutcher et al. (1994) for the Barnard 1 cloud have found that the inner envelope is marginally magnetically subcritical whereas the densest region is somewhat supercritical. The observational results were shown to be in good agreement with a numerical model that, however did not include the observed non-thermal motions. Crutcher (1999) has summarized the observations of magnetic fields in a number of clouds, and found that they are magnetically supercritical. In this sample, which tends to focus on the central regions of clouds, there is no clear case in which a cloud is magnetically subcritical but GMCs are all supercritical with $M/M_\phi \simeq 2$.

With these results, we can now address the issue of whether molecular clouds and their constituents are gravitationally bound. The virial theorem (eq. 2.4) enables us to write the total energy $E = T + E_M + W$ as:

$$E = \frac{3}{2}\left[P_0 - P_G\left(1 - \frac{E_M}{|W|}\right)\right] V_{cl} \tag{2.8}$$

In the absence of a magnetic field, the condition that the cloud be bound (*i.e.*, E < 0) is simply $P_G > P_0$. This criterion is used even for magnetized clouds, bearing in mind that using the total ambient gas pressure for P_0 is an overestimated and that the analysis is approximated because we have used the time-average virial theorem.

For GMCs, the surface pressure is that of the ambient interstellar medium. In the solar vicinity, the total interstellar pressure, which balances the weight of the ISM, is about 2.8×10^4 K cm^{-3} (Boulares & Cox, 1990). Of this, about 0.7×10^4 K cm^{-3} is due to cosmic rays, and since they pervade both the ISM and a molecular cloud, they do not contribute to the support of a

cloud and may be neglected. The magnetic pressure is about 0.3×10^4 K cm^{-3} (Heiles, 1996), leaving $P_0 \simeq 1.8 \times 10^4$ K cm^{-3} as the total ambient gas pressure.

What is the minimum value of P_G for a molecular cloud? According to van Dishoeck & Black (1988), molecular clouds exposed to the local interstellar radiation field have a layer of C^+ and C^0 corresponding to a visual extinction of 0.7 mag. If we require at least 1/3 of the carbon along a line of sight through a cloud to be in the form of CO in order for it to be considered "molecular", then the total visual extinction must be $\bar{A_V} > 2$ mag (allowing for a shielding layer on both sides). According to equation (2.6), this gives $P_G \gtrsim 2 \times 10^4$ K cm^{-3} $\sim P_0$, verifying that molecular clouds as observed in CO are at least marginally bound. Note that if we defined molecular clouds as having a significant fraction of H_2 rather than CO, the minimum column density required would be substantially less and the clouds might not be bound. Furthermore, the conclusion that CO clouds are bound depends on both the interstellar pressure and on the strength of the FUV radiation field, and CO clouds may not be bound everywhere in the Galaxy or in other galaxies (Elmegreen, 1993).

GMCs in the solar neighborhood typically have mean extinctions significantly greater than 2 mag, and as a result P_G is generally significantly greater than P_0. For GMCs in the solar neighborhood, $P_G \sim 2 \times 10^5$ K cm^{-3}, an order of magnitude greater than P_0 (e.g. Williams et al., 1995). Thus if GMCs are dynamically stable entities (the crossing time for a GMC is about 10^7 yr, smaller than the expected lifetime - Blitz & Shu, 1980), then GMCs must be self-gravitating. In the inner Galaxy where P_0 is expected to be greater, the typical GMC linewidths also appear to be somewhat greater than those found locally (Sanders et al., 1985), and thus P_G is still comfortably greater than P_0.

For clumps within GMCs, the surface pressure is just the mean pressure inside the GMC, $P_G(\mathrm{GMC}) \propto \Sigma^2(\mathrm{GMC})$, so the virial theorem becomes $\bar{P}(\mathrm{clump}) \propto \Sigma^2(\mathrm{GMC}) + \Sigma^2(\mathrm{clump})$. Most clumps observed in ^{13}CO have $\Sigma(\mathrm{clump}) \ll \Sigma(\mathrm{GMC})$ and are therefore confined by pressure rather than gravity; on the other hand, much of the mass is in massive star-forming clumps that have $\Sigma(\mathrm{clump}) \gtrsim \Sigma(\mathrm{GMC})$ and are therefore gravitationally bound (Bertoldi & McKee, 1992).

2.2.2 Structure analysis techniques

Molecular cloud can be mapped via radio spectroscopy of molecular lines (e.g. Bally et al., 1987), continuum emission from dust (e.g. Wood et al., 1994), or stellar absorption by dust (e.g. Lada et al., 1994). The first gives kinematical as well as spatial information and results in a three dimensional cube of data, whereas the latter two results in two dimensional datasets. Many different techniques have been developed to analyze these data which we discuss briefly.

Stutzki & Guesten (1990) and Williams et al. (1994) used the most direct approach decomposing the data into a set of discrete clumps; the first based on recursive triaxial Gaussian fits, and the latter by identifying peaks of emission and then tracing contours to lower levels. The resulting clumps can be considered to be the "building block" of the cloud and may be analyzed in any number of ways to determine a size-linewidth relation, mass spectrum, and variations in cloud conditions as a function of position

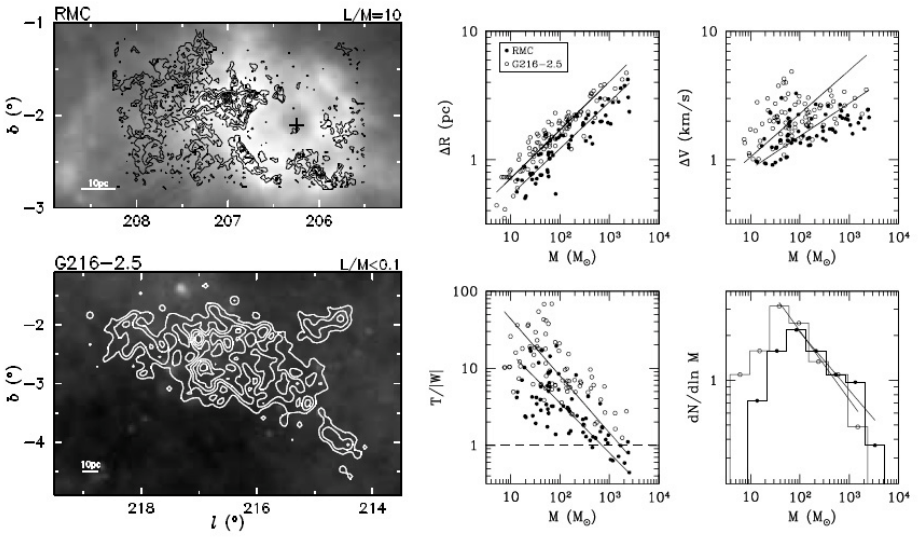

Figure 2.1: Structure in the Rosette and G216-2.5 molecular clouds by Williams et al. (2000). The two left panels show contours of velocity integrated CO emission (with levels at 15 K km s^{-1} for the RMC and 1.8 K km s^{-1} for G216-2.5) overlaid on a greyscale image of the IRAS 100 μu intensity (1.1 to 2.5 MJy sr^{-1} for the two clouds). The Rosette cloud is IR bright, indicative of its high SFR, but G216-2.5 has a very low IR luminosity due to a lack of star formation within it. The four rightmost panels show power law relations between clump mass and size, linewidth, energy balance, and number (i.e. clump mass spectrum) for the two clouds. The solid circles represent clumps in the RMC, and open circles represent clumps in G216-2.5. Each relationship has been fit by a power law: note that the power law exponent is approximately the same for the clumps in each despite the large difference in star formation activity.

(Williams et al., 1995). However, there are caveats associated with each method of clump deconvolution. Since the structure in a spectral line map of a molecular cloud is not, in general, gaussian, the recursive fitting method of Stutzki & Guesten (1990) tends to find and subsequently fit residuals around each clump, which result in a mass spectrum that is steeper than the true distribution. On the other hand, the contour tracing method of Williams et al. (1994) has the tendency to blend small features with larger structures and results in a mass spectrum that is flatter than the true distribution.

2.2.3 Clumps

Clumps decomposition methods, such as those describe above, can be readily visualized and have an appealing simplicity. In addition, as for all automated techniques, these algorithms offer an unbiased way to analyze datasets, and are still a valid and useful tool for cloud comparisons, even if one does not subscribe to the notion of clumps within clouds as a physical reality (Scalo, 1990).

In a comparative study of two clouds, Williams et al. (1994) searched for differences in cloud structure between a star forming and non-star forming GMC. The datasets they analyzed were maps of ^{13}CO(1-0) emission with

similar spatial (0.7 pc) and velocity resolution (0.68 km s^{-1}), but the two clouds -although of similar mass $\sim 10^5$ $M_\odot$- have very different levels of star formation activity. The first, the Rosette molecular cloud, is associated to an HII region powered by a cluster of 17 O and B stars and also contains a number of bright infrared sources from ongoing star formation deeper within the cloud (Cox et al., 1990). The second cloud, G216-2.5, originally discovered by Maddalena & Thaddeus (1985), contains no IRAS sources from sites of embedded star formation and has an exceptionally low far-infrared luminosity to mass ratio (Blitz, 1990), $L_{IR}/M_{cloud} < 0.07$ $L_\odot/M_\odot$, if compared to more typical values of order unity (see Williams & Blitz, 1998).

Almost 100 clumps were catalogued in each cloud, and sizes, line-widths, and masses were calculated for each. These basic quantities were found to be related by power laws with the same index for the two clouds, but with different offsets (Fig. 2.1) in the sense that for a given mass, clumps in the non-star forming cloud are larger, and have greater linewidths than in the star forming cloud. The similarity of the power law indices suggests that, on these scales, $\sim$ few pc, and at the low average densities, $\langle n_{H_2} \rangle = 300$ cm^{-3}, of the observed clumps, the principal difference between the star forming and non-star forming cloud is the change of scale rather than the collective nature of the structures in each cloud.

Fig. 2.1 shows that the kinetic energy of each clump in G216-2.5 exceeds its gravitational potential energy, and therefore no clump in the cloud is bound (although the cloud as a whole is bound). On the other hand, Williams et al. (1995) showed that, for the Rosette molecular cloud, the star formation only occurs in the gravitationally bound clumps in the cloud. Therefore, the lack of bound clouds in G216-2.5 may explain why there is no star formation currently taking place within it.

Even in Rosette cloud, most clumps are not gravitationally bound. These unbound clumps have similar density profiles, $n(r) \propto 1/r^2$, but contain relatively little dense gas as traced by CO(3-2) or CO(2-1) (Williams & Blitz, 1998). The unbound clumps are "pressure" confined in that their internal kinetic pressure, which is primarily turbulent, is comparable to the mean pressure of the ambient GMC (Bertoldi & McKee, 1992). Simulations suggest that these clumps are transient structures.

The nature of the interclump medium remains unclear: Blitz & Stark (1986) have postulated that it is low density molecular gas, but this has been questioned by Schneider et al. (1996). Blitz (1990, 1993) showed that atomic envelopes around molecular clouds are quite common and that the atomic gas plausibly pervades the interclump medium. Williams et al. (1995) showed that the HI associated to the molecular gas in the Rosette has about the same turbulent pressure, and suggested that it could serve as the confining medium.

Cloud, clump, and core density profiles are reflections of the physics that shape their evolution, but the density profiles of clouds and clumps have received scant attention. For clouds, which often are quite amorphous without a clear central peak, the density profile is often difficult to define observationally. For clumps, Williams et al. (1995) showed that surface density profiles of pressure bound, gravitationally bound, and star-forming clumps have similar power law indices close to 1. Formally, the fits range from -0.8 to -1.2, but these differences do not appear to be significant. For a spherical cloud of infinite extent, $\Sigma(r) \propto r^{-1}$ implies $\rho(r) \propto r^{-1}$, suggesting that the (turbulent) pressure support is spatially constant. However,

McLaughlin & Pudritz (1996) argued that for finite spheres, the volume density distribution can be considerably flatter than that inferred for infinite clumps. Density distributions inferred from observations also require consideration of beam-convolution effects. It is nevertheless astonishing that both strongly self-gravitating clumps and those bound by external pressure have such similar, perhaps identical density distributions.

2.3 Star formation in molecular clouds

The star formation is a process which owes its origin to the gravitational collapse of molecular cloud clumps into cores. Accordingly with the virial theorem (Eq. 2.1), if the force due to the gas pressure dominate over the force of gravity the cloud expand, while if the kinetic energy is too low, the cloud collapse. If a molecular clump gets cold and dense enough that its mass is greater than the Jeans mass[1], it collapse under its own gravity in a free-fall time $t_{ff} = \left(\frac{3}{4\pi G\bar{\rho}}\right)^{1/2} \simeq \frac{5\times10^7}{[n_H(cm^{-3})]}$, where G is the gravitational constant and $\bar{\rho}$ is the mean mass density. This collapse is nearly isothermal as a result of an efficient cooling by molecular lines and dust grains, which re-radiate in the IR range the observed gravitational potential energy. Neglecting the magnetic field effects, in order to support the weight of the cloud's outer layers, the thermal pressure must increase toward the center and, since T is constant, this translates into a rising density toward the cloud center. Therefore the inner part of the cloud begins to collapse well before the outer regions: this process is called *inside-out collapse*.

Following Shu et al. (1987), it is customary to describe the star formation process in six phases, represented in Fig. 2.2. The first phase consists of the development of dense cores inside molecular clouds. The onset of the inside-out gravitational collapse and the formation of a protostar provides the next phase. Subsequently, the formation of an accretion disk and a bipolar outflow occurs, as a consequence of the conservation of angular momentum. The infall of material is stropped and the surrounding dust envelope is swept away, leaving a visible star-disk system. As long as the star slowly contracts toward the main sequence, coagulating dust grains and forming planetesimals in the disk, its central temperature increases until hydrogen ignites and halts further contraction: a new main-sequence star is born, possibly surrounded by a planetary system. For a main-sequence star, the nuclear energy becomes sufficient to support the star against collapse. Although from the observational point of view it is generally difficult to establish the evolutionary stage of an object, the theoretical point of view is clear: in the protostellar phase the luminosity is entirely provided by the accretion, in the pre-main-sequence phase by contraction, and, once in the Zero Age Main Sequence (ZAMS) phase, by the nuclear burning of hydrogen.

[1]The Jeans mass, M_J, represents the minimum mass needed to start the collapse of the clump:

$$M_J \sim \left(\frac{5kT}{G\mu m_H}\right)^{3/2} \left(\frac{3}{4\pi\rho_0}\right)^{1/2} \approx 6M_\odot \left(\frac{T}{K}\right)^{3/2} \left(\frac{\rho_0}{gcm^{-3}}\right)^{-1/2}$$

where μ is the mean molecular weight per particle, $m_H = 1.67\times10^{-24}\ g$ and ρ_0 (g cm^{-3}) is the initial mass density of the cloud.

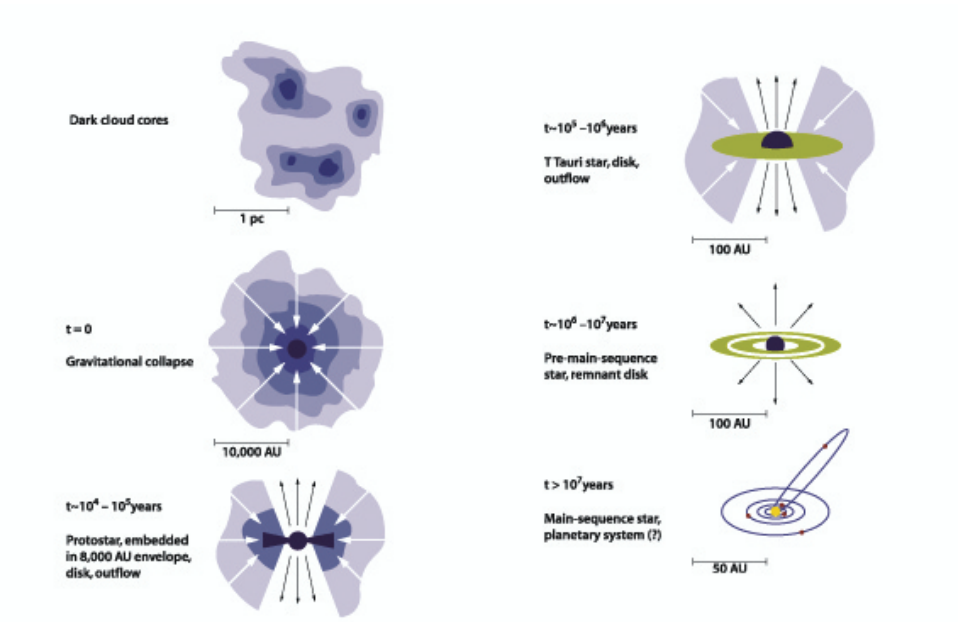

Figure 2.2: Phases of the star formation. Based on an original sketch by Frank Shu.

Although this paradigm has been very successful in explaining what is observationally known about the formation of low-mass stars (see e.g. Lada, 1991), its applicability to the formation of high-mass[2] stars is arguable. The formation process of massive stars cannot be simply "scale-up" version of the way in which isolated lower mass stars form.

High-mass stars have evolutionary timescales much shorter than low-mass stars. They begin to burn the hydrogen and reach the main sequence before they stop accreting matter from the surrounding protostellar enveloped. The formation of a massive disk, and so the appearance of molecular outflow and jets, in the accretion phase remain not clear.

Different models have been realized to clarify the problem of the massive disk but in the accretion phase, a definite massive star formation theory is still lacking. During their formation process, high-mass stars produce large bipolar outflows that strongly interact with environment, and produce strong fields of UV radiation, that result in the formation of HII and photodissociation regions. In addition, high-mass stars conclude their relatively short life in a violent supernovae explosion introducing heavier elements in the ISM and triggering star formation through the shocks associated with these events.

The life-history of a star is mainly determined by its initial mass, and the knowledge of the initial distribution of stellar masses at birth and of how this quantity varies through space and time within galaxy. The stellar *birthrate* is expressed in terms of the SFR and the initial mass function

[2]High-mass stars are defined as stars of spectral type B3 or earlier, with mass greater than $\sim$8 $M_\odot$ and luminosity greater than 10^3 $L_\odot$. This mass limit, the separation between low- and high-mass stars, is not totally arbitrary, but for stars with masses higher than 8 $M_\odot$, however, the mechanism of star formation is not well understood.

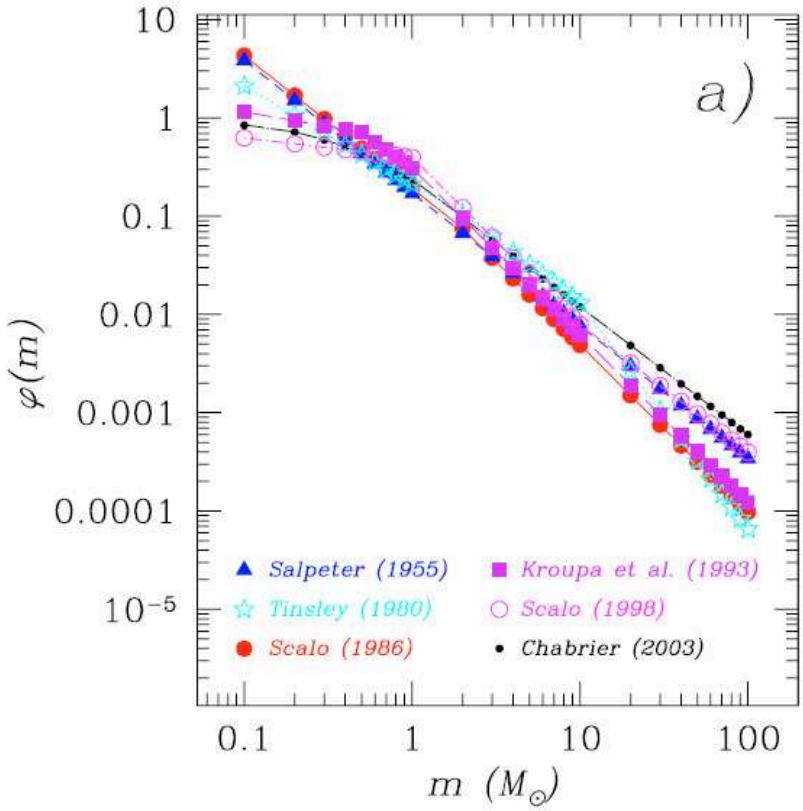

Figure 2.3: Comparison between stellar IMFs from different recent works (Romano et al., 2005).

(IMF), that defines the distribution in mass of a freshly stellar population. The IMF, $\varphi(M)$, is simply described by a power law and Salpeter (1955) have defined φ in the solar neighbourhoods in the form:

$$\varphi(M) \propto M^{-1.35} \tag{2.9}$$

suggesting that most stars that form in the solar neighbourhood are low-mass stars.

In Fig. 2.3 Romano et al. (2005) have compared Salpeter (1955), Tinsley (1980), Scalo (1986), Kroupa et al. (1993), Scalo (1998), and Chabrier (2003) IMFs. For the Chabrier (2003) IMF the dots for $m \geq 1$ $M_\odot$ display a power-law form with an exponent of -1.3. It is immediately seen that a Salpeter (1955) or a Scalo (1986) IMF predict many more stars at the very low end of the distribution than a Scalo (1998) or a Chabrier (2003). Tinsley (1980) IMF lies somewhere in the middle, while it predicts the highest fraction of stars in the mass range 2-10 $M_\odot$. This figure suggests that the IMF is well described by multi-slope expressions.

Typical values of SFR in local star-forming range from 0.01 to 100 $M_\odot$ yr^{-1} (Cram et al., 1998), and galaxies in the middle of the merging

process show SFR up to 100-200 $M_\odot$ yr^{-1} and higher values of SFR characterize ultra luminous starburst galaxies. In the study of star formation there have also been attempts to parametrize the SFR as a simple function of the gas distribution. Schmidt (1959), for the first time, have described the conversion of the gas mass into stars as a power-law function of local gas density SFR $\propto \rho_{gas}^N$. Schmidt (1959), observing HI and stars, have concluded that the power-law index has a value of order 2. Today, with the inclusion of the molecular component in the ISM, the situation is different. Kennicutt (1998c) have found N = 1.4 for global star formation and total (HI + CO) gas surface density in a sample of "normal" galaxies.

2.4 Molecular gas content

The molecular gas content in galaxies is estimated and analyzed using different tools, such as, the X conversion factor, the intensity line ratio, and the excitation temperature. In this section, we discuss the information that we can obtain by these parameters and their limits.

2.4.1 CO-H_2 conversion factor

As said in the Chapter 1, a difficulty linked to the measurement of the X value is that it is determined by various factors, such as the metallicity, the temperature, the cosmic ray density, and the UV radiation field (see, for instance, Boselli et al., 2002).

Theory and observations suggest that the gas temperatures in systems with high SFR can be quite high, so the use of the standard conversion factor will lead to serious systematic overestimates of the amount of the molecular gas. This consideration is probably valid not only for the galaxies with unusually high global rates of star formation, such as the infrared-luminous galaxies discovered by IRAS, but also for the nuclear regions of many less infrared-luminous galaxies.

Also the dependence of the CO-H_2 conversion factor on the metallicity is quite controversial. Some calculations show that CO emission from an ensemble of clouds in an external galaxy does not depends strongly on metallicity as long as the individual clouds are optically thick in CO (Dickman et al., 1986). However, models of individual low-metallicity clouds suggest that such clouds are optically thin in CO, which produce a strong dependence of the CO-H_2 conversion factor on metallicity (see Maloney & Black, 1988). If the CO-H_2 conversion factor is strongly dependent on the metallicity, then molecular gas masses in irregular galaxies, in the outer regions of spiral galaxies, and in other low metallicity systems may be significantly underestimated. Galaxies with lower metallicity generally have a higher X factor: Wilson (1995), studying 5 Local Group galaxies, have found that the X conversion factor increases as the metallicity of the host galaxy decreases, with the conversion factor increasing by a factor of 4.7 for a factor of 10 decrease in metallicity.

The X value also seems to change with the morphological type of the galaxies. Nakai & Kuno (1995), studying the CO-H_2 conversion factor in the M 51 galaxy and comparing their results with those present in literature for other nearby galaxies, have found that galaxies early-type -earlier than Scd (M 31, M 33, M 51, NGC 891)- show values from comparable to smaller ($\approx$ 1-3) than the mean Galactic value, while extremely late-type or

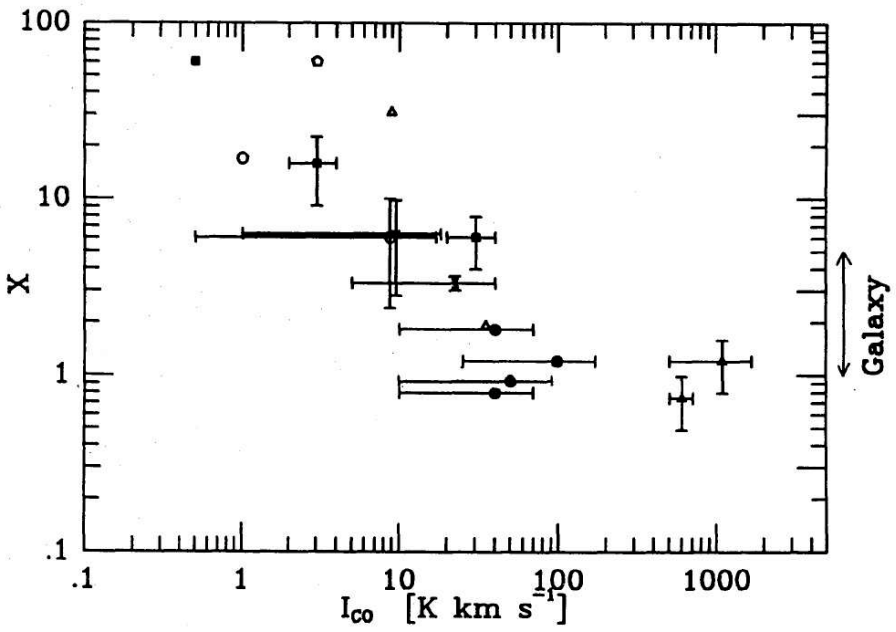

Figure 2.4: The X ratio expressed in 10^{20} cm^{-2} (K km s^{-1})$^{-1}$ as a function of I_{CO} for some nearby galaxies (by Nakai & Kuno, 1995).

irregular galaxies (IC 10, NGC 55, LMC, SMC), which moreover have a low abundance of heavy elements, tend to show larger values (> 4).

Another interesting aspect is the suspicion of a relation existing between the X conversion factor and the I_{CO}. Galaxies or observed positions with small I_{CO} ($I_{CO} <$ 20-40 K km s^{-1}) show a larger X. Nakai & Kuno (1995) showed that the galaxy M 51 is an example of this behaviour: $I_{CO} <$ 20 K km s^{-1} and the X derived value is a factor 2.6 lower than the mean Galactic value (see Fig. 2.4).

2.4.2 Intensity line ratios

The line ratio between different molecular species or simply between two transitions of the same molecule is usually used to derive the physical conditions of the gas. It is well known that the filling factor of molecular clouds in a galaxy is often low. Thus, integrated intensities are generally not a good measure of the physical conditions of individual molecular clouds because the signal is diluted by the large radio telescope beams, which also cover much empty space. Using the ratio of two integrated intensities helps cancel out the effects of beam dilution, assuming that similar regions of space are responsible for the emission at both frequencies. The physical conditions recovered from the analysis of line ratios are the average conditions for all clouds within the beam. In other words, mapping a galaxy in many transitions helps to increase our understanding of the molecular gas dynamics, since different transitions and molecules do not necessarily

trace the same gas (e.g. Petitpas & Wilson, 1998; Kohno et al., 1999). As already said before, the CO molecule -for instance- doesn't map regions at high density, and because stars are formed from dense cores of molecular clouds rather than their diffuse envelopes (e.g., Lada, 1992), it is essential to study the properties of dense molecular gas in order to understand star formation in galaxies and in starburst phenomena. Dense molecular material is investigated by observing the molecules referred to as "high-density tracers", which require larger hydrogen density than that of CO for their collisional excitation, such as HCN, HCO^+, CS, and so on (e.g., Henkel et al., 1998; Mauersberger et al., 2003; Nakanishi et al., 2005; Graciá-Carpio et al., 2006; Papadopoulos, 2007; Knudsen et al., 2007; Iono et al., 2007). For example, the CO(1-0) emission is excited even in low-density molecular gas (n_{H_2} ∼500 cm^{-3}), whereas HCN(1-0) emission traces very dense molecular clouds ($n_{H_2} > 10^4$ cm^{-3}) due to its larger dipole moment (μ_{HCN} = 3.0 debye, whereas $\mu_{CO} = 0.10$ debye).

The intensity of a millimeter emission line is dependent on three quantities, the excitation temperature, (T_{ex}), the optical depth (τ), and the surface filling factor (σ). In general, we can write:

$$T_R = \sigma \left[f_\nu \left(T_{ex} \right) - f_\nu \left(T_{BG} \right) \right] \left(1 - e^{-\tau} \right) \tag{2.10}$$

where $f_\nu \left(T \right) = \frac{h\nu/k}{e^{h\nu/kT}-1}$ and T_R is, to within a couple of efficiency factors, the quantity observed at the telescope, and T_{BG} is the temperature of the microwave background (2.7 K). Defining R_{21} as the ratio of the CO(2-1) to the CO(1-0) transitions, we can write:

$$\begin{aligned} R_{21} &= \frac{T_R(CO(2-1))}{T_R(CO(1-0))} \times \\ &\quad \frac{\sigma_{21} \left[f_\nu(T_{21}) - f_\nu(T_{BG}) \right] \left(1 - e^{-\tau_{21}} \right)}{\sigma_{10} \left[f_\nu(T_{10}) - f_\nu(T_{BG}) \right] \left(1 - e^{-\tau_{10}} \right)} \end{aligned} \tag{2.11}$$

A standard assumption is that $\sigma_{21} = \sigma_{10}$, i.e. when the $1 \rightarrow 0$ and $2 \rightarrow 0$ emissions come from the same volume. This equation can be simplified in two limiting cases: the optically thin case and the optically thick case. In the optically thin case, it is possible to make the assumption $(1 - e^{-\tau}) \rightarrow \tau$. Thus, the equation (2.11), ignoring the microwave background terms (which are less than 10% if T_{ex} is greater than 10 K), becomes:

$$R_{21} = 4e^{-h\nu_{21}/kT_{21}} \tag{2.12}$$

This equation shows that, in the optically thin limit, the R_{21} line ratio is a direct measure of the 2→1 excitation temperature.

In the optically thick case, making the assumption $(1 - e^{-\tau}) \rightarrow 1$, the R_{21} can be expressed as:

$$R_{21} = 2\frac{e^{5.53/T_{10}} - 1}{e^{11.1/T_{21}} - 1} \tag{2.13}$$

The analysis R_{21} ratio as a function of temperature for the limiting cases, optically thin and thick, has shown two important things. First, for high temperatures, the R_{21} ratio asymptotically approaches a value of 4 in the

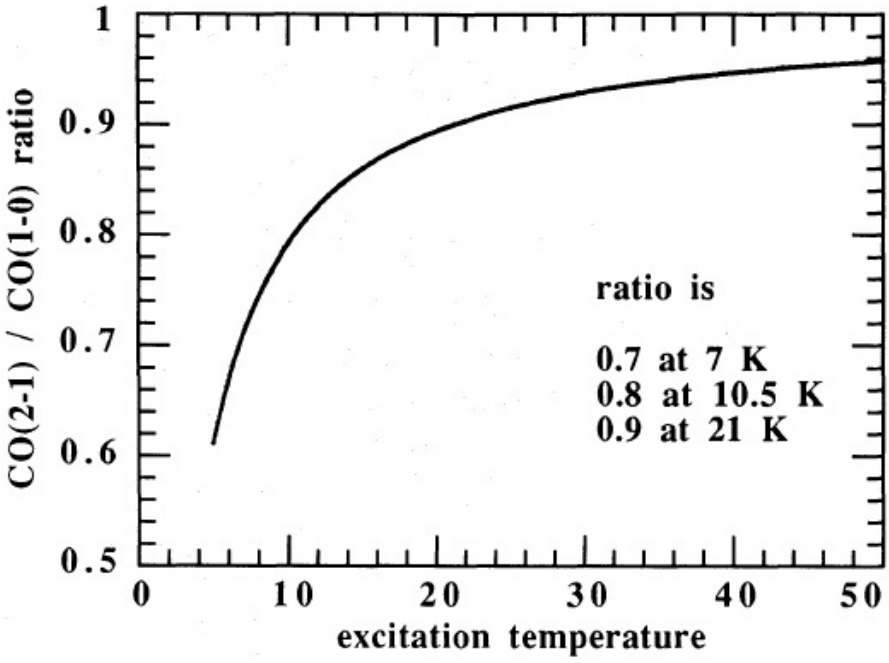

Figure 2.5: R_{21} ratios versus excitation temperature in Kelvin for optically depth $\tau \gg 1$ in both lines (by Braine & Combes, 1992).

optically thin case, while it only approaches 1 in the optically thick case. If 1 is the limit for an optically thick gas, R_{21} ratios > 1 are signatures of optically thin CO emission. Second, in the optically thin limit, the R_{21} ratio does not drop below 1 until the excitation temperature drops below 8 K. This situation is improbable, but not impossible, especially if the excitation of the gas is subthermal.

The ^{12}CO lines are optically thick in most galaxies, including the Milky Way, but there are other galaxies where the problem is still open, like M 82 (Loiseau et al., 1990) or NGC 3628 (Reuter et al., 1991). When studying the line ratio for a large sample (118) of nearby spiral galaxies, Braine & Combes (1992) saw that subthermal excitation or different gas filling factors are only required for explaining line ratios less than 0.7.

With line ratios of 0.7, 0.8, and 0.9, the excitation temperatures are expected to be 7 K, 10.5 K, and 21 K, respectively (see Fig. 2.5). These low line ratios can be explained considering that at high gas densities in the heating mechanism, the dust-gas collisions are more important than cosmic rays that ionize H_2 or via formation of H_2 on dust grains. When neglecting the heating from gravitational collapse or magnetic sources and assuming the gas in local thermal equilibrium ($T_{ex} = T_{kin}$), Braine & Combes (1992) derived a relationship between gas temperature and dust temperature at high densities. At gas densities of 10^4 cm^{-3}, which is required to approximately thermalize the J = 2 level of CO, and dust temperatures of 30 K, the equilibrium gas temperature is 10 - 13 K. Considering that in the clouds the dust is probably warmer in the vicinity of OB stars and lower elsewhere, the gas heated by the warm dust at 50 - 60 K will reach the thermal equilibrium

at temperatures of 15 - 20 K. The J = 2 level of CO is populated at these temperatures, and Braine & Combes (1992) computed that the expected line ratios are between 0.7 and 0.9. In addition, it is important to remember that the CO emission is not always thermalized and that the excitation temperature may change along the line of sight and within a single beam.

2.5 Distribution and dynamics of the CO

Large-scale CO maps of nearby galaxies now available, extend our knowledge on global properties, radial gradients, and spiral structure of the molecular ISM. Millimetric interferometers reveal high velocity gradients in galaxy nuclei, and formation of embedded structures, like bars within bars.

2.5.1 Radial and vertical distribution

The HI and CO (or H_2) radial distribution can strongly differ from galaxy to galaxy: normally in the center the $N(H_2)/N(HI)$ ratio can reach the value of 10 or 20, and it falls below 1 in the outer parts. All components related to the SF, such as the blue luminosity from stars, the H_α (gas ionized by young stars), the radio-continuum (synchrotron related to supernovae), and also the CO emission, follow an exponential distribution, but this not the case of the HI gas that is extending much beyond the "optical" disk ($R_{HI} = 2 - 4\,R_{opt}$).

The HI gas has often a small deficiency in the central regions of the galaxies. It is possible that the atomic gas is transformed in molecular phase in the denser central parts of the galaxies, where the HI and CO distributions appear complementary. However this is not the general situation, and all possibilities have been observed, including central gaseous depletion, both in CO and HI (like M 81, M 31, or NGC 7331).

Since the HI gas is coming from dissociated molecular gas in photodissociation regions (PDRs), Smith et al. (2000) have proposed that the volumic density of local H_2 can be deduced from measurements of the HI column density coupled to the FUV photon flux. Applying this idea to M 101 galaxy, they have found that the molecular gas with a range of density from 30 to 1000 cm^{-3} is located near star-forming regions out to the distance of ∼26 kpc from the center, close to the photometric limit of R_{25}. Concerning the vertical distribution of the molecular gas, we know that the galaxy disks -both the Milky Way and external galaxies seen edge-on- have much narrower distribution in CO emission than HI. This aspect suggests that the molecular gas is more confined to the plane due to a much lower vertical velocity dispersion. On the contrary, the face-on galaxies -both in CO (Combes & Becquaert, 1997) and HI (Kamphuis & Briggs, 1992)- exhibit velocity dispersion with similar values between them and constant with the radius. Combes & Becquaert (1997) have interpreted the constancy of the velocity dispersion ($\sigma_v \sim 6$ km s^{-1}) as due to a feedback mechanism involving gravitational instabilities and gas dissipation. The similarity of the CO and HI velocity dispersions suggests that the two components are well mixed, and they are only two different phases of the same kinematical gas component. The gas can be transformed from the atomic phase to the molecular one and vice-versa several times during a vertical oscillation. The possibilities are that 1) the H_2 gas follows the HI, but the CO is photodissociated at high altitudes, 2) the H_2 is not excited, or 3) the H_2 could

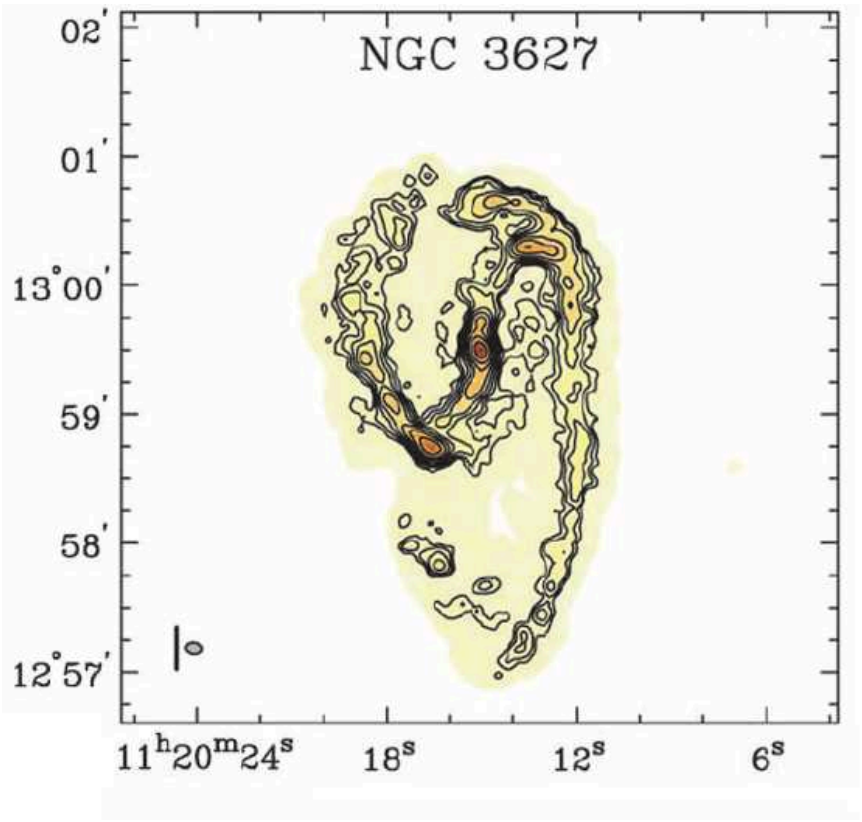

Figure 2.6: ^{12}CO(1-0) integrated intensity contours overlaid on a false-color representation of the CO emission for NGC 3627. The contours are logarithmically spaced at half magnitude intervals, or 1.59 times the previous interval (by Helfer et al., 2003).

disappear since the chemistry time-scale ($\sim 10^5$ yr) is much smaller than the dynamical z-time-scale ($\sim 10^8$ yr).

2.5.2 Dynamics: bars, shells and tidal dwarfs

The dissipative character of the gas is fundamental for the formation of bars, and for the transfer of angular momentum to the outer parts, to allow a radial inflows. The molecular component is the best tool to trace the gas behaviour in galaxy centers. High resolution CO interferometric surveys (such as, BIMA Survey of Nearby Galaxies, Regan et al., 2001 and Helfer et al., 2003, and NUclei of GAlaxies survey (NUGA), García-Burillo et al. 2003) have detected structures in CO emission: bars and rings in the centre and spiral arms in the disk. Fig. (2.6) shows that the NGC 3627 galaxy of the BIMA survey has spiral arms and a bar well traced in CO. Molecular bars are even detected in galaxies not classified as barred according to their optical morphology.

In general, barred galaxies show characteristic features corresponding to offset dust lanes seen in optical. When these two features are seen only to start from the nucleus, they are called *twin-peaks* (Kenney et al., 1992) and correspond to the presence of an inner Lindblad resonance, implying orbits

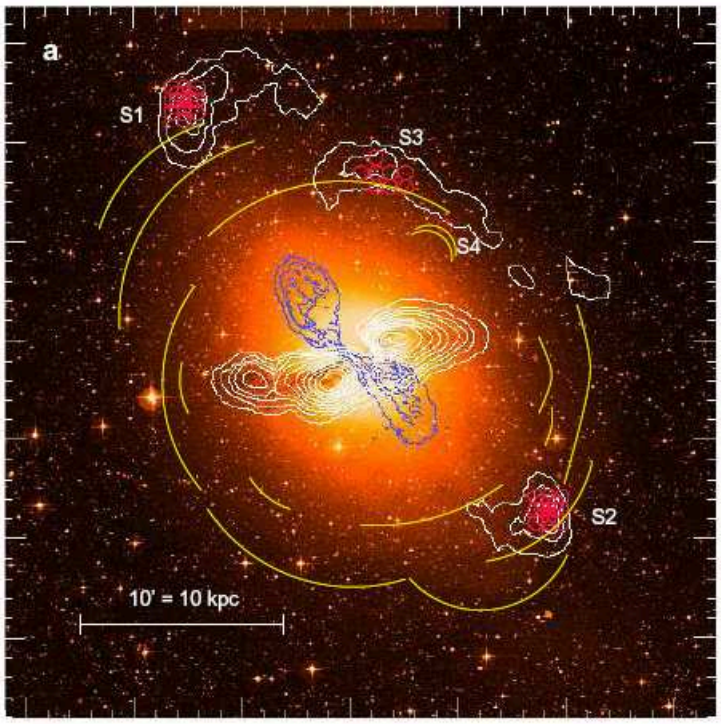

Figure 2.7: A Digitized Sky Survey image of Cen A with the HI gas superimposed in white. The positions observed in CO are marked in red whose size corresponds to the SEST 44″ beam of CO(1-0). The blue contours correspond to the inner 6 cm radio continuum lobes (by Charmandaris et al., 2000).

perpendicular to the bar in the center. The gas is often concentrated in resonance rings (nuclear rings, cf Sakamoto et al., 1999; Thornley et al., 1999), or in nuclear spirals. It is often difficult to discriminate between several possibilities to account for the non-circular motions observed: nuclear bars or warps, as in the Seyfert galaxies NGC 1068 and NGC 3227 (Schinnerer et al., 2000). Sheth et al. (2002) have also compared the molecular gas distribution and star formation activity, focusing on the bar region. They have found that the star formation activity, traced using the H_α emission line, is offset toward the leading side of the CO.

Different simulations have been performed to explain this CO-H_α distributions. Along the spiral arms, analogous offsets toward the leading side of the molecular gas or dust lanes has been interpreted as evidence of star formation induced by a spiral density wave (Vogel et al., 1988; Rand, 1993).

The molecular gas can be also detected far from the galaxy centers in shells, outside the optical image of the galaxy. The shells are formed by stars of disrupted companions, by a phase-wrapping process (Quinn, 1984), and an example is well represented by the shells in Centaurus A detected by Charmandaris et al. (2000) (see Fig. 2.7). A large fraction of elliptical galaxies possess shells (Schweizer & Seitzer, 1992), and this is believed to support the hierarchical merging scenario for their formation, while in a merging event, the gas is expected to dissipate and fall to the center (Weil

& Hernquist, 1993). Also the atomic gas has been observed associated to shells (Schiminovich et al., 1994). In Centaurus A the 10% of the gas in shells is atomic, while the 50% is molecular (Charmandaris et al., 2000). Moreover, the H_2/HI ratio is the same in the nuclear disk and in the shells. To explain how in Cen A the gas has been enriched in metals far from the nucleus, Graham (1998, 1999) have proposed that this enrichment happened in a recent star formation episode triggered in the shell gas by the impact of the radio jet. In fact, in Cen A the shells detected in CO are precisely aligned with the radio jet, and the recently formed stars could have enriched the observed gas in metals and account for the CO detection.

Finally, tidal dwarfs are small systems becoming gravitationally bound within tidal tails dragged by the interaction between two massive gas-rich galaxies. The collapse of the gas in these systems triggers new star formation (Duc & Mirabel, 1998). Braine et al. (2000), reporting the discovery of the CO emission in two tidal dwarf galaxies (Arp 105 and Arp 245), have noted that the concentration of molecular gas in both cases peaks at the same location as the maximum in atomic hydrogen density, unlike the situation in most gas-rich galaxies. They inferred from this that the molecular gas formed from the atomic hydrogen, rather than being torn in molecular form from the interacting galaxies. Star formation in the tidal dwarf galaxies therefore appears to mimic the process in normal spiral galaxies like our own.

2.6 CO as a function of type and environment

Different surveys have been conducted to establish whether galaxies can be characterized by a canonical gas content that may vary significantly along the Hubble sequence (early-type versus late-type objects), and/or depend on the particular environment (isolated versus strongly interacting galaxies) (such as, Knapp et al., 1989; Young & Knezek, 1989; Young & Scoville, 1991; Bregman et al., 1992; Fabbiano et al., 1992; Burstein et al., 1997; Casoli et al., 1998; Beuing et al., 1999; Bettoni et al., 2003; Casasola et al., 2004). As already said in the Chapter 1, a global study of the ISM content in galaxies requires a multi-wavelength approach: FIR observations at 60 and 100 μm trace the warm dust content, while those at 140-200 μm the cold dust; mm lines of carbon monoxide and the 21cm line of HI must be used to infer the molecular and atomic gas content respectively, and the X-ray wave-band is used to study the hot gas component.

In general elliptical galaxies are poorer in cool gas than spirals. This poverty, combined with the fact that comparatively few giant ellipticals lie conveniently close to the Milky Way, makes them hard to observe at 21 cm, 2.6 mm or in the IR, and hinders quantification of their cool ISM content. Most elliptical galaxies possess accreted gas, already detected in HI (Knapp et al., 1989; van Gorkom & Schiminovich, 1997), that appears to be unrelated to the underlying stellar population. It may be the remnant of the merger event at their birth, or accretion of small gas-rich companions.

The principal problem linked to the CO surveys is that the results obtained can have strong biases due to poor statistics (uneven coverage along the Hubble sequence), and also due to the inclusion of galaxies which are known to be "peculiar". For instance, the selection of galaxies candidate to be observed in CO surveys have been typically based on FIR criteria, that tend often to favour the inclusion of "peculiar" galaxies in surveys and introduce a bias against "normal" systems.

In first approximation, we can say that the average molecular content is comparable to the atomic one, with the $M(H_2)/M(HI) \sim 1$, but there are even examples where $M(H_2)/M(HI) \sim 0.2$, as found for instance by the CO survey of Casoli et al. (1998) near the Coma cluster.

In the literature there are also molecular gas surveys that have investigated morphological sub-classes of galaxies with specific characteristics. Combes et al. (2007), for instance, recently presented a CO survey of E/S0 galaxies already observed in the optical with the SAURON integral-field spectrograph (Peletier et al., 2001). They have found that early-types are not always devoid of gas, and can even show a substantial amount of CO emission. In addition, Combes et al. (2007) did not find strong correlations between the CO content and most stellar parameters, and interpreted this result compatible with the idea that, in a significant number of their sample galaxies, the molecular gas has been accreted from the outside and has properties rather independent from the old, pre-existing stellar component. Other CO surveys (such as, Bettoni et al., 2001; Boselli et al., 2002; Bettoni et al., 2003; Casasola et al., 2004) studied the molecular gas properties of galaxies spanning a large range of morphological type and luminosity, and belonging to different environments (clusters - field). Boselli et al. (2002), considering only late-type galaxies, have found that low-mass, dwarf galaxies have higher molecular gas masses (per unit galaxy mass) than early-type, massive spirals. The molecular gas fraction in clouds or complexes is $\sim$15% of the total HI reservoir for all late-type galaxies. Strongly interacting galaxies of their sample have, on average, a molecular gas content comparable to isolated-unperturbed objects, and the efficiency in transforming gas into stars is roughly constant in galaxies of different type, luminosity, and environment.

Another example of molecular gas investigation for galaxies of different typologies is our work, Casasola et al. (2004). Compiling a catalogue of more than 1000 galaxies with strong signs of interaction and/or perturbation and considering all morphological types, we studied their gas content properties in comparison with galaxies considered normal, or not in interaction with the environment. First, we have found that the morphological type has a role in determining the properties of these stellar systems, and that may be not correct to mix together interacting galaxies of all morphological types. Secondly, we saw that interacting or disturbed galaxies have always more gas than normal ones, and that this gas is mainly in the form of atomic hydrogen in early-type systems, while it is in molecular form for galaxies of latest types. Fig. (2.8) shows in detail the results found: galaxies classified as early-type ($t < 0$) have dust and HI overabundance, even with respect to their molecular gas, while those classified as late-type ($t > 0$) are richer in molecular gas and are quite normal, on average, for dust and atomic gas content. All interacting galaxies, from ellipticals to late spirals, have a higher X-ray luminosity to normal ones.

Another suggestion on the reality of the higher molecular masses for interacting galaxies comes from the analysis of the star formation rates and efficiencies. We have also found that galaxies in interaction appear more luminous in the infrared (Fig. 2.9) because of the higher number of newly formed stars heating the dust (Thronson & Telesco, 1986). This higher star formation rate does not correspond to a different efficiency in star formation per unit of calculated H_2 mass (see Fig. 2.10). This may be explained if the higher star formation is simply due to a higher molecular gas quantity.

We explained the excess of the molecular gas discussing the early-type

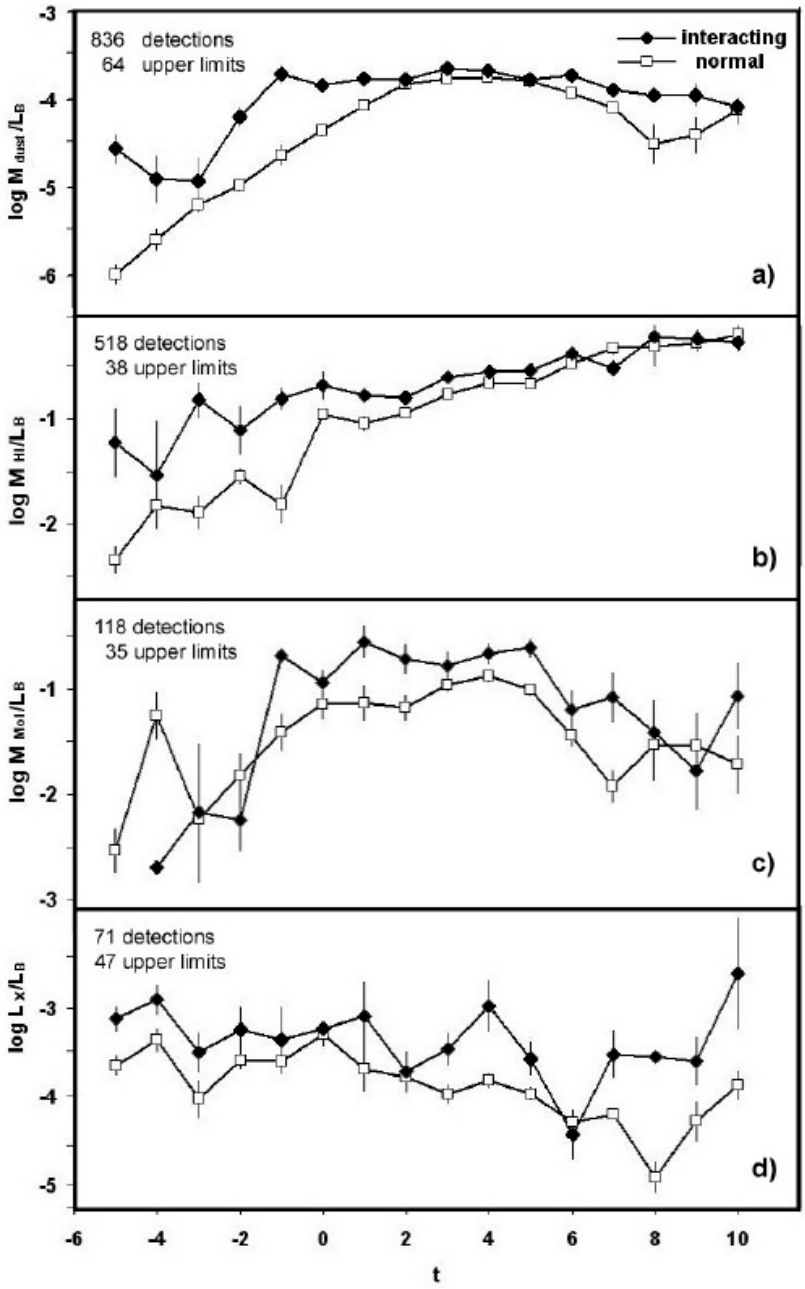

Figure 2.8: Comparison between mean values for interacting galaxies and corresponding means for normal galaxies (Bettoni et al., 2003) for dust, atomic gas, molecular gas, and hot gas component. Bars represent 1 σ errors (by Casasola et al., 2004).

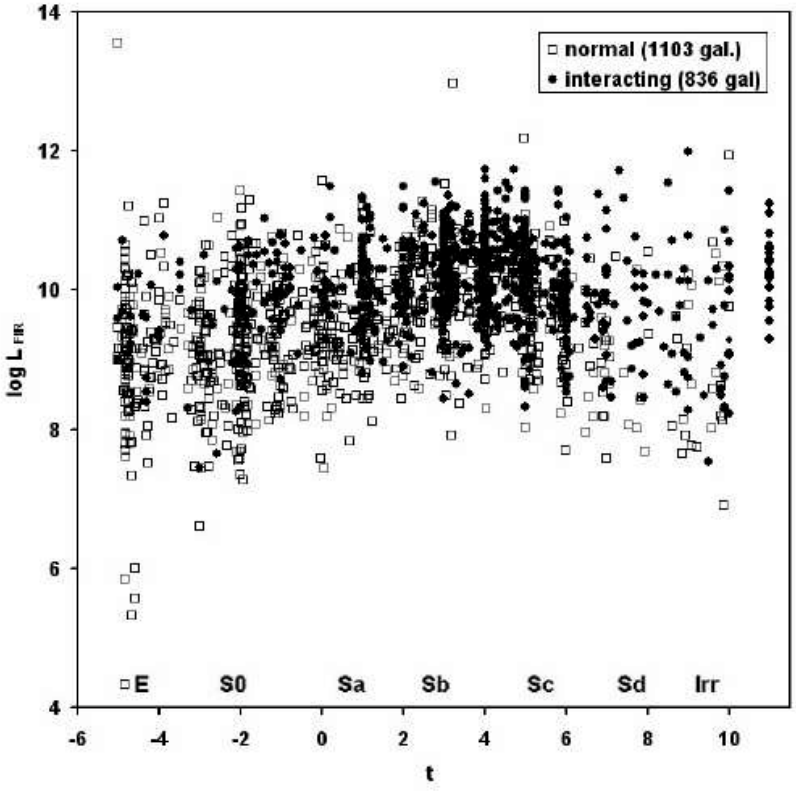

Figure 2.9: The absolute far infrared luminosities versus morphological type code for interacting galaxies (full circles) compared to the normal galaxies included in the sample of Bettoni et al. (2003) (by Casasola et al., 2004).

systems separately from the spiral ones. A galaxy that appears now as an elliptical may be in the final stage of a merging process, after the complete fusion of the stellar content of two galaxies. Alternatively, it may be a galaxy deprived of the gas because of a close encounter with a more massive one. In both processes, one may expect that the pre-existing gas in the two systems would be heated, with the conversion of molecular gas in atomic form and by the creation of an X-ray component. This scenario agrees with the higher HI and X-ray contents found in interacting early-type galaxies.

A more complicated scenario appears from the data concerning galaxies classified as spirals. In these systems the mean HI and dust content seems to be similar to that of an unperturbed, normal galaxy of the same morphological type. In addition to the excess in X-ray luminosity, these galaxies seem to have a molecular gas content always one order of magnitude higher than that of normal galaxies. There are two possible explanations for this effect. The first possibility is that during the collision the galaxies stimulate a gas inflow by means of gravitational torques, that enhance the CO luminosity because of a massive accumulation of molecular gas (Combes et al., 1994). We tested the idea that the gas is simply exchanged by the two components of the same pair, enriching one of them and depauperating the other. This explanation has been resulted not sufficient to justify the molecular mass

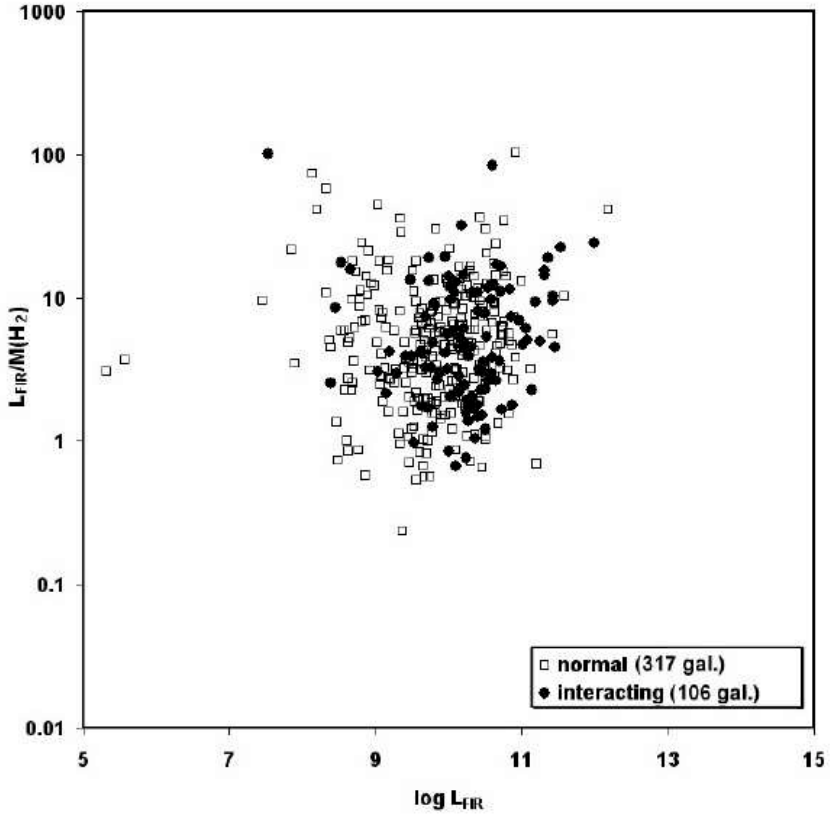

Figure 2.10: The star formation efficiency per unit of molecular gas mass, indicated by the ratio $L_{FIR}/M(H_2)$, plotted versus the far infrared luminosity. Interacting and normal galaxies appear to have similar ranges of values, even if interacting galaxies are more luminous in the infrared. (by Casasola et al., 2004).

excess that characterizes the late-type interacting galaxies.

The second, completely different possibility is that the molecular gas excess is not real but due to different physical conditions inside the galaxy. The molecular mass is determined from CO line adopting a constant value for the X conversion factor between H_2 and CO. This value depends on the metallicities or on the physical conditions of the molecular gas, and in different kinds of galaxies may assume a wide range of values (see Section 2.4.1). An overestimate of the molecular mass may derive by the assumption of a X factor lower than real. Among the various possibilities, the presence of gas of high temperature may overestimate the H_2 mass. Probably the correct interpretation is the combination of the two possibilities, even if in some cases, such as "Antennae" or "Atoms for Peace", the molecular gas excess is real and accompanied by atomic one.

2.7 CO at high redshift

As already said, the importance of the molecular medium in the history of the Universe is directly related to that of the star formation. The features of the global star formation history are now reasonably well established. They are inferred not only from the analysis of the age of stellar populations in local galaxies, but, since about a decade, directly and more accurately from the observation and census of high-z star forming galaxies. The majority of the stellar mass of the Universe was thus formed in progenitors of spiral galaxies between z = 0.5 and 1.5. Another important fraction is formed at higher redshift, including most of the stellar mass of elliptical galaxies. The exploration of the properties of the prominent molecular medium at these epochs of star formation in the Universe is fundamental to understand in detail the evolution of galaxies. This is mostly out of reach with current millimeter capabilities.

After the early millimetre detection of dust and CO in exceptional high-z objects, mostly strongly lensed, (Brown & Vanden Bout, 1991, 1992; Solomon et al., 1992; Barvainis et al., 1992, 1994; McMahon et al., 1994), it was realized that CO could be detected with current equipment in the brightest high-z ultra-luminous infrared galaxies (ULIRGs). After about ten years of major efforts with millimetre facilities, there are 36 CO detections with z between 1.06 and 6.42 collected in the paper of Solomon & Vanden Bout (2005) (this list of detections is constantly increasing with new detections, e.g. Kneib et al., 2005; Iono et al., 2006; Willott et al., 2007). The list of CO detections includes 14 submillimetre galaxies (SMGs) (and one Lyman Break Galaxy) with z=1.06-3.41, 16 quasi-stellar objects (QSOs) with z=1.42-6.42, and 5 radio galaxies with z=2.39-5.20. We can note that all the 11 objects with z>3.5 are prominent AGN.

In all objects with z>2, at least one line was detected in the 3 mm atmospheric window, corresponding to relatively high rotation number, mostly J=3-2, 4-3 and 5-4 (in a few cases up to J=7-6). Low-J lines, J=1-0 or 2-1, were detected in the cm range in ten cases, mostly with the Very Large Array (VLA). The value of the ratio of the intensities may provide information about the CO rotational temperature, and hence, the kinetic temperature and the H_2 density. However, an accurate modelling of CO line formation remains difficult in the absence of detailed information about the extension and the structure of CO emission, and the clumpiness of the molecular gas (see e.g. Combes et al., 1999; Solomon & Vanden Bout, 2005). This limits the corresponding diagnosis that it could provide for the emitting galaxy. However systematic programmes, such as the one recently carried out on SMGs at the IRAM-interferometer (Neri et al., 2003; Greve et al., 2005; Tacconi et al., 2006), are efficient in providing basic information about the properties of such starburst galaxies at high redshift.

The fact that more than half the high-z galaxies where CO has been detected, are AGN, mainly bright QSOs and powerful radio galaxies, is probably due to the combination of two reasons. First, there is a high probability of finding strong starbursts in the host galaxies of such AGN as proven by the many detections of dust submillimeter emission. MAMBO-IRAM studies showed that the probability to detect 1.2 mm continuum with a flux density $\gtrsim$ 2 mJy is as high as 25-30% around bright QSOs with z $\gtrsim$ 2 (Omont et al., 1996; Carilli et al., 2001; Omont et al., 2001, 2003; Beelen et al., 2004). Secondly, there is a general good correlation between CO and FIR emission, and the FIR emission is strong in many of these AGNs. It is also much easier to have a good determination of the redshift of the molecular

gas of AGN, so that it is accurate enough to warrant that the CO line lies within the narrow bandwidth of millimetre detectors used up to now. This explains in particular the absence of non-AGN sources among current CO detections with $z > 3.5$.

All other emission lines from the bulk of the interstellar gas of these high-z starbursts are significantly more difficult to detect than CO (such as, HCN, HCO^+, HNC, CN and the fine structure lines of C_I and C_{II}).

Chapter 3

Relations between ISM tracers

Introduction

The observations of galaxies at various wavelengths allow the study of the relationships between different phases of the interstellar gas and between gas, dust, and stars. Some of these relations have already been known for many years, such as the one between CO and FIR luminosities (Sanders & Mirabel, 1985; Sanders et al., 1986; Solomon & Sage, 1988; Devereux & Young, 1991). Others, connected with X-ray emission, have been studied even more recently (Griffiths & Padovani, 1990; David et al., 1992; Ranalli et al., 2003).

In this Chapter we present a statistical and interpretative study on relations existing between different tracers of the interstellar medium in galaxies. The results of this work are collected in the paper G. Galletta, V. Casasola, L. Piovan, E. Merlin, and D. Bettoni, A&A, 462, 495, 2007.

3.1 Emissions and star formation

It is known that fluxes emitted by a galaxy at different wavelengths may be linked by means of the star formation mechanism (see David et al., 1992; Ranalli et al., 2003). For instance, the formation of massive stars generates heating of the dust clouds in which they are embedded by absorption of their UV radiation, and produces a re-emission of this energy in the FIR range. This process links the current SFR to the IR emission at 60 and 100 μm (Thronson & Telesco, 1986). The ionizing radiation of stars may also produce evaporation of the molecular clouds. Inside these clouds, where the particle density is high enough to produce a significant number of collisions between H_2 and CO molecules, these are excited and produce photons, but in optically thick regions. The warming by the UV stellar light makes these regions less dense, thereby making visible CO lines at their edge. Because of this mechanism, these lines are considered tracers of the cold molecular hydrogen that does not emit observable lines, as already discussed in the Chapter 2. The newly formed stars are also responsible for the X-ray emission produced by very massive stars, by core-collapse SN, and by high-mass X-ray binaries. According to the these mechanisms, we expect that galaxies with active star formation will have a FIR emission, but also CO and X-

Table 3.1: Sample of galaxies.

Number	Property
2953	the whole sample
1915	normal galaxies
1038	interacting galaxies
253	galaxies with spectral classification of the nucleus
231	AGNs (Seyfert 1, 2, or 3)
1764	galaxies with FIR fluxes
391	galaxies with X-ray fluxes
434	galaxies with CO(1-0) line intensities

ray emissions induced by more massive stars, linked by different kinds of relations.

When the star formation decreases or vanishes, the FIR emission decreases as well, but it may be fed by the stellar light absorbed and re-emitted in the infrared by dust (cirrus), while low-mass X-ray binaries and Type I SN contribute to the high energy galaxy spectrum. In addition, AGB stars, surrounded by dust, and cooling flows of the interstellar medium ejected by supernovae may together produce additional IR and X emission.

3.2 The sample

The selected sample has been realized collecting data on galaxies starting from the original data on fluxes in the 60, 100 μm, CO(1-0) lines, and in the soft X-ray used to compile our previous catalogues (Bettoni et al., 2003; Casasola et al., 2004). The merging of these two catalogues produced data for a total of 2953 galaxies: 1764 stellar systems have values of FIR fluxes (1837 have 100 μm flux), 391 have soft X-ray fluxes, and 434 with values for the CO(1-0) line luminosity. We extracted the values of the distance moduli, blue absolute magnitudes, and morphological classification for all galaxies from the LEDA catalogue (Paturel et al., 1997).

These are 1038 galaxies with evident signs of interactions or disturbed morphologies according to the catalogues of Arp (1966), Arp & Madore (1987), and Vorontsov-Velyaminov (1959). We referred to them as "perturbed galaxies". The remaining 1915 galaxies that appear neither morphologically nor dynamically perturbed are called "normal galaxies". In our sample, there are 253 galaxies that have a spectral classification for the nucleus, and 231 of these appear to host an AGN (Seyfert 1, 2 or transition type, Seyfert 3 or Liner) according to the classifications of Ho et al. (1997) and Véron-Cetty & Véron (2003). Most of the remaining 2722 galaxies lack information about nuclear spectrum or have spectra of HII regions (22 starburst spectra). They have not been included in any AGN catalogue and, for this reason, we referred to them as "non active galaxies" and to the others as "active galaxies". The characteristics of the selected sample are summa-

rized in the Table 3.1 [1]. With all these data, we crossed various tracers to understand and revisit main relations existing between X, FIR, CO, and B luminosities.

3.3 Results

3.3.1 Cold gas and warm dust

From the literature we know that the global galaxy luminosity derived from CO(1-0) line is directly related with the flux at 100 μm (Sanders & Mirabel, 1985; Solomon & Sage, 1988; Bregman et al., 1992; Combes et al., 2007). In these works the principal goal was to understand the relationship between the molecular gas content and star formation through comparisons of CO emission and various optical tracers of young stars. The FIR emission is a tracer of star formation, and in particular it is considered a valuable tool since the FIR can, in principle, trace the stellar population that is hidden by dust within the galaxy. From the literature we know that, in spite of the diversity between the galaxies (e.g. morphological type) and between their physical properties (e.g. very bright or low in infrared), a correlation exists between the total CO and 100 μm luminosities. If the infrared emission arises from dust heated by stars forming in molecular clouds (Telesco & Harper, 1980; Rieke et al., 1980) and if the CO emission traces the mass of H_2, such a correlation would suggest that more star formation occurs when more molecular gas is present.

Using the data collected in our large sample we tested this relation using galaxies of different morphological types, activity, and interaction. In Figs. 3.1 and 3.2 we plotted the logarithm of the flux measured from CO(1-0) line versus the logarithm of the IRAS flux at 100 μm for 193 galaxies with classification from E to Sb and 178 from Sbc to Sm. The relation found by Bregman et al. (1992) for a sample of early-type galaxies, log S_{CO} = log S_{100} - 1.76, is also plotted as comparison. Active and non-active galaxies appear mixed together without clear differences and have been plotted together. The same behaviour appears for interacting and non interacting galaxies, which are not distinguished in our plots.

For galaxies of all morphological types, activity and nature of the interaction, we found:

$$logS_{CO} = 1.06\ logS_{100} + 2.02 \tag{3.1}$$

where the S_{100} flux is expressed in mJy and the S_{CO} flux in Jy km/s. The equation (3.1) has a correlation coefficient of 0.74 and a σ of 0.37.

A similar relation exists between the CO fluxes and the FIR magnitude, defined as:

$$m_{FIR} = -2.5\ log(2.58\ S_{60} + S_{100}) + 22.25 \tag{3.2}$$

where S_{60} and S_{100} are the fluxes at 60 and 100 μm respectively and are expressed in mJy. We found for all the galaxy types:

$$logS_{CO} = 0.41\ m_{FIR} + 6.86 \tag{3.3}$$

[1] This sample may appear biased through perturbed and active galaxies, because usually these systems are 1/10 of normal galaxies at z = 0. The problem is resolved noting that not all galaxies of our sample possess both CO, IR, X, and B fluxes and so the relations between different tracers of the ISM, later presented, consider sub-samples of the very large initial sample.

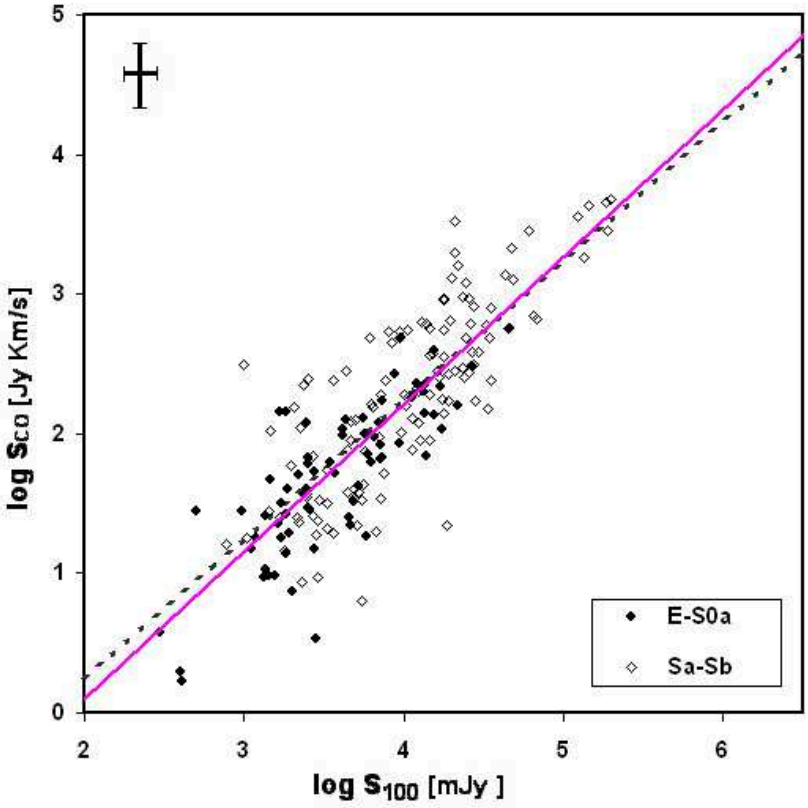

Figure 3.1: The relation between the CO(1-0) line flux and 100 μm one, plotted as a pink-full line, for early-type galaxies and early spirals from E to Sb. The representative points of galaxies are plotted with different symbols. The cross at the upper left of the figure represents the mean errors for the fluxes in the whole sample. For comparison, the relation found by Bregman et al. (1992) for a sample of early-type galaxies is shown as a dotted line.

with a correlation coefficient of 0.69 and a σ of 0.40. This result is based on 179 early-type galaxies shown in Fig. 3.3, and 170 late-type galaxies shown in Fig. 3.4.

We noted that irregular galaxies are not fitted by these relations but are widespread. In our sample there are just 10 irregular galaxies with data both at 100 μm (or m_{FIR}) and S_{CO}, and their representative points have not been plotted in Figs. 3.2 and 3.4.

3.3.2 X-ray component

In addition to the relationship between dust and cold gas, we were interested to understand what relations exist between L_X (X-ray luminosity) and the other global galaxy properties. From the literature, it is known the existence of a proportionality between L_X produced by the many discrete sources present and L_B, the blue luminosity of the whole galaxy. This relation has been studied in detail by Ciotti et al. (1991) and Beuing et al. (1999). It appears that late-type galaxies have a global X-ray luminosity directly

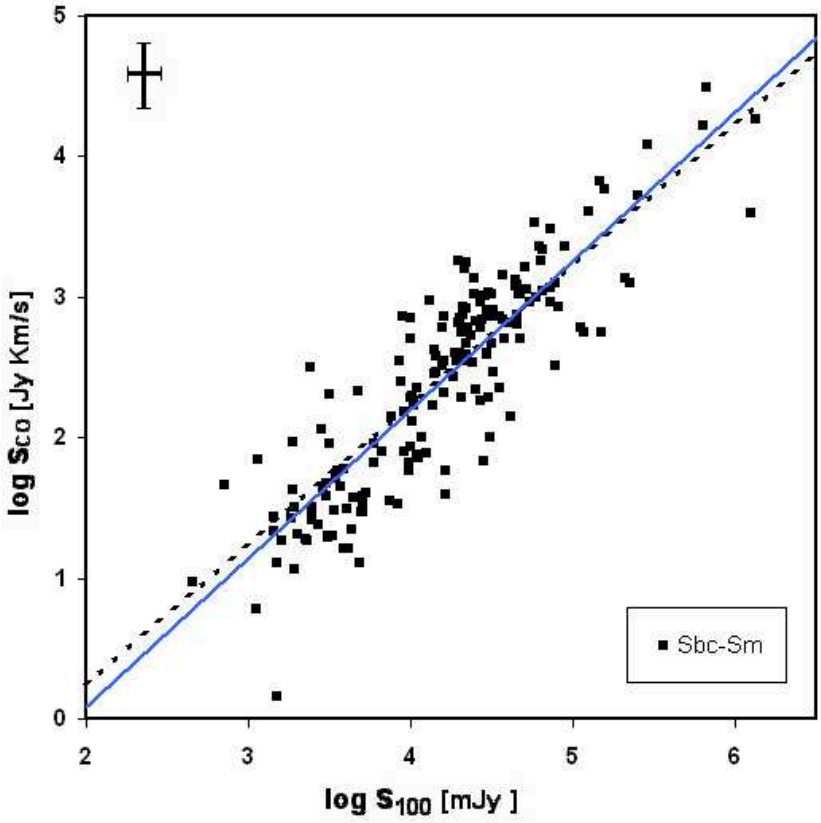

Figure 3.2: The same of Fig. 3.1 obtained for late spiral galaxies from Sbc to Sm. The relation between the flux from the CO(1-0) line and at 100 μm is plotted as a blue-full line. Also in this case the relation found by Bregman et al. (1992) for a sample of early-type galaxies is shown as a dotted line.

proportional to L_B, while early-type systems are dominated by emission produced by hot diffuse gas and their L_X is proportional to the square power of the blue luminosity, as discussed by Beuing et al. (1999). For this reason, we studied and discussed early- and late-types separately.

Late-type galaxies

For late-type galaxies, we found that the X-ray luminosity of galaxies with a morphological type later than Sb can be fitted by a linear relation as a function of L_B (see Fig. 3.5). The direct proportionality is expressed by the equation:

$$logL_X = logL_B - 3.85 \tag{3.4}$$

where the luminosities are expressed in solar units. This equation has a σ of 0.61 based on 63 galaxies.

Also considering the galaxy area D^2_{kpc}, calculated from the apparent diameter measured at the 25 mag arcsec^2 isophote and converted in kpc^2, instead of the blue luminosity, we found that the relation is still present, but

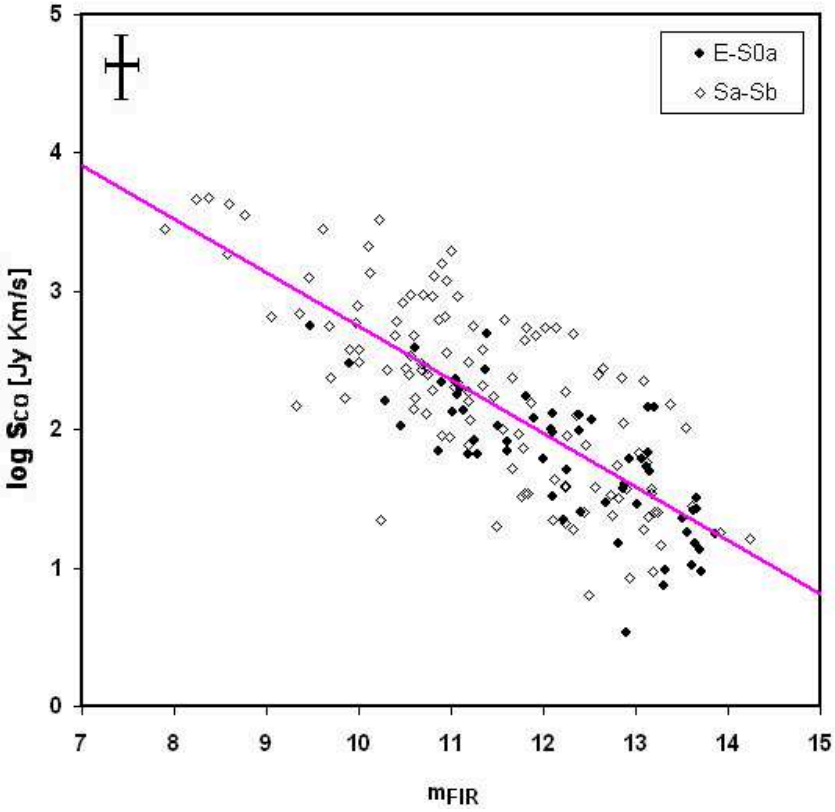

Figure 3.3: The relation between m_{FIR} and CO(1-0) flux, plotted as a pink-full line, for early-type galaxies and early spirals from E to Sb. The representative points of galaxies are plotted with different symbols. The cross at the upper left of the figure represents the mean errors for the fluxes in the whole sample.

with a wider spread. In this case the relation becomes:

$$logL_X = logD^2_{kpc} + 3.83 \tag{3.5}$$

with a σ of 0.80 for a sample of 64 galaxies.

Some authors (Griffiths & Padovani, 1990; David et al., 1992; Ranalli et al., 2003) have found a relation similar to that of Ciotti et al. (1991), using 60 μm fluxes or FIR luminosities. The values of the FIR luminosity are calculated using the formula:

$$logL_{FIR} = 2.59 + log(2.58\ S_{60} + S_{100}) + 2log\ d \tag{3.6}$$

where L_{FIR} is in solar luminosity, fluxes are in mJy, and the galaxy distance d is in Mpc.

Using the data of our catalogue, we have found a relation between L_X and L_{FIR} for late-type galaxies. In particular, we deduced that $L_X \propto L^{0.90}_{FIR}$, very similar to the $L_X \propto L^{0.88}_{FIR}$ found by Ranalli et al. (2003) for fluxes between 0.5 and 2 keV, and to $L_X \propto L^{0.95}_{FIR}$ found by David et al. (1992) using fluxes between 0.5 and 4.5 keV. Then, forcing the relation between

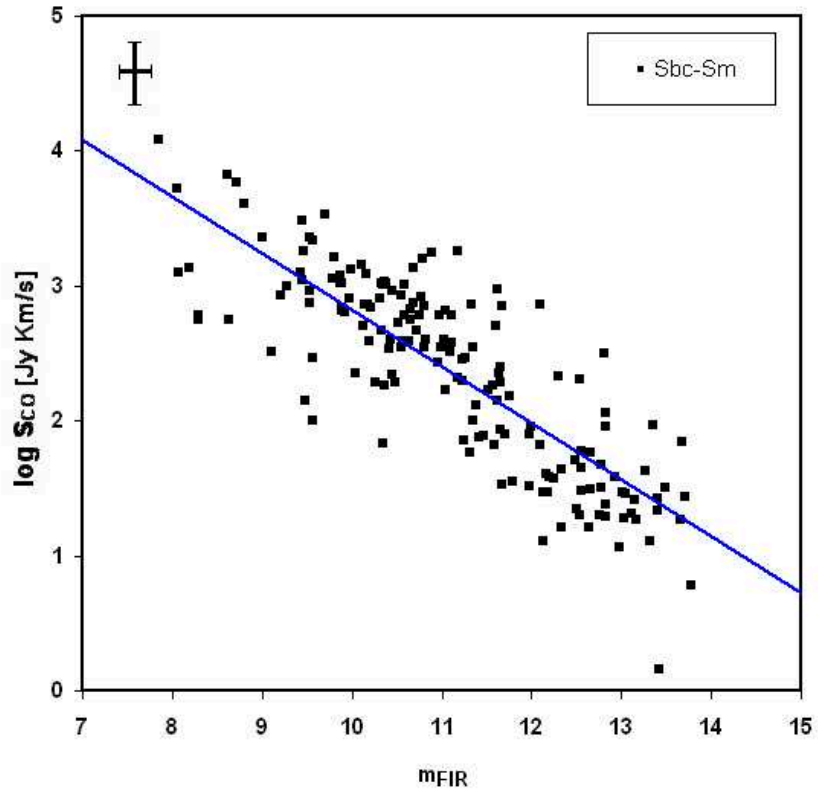

Figure 3.4: The same of Fig. 3.3 obtained for late spiral galaxies from Sbc to Sm. The relation between m_{FIR} and CO(1-0) flux is plotted as a blue-full line.

L_X and L_{FIR} to a linear proportionality we found:

$$logL_X = logL_{FIR} - 3.18 \tag{3.7}$$

with a σ of 0.47 based on 147 galaxies. This relation is plotted in Figs. 3.6, 3.8, and 3.10.

We noted that the B and FIR luminosities are also connected in late-type galaxies by means of a linear relation fitted by:

$$logL_{FIR} = logL_B - 0.38 \tag{3.8}$$

with a σ of 0.5. Combining this equation with the (3.4), we obtained:

$$logL_X = logL_{FIR} - 3.47, \tag{3.9}$$

similar to the result of equation (3.7) and to that found by Ranalli et al. (2003). This is an independent way to confirm our results and to verify the existence of a global link between L_{FIR}, B light, and X-ray emission. The connection between B luminosity, or galaxy area, and X, or FIR luminosities, will be discussed in Section 3.4.

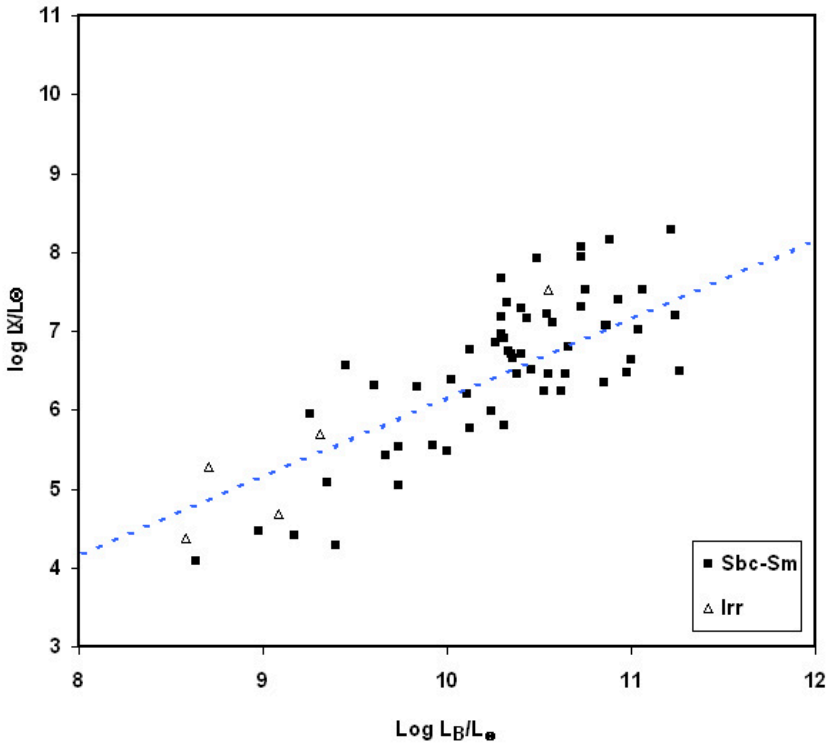

Figure 3.5: The X-ray luminosity plotted versus the blue luminosity, in solar units, for late-type, non-active galaxies. The relation corresponding to emission caused by discrete sources, indicated in Eq. (3.4) is plotted as a dotted line.

Early-type galaxies

Considering the early-type galaxies, the correlations involving X-ray emission become less evident. In this case, the relation between soft X-ray and B luminosities is:

$$logL_X = 2\ logL_B - 13.57 \tag{3.10}$$

with a σ of 0.73 based on 224 galaxies (see Fig. 3.7). The above formula agrees well with the expected relation for X-ray emission coming from hot diffuse gas, as discussed by Beuing et al. (1999).

This relation still holds if D^2_{kpc} (kpc^2) is used, instead of L$_B$, and it becomes:

$$logL_X = 2logD^2_{kpc} + 1.51 \tag{3.11}$$

with a σ of 0.85 for 226 early-type galaxies from E to Sb.

In Fig. 3.7, one can note that many galaxies with high blue luminosity, indication of high masses and of recent star formation, lie quite far from the mean line, with different behaviour than late-type galaxies.

This disagreement with behaviour found for the late-type galaxies becomes even more evident considering the link between the X-ray fluxes and the FIR luminosities. This behaviour is clearly shown in Fig. (3.8). To understand this apparent disagreement we used a theoretical analysis of the FIR emission, discussed later.

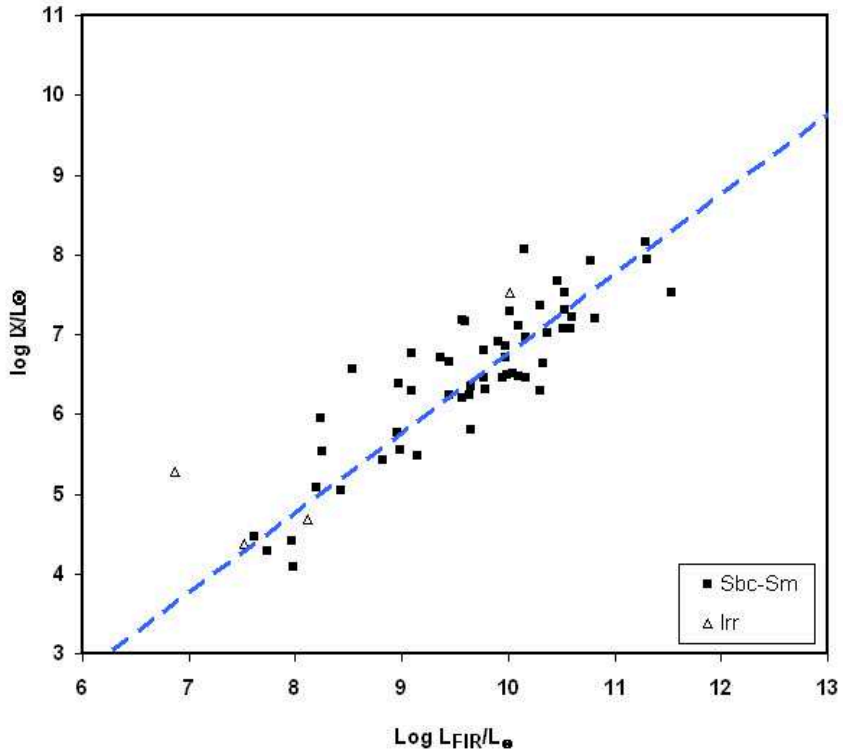

Figure 3.6: The X-ray luminosity plotted versus the FIR luminosity, in solar units for the late-type, non-active galaxies. The linear relation indicated in Eq. (3.7) is plotted as a dashed line.

Active galaxies

Finally, active galaxies (Seyfert 1, Seyfert 2, and Liners) have X-ray, B, and FIR fluxes that are not linked. This happens because, an X-ray emission from nucleus adds to mechanisms stimulating the light emission at the different wavebands present in non active galaxies. In fact, the points representative of these active galaxies are spread in the plot over the discrete source line and around the diffuse gas line (see Fig. 3.9). In the L_X–L_{FIR} diagram (Fig. 3.10) the spread is similar to that of early-type galaxies plotted in Fig. 3.7, but we separately plotted the active galaxies because of the particular nature of their X-ray emission, due to the nuclear contribution.

3.4 Discussion

Our data confirm and extend the previous relations between various tracers of the ISM in galaxies of different morphological types. In the literature the relation found by Bregman et al. (1992) between S_{CO} and S_{100} indicates a direct proportionality (slope=1) between the two fluxes and differs from that of Solomon & Sage (1988), which exhibits a steeper gradient. Our relation (3.1) agrees quite well with the proportionality found by Bregman et al. (1992), the slope we found being equal to 1.06. The similarity between

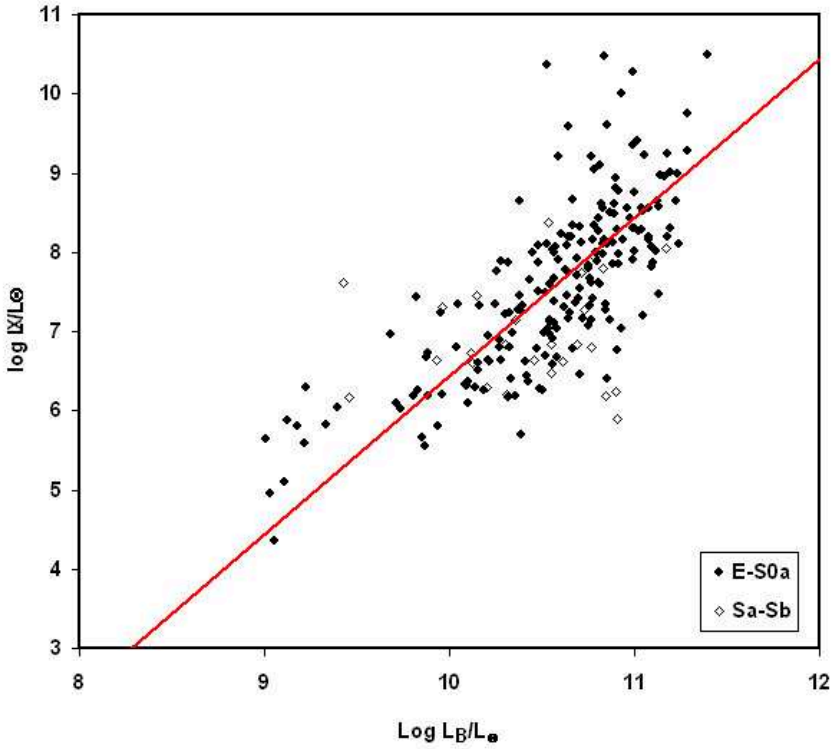

Figure 3.7: The X-ray luminosity plotted versus the blue luminosity, for early-type, non-active galaxies. The relation corresponding to emission caused by diffuse gas, valid for early-type galaxies and indicated in Eq. (3.10) is plotted as a red-full line.

the two curves shown in Figs. 3.1 and 3.2 for early- and late-type galaxies respectively, is evident. As described in Section 3.1, this link derives from the excitation of gas clouds by the currently forming stars and by the warming of the dust in the galaxy.

3.4.1 Late-type galaxies

In late-type galaxies (t>Sb) our data show the existence of a linear relation between soft X-ray fluxes and other indicators of recent and current star formation, such as the B and FIR luminosity, respectively (see Eqs. 3.4 and 3.7). This has been known since the first X-ray observations of large samples (Fabbiano et al., 1992), and this connection between B and X-ray luminosity in late-type galaxies has been interpreted as due to the contribution of discrete X-ray sources, whose number is proportional to the quantity of already formed stars (Ciotti et al., 1991; Beuing et al., 1999). The work of Kim & Fabbiano (2004) showed that the X-ray luminosity produced by discrete sources is related to B luminosity by a similar relation, with an intercept value of -3.63, similar to our -3.85 of Eq. 3.4.

In addition to the interstellar radiation, the X-ray emission is also produced by HII regions, where there is an ongoing vigorous star formation (David et al., 1992). This latter contribution appears more evident in FIR light and may explain the existence of a similar linear relation between L_X

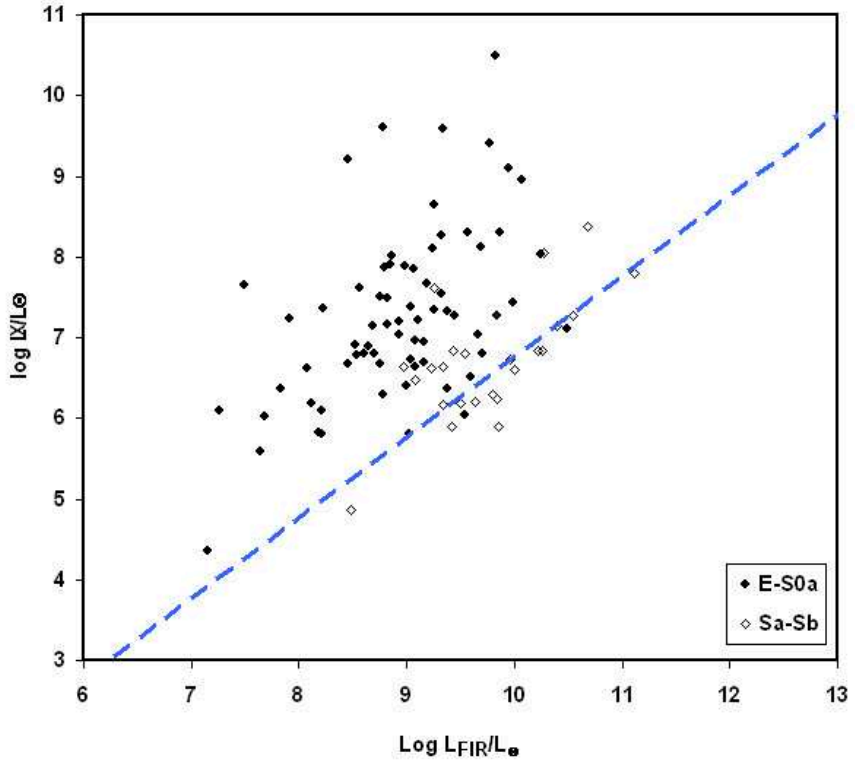

Figure 3.8: The X-ray luminosity versus the FIR luminosity for the early-type, non-active galaxies. The linear relation for late-type, non-active galaxies indicated in Eq. (3.7) is plotted as a blue-dashed line.

and L_{FIR}.

3.4.2 Early-type galaxies

In early-type galaxies the behaviour of the relations found for late types is quite different. For most of these galaxies, the star formation is exhausted and it may be present in a few of them, eventually fed by gas accretion phenomena. Different mechanisms have been suggested to explain the X-ray emission in this kind of galaxies. In particular, the main ones are the thermal emission due to hot ISM and the emission generated by a relatively old population of objects at the end of their stellar evolution, composed of Type I supernovae remnants and low-mass X-ray binaries that have not yet evolved. The X-ray emission for the fainter galaxies is compatible with discrete sources and seems to be dominated by objects with accretion disks, while for the brighter objects the emission from hot diffuse gas still present in the galactic-potential well appears as an additional component (Beuing et al., 1999). The number size of this population of relatively old objects is well represented by the total blue luminosity of the galaxy. For this reason the X-ray fluxes are still linked in early-type galaxies to the total blue luminosity, representing the more recent part of the history of star formation in the galaxy.

In the FIR, mechanisms different from the emission from warm dust

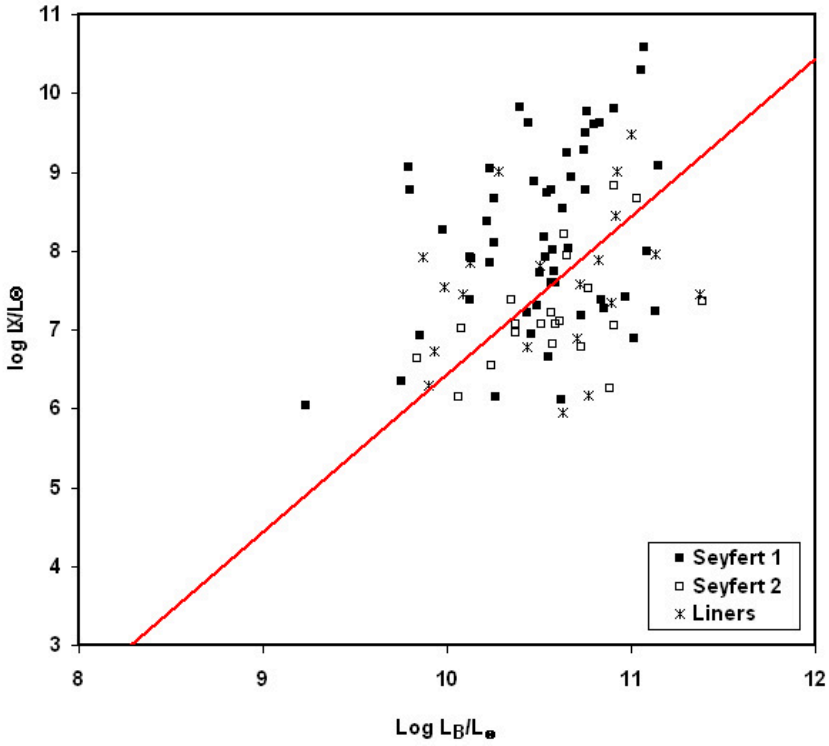

Figure 3.9: The X-ray luminosity plotted versus the blue luminosity for active galaxies, separated according to the type of activity. The relation corresponding to emission caused by diffuse gas, valid for early-type galaxies and indicated in Eq. (3.10) is plotted as a full line.

heated by the newly born stars predominate, since the star formation in most of these systems is almost exhausted. This nature of the FIR emission in early-type galaxies is also confirmed by Impey & Gregorini (1993). Studying a sample of 140 radio galaxies, they have found that radio galaxies have FIR emission with similar color temperatures to normal ellipticals, and that it represents the star formation more closely tied to the active nucleus than to the global properties of the galaxy. The FIR emission comes from circumstellar dusty shells around AGB stars and from the interstellar medium, due to the outflow of dust-rich gas from AGB and RGB stars. The origin of the IR flux in galaxies is most likely due to the dust present in the diffuse ISM that emits heated up by the galactic radiation field. Therefore to match the IR emission, one has to allow for some amount of diffuse ISM. An interesting question is therefore how much gas can be present today in an elliptical galaxy and how it is distributed across the galaxy.

The key point for interpreting the observed trends is that we are dealing with an emission coming from dust distributed over the whole galaxy and heated by an interstellar radiation field due to stars of any age. The situation is quite different from what happens, for instance, in starburst galaxies where high optical depth dusty regions reprocess the light coming from newly born stars embedded in the parental environment. We can therefore conclude that in most of our early-type galaxies, the mechanism of IR emission is

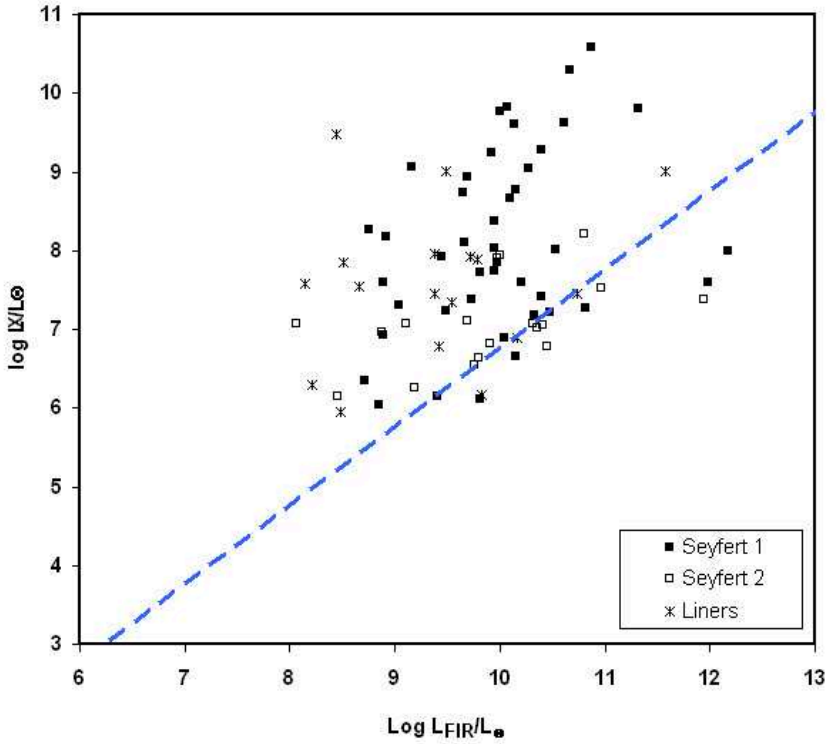

Figure 3.10: The X-ray luminosity versus FIR luminosity for active galaxies. The linear relation for late-type galaxies indicated in Eq. (3.7) is plotted as a dashed line.

not strictly related to the star formation, and the link between the younger generations of stars and dust emission is lost. For these reasons one may expect that the soft X-ray luminosity in early-type galaxies is traced by the total blue luminosity *but not* by the FIR luminosity. With the end of the star formation, the FIR emission of these galaxies has faded out and an early-type galaxy with the same L_X of a late-type will have a lower L_{FIR}. This could explain the location of the points in Fig. 3.8, on the left side of the linear relation.

3.5 Modelling early-type galaxies

To understand the nature of the relations observed between L_X, L_B, and L_{FIR} for early-type galaxies of our large sample, one has to consider the various components of a galaxy (stars, gas, and dust) and to know their mutual interactions. To check if our interpretation on the L_X-L_{FIR} relation for early-type galaxies is correct, we applied a detailed chemo-dynamical spectrophotometric model to our observations, with the collaboration of colleagues experts in the theoretical modelling of galaxies. The details of this model, that are not included in this Thesis, are described in the paper G. Galletta, V. Casasola, et al., A&A, 462, 495, 2007. Now we will describe how the model helped us to interpret observational results.

The model can compute L_B and L_{FIR} luminosities but not L_X ones.

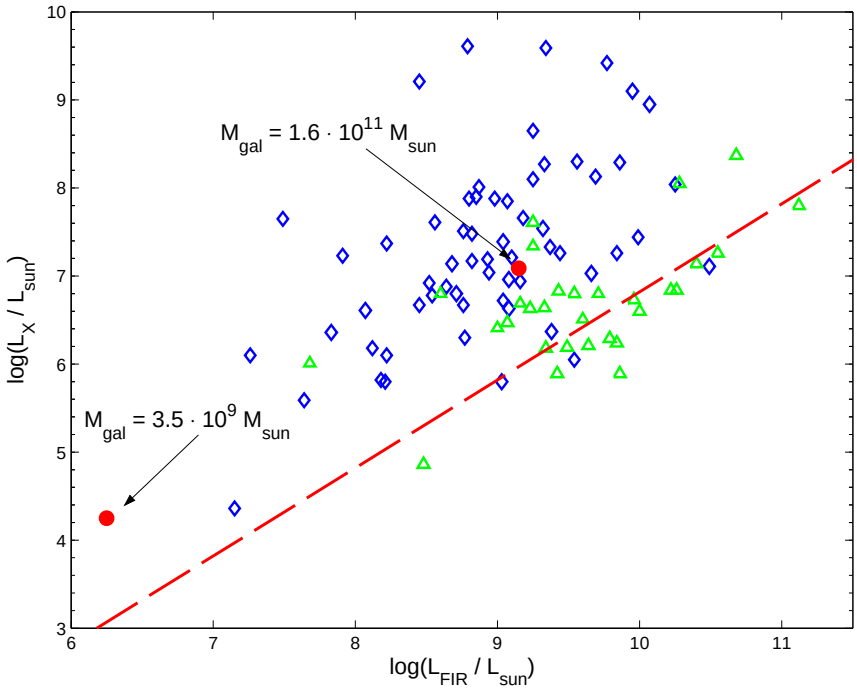

Figure 3.11: L_{FIR} versus L_X diagram as in Fig. 3.8 with the values deduced for the two template models of the early-type galaxy (filled circles). The diamonds represent the E-S0 galaxies, the triangles the S0a-Sb galaxies. The masses of the two theoretical models are also indicated. The galaxy with $\log L_X/L_\odot > 10$ present in Fig. 3.8 is not plotted here.

Then, we assumed that the X-ray luminosity is proportional to L_B according to the relation (3.10), estimating the expected X-ray flux and defining a representative point in the L_{FIR} versus L_X plot.

We considered two template models in which all the parameters are fixed using the dynamical simulations of Merlin & Chiosi (2006). The two values of L_{FIR} and L_X obtained for galaxies with values of $3.5 \times 10^9 M_\odot$ and $1.6 \times 10^{11} M_\odot$ baryonic mass models are plotted in Fig. 3.11. The less massive galaxy fits well into the region defined by the observed galaxies. The calculated levels of emission L_X and L_{FIR} of this galaxy are very low, and for this reason they belong to a region where we do not have enough observations. Its weak L_{FIR} emission can be explained by the dynamical evolution in which almost all the gas is exhausted to form stars and depleted by very efficient galactic winds. Even if the trend of this galaxy is similar to the expected one for early-type galaxies (the model is above the linear relation), nothing more can be said because of the lacking of observations in this region of the L_{FIR} versus L_X plot.

Much more interesting is the model of higher mass. The calculated luminosities with the model seem to agree well with the observations of early-type galaxies (above the linear relation). However, the model needs to be checked against other possibilities in order to understand how the various parameters influence the spread of early-type galaxies into the observational data.

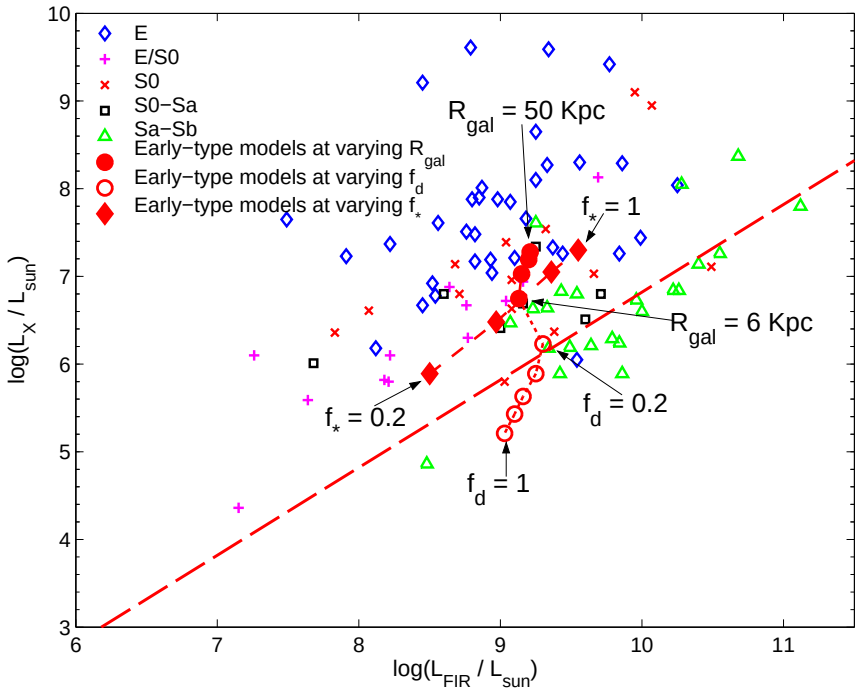

Figure 3.12: Models of the $1.6 \times 10^{11} M_{\odot}$ baryonic mass galaxy in the L_{FIR} vs. L_X diagram with the variation of the galactic radius (filled circles), the mass of stars (filled diamonds), and finally, the mass of gas (empty circles). We represented: E galaxies (empty diamonds), E/S0 galaxies (pluses), S0 galaxies (crosses), S0s galaxies (empty squares), Sa-Sb (empty triangles). The galaxy with $\log L_X/L_{\odot} > 10$ present in Fig. 3.8 is not plotted here.

3.5.1 The galactic radius and mass of stars and gas

We started checking the effects of the geometrical parameters and of the masses of stars/gas. Using the model of $1.6 \times 10^{11} M_{\odot}$ baryonic mass, we tried to vary the galactic radius, keeping the galactic nucleus in the centre of mass of the stellar component. The radii considered range from 6 kpc to 50 kpc, while all the other parameters of the model are fixed. Fig. 3.12 shows that for larger radii there is an increase in both L_{FIR} and L_X, with a more emphasized increase in L_X. Since the density profile is unchanged, the two observed increases in luminosity are simply due to the bigger amount of material considered. However, the increase in L_X is stronger than that observed in L_{FIR}. This difference can be explained considering that L_X is linearly related to L_B, which is directly connected to the stellar luminosity. Since the stellar component is more massive and more concentrated toward the centre than the gaseous one, increasing radius the model must contain more stars and more gas, but the added amount of stars is bigger than the gaseous one, shifting L_B (and so linearly L_X) more than L_{FIR}.

Another performed test investigated the dependence of the model from the amount of stars or gas. Fig. 3.12 shows a shift of the model at the smallest radius changing the mass of stars inside R_{gal}, going in fractions from $f_* = 0.2$ to $f_* = 1.0$ of the total amount of stars in the dynamical model

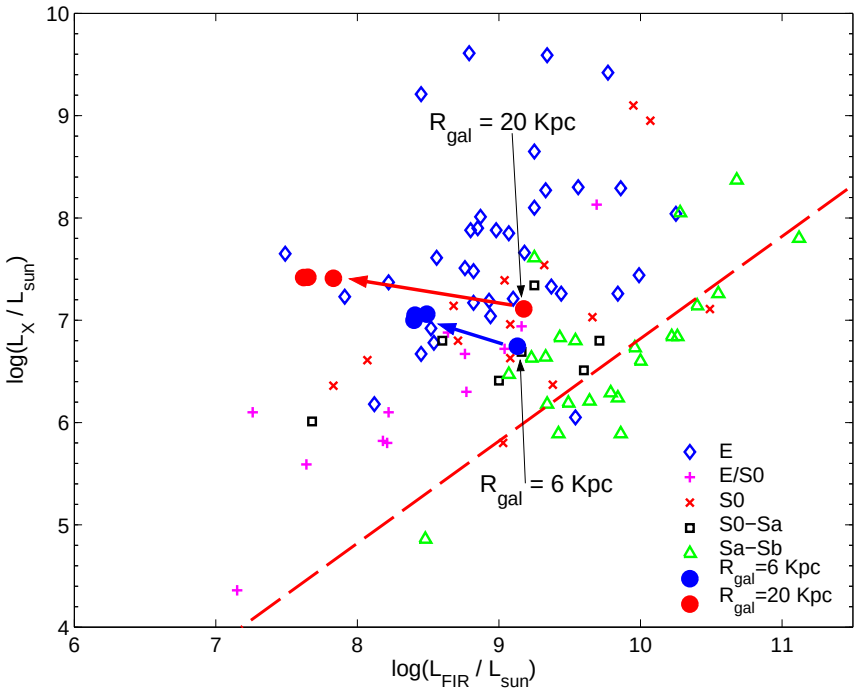

Figure 3.13: Models of the more massive galaxy of $1.6 \times 10^{11} M_{\odot}$ baryonic mass in the L_{FIR} vs. L_X diagram for various core radii r_c^{stars} and r_c^{gas}, plotted as filled circles. The thin arrows indicate the original model, while the thick arrows indicate the shift of the model for various core radii. We represented: E galaxies (empty diamonds), $E/S0$ galaxies (pluses), $S0$ galaxies (crosses), $S0s$ galaxies (empty squares), $Sa - Sb$ (empty triangles). The galaxy with $\log L_X/L_{\odot} > 10$ present in Fig. 3.8 is not plotted here.

(f_* = number of stars inside R_{gal}/total number of stars in the dynamical model). The resulting effect is to move the point along a line almost parallel to the linear relation: a smaller amount of stars implies a lower luminosity L_B (and L_X), but also a lower L_{FIR} because the weaker radiation field makes dust cooler and shifts the peak of dust emission to wavelengths longer than 100 μm.

Fig. 3.12 also shows five models obtained fixing the amount of stars and varying the mass of gas and dust from $f_d = 0.2$ to $f_d = 1.0$ of the total. Increasing the mass of diffuse gas and dust, the models are shifted far from the linear relation. In fact, a larger amount of diffuse gas/dust (fixing all the parameters and with the star formation stopped) implies more absorption of the stellar radiation and therefore a lower L_B (and L_X) with L_{FIR} unchanged or lower. Also in this case, this happens because a strong increase of the mass of dust makes the average stellar radiation field weaker, and therefore the increased emission of dust (due to the bigger mass) peaks at wavelengths longer than 100 μm leaving L_{FIR} almost unchanged.

3.5.2 The scale radii

Also considering King's laws, that describe the distribution of the stellar and gaseous components, one can find geometrical parameters interesting to

examine. The adopted expression for the star and gas density profiles is:

$$\rho_i = \rho_{0i} \left[1 + \left(\frac{r}{r_c^i} \right)^2 \right]^{-\gamma_i} \tag{3.12}$$

where "i" stands for "*stars*" or "*gas*", and r_c^i are the corresponding scale radii. The averaged profiles used for the models of Figs. 3.11 and 3.12 are both characterized by $r_c^i \simeq 0.5$, allowing for a concentrated amount of stars and gas in the inner regions. We investigated what happens if we allow for a uniform distribution of one or both of the physical components, keeping all the other parameters fixed. We considered three cases: 1) an uniform distribution of gas keeping the stellar one fixed ($r_c^{gas} \rightarrow \infty, r_c^{stars} \simeq 0.5$), 2) an uniform distribution of stars keeping fixed the gaseous one ($r_c^{stars} \rightarrow \infty, r_c^{gas} \simeq 0.5$), 3) an uniform distribution of both the components ($r_c^{stars} \rightarrow \infty, r_c^{gas} \simeq \infty$). Fig. 3.13 shows the obtained results for two radii of the galaxy model ($R_{gal} = 6$ kpc and $R_{gal} = 20$ kpc), and for the three different distributions. All the configurations suggest the same result, a lower L_{FIR} and a slightly higher L_X.

To explain this trend we considered that for $r_c^{stars} \simeq r_c^{gas} \simeq 0.5$ the diffuse ISM and the stars are both concentrated in the inner region of the galaxy with a density of stars/gas of many orders of magnitude higher than the outer regions. This situation favors the production of high L_{FIR} because regions of higher density of dust are the same in which the higher radiation field exists. In addition, the spatial distribution of the ISM favors the interaction with the stellar radiation. Destroying the coupling between stellar emission and density of gas, the L_{FIR} emission becomes weaker. With the radius of 20 kpc the dust emission is weaker because in all three cases one or both the components are distributed over a huge galactic volume with a low density of gas, eventually coupled with a weak radiation field. With the radius of 6 kpc, the galaxy is small enough to keep a acceptable value of L_{FIR} although the coupling in the central regions is destroyed.

3.5.3 The star formation history

Also the star formation history has an important role in the position of the galaxies in the L_{FIR} versus L_X plot. Considering real galaxies of the Local Universe, three spiral galaxies (M 100, M 51 and NGC 6946) and two starburst galaxies (Arp 220 and M 82), we computed their L_{FIR} and L_X by the SEDs and the models by Piovan et al. (2006). The SFHs of these galaxies allowed to cover an acceptable number of different star formation histories. These SFHs, unlike the ones of the ellipticals obtained by dynamical simulations, never end, while for the two starbursters, a strong burst of star formation is added in the last millions of years. In this way, an amount of L_{FIR} comes from the young and deeply obscured regions of star formation and not only from the diffuse component.

Fig. 3.14 shows the obtained results: the three models of spirals are located near the linear relation, the two starbursters are below the line, and the model of Arp 220 -powered by a huge burst of star formation- falls well below the linear relation. These results are quite similar to observational data: for M 100 we get ($\log L_{FIR}$, $\log L_X$)=(10.28, 7.29), close to observed values (10.37, 7.01), for Arp 220 we have ($\log L_{FIR}$, $\log L_X$)=(11.92, 7.17) compared with (11.99, 7.60), and for M 82 we get ($\log L_{FIR}$, $\log L_X$)=(10.15,

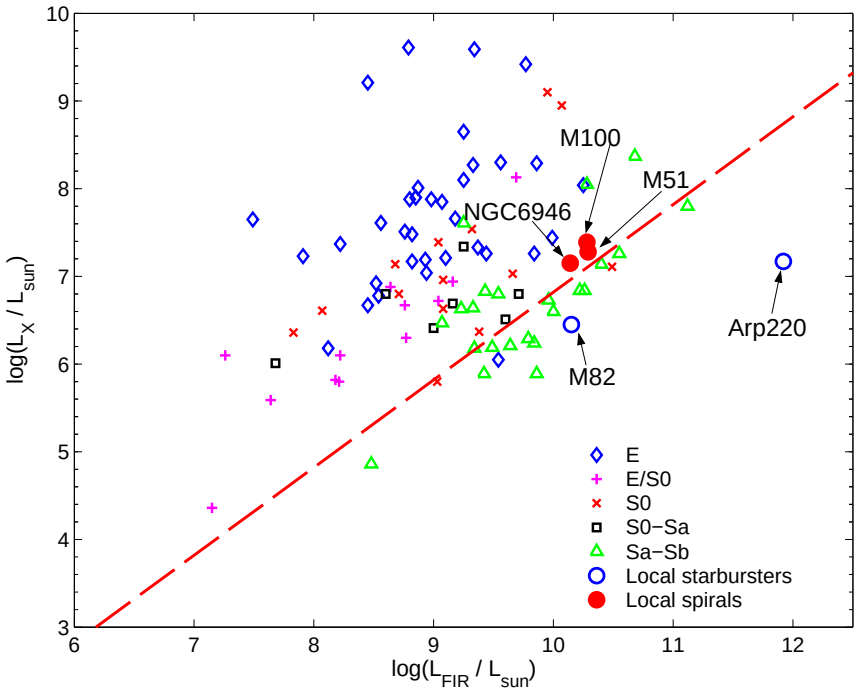

Figure 3.14: L_{FIR} versus L_X for galaxy models of spirals and starbursters. Five theoretical models, taken from Piovan et al. (2006), are represented: three spirals (M 100, M 51 and NGC 6946) and two starbursters (Arp220 and M82). Different morphological types are plotted as in Fig. 3.13. The galaxy with $\log L_X/L_\odot > 10$ present in Fig. 3.8 is not plotted here.

6.45) against (9.79, 6.31). Even if these galaxy models reproduce well real galaxies, they differ in many parameters from the early-type galaxy model of $1.6\times10^{11}M_\odot$, like geometry and mass. These parameters, in combination with the SFH, determine the position of the models in the L_{FIR} versus L_X plot. To isolate the effect of the SFHs, they have been re-calculated for the galaxy models considering the mass of $1.6\times10^{11}M_\odot$ of the early-type galaxy model. Then, the next step has been to fix all the geometrical parameters to the same values as for the average model of the $1.6\times10^{11}M_\odot$ early-type galaxy. Fig. 3.15 shows the final results obtained as a function of the SFH for the galaxy of $1.6\times10^{11}M_\odot$, keeping all the other parameters fixed. By this figure we noted that the effect of varying the SFH at fixed mass is to enhance the L_{FIR}, keeping the L_X almost fixed and shifting the points toward the linear relation at higher infrared luminosities. This is due to the efficient reprocessing of the light coming from young stars, occurring in the dusty star-forming regions. To explain this point, one can consider the relative contribution to L_{FIR} coming from the regions of star formation (let us define it f_{SFR}) and from the diffuse interstellar medium (f_{ISM}). We get the values ($f_{SFR}=10.15, f_{ISM}=10.48$), ($f_{SFR}=10.02, f_{ISM}=10.45$), ($f_{SFR}=9.98, f_{ISM}=10.37$) for the three models with spiral-like SFHs, while we have ($f_{SFR}=10.97, f_{ISM}=10.47$) and ($f_{SFR}=11.93, f_{ISM}=10.56$) for the models with starburst-like SFHs. The stronger contribution

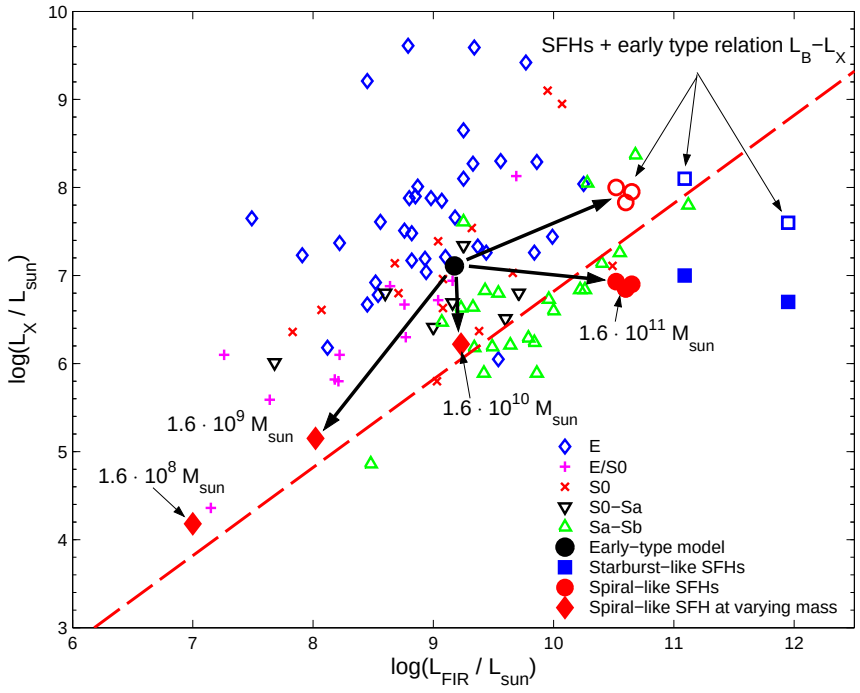

Figure 3.15: L_{FIR} versus L_X for galaxy models of fixed $1.6 \times 10^{11} M_\odot$ baryonic mass for various SFHs (large circles and squares) or at fixed SFH for various masses from $1.6 \times 10^8 M_\odot$ to $1.6 \times 10^{11} M_\odot$ (large filled diamonds). Large circles and squares represent, respectively, models with spiral-like SFH and starburst-like SFH. Large filled circles and squares are obtained using Eq. 3.4, while large open circles and squares depend on Eq. 3.10. Different morphological types are plotted as in Fig. 3.13. The galaxy with $\log L_X/L_\odot > 10$ present in Fig. 3.8 is not plotted here.

arises from star forming regions, and the higher L_{FIR} is obtained when L_B (and L_X) are almost unchanged. Fig. 3.15 also shows both the results obtained by applying the early-type linear relation between L_X and L_B (Eq. 3.10) and the late-type one (Eq. 3.4). However, the SFHs used are typical of late-type galaxies (or starbursters), while it is physically much sounder to apply Eq. (3.4) to obtain the L_X luminosity. Finally, we also calculated a sequence of models in which one of the SFHs of the spirals has been chosen (NGC6946) with all the parameters fixed and only the mass varied. Fig. 3.15 shows that the effect of varying the mass is to diagonally shift the object by almost along the relation. This shift is due to the smaller amount of emission from stars and gas.

3.6 Conclusions

Considering a large sample of galaxies of all the morphologies, activity, and interaction, we re-defined the relations existing in a galaxy between various tracers of the ISM. Studying the known relationship between the CO and the 100 μm fluxes for early-type galaxies, we found that it is also valid for late-type systems. In these galaxies, the X-ray flux also appears linked to B

and FIR emissions. Only the relation between L_X and L_{FIR} for early-type galaxies, both active and non-active, is lacking.

With the help of chemo-dynamical models coupled with dusty evolutionary population synthesis, we tried to understand and interpret the observed behaviour. The models confirmed our hypothesis about a connection between the end of the star formation and the "migration" of the early-type galaxies above the linear relation in the L_X versus L_{FIR} plot. The observed lack of a direct relation between L_X and L_{FIR} for early-type galaxies and is probably due to the different mechanisms producing FIR light in galaxies where the active star formation is no longer active. In early-type galaxies it is possible that the mechanism of IR emission is no longer strictly related to the ongoing star formation and to the reprocessing of the radiation in the dense regions where new stars are born. In this scenario, the FIR emission comes most likely from circumstellar dusty shells around AGB stars and from an interstellar diffuse medium due to the outflow of dusty gas from AGB and RGB stars.

Defining the origin of the FIR emission, we also noted that the SFH of the galaxies has the stronger effect on the position of early-type galaxies in the L_X versus L_{FIR} plot, while other parameters, such as the radius of the galaxy and the scale radii of stars and gas, play a secondary role, even if they can contribute to the scatter of the models in the region above the linear relation. However, the main role in explaining the scatter of the points along the linear relation (L_X versus L_{FIR}) is played by the mass.

To give a complete scenario, it is important to note that in the literature it has been also considered the opposite possibility, where FIR emission and star formation are linked between them in early-type galaxies similarly to late-type systems. Combes et al. (2007), for their sample of 43 E/SO galaxies, have identified the material fueling (residual) star formation in early-type galaxies, and have demonstrated that it is actively being transformed. They have not found strong correlations between the CO content and most stellar parameters (H_β, Fe5015, and Mgb), but have interpreted this result as compatible with the idea that, in a significant number of their sample galaxies, the molecular gas has been accreted from the outside and has properties rather independent from the old, pre-existing stellar component.

Chapter 4

Messier 81

Introduction

In this Chapter we present the results obtained studying the molecular gas component of the nearby galaxy Messier 81. Although M 81 has been studied in all components of its interstellar medium (ISM), from radio (e.g. Beck et al., 1985; Bietenholz et al., 1996), through optical and UV (e.g. Ho et al., 1996), to X-ray bands (e.g. Pellegrini et al., 2000), the physics of the molecular gas is yet not much understood. Here, we analyze and interpret recent observations of the CO molecule in the central region of M 81, published in the paper V. Casasola, F. Combes, D. Bettoni, G. Galletta, A&A, 473, 771, 2007.

4.1 The idea

Messier 81 in Ursa Major is one of the most conspicuous spiral galaxies in the sky, and one of the nearest beyond the Local Group (Fig. 4.1). The pronounced grand-design spiral galaxy M 81 forms a physical triplet with its neighbors, M 82 and NGC 3077, and is the brightest and probably dominant galaxy of the group called M 81 group (see Fig. 4.2). A few tens of million years ago, which is semi-recently on the cosmic time scale, a close encounter occurred between the galaxies M 81 and M 82. During this event, the larger and more massive M 81 has dramatically deformed M 82 by gravitational interaction. The encounter has also left traces in the spiral pattern of the brighter and larger galaxy M 81, first making it overall more pronounced, and second in the form of the dark linear feature in the lower left of the nuclear region. The galaxies are still close together, their centers separated by a linear distance of only about 150,000 light years.

Why Messier 81 galaxy?

We chose M 81 galaxy because it shows an anomalous behaviour in the molecular gas content and properties if compared to galaxies with similar distances and morphological type. The molecular gas content of M 81 has always been a puzzle as seen in the first observations by Solomon & de Zafra (1975) and Combes et al. (1977). The CO emission appears very weak in this galaxy, especially in the central regions, and the molecular content seems to be confined to the HII regions in the spiral arms, between 4 and 7 kpc from the center (Solomon et al., 1987; Brouillet et al., 1988, 1991; Sage & Westpfahl, 1991; Sakamoto et al., 2001). Two studies (Solomon & de Zafra, 1975; Combes et al., 1977) have searched the molecular gas in the

Figure 4.1: Optical image of Messier 81 by http://www.nasa.gov/.

center of M 81, but they have only found upper limits or failed to detect any - probably due to the low CO emission - so they did not draw any conclusions from this result. The first detection of the molecular gas in the center of M 81 was by Sage & Westpfahl (1991), who have found that the peak intensities are a factor 4 lower than those observed by Brouillet et al. (1988) in the outer disk. After the weak detection by Sage & Westpfahl (1991) only Sakamoto et al. (2001) have studied the CO emission in the center of M 81.

In addition to the weak CO emission, the HI profile also reflects a central deficiency in atomic gas. The HI gas is abundant only in the inner spiral arms of the galaxy (Visser, 1980; Allen et al., 1997), and the shapes and the motions observed in HI in the spiral arms quite clearly obey the predictions of the density-wave theory. This strong density wave is attributed to the tidal interaction with the other galaxies of the M 81 group, especially M 82 and NGC 3077 (Kaufman et al., 1989).

In general, interacting galaxies like M 81 possess higher CO luminosity by almost an order of magnitude than non-interacting galaxies, as described in the Chapter 2 and as found by Braine & Combes (1993), Combes et al. (1994), and Casasola et al. (2004). Therefore M 81 has a remarkably poor CO emission, and for this reason it is a kind of prototype of CO-poor galaxy, as is Andromeda or the center of NGC 7331.

M 81 is also a good candidate for exploring the problem of the varying CO to H_2 conversion ratio, whose properties have been described in the Chapter 2. The X ratio is well-known for varying substantially in dwarf galaxies, for which the metallicity is deficient (Rubio et al., 1993; Taylor et al., 1998), while for galaxies like M 81 that are giants with normal metallicity, the

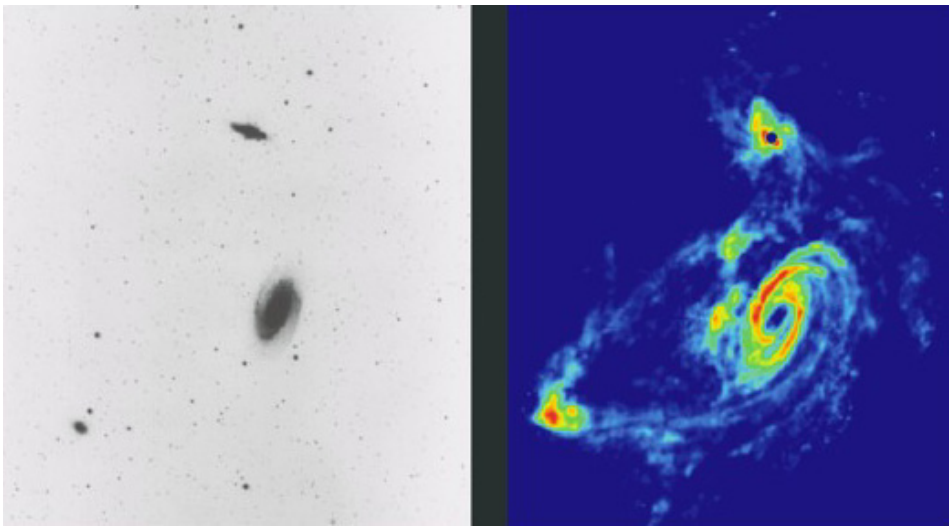

Figure 4.2: *Left*: Stellar light distribution of the M 81 group (from the Digital Sky Survey), shown in a reversed greyscale (dark regions are brighter). Most of the light in this image comes from stars in the galaxies. *Right*: 21 cm HI distribution of the M 81 group. This radio image, obtained with the VLA, shows the hydrogen gas, including streamers of gas connecting the galaxies. From this radio image, it becomes apparent that this is an interacting group of galaxies, not isolated objects. Image courtesy of NRAO/AUI.

problem of the low CO emission has not been yet explored much. The CO to H_2 conversion ratio for M 81 is suspected - on the base of the observations that are already available - of departing significantly from the mean ($X = 2.3 \times 10^{20}$ mol cm^{-2} (K km s^{-1})$^{-1}$, Strong et al., 1988), because galaxies with low CO content, such as M 31, NGC 55, or LMC, show a much larger X factor (Nakai & Kuno, 1995).

4.2 Observations

The observations were made from 2 from 6 January 2006 and from 31 March to 1 April 2006 at the IRAM 30 m telescope at Pico Veleta (Fig. 4.3), near Granada (Spain). The receiver cabin of the 30 m offers 8 spectral line receivers for the 3 mm, 2 mm, 1.3 mm (low), and 1.3 mm (high) bands. The 8 receivers are installed in 4 cryostats and are called A, B, C, and D. The nomenclature uses the letter of the cryostat and the band center in GHz, e.g. A100 is the 3 mm receiver in A cryostat, and C270 is the 1.3 mm receiver (upper part of the band) in C cryostat. Up to 4 receivers can simultaneously be used and possible combinations are given by the optical layout in the receiver cabin. The half power beam widths (HPBW) for these receivers range from $9''$ to $34''$[1]. Recently another receiver has been added, the HEterodyne Receiver Array (HERA)[2], with 9 dual polarisation pixels (18 channels) arranged in the form of a square center-filled 3×3 array. The distance between pixels on the sky is $24''$, i.e. close to twice the beam width

[1]For details on A, B, C, and D receivers see Wild (1999), The 30 m Manual-IRAM.
[2]For details on the HERA receiver see Schuster et al. (2004).

Figure 4.3: A view of the IRAM 30 m telescope. Photo by C. Risacher, B. Thomas and P. Hily-Blant.

(HPBW) at 230 GHz. HERA cannot be combined with other receivers.

For M 81, we used two different configurations for the two observing runs and we covered the central $90'' \times 90''$, where at the distance of M 81, $1'' = 17.4$ pc. In the first observing run we used the A100, A230, B100, and B230 receivers, which simultaneously observed at both 115 GHz (A100 and B100, at $\lambda \simeq 2.6$ mm, where λ is the wavelength) and 230 GHz (A230 and B230, at $\lambda \simeq 1.3$ mm). We used the 1 MHz back-ends with an effective total bandwidth of 512 MHz at 2.6 mm and an autocorrelator at 1.3 mm. We also used the 4 MHz filterbanks with an effective total bandwidth of 1024 MHz at 1.3 mm. These arrangements provided a velocity coverage of 1300 km s^{-1} in both the CO(1-0) and CO(2-1) lines, and all the measurements were performed in "wobbler-switching" mode. This observing mode has a minimum phase time for spectral line observations of 2 sec and a maximum beam throw of $240''$. The advantage of the "wobbler-switching" mode is to give very flat baselines without any ripple in most cases. The half power beam widths (HPBW) are $22''$ and $12''$ for the CO(1-0) and CO(2-1) lines, respectively, and the typical system temperatures were ∼100 K at 115 GHz and ∼400 K at 230 GHz. The positions observed with A and B receivers were 81 for both lines.

In the second observing run, we used the HERA receiver tuned to the CO(2-1) line. The sampling was $6''$, and a homogeneous mapping procedure was used to regularly sweep a 12×12 pixel map, filling the intrinsic square of $66'' \times 66''$. The typical system temperature was ∼400 K. Also in this case we used the "wobbler-switching" observing mode, and the pointing accuracy was $\sim 3''$ rms. The WILMA backend was used, providing a 1 GHz bandwidth for each of the 18 receivers. The bands contain 2×465 MHz

Table 4.1: Fundamental parameters for M 81 (at a distance of 3.6 Mpc adopted for M 81, $1''$ is ∼17.4 pc, assuming $H_0 = 70$ km s^{-1} Mpc^{-1}).

R.A. (J2000.0)	Dec (J2000.0)	V (km/s)	ν GHz	line
09:55:33	69:03:55	-34	115.271	^{12}CO(1-0)
			230.538	^{12}CO(2-1)

(=930 MHz) channels spaced by 2 MHz of resolution. The total bandwidth corresponds to 1300 km s^{-1} with a velocity resolution of 2.6 km s^{-1}. The map realized with HERA included 144 positions.

The used line intensity scale is in units of T_{mb}, the beam-average radiation temperature. The value of T_{mb} is related to T_A^*, the equivalent antenna temperature -corrected for rear spillover and ohmic losses- reported above the atmosphere, by $\eta = T_A^*/T_{mb}$, where η is the telescope main-beam efficiency, η defined as the ratio between the beam efficiency B_{eff} and the forward efficiency F_{eff}, $\eta = B_{eff}/F_{eff}$. The beam efficiency is usually derived from continuum measurements of planets, while the forward efficiency is obtained by pointing the antenna at different elevations and measuring the T_A^* of the sky at each step. The sky temperatures are successively fitted by an exponential function of the air mass, and the forward efficiency is derived with the atmospheric opacity. At 115 GHz $\eta = 0.79$, while $\eta = 0.57$ at 230 GHz.

The data were reduced with the GILDAS software package[3]. Some spectra with random, highly non-linear baselines were suppressed, and linear baselines were subtracted from all the remaining spectra. In Table 4.1 the fundamental parameters for the M 81 observations are summarized.

4.3 Molecular gas emission

4.3.1 A and B receivers

The region observed with the A and B receivers of the IRAM 30 m telescope in the two CO lines covers the central ∼ 1.4 kpc of M 81. The size and the location of the region covered by our CO observations are shown in Fig. 4.4 as a square superposed on a *GALEX* image of the galaxy.

The CO emission, both in CO(1-0) and CO(2-1) lines, comes from different regions of the galaxy nucleus. In agreement with Sage & Westpfahl (1991) and Sakamoto et al. (2001), we found that the nucleus presents some regions devoid of molecular gas, but also that there are other regions in which the CO is clearly detected and the signal is strong (Figs. 4.5 and 4.6).

In particular, the central ∼300 pc region is devoid of CO(1-0) emission in agreement, for instance, with Brouillet et al. (1988) and Sakamoto et al. (2001), but there is a main molecular gas clump structure at a distance of around 460 pc from the nucleus in the northeast direction (Fig. 4.7), which is very similar to the maximum intensity detected by Sakamoto et

[3]For details on GILDAS see http://www.iram.fr/IRAMFR/GILDAS/.

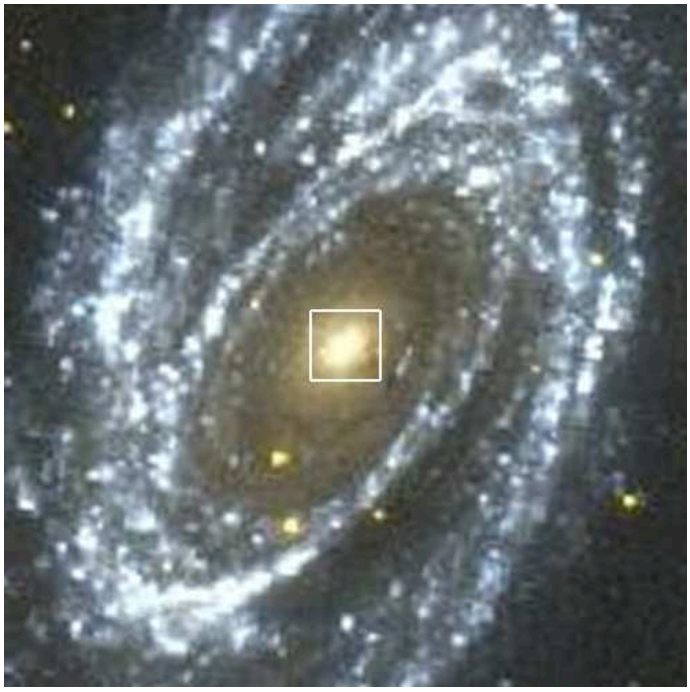

Figure 4.4: The field of our observations (white box, 80 arcsec in size) superposed on a *GALEX* composite image of M 81. In the figure, FUV is in the blue channel and NUV the yellow one.

al. (2001). In addition to the CO arc in the northeast direction, we also detected emission to the southwest one.

4.3.2 HERA receiver

The observations done with the HERA receiver cover the central $\sim$ 1.3 kpc, similar at the central $\sim$ 1.6 kpc reported above observed with the A and B receivers. These observations confirm that the molecular gas emission in the M 81 center is at a low temperature. Fig. 4.8 shows the spectral map and Fig. 4.9 the integrated contours obtained with our observations. HERA observations performed for the ^{12}CO(2-1) line also reveal "islands" of molecular gas in the nuclear region. There are regions completely devoid of emission, but also central offsets with a faint but detectable emission. The pointings with signals $\geq 2\sigma$ have peak temperatures between 16 mK and 65 mK. There is good correspondence between the emission in CO(2-1) found with HERA receiver and with A and B receivers, as shown in Fig. 4.10 where the distributions found with the two observing configurations overlap.

4.3.3 Line ratio

As described in the Chapter 2, the combination of observations of CO(1-0) and CO(2-1) lines allow to compute the line ratio and to study the physical properties of the gas more in detail, such as excitation temperature and optical depth. The study of the R_{21}=I_{21}/I_{10} line is usually simplified separating

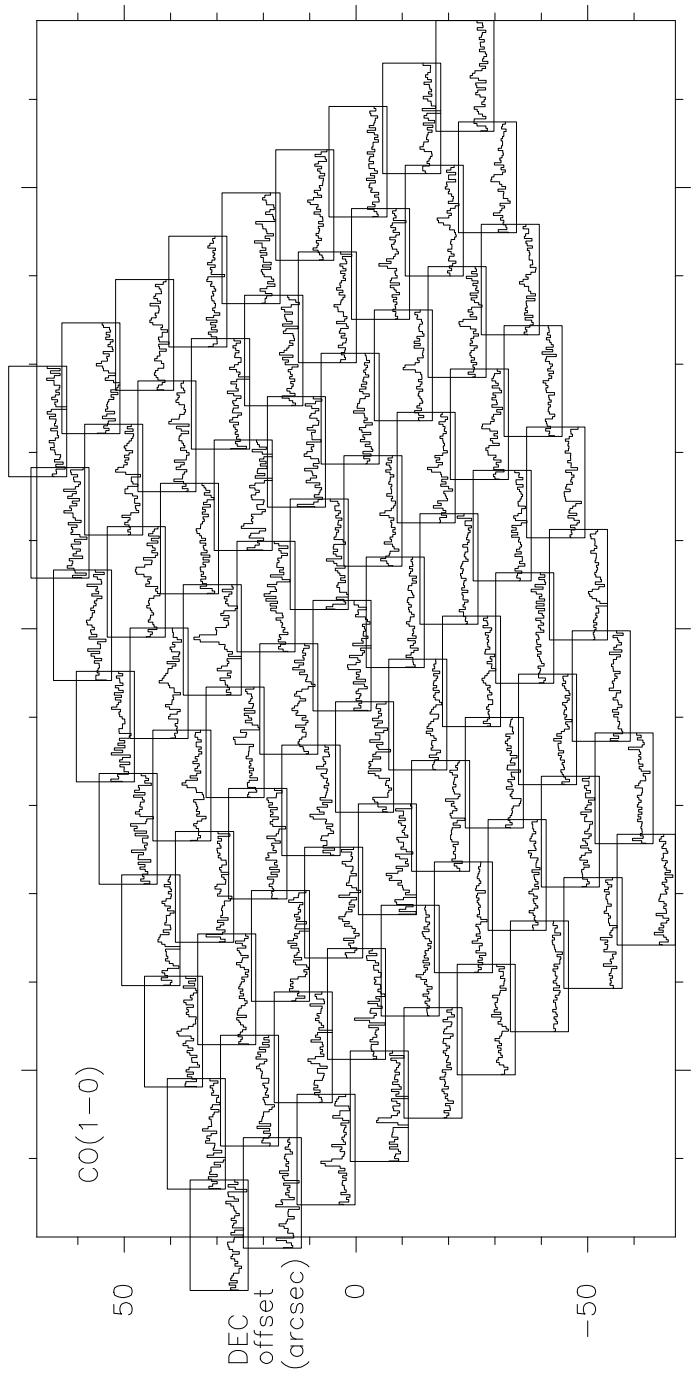

Figure 4.5: ^{12}CO(1-0) map of the observed M 81 central region. Each spectrum has a velocity scale from -600 to 600 km s^{-1}, and a temperature scale from -20 to 70 mK. The positions are offsets relative to the M 81 nucleus assumed of coordinates RA$_{J2000.0} = 09^h\ 55^m\ 33^s$, DEC$_{J2000.0} = 69^\circ\ 03'\ 55''$.

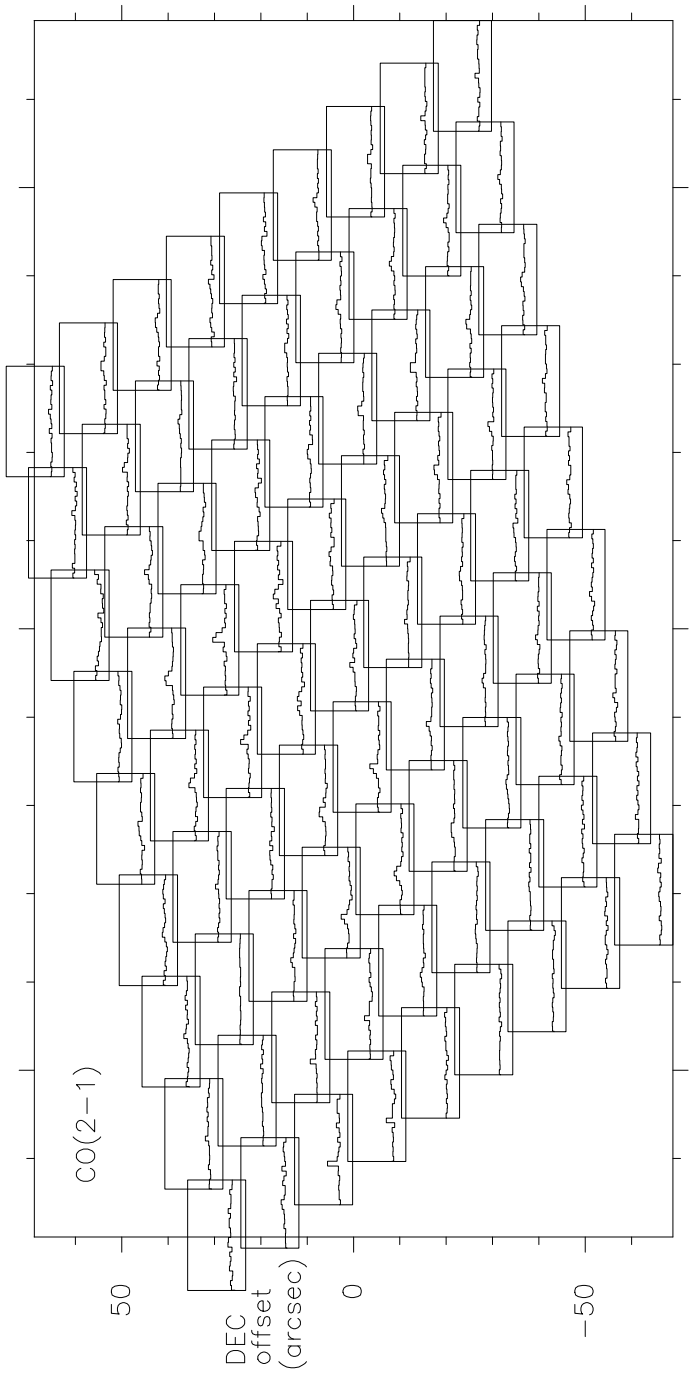

Figure 4.6: ^{12}CO(2-1) map of the observed M 81 central region. Each spectrum has a velocity scale from -600 to 600 km s^{-1}, and a temperature scale from -20 to 70 mK. The positions are offsets relative to the M 81 nucleus assumed of coordinates $\mathrm{RA}_{J2000.0} = 09^h\ 55^m\ 33^s$, $\mathrm{DEC}_{J2000.0} = 69^\circ\ 03'\ 55''$. The ^{12}CO(2-1) observations are convolved to the ^{12}CO(1-0) beam resolution (22″).

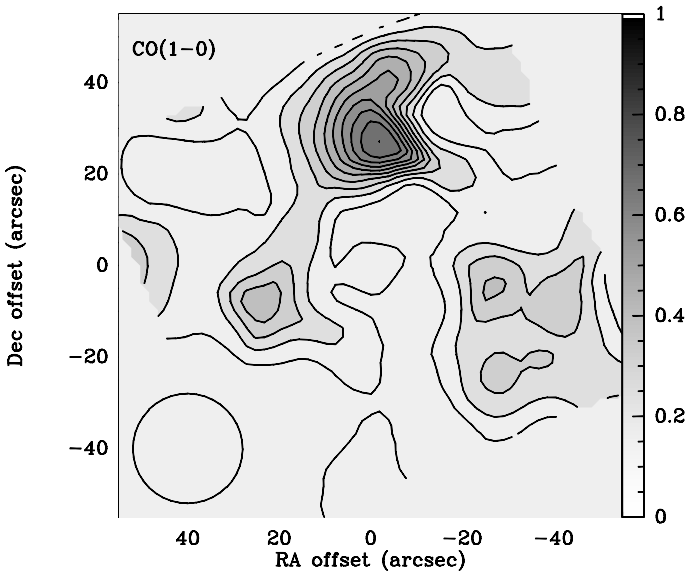

Figure 4.7: Integrated ^{12}CO(1-0) emission. The contour levels are between 0.701 to 7.01 K km/s in steps of 0.701 K km/s. The beam of 22″ is indicated at the bottom left.

two limiting cases: the optically thin case and the optically thick case. R_{21} ratios of 1 represent the limit for an optically thick gas, while R_{21} values $>$ 1 are signatures of optically thin CO emission. In most galaxies ^{12}CO lines are optically thick even if the problem is still open.

We computed the R_{21} integrated intensity ratios for the offsets observed with A and B receivers in the M 81 center, after smoothing the ^{12}CO(2-1) data to the ^{12}CO(1-0) beam resolution (22″) and correcting for the different beam efficiencies. In Table 4.2 the main results of the Gaussian fits of the observations are listed.

The first striking note is the low temperature both in CO(1-0) and CO(2-1) transitions, which characterizes the emission of all observed positions in the M 81 central region. For those detections $\geq 2\sigma$, the average brightness temperature in CO(1-0) is 33.44 mK, while in CO(2-1) it is 21.47 mK. The R_{21} ratios found in the central regions of M 81 are quite low: where the CO(1-0) emission is particularly weak, that of the CO(2-1) line appears weaker or difficult to detect, producing a low R_{21} value. The average R_{21} ratio for the center of M 81 is 0.68, a value atypical of galactic nuclei. Actually, in CO surveys (Braine & Combes, 1992) the central regions (inner kpc) of the galaxies have, on average, R_{21} ∼0.89, rarely reaching higher ratios (e.g. for NGC 3310). According to Braine & Combes (1992), this happens because the inner molecular gas is optically thick in ^{12}CO lines and is cool but not cold (T $>$ 10 K). Our low ratio for M 81 is lower than the average value of 0.89 for galaxies similar in morphology and distance. In addition, isolated galaxies appear to have line ratios that are lower than interacting/perturbed galaxies (Braine & Combes, 1992). M 81 exhibits a low value, despite being a classical example of interaction.

Studies of the disk in single galaxies show, in general, lower line ratios than those in the galactic nuclei. IC 342 (Eckart et al., 1990), NGC 6946 (Casoli et al., 1990), and M 51 (García-Burillo et al., 1993) are examples

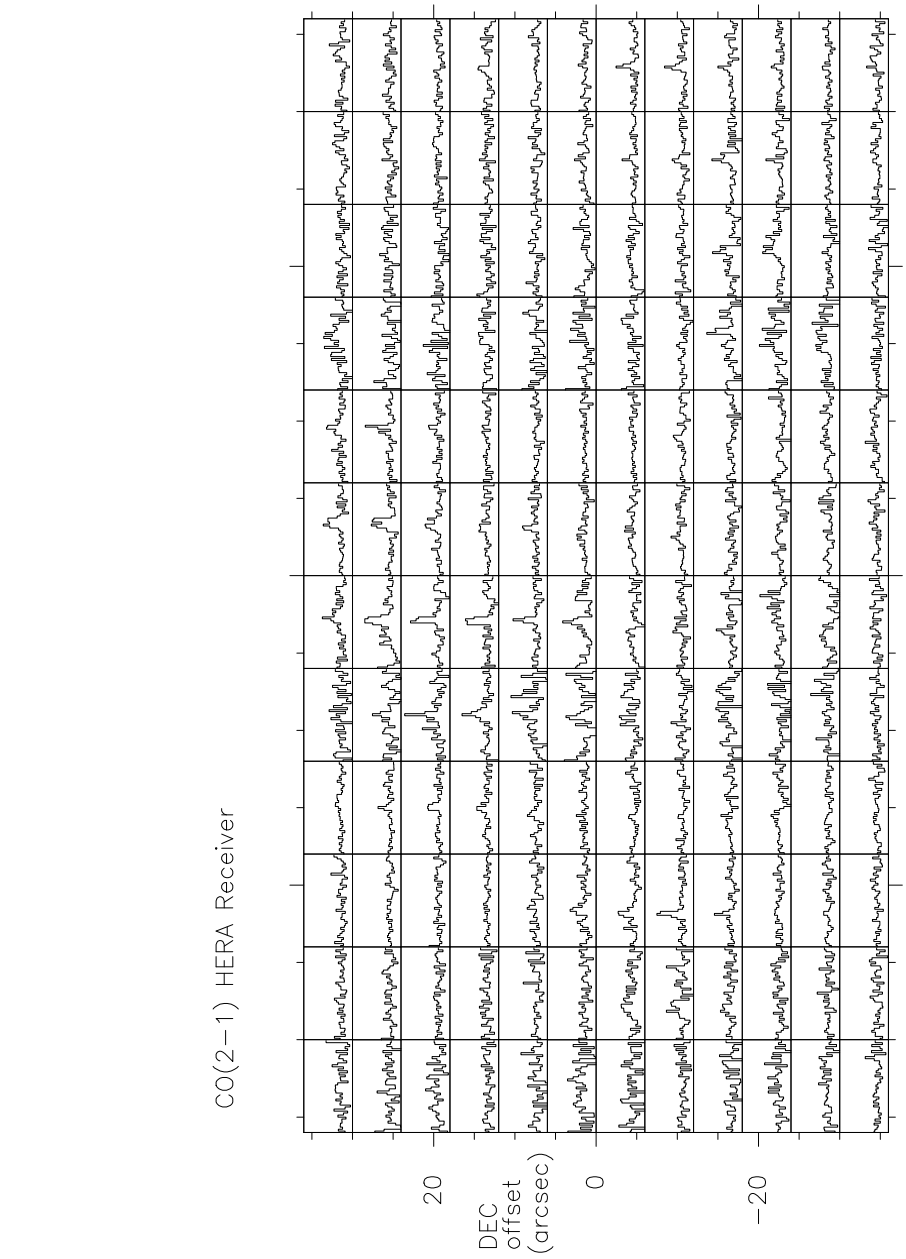

Figure 4.8: ^{12}CO(2-1) map of the M 81 central region observed with the HERA receiver. Each spectrum has a velocity scale from -600 to 600 km s^{-1} and a temperature scale from -20 to 70 mK. The positions are offsets relative to the M 81 nucleus assumed of coordinates $\mathrm{RA}_{J2000.0} = 09^h\ 55^m\ 33^s$, $\mathrm{DEC}_{J2000.0} = 69^\circ\ 03'\ 55''$.

Table 4.2: CO(J=1-0) and CO(J=2-1) intensity lines where CO emission is detected (detection level $\geq 2\sigma$). Columns (1) and (2) are the offsets ($\Delta\alpha$ and $\Delta\beta$) referred to the center of the galaxy, which coordinates are given in Table 4.1; columns (3) and (6) are the beam-average radiation temperatures (T_{mb}) for the two transitions; columns (4) and (7) are the line-widths (Δv) for the two transitions; columns (5) and (8) are the CO intensities of the two transitions obtained from Gaussian fits; column (9) is the $R_{21} = I_{21}/I_{10}$ convolved line ratios.

Offset $\Delta\alpha$ ($''$)	Offset $\Delta\beta$ ($''$)	$T_{mb}(1-0)$ [mK]	Δv(1-0) [km s^{-1}]	$\int T_{mb}(1-0)$dv [K km s^{-1}]	$T_{mb}(2-1)$ [mK]	Δv(2-1) [km s^{-1}]	$\int T_{mb}(2-1)$dv [K km s^{-1}]	R_{21}
(1)	(2)	(3)	(4)	(5)	(6)	(7)	(8)	(9)
-51.9	-30.1	29.04	74.01	2.15	10.23	83.21	0.85	0.40
-47.2	-19.1	30.16	59.01	1.78	12.73	82.55	1.05	0.59
-42.5	-8.0	28.34	88.23	2.50	14.55	115.60	1.68	0.67
-37.8	3.0	16.97	79.81	1.35				
-36.2	-23.8	34.22	59.89	2.05	16.67	87.36	1.46	0.71
-31.5	-12.7	38.18	52.72	2.01	23.87	73.12	1.75	0.87
-26.8	-1.7	18.09	150.30	2.72	20.39	97.33	1.98	0.73
-25.1	-28.4	31.67	61.07	1.93	25.13	52.02	1.31	0.68
-20.4	-17.4	33.16	47.82	1.59				
-19.1	47.2	31.85	56.16	1.79				
-8.0	42.5	38.36	96.15	3.69	16.16	70.65	1.14	0.31
-1.7	26.8	68.42	102.50	7.01	40.16	102.10	4.10	0.58
3.0	37.8	27.99	152.80	4.28	24.86	116.50	2.90	0.68
6.4	-15.7	12.52	113.40	1.42				
9.4	22.1	39.60	78.91	3.12				
14.1	33.1	34.47	66.19	2.28	22.30	80.29	1.79	0.78
15.7	6.4	41.16	44.16	1.82	18.33	94.03	1.72	0.95
22.1	-9.4	31.75	96.58	3.07	20.61	121.10	2.50	0.81
26.8	1.7	21.40	67.65	1.45	22.95	58.55	1.34	0.93
33.1	-14.1	21.76	43.95	0.96				
48.9	-7.7	58.60	32.25	1.89	19.20	52.02	1.00	0.53
53.6	3.3	47.86	55.29	2.65	35.44	61.72	2.19	0.83

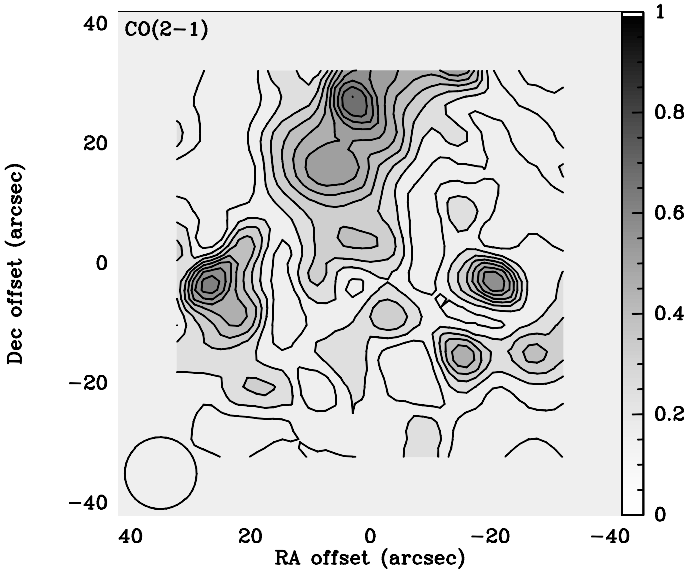

Figure 4.9: Integrated ^{12}CO(2-1) emission observed with the HERA receiver. The contour levels are between 0.410 to 4.10 K km/s in steps of 0.410 K km/s. The beam of $12''$ is indicated at the bottom left.

in which the R_{21} ratio typically decreases from ∼1 in the galactic nuclei to 0.4-0.6 in the spiral arms.

To test if R_{21} in M 81 shows a similar trend and the ratio decreases, it is necessary to use data present in the literature. There is only one observational study on M 81 with data of the spiral arms in both CO(1-0) and CO(2-1) lines (Brouillet et al., 1991). We used Fig. 2 of Brouillet et al. (1991), here shown in Fig. 4.11, to study only the fields with detections for the two lines and computed the corresponding R_{21} ratios after the transformation from detected T_A^* to T_{mb}, needed for the comparison with our data. The results of this analysis are collected in Table 4.3, where we can note that R_{21} line ratio spans in a wide range of values, without a clear radial trend. For instance, the regions N5 and N7, that are in the same area of the northeastern spiral arm, show very different values for R_{21}. This confirms the "anomalous" R_{21} behavior of M 81 with respect to other spiral galaxies.

In conclusion, M 81 is a galaxy with low intensity and an anomalous behavior of CO lines. In this respect, it is similar to the central CO-poor galaxies NGC 7331 (Young & Scoville, 1982; Young et al., 1995), which has $R_{21} \sim 0.54$ (Israel & Baas, 1999) and M 31, where similar low ratios have been found for individual dark clouds in the central region (Allen & Lequeux, 1993). In this case, the authors have attributed this fact to a subthermal excitation of the gas, at least for the CO(2-1) transition. These low ratios may be understood if coming from cool or cold, diffuse gas with a molecular hydrogen density (n(H_2)) not high enough to excite the CO molecules.

4.4 Clumping properties of the gas

As described in the Chapter 2, there is evidence that molecular clouds have a high degree of internal fragmentation on all scales, and in this case the

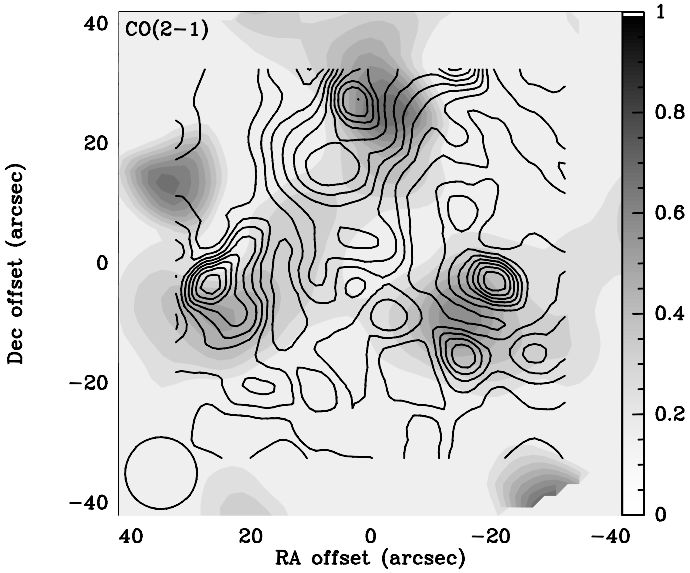

Figure 4.10: Integrated ^{12}CO(2-1) emission detected with the HERA receiver superposed on the ^{12}CO(2-1) emission found with A and B receivers. The contour levels are the same as shown in Fig. 4.9 between 0.410 to 4.10 K km/s in steps of 0.410 K km/s and the intensity levels detected with A and B receivers are in grey scale. The beam of 12″ is indicated at the bottom left. The intensity peaks detected with the two observing configurations agree quite well between them.

medium is defined as clumpy. Regan et al. (2001) and Helfer et al. (2003), with the BIMA SONG, have produced CO maps that display a remarkable variety of molecular gas morphologies, and the CO surface brightness distribution shows substructures with dimensions of a few hundred parsecs. Sakamoto et al. (1999) have found a similar result with a CO aperture-synthesis of the central regions of 20 nearby spiral galaxies using the Nobeyama and Owens Valley millimetric arrays with a typical resolution of 4″. In many galaxies they have detected CO clumps of subkiloparsec size that they have defined as giant molecular associations (GMAs).

There are several different methods of decomposing clumps in a 3-dimensional space; i.e. position-position-velocity space, and all the techniques developed allow characterization of the clumpy structure: size, line width, and one of the most important parameters of a clump, the mass. The algorithms generally used to study the clumpy nature of the gas are GAUSSCLUMPS (Stutzki & Guesten, 1990; Kramer et al., 1998) and GAUSSFIND (Williams et al., 1994). GAUSSFIND contours the cube into discrete intervals specified by the user, and then works its way through the contouring levels identifying isolated peaks as possible individual clumps. It then assigns all pixels above the lowest contouring interval to one or the other clump. Finally it merges clumps which are closer than the spatial or velocity resolution. The advantage of this algorithm is that it has no preconceptions of the shape of the clouds and hence readily deals with the complex structure of GMCs. On the other hand, the contouring technique tends to clip away too many pixels which can lead to incorrect calculation of sizes and linewidths. This may be particularly problematic for data cubes with low dynamic range. GAUSSCLUMPS avoids such problems of noisy or low dynamic range data

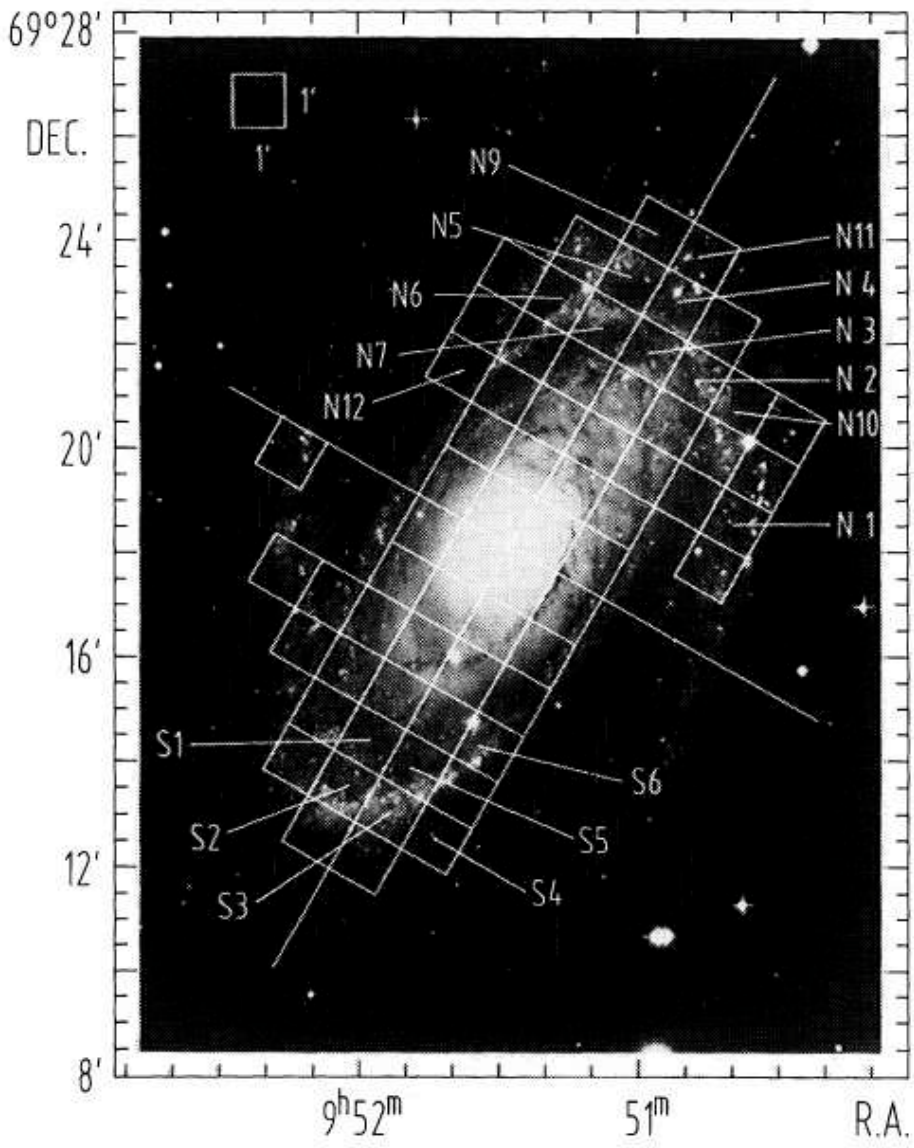

Figure 4.11: Observation grid of Brouillet et al. (1991) superimposed on a photograph of M 81 (Hale Observatories). The 17 CO detected positions are marked on the figure.

Table 4.3: R_{21} line ratio for spiral arms of M 81 by Brouillet et al. (1991). Columns (1) and (2) are the fields and the corresponding coordinates respectively defined in Fig. 2 of Brouillet et al. (1991); columns (3) and (4) are the intensities lines I_{10} and I_{21} respectively computed from the T_A^* detected by Brouillet et al. (1991); column (5) is the $R_{21} = I_{21}/I_{10}$ line ratio.

Field	Offsets ($''$,$''$)	$\int T_{mb}(1-0)\mathrm{dv}$ [K km s^{-1}]	$\int T_{mb}(2-1)\mathrm{dv}$ [K km s^{-1}]	R_{21}
N1	(0,0)	1.14	2.11	1.85
N5	(0,0)	1.52	0.70	0.46
	(10,0)	1.27	1.05	0.83
	(-10,0)	1.39	0.70	0.50
	(20,0)	0.89	0.53	0.59
	(-20,0)	1.52	1.05	0.69
	(20,-10)	2.03	1.05	0.52
N7	(0,0)	2.53	1.23	0.49
	(20,0)	1.52	1.93	1.27
	(-20,0)	2.28	1.05	0.46
	(0,20)	0.51	1.40	2.77
	(0,-20)	1.39	4.04	2.90
S2	(-10,0)	0.76	1.05	1.39
	(0,-10)	2.03	2.28	1.13
	(20,0)	2.03	1.40	0.69
	(-20,0)	1.65	1.40	0.85

by directly fitting clouds in the data cube. It tries to fit peaks of emission with an 11-parameter gaussian, also taking into account the resolution of the observations. The biggest disadvantage of this method is that it is restricted to defining clumps as gaussian, which is seldom the shape of the observed molecular emission. However, usually the results of the two algorithms agree with each other. In general, GAUSSCLUMPS is able to more easily find low-mass clumps than GAUSSFIND; and since M 81 shows a weak CO emission, we decided to use GAUSSCLUMPS. In addition, this algorithm can work with the package GILDAS, already used here.

In Figs. 4.9 and 4.10 it appears difficult to distinguish individual structures, such as molecular clouds -probably present- and estimate their characteristic parameters (dimension, mass, etc.). To study the molecular gas structure on a small scale, it is necessary to use specific tools to identify single CO clouds.

Before to describe the performed molecular structures identification, it is necessary to remember that, although very used, neither automated clump finding algorithms method is particularly well-suited to analyse GMC properties, as very recently noted by Sheth et al. (2007). The reason of this limits has more to do with molecular clouds than the algorithms themselves. Molecular cloud structure is extremely complex, at least as observed in the Milky Way. These algorithms tend to divide a complex into as many subdivisions as allowed by the resolution of the data. Hence these methods seldom find structures which are larger than one or two resolution elements. For example, if the resolution of a survey is 5 pc, these methods will not

find a 100 pc complex because peaks of emission located more than 5 pc apart will be classified as separate clouds. The bias thus introduced is not fatal because cloud/clump properties in equivalent datasets (i.e. datasets with similar resolutions and noise characteristics) may still be compared, but generalizations about a galaxy's cloud population can not be drawn. This is especially pertinent to extragalactic objects, where higher resolution observations are continually being achieved with improvements in millimeter single-dish and interferometer astronomy.

Since molecular clouds generally have fairly sharp edges, the simplest cloud identification algorithms is the integrated intensity contouring method where one identifies the contour level associated with the edge of the cloud (e.g. Sanders et al., 1985; Dame et al., 1986) in a 3 dimensional cube. The obvious shortcoming of this method is that it ignores the structure in the clouds. Another obvious disadvantage of the method is that it is difficult to automate and is quite time consuming because one has to make three different moment maps along the different axes and decide what the distinct complexes are. This method may suffer from blended emission but this confusion is limited in extragalactic sources. Rosolowsky & Leroy (2006) has recently introduced a new method for identifying and analyzing molecular clouds which may avoid many of the biases discussed above; this method may be a useful tool for future surveys of molecular clouds in nearby spirals with CARMA and ALMA.

Sheth et al. (2007), although have noted the limits of the two automated algorithms, comparing CLUMPFIND and GAUSSCLUMP for M 31, M 33 and Milky Way molecular clouds have found that GAUSSCLUMP is better at recovering cloud properties than CLUMP FIND for low dynamic range data. Their tests have revealed that such algorithms are resolution dependent and the inherent clumpy nature of molecular emission prevents these methods from identifying clouds larger than one or two resolution elements. Hence they have cautioned against using these methods to characterize GMC populations in galaxies. Still, these may be used to quickly compare properties of clouds in data with similar noise and resolution characteristics.
In the following section we will describe the results obtained with the application of the GAUSSCLUMP algorithm to our observations of the M 81 galaxy.

4.4.1 Molecular Associations

The first application of GAUSSCLUMPS to CO(2-1) data obtained using HERA receiver found 27 molecular associations in the central 1.3 kpc; however, it is necessary to fix the constraints to check misidentification. The algorithm forces the unresolved clumps to have a size corresponding to the spatial and velocity resolutions, so if the 3D size of a clump is exactly equal to the resolution in each axis, this clump could be an artefact. With a beam of $12''$, only clumps with the intrinsic FWHM size (beam deconvolved) $\Delta\xi > 10''$ are realistic, so all the other clumps have been discarded. The second constraint is on the intrinsic brightness temperature (corrected for beam dilution), which must be at least 5 times the noise level of the original map, T > 0.035 K (Stutzki & Guesten, 1990). After applying these constraints, the number of molecular associations found in the M 81 central region has become 16 and their properties are listed in Table 4.4.

Considering that the Gaussian-shaped molecular associations have two principal axes, we found a mean intrinsic diameter for all molecular structures identified of $14''$ ($\sim$250 pc). Molecular structures with these dimensions

are defined as GMAs. The maximum GMA peak intensity is 0.070 K, the mean intensity is 0.046 K and the mean velocity FWHM 13.5 km s^{-1}.

Summing up the area corresponding to the intrinsic FWHM extent of the fitted GMAs in the selected field, one obtains a total area covered by GMAs that is from 2.2 to 4.5 times smaller than the field, therefore the filling factor of the GMAs is low, about 0.3.

4.4.2 GMAs masses

For an optically thin gas, or at the other extreme for a completely optically thick gas (Kramer et al., 1998), the mass of a molecular association is proportional to the fitting parameters of GAUSSCLUMPS: the molecular association intensity, the molecular association velocity width, and the spatial FWHMs along both two principal axes:

$$M \propto T_{pk} \times \Delta \mathrm{v} \times \Delta x_1 \times \Delta x_2 \tag{4.1}$$

We computed the mass in two hypotheses, optically thin gas and optically thick gas.
For the estimation in the optically thin case, we adopted the Rayleigh-Jeans approximation, where: $f(T_{ex}) = \frac{h\nu/k}{1-exp[-h\nu/kT_{ex}]} \sim T_{ex}$, since $T_{ex} > 15$ K. Local Thermodynamic Equilibrium (LTE) is also assumed, meaning that T_{ex} is the same for all levels. The total CO column density N_{CO} is related to the population N_i of level i by $N_i/N_{CO} = g_i exp\left[-E_i/kT_{ex}\right]/Q$, where g_i and E_i are the degeneracy factor and the energy of the level i, and Q the partition function is $Q(T) = 2kT/h\nu_{1-0} = T(K)/2.76$. This total CO column density, derived from the integrated intensity of the CO(2-1) line, is given by the following equation, in the optically thin limit:

$$\frac{N_{CO}}{(mol/cm^2)} = 1.2 \times 10^{13} \times T_{ex}\,(K) \int T_{mb}\,(K)\,\mathrm{dv}\,(km/s) \tag{4.2}$$

The corresponding molecular mass (taking into account helium) is

$$\begin{aligned} \frac{M}{(M_\odot)} &= 1.2 \times 10^{13} \frac{m_{H_2}}{(M_\odot)} \frac{N(H_2)}{N(^{12}CO)} \times T_{ex}\,(K) \\ &\quad \times \int\int T_{mb}\,(K)\,\mathrm{dv}\,(km/s)\,dA(cm^2) \end{aligned} \tag{4.3}$$

In terms of fitting parameters in Table 4.4 (see Chi & Park, 2006) and when assuming an excitation temperature of $T_{ex} \simeq 15$ K, an abundance ratio $N(H_2)/N(^{12}CO) \simeq 10^4$, and a distance of 3.6 Mpc adopting $H_0 = 70$ km s^{-1} Mpc^{-1}, Eq. (4.3), valid in the optically thin case, becomes:

$$\frac{M_{thin}}{(M_\odot)} = \frac{T_{mb}}{(K)} \times \frac{\Delta \mathrm{v}}{(km/s)} \times \frac{\Delta x_1}{('')} \times \frac{\Delta x_2}{('')} \times 10.5 \tag{4.4}$$

In this hypothesis, the ratio between the observed peak brightness temperature and the excitation temperature is the filling factor of the porous molecular associations, on the order of 3 $\times 10^{-3}$. Applying Eq. (4.4), we found very small molecular association masses contained in a low mass range, from

$7.37 \times 10^2 M_\odot$ to $3.83 \times 10^3 M_\odot$, with a mean value of $1.31 \times 10^3 M_\odot$. The masses computed in the optically thin case for all molecular associations are listed in Table 4.5.

In the optically thick case, the molecular mass of the molecular associations is determined by the H_2 density (N_{H_2}) using the *standard X* conversion factor value ($X = 2.3 \times 10^{20}$ mol cm^{-2} (K km s^{-1})$^{-1}$, Strong et al., 1988), $N_{H_2} = X \int T_{CO(1-0)} \mathrm{dv}$. Since we resolved single GMAs in the CO(2-1) transition, using the mean $R_{21} = I_{21}/I_{10}$ value computed here ($\overline{R}_{21} = 0.68$), the H_2 density can be expressed by:

$$\begin{aligned} \frac{N_{H_2}}{(mol/cm^2)} &= \frac{X}{\left(\frac{mol/cm^2}{Kkm/s}\right)} \times \frac{1}{R_{21}} \int T_{CO(2-1)}\,(K)\,\mathrm{dv}\,(km/s) \\ &= 3.4 \times 10^{20} \int T_{CO(2-1)}\,(K)\,\mathrm{dv}\,(km/s) \end{aligned} \tag{4.5}$$

and the corresponding molecular mass is:

$$\begin{aligned} \frac{M}{(M_\odot)} &= 3.4 \times 10^{20} \frac{m_{H_2}}{(M_\odot)} \\ &\quad \times \int\int T_{CO(2-1)}\,(K)\,\mathrm{dv}\,(km/s)\,dA(cm^2) \end{aligned} \tag{4.6}$$

In terms of fitting parameters in Table 4.4 and assuming a distance of 3.6 Mpc, Eq. (4.6) gives the GMA mass in the optically thick limit:

$$\frac{M_{thick}}{(M_\odot)} = \frac{T_{mb}}{(K)} \times \frac{\Delta \mathrm{v}}{(km/s)} \times \frac{\Delta x_1}{(\prime\prime)} \times \frac{\Delta x_2}{(\prime\prime)} \times 1.97 \times 10^3 \tag{4.7}$$

Applying Eq. (4.7), the GMA masses range from $1.38 \times 10^5 M_\odot$ to $7.20 \times 10^5 M_\odot$, with a mean value of $2.46 \times 10^5 M_\odot$. The total mass of the GMAs is $3.22 \times 10^5 M_\odot$. The masses computed in the optically thick case for all GMAs are listed in Table 4.5.

That the masses obtained through the optical thin hypothesis are much lower than those calculated in the optically thick case is not "anomalous": instead, it is expected that the optical thin hypothesis underestimates the masses, since GMAs have a rich substructure of subclumps with high column density. The subclumps are probably optically thick, as is generally the case in external galaxies, as suggested by the high ^{13}CO emission commonly observed. Anyway, we decided to also analyze the optically thin case because M 81 represents an extraordinary laboratory where all possibilities should be considered even if unusual for similar galaxies.

4.4.3 Virial equilibrium

An alternative way of determining GMA masses is to compute their virial mass. Assuming a balance between the total kinetic energy T of a GMA and the gravitational potential Ω, and neglecting external pressure, the virial mass M_{vir} of the clouds can be calculated using the formula:

Table 4.4: GMAs identified in the M 81 center with GAUSSCLUMPS. Column (1) is the GMA number; columns (2) and (3) are the GMA center positions referred to the center of the galaxy, which coordinates are given in Table 4.1; column (4) is the GMA center velocity; column (5) is the GMA peak intensity; column (6) and (7) are the GMA spatial FWHMs along the two principal axis; column (8) is the orientation of the first principal axes (counterclockwise from west); column (9) is the GMA velocity FWHM; column (10) is the GMA internal velocity gradient; column (11) is the direction of internal velocity gradient (counterclockwise from west).

Number	$\Delta\alpha$	$\Delta\delta$	v_0	T_0	Δx_1	Δx_2	φ	Δv	dv/dr	φ_v
	[″]	[″]	[km s $^{-1}$]	[K]	[″]	[″]	[°]	[km s $^{-1}$]	[km s $^{-1}$]	[°]
(1)	(2)	(3)	(4)	(5)	(6)	(7)	(8)	(9)	(10)	(11)
1	6.9	20.0	6.13	0.07	15.8	19.2	83.7	17.2	1.67	88.2
2	9.4	8.8	238.31	0.06	12.0	12.1	5.9	12.1	2.76	-111.8
3	-14.8	-16.1	133.76	0.05	12.0	12.1	101.3	12.1	2.29	-106.3
4	-7.1	27.3	132.12	0.05	12.0	17.2	94.5	13.9	2.05	-69.7
5	4.4	-20.2	341.63	0.05	12.0	12.1	36.9	12.1	1.72	-138.2
6	8.9	2.7	524.09	0.05	12.0	19.0	43.8	14.3	2.04	-90.2
7	-17.3	-20.6	-21.47	0.04	12.0	17.2	48.5	13.9	1.40	-86.3
8	9.2	-28.2	264.09	0.04	12.0	12.1	56.9	12.1	3.04	-149.6
9	-15.7	-20.2	185.01	0.04	12.0	16.8	65.1	13.8	1.69	44.6
10	-14.7	-27.0	263.61	0.04	12.0	12.1	63.6	12.1	4.41	28.6
11	7.9	9.0	30.24	0.04	12.0	13.0	121.2	12.5	3.42	-33.7
12	1.6	27.2	56.42	0.04	12.0	23.6	88.8	15.1	1.39	-105.3
13	8.4	-15.5	316.24	0.04	12.0	12.1	87.7	12.1	5.83	4.7
14	9.2	-14.9	82.50	0.04	12.0	12.1	22.6	12.1	3.62	115.8
15	-32.9	-9.2	-22.05	0.04	12.9	20.0	81.0	15.3	1.04	-18.8
16	-14.5	21.9	-22.41	0.04	19.0	12.1	29.3	14.5	2.18	42.0

$$M_{vir} = K \times D_e \times \Delta \mathrm{v}^2 \tag{4.8}$$

where M_{vir} is in $M_\odot$, D_e is the effective diameter in pc of the equivalent sphere of radius $R = (\Delta x_1 \Delta x_2/4)^{0.5}$, and Δv is in km s^{-1} (Solomon et al., 1987). We assumed that the cloud is a sphere with a power-law ($\alpha = 1$) density distribution. In this case, the constant K in formula (4.8) is equal to 95. The rougher assumption of uniform density (4.8) would have instead produced K=104. Here, the hypothesis of spherical shape for the cloud makes the formula independent of the galaxy inclination.

A comparison between the virial mass and the mass computed from the observed intensity lines (M_{obs}) in the optical thick hypothesis is informative for the physical state of the clouds, their optical thickness, and for the actual $X = N(H_2)/I(CO)$ conversion factor.

The virial masses of the 16 GMAs we identified span from 2.92×10^6 to $8.54 \times 10^6 M_\odot$, with a mean value of $4.31 \times 10^6 M_\odot$. In calculating M_{vir}, we neglected the mass of the atomic hydrogen ($M_{HI} = 0$) since Allen et al. (1997), studying the HI profile in M 81, have found a deficiency of atomic hydrogen in the central $\sim$3 kpc, and the HI emission only begins to be significant in the inner spiral arms beyond $\sim$5 kpc from the nucleus.

We also checked that the stars do not contribute significantly to the mass inside the volume of a GMA. In the hypothesis that the H_2 mass is computed from the virial mass, resolved GMAs have mean surface densities ranging from 84 M$_\odot$/pc^2 to 118 M$_\odot$/pc^2 with a mean value of 91 M$_\odot$/pc^2. The mean value of the mass-to-light ratio of visible matter expected for M 81 is M/L$_B$ = 5.5 M$_\odot$/L$_\odot$ (see Tenjes, 1994). From the exponential surface brightness distribution of the stellar disk of the galaxy, we then deduced a mean stellar surface density of 36 M$_\odot$/pc^2 in the region. In addition, if we consider that GMAs normally have a thickness of about 50 pc while the stars are distributed in regions that are at least ten times thicker, the actual mean volumic stellar density is negligible with respect to the molecular density inside a GMA.

All the GMAs have a virial mass $\gg$ of the mass computed from CO observations, and the mean ratio $\alpha_{vir} = M_{vir}/M_{obs}$ computed for our GMAs is $\alpha_{vir} \simeq (10 - 20) \gg 1$. The α_{vir} ratios computed for all the GMAs are listed in Table 4.5.

4.4.4 The X factor for M 81

As said in both the Chapter 1 and 2, the value of the conversion factor between the H_2 and the CO integrated intensity is subject to debate. The X factor is determined by various factors depending on the small scale physics and chemistry of the gas, such as the metallicity, the temperature, the cosmic ray density, and the UV radiation field (Maloney & Black, 1988; Boselli et al., 2002), and on morphological type of the galaxies and/or I_{CO} (Nakai & Kuno, 1995). Since M 81 shows atypical properties for its molecular gas, the X ratio is also suspected of departing significantly from the mean Galactic value and in general from that of galaxies with the same morphological type. Thus, M 81 represents an exceptional laboratory to explore the variation of the X ratio.

We derived the X conversion factor for all individually resolved molecular associations assuming the virial equilibrium for single molecular complexes

Table 4.5: Properties of the GMAs derived by application of GAUSSCLUMPS. Column (1) is the GMA number as defined in Table 4.4; column (2) is the effective radius of the GMAs; columns (3), (4), and (5) are the masses of the GMAs computed in the optically thin limit, in the optically thick limit, and using the virial theorem, respectively; column (6) is the ratio $\alpha_{vir} = M_{vir}/M_{obs}$ for each GMA, where $M_{obs} = M_{thick}$; column (7) is the derived X conversion factor for each GMA.

Number	R_{eff}	M_{thin}	M_{thick}	M_{vir}	α_{vir}	X
		10^3	10^5	10^6		10^{21}
	[pc]	$[M_\odot]$	$[M_\odot]$	$[M_\odot]$		[mol cm^{-2} (K km s^{-1})$^{-1}$]
(1)	(2)	(3)	(4)	(5)	(6)	(7)
1	151.88	3.83	7.20	8.54	11.86	2.3
2	105.08	1.11	2.08	2.92	14.07	2.7
3	105.08	0.92	1.73	2.92	16.89	3.3
4	125.28	1.50	2.83	4.60	16.27	3.1
5	105.08	0.92	1.73	2.92	16.89	3.3
6	131.67	1.71	3.21	5.12	15.93	3.1
7	125.28	1.20	2.26	4.60	20.34	3.9
8	105.08	0.74	1.38	2.92	21.11	4.1
9	123.81	1.17	2.19	4.48	20.43	3.9
10	105.08	0.74	1.38	2.92	21.11	4.1
11	108.91	0.82	1.54	3.23	21.04	4.1
12	146.74	1.79	3.37	6.36	18.86	3.6
13	105.08	0.74	1.38	2.92	21.11	4.1
14	105.08	0.74	1.38	2.92	21.11	4.1
15	140.06	1.66	3.11	6.23	20.03	3.9
16	132.22	1.40	2.63	5.28	20.10	3.9

and using the large velocity gradient (LVG) approximation for the formation of the CO line (Sanders et al., 1984; Young & Scoville, 1984). This method has also been used to derive the conversion factor in nearby spiral galaxies such as M 31, M 33, and the Magellanic Clouds (Wilson & Scoville, 1990, 1992; Arimoto et al., 1996).

In practice, we computed the X ratio ($X = N(H_2)/I_{CO}$) deriving the H_2 density from the virial masses ($N(H_2) = M_{vir}/(m_{H_2} \times dA)$, where m_{H_2} is the mass of the hydrogen molecule and dA the area occupied by the cloud), and I_{CO} is the CO observed intensity. For the individually resolved GMAs of M 81, assumed virialized, we found that the X conversion factor takes a much higher value than the mean Galactic value for all clouds, ranging from ∼10 to ∼18 times higher than the *standard* X and a mean value of $X = 3.6 \times 10^{21}$ mol cm^{-2} (K km s^{-1})$^{-1}$. The X conversion factor values computed for all the GMAs are listed in Table 4.5.

Our X factor values are high, not only if compared to the *standard* Galactic factor, but also with respect to values found in other nearby galaxies where the X ratio has been obtained with the same method we used. Studying a sample of nearby spiral and dwarf irregular galaxies, Arimoto et al. (1996) have derived X values using CO data found in the literature and computed the corresponding virial mass. They have found galaxies with both X values lower and higher than in the Galaxy, such as M 31 with $X = 1.8 \times 10^{20}$ mol cm^{-2} (K km s^{-1})$^{-1}$, M 33 with $X = 4.1 \times 10^{20}$ mol cm^{-2} (K km s^{-1})$^{-1}$, and IC 10 where $X = 6.6 \times 10^{20}$ mol cm^{-2} (K km s^{-1})$^{-1}$. Even if they have found high X values, these H_2-to-CO conversion factors are smaller than our X ratios obtained for M 81. Arimoto et al. (1996) have found a X ratio (=3.1×10^{21} mol cm^{-2} (K km s^{-1})$^{-1}$) only for the SMC within the same order of magnitude of M 81. They have specified that this value has been obtained by considering virial masses and CO luminosities for larger-scale complexes in the SMC and that this high X would be due to a smaller amount of CO in a diffuse medium that is metal dependent, as well as photo-dissociated by the strong UV field, and can be present only in dense molecular clouds.

4.5 Comparison with previous works

Our molecular gas detections in the center of M 81 agree with the only two works present in the literature that report CO emission in the nuclear region of this galaxy (Sage & Westpfahl, 1991; Sakamoto et al., 2001). In comparison with the GMCs in the outer regions of M 81 (Taylor & Wilson, 1998; Brouillet et al., 1998), the CO emission that we detected in the M 81 center is particularly cold and unusual. The masses we found for GMAs in the CO(2-1) map are similar to the higher masses observed in M 33 (Wilson & Scoville, 1990), and higher than what is measured in the SMC (Rubio et al., 1993; Bot et al., 2007).

Our first result is that the nuclear region of M 81 (within ∼300 pc) appears devoid of CO emission, in agreement with Brouillet et al. (1988) and Sakamoto et al. (2001). However, we detected CO emission outside the 300 pc radius. This supports the claims of Sage & Westpfahl (1991) who, found CO emission when observing one offset towards the center galaxy with the NRAO 12m telescope and a beam of 55″ (see Fig. 1 of Sage & Westpfahl, 1991, here shown in Fig. 4.12). There is a good correspondence

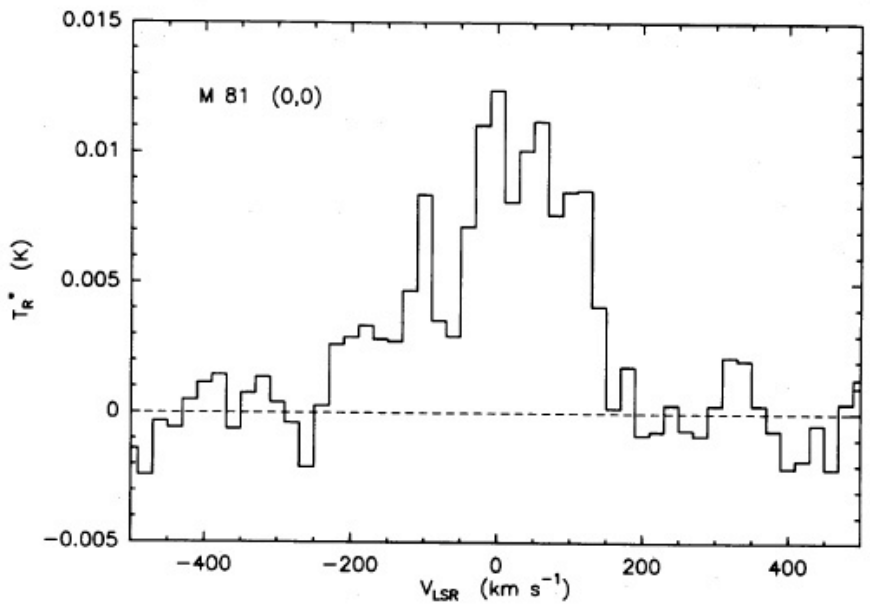

Figure 4.12: The reduced ^{12}CO spectra for the offset (0,0) in M 81 galaxy observed with the NRAO 12m telescope by Sage & Westpfahl (1991). The assumed center position is R.A.(1950) = $09^h\ 51^m\ 27.5^s$, DEC(1950) = $69^\circ\ 18'\ 10''$. The abscissa shows velocity with respect to the local standard of rest and the ordinate shows antenna temperature corrected for atmospheric absorption and antenna losses.

between our velocity profile and theirs.

A more useful and interesting comparison can be done between our results and those of Sakamoto et al. (2001). In detail, the "pseudoring" that we detected at $\sim$ 460 pc from the nucleus in the northeast direction (Fig. 4.7) corresponds to the maximum intensity of Sakamoto et al. (2001). Observing the central kiloparsec with the Nobeyama Millimetric Array-NMA (resolution of $6.9\,''\times 5.8\,''$ that corresponds to $\sim 120\times100$ pc at the distance of M 81), they have produced maps only for the ^{12}CO(1-0) line. Since they have made interferometric measurements, with an FWHM primary beam of $1'$ and a beam of $\sim 7''$, extended emission seen with the $22''$ IRAM CO(1-0) beam is filtered out.

In spite of this, the total mass of molecular gas that we found, assuming the same *standard X* factor value of Strong et al. (1988), is quite comparable to that of Sakamoto et al. (2001): our resolved GMAs in CO(2-1) emission have a total mass of $3.22\times10^6 M_\odot$, only a little bit lower than $\sim 1\times10^7 M_\odot$ found by Sakamoto et al. (2001) for the "pseudoring" in CO(1-0) emission. In addition to the result of Sakamoto et al. (2001), who have found the molecular gas mainly located in a lopsided distribution in the northeast direction (see Fig. 2 by Sakamoto et al. (2001), here shown in Fig. 4.13), we also detected some emission towards the southwest. Our peak temperatures for the ^{12}CO(1-0) line are very low, ranging from $\sim$15 to $\sim$64 mK, lower than the average peak brightness temperature ($\sim$0.3 K) of each GMA found by Sakamoto et al. (2001). This is compatible with the different beam sizes,

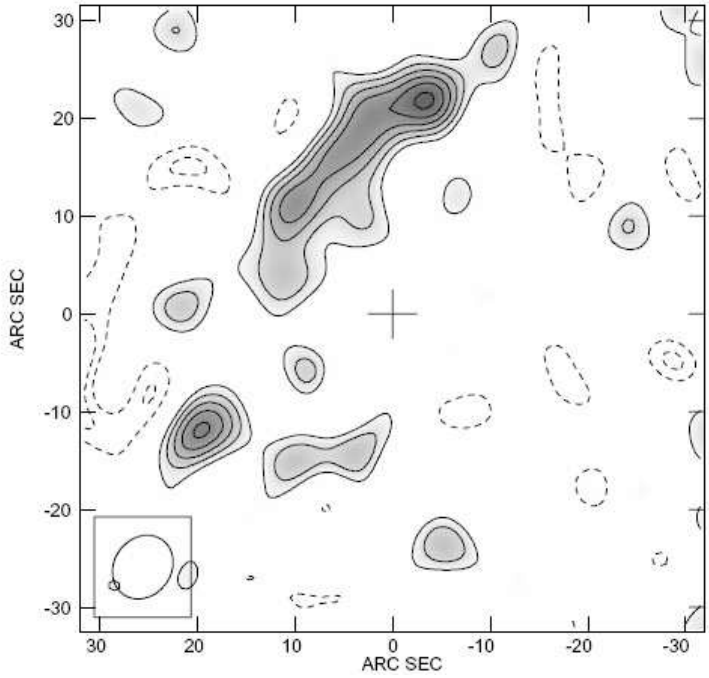

Figure 4.13: Integrated intensity map of CO J=1-0 in the central peak of M 81 with the with the Nobeyama Millimetric Array-NMA by Sakamoto et al. (2001). Contours are at -3, -2, 2, 3, 4, 5, 6, and 7× 1.1 Jy beam^{-1} (=1 σ). The synthesized beam of 6.9 ″× 5.8 ″ in FWHM is shown in the bottom left corner.

the synthesized beam of the interferometer being 10 times smaller in surface.

Another useful comparison can be made with molecular clouds identifications in other external galaxies. The masses ($\sim 10^5 M_\odot$) and the diameters ($\sim$ 250 pc) of the CO clouds identified in M 81 are not much unusual for giant galaxies of the same type (Taylor et al., 1998). Even if in general the GMCs and GMAs in the galaxies of the Local Group are very similar, there is evidence of variations in the properties of the molecular clouds of galaxies of different morphologies, which range from early-type spirals (M 31 and M 81) to late-type spirals (M 33 of Scd morphological type) and from dwarf irregulars (IC 10) to dwarf ellipticals (NGC 205). For the variety of characteristics found in clouds of galaxies of these sub-morphological types, Taylor et al. (1998) have concluded that in general very late-type galaxies should have smaller and less massive GMCs than early-type galaxies. Our results agree with this conclusion.

Finally, we know that, in the Local Group and in systems in interaction with the Local Group, macroscopic properties of molecular clouds are related by power relationships, first noted by Larson (1981) and then studied in detail by Solomon et al. (1987). In particular, Solomon et al. (1987) have found a tight relationship between the Galactic dynamical molecular cloud masses, measured by the virial theorem, and the CO luminosity ($M_{vir} \propto (L_{CO})^{0.81}$). For several external galaxies, this power law is even valid if with little variations of the power index (Rand & Kulkarni, 1990; Rand, 1995;

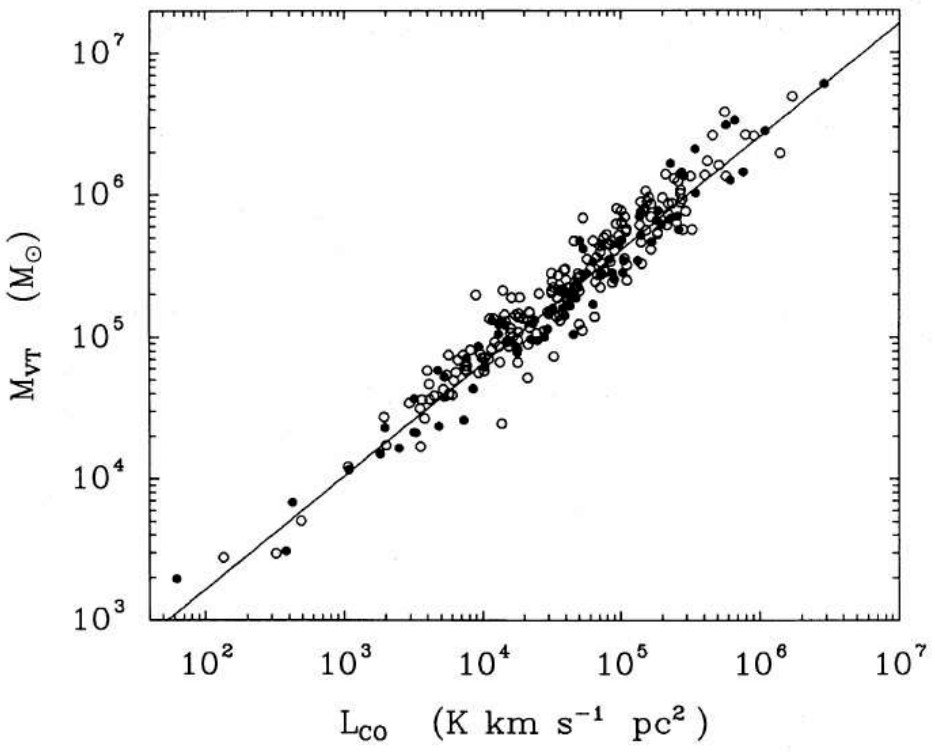

Figure 4.14: The virial mass-CO luminosity relation for 273 clouds in the Galaxy (Solomon et al., 1987). The clouds range from 2 to 15 kpc and in flux over more than two orders of magnitude. The solid circles are calibrator clouds with known distances and the open circles are for clouds with distance ambiguity. The fit is $M_{vir} = 39(L_{CO})^{0.81} M_\odot$.

Rosolowsky & Blitz, 2005). It is interesting to test if M 81 also shows non-typical behavior in this case. Our very weak CO detections correspond to CO luminosities of the order of magnitude 10^4 K km s^{-1} pc^2 with virial masses within an order of magnitude of 10^6 $M_\odot$ (see Table 4.5). Comparing our results with the Fig. 2 of Solomon et al. (1987), here shown in Fig. 4.14, we can see that with the $L_{CO} = 10^4$ K km s^{-1} pc^2 virial masses we infer are overestimated by more than one order of magnitude with respect to the typical trend in our Galaxy, but also in external galaxies. This result agrees with the indications given by the α_{vir} ratios calculated in Section 4.3, and in general it confirms the unusual scenario in the molecular gas properties of M 81.

4.6 Discussion

4.6.1 The X problem

The X factor peculiarity does not appear to be due to a particular metallicity, since M 81 has a metallicity of Z=0.03, without any evident gradient from the central region to the outer disk (Kong et al., 2000). This "normal" metallicity value would produce a X conversion factor similar to that of the

Milky Way. Some regions in M 81, however, have higher metallicity and are mostly located in the spiral arms and HII regions. But in general, our estimate of the X factor appears significantly high.

A possible source of error may be the assumption of a fully virial equilibrium for the observed clouds. Under this hypothesis, we calculated the X factor using $X = M_{vir}/L_{CO}$, where the M_{vir} has been computed with Eq. (4.8), and L_{CO} is the CO luminosity derived from our observations. The application of the virial theorem to complex molecular structures may not be completely appropriate, even if the expected deviation cannot be higher than a factor $\sim$2. However, if the GMAs are not virialized and the *standard* X factor is applied, the molecular content of M 81 would be exceptionally low, so M 81 would be peculiar in both cases.

4.6.2 Heating of the gas

The reason for the non-typical results on the molecular gas in M 81 is probably the exceptionally low CO excitation temperature that seems to characterize the center of this galaxy. Why is the molecular gas absent or subthermally excited in the M 81 center?

A possible link could exist between low CO emission and the lack of ultraviolet emission that appears to characterize the M 81 central region. The ultraviolet image of M 81 realized with the satellite Galaxy Evolution Explorer (*GALEX*) clearly shows a lack of recent star formation, traced by the UV emission, in the nuclear region that we observed in CO (see Fig. 4.4).

The existence of a link between molecular gas and far-ultraviolet (FUV) emission can be justified considering that the interstellar medium is excited, dissociated, and ionized by the FUV photons produced by young O and B stars. Atomic gas in the ISM recombines into molecular form mainly through the catalytic action of dust grain surfaces. Hydrogen nuclei cycle repeatedly from the molecular (H_2) to the atomic phase and back again at rates that depend on the incident FUV flux, the total volume density of the gas, and the dust-to-gas ratio. The action of the FUV flux that interacts with the surface of the molecular clouds can strongly affect their physics and chemistry by heating, dissociating, and exciting the gas.

In regions of the ISM where the physics is dominated by FUV photons - called photodissociation regions (PDRs)- useful information can be obtained on the physical state of the gas from observations of the spectral lines emitted by the excited atoms and molecules in those regions.

In M 81 the possibility that low CO emission and weak FUV flux are correlated has already been proposed by Knapen et al. (2006). When observing a region of the western spiral arm in M 81, they have explained the lack of or very weak CO(1-0) emission, observed far from FUV sources, as a consequence of insufficient heating and excitation of the molecular gas. Usually, a lack in the CO emission is instead interpreted as due to the absence of measurable quantities of molecular gas or due to a low density gas not heated sufficiently to detect it. The limit of this interpretation, based on the linear proportionality between the CO surface brightness and the column density of the molecular hydrogen, is to neglect effects linked to local heating mechanisms. If the explanation of Knapen et al. (2006) is correct, the flux of cosmic rays and the FUV surface brightness would be too low to heat the ISM, and in particular, the molecular component. It is possible that this correlation of low-FUV/low-CO is also applicable to the central region that we observed.

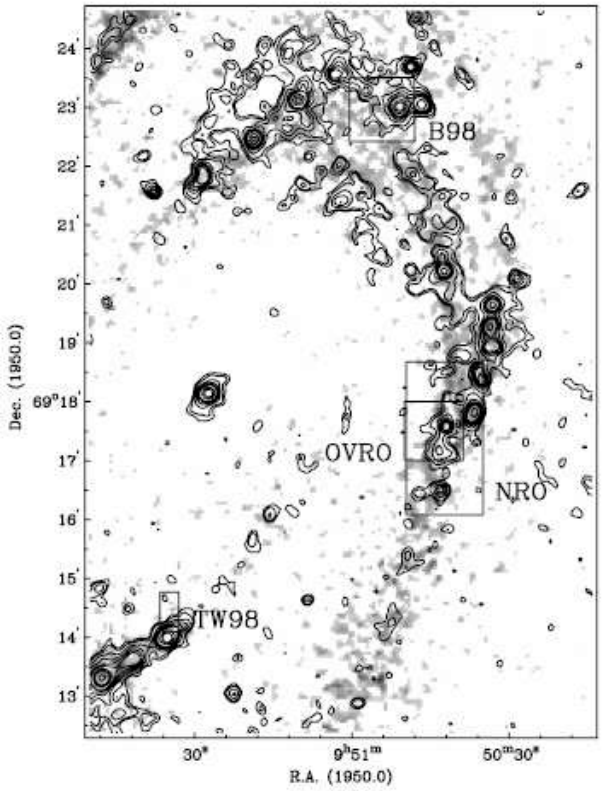

Figure 4.15: FUV contours overlaid on a grey-scale representation of the HI integrated intensity map of the western part of the inner disk of M 81 (Knapen et al., 2006). Overlaid are the fields of NRO and OVRO observations by Knapen et al. (2006), as well as the fields observed by Brouillet et al. (1998) (labelled B98), and by Taylor & Wilson (1998) (labelled TW98, but we didn't use these observations). Contours levels for the FUV are 2.3, 3.1, 4.6, 6.2, 7.7, 9.2, 13.9, 18.5, and 36.9 $\times$ 10^{-18} erg cm^{-2} s^{-1} $\AA^{-1}$ arcsec^{-2}. Grey levels for the HI vary linearly from 1.5 (light) to 7.3 $\times$ 10^{21} atoms cm^{-2} (dark). FUV and HI data from Allen et al. (1997).

To verify this interpretation, we performed aperture photometry in the FUV emission on three fields already observed in CO: our central region of 1.6 kpc, the field of spiral arms observed by Brouillet et al. (1998), and that - again on the spiral arms - observed by Knapen et al. (2006). The fields selected on the spiral arms are the same of Fig. 2 of Knapen et al. (2006) here shown in Fig. 4.15. We used the FUV-*GALEX* image of M 81 expressed in intensity and already sky-subtracted and performed the aperture photometry using the task QPHOT[4] of IRAF[5], able to do a quick aperture photometry. This procedure allowed us to know the FUV flux emitted in regions observed in CO(1-0) and hence to compute the ratio between the two emissions in different fields, but of similar dimensions, of the galaxy. The aperture photometry was done with a radius of 40″ for our central region and for the one observed by Knapen et al. (2006) with

[4]QPHOT = Quick Aperture Photometer.

[5]IRAF = Image Reduction and Analysis Facility.

Table 4.6: Comparison of the results obtained applying the aperture photometry at the FUV-*GALEX* image of M 81 in different regions observed in CO(1-0). Column (1) gives the references relatively to CO(1-0) emission; column (2) is the CO(1-0) integrated intensity in units of K km s^{-1}; column (3) is the FUV flux obtained by the aperture photometry in units of 10^{-14} erg cm^{-2} s^{-1} $\AA^{-1}$; column (4) is FUV flux expressed in terms of the G_0 Hading unit; column (5) is the ratio between the CO(1-0) integrated intensity and the FUV flux in units of 10^{14} K km s^{-1}/(erg cm^{-2} s^{-1} $\AA^{-1}$).

Reference	I_{CO}	F_{FUV}	G_0	I_{CO}/F_{FUV}
Brouillet et al. (1998)	25.90	1.37	0.51	18.88
Knapen et al. (2006)	20.26	1.48	0.35	13.65
This paper	53.50	1.13	0.31	47.18

the Nobeyama Radio Observatory (NRO), and with a radius of 32″ for the field observed by Brouillet et al. (1998). The results of the aperture photometry are summarized in Table 4.6. We expressed the FUV fluxes in terms of the Hading unit, since it is one of the units usually used to model PDRs (e.g. Kaufman et al., 1999; Allen et al., 2004). In these models each one-dimensional semi-infinite slab of gas with constant density of H nuclei is subjected to an equivalent one-dimensional flux of FUV photons G_0 measured in units of 1.6×10^{-3} ergs cm^{-2} s^{-1} over the photon energy range 6 - 13.6 eV. In these units, the average interstellar radiation field over 4π sr is $G_0 = 1.7$ (Draine, 1978; Allen et al., 2004).

The central region emits a weak FUV flux, within the same order of magnitude as that emitted in the two fields of the spiral arms, and the higher ratio between CO and FUV emissions in nuclear region is mainly due more to the higher molecular gas intensity. If the low FUV emission is not able to heat the molecular gas sufficiently in the spiral arms, in the central region at the same quantity of FUV flux corresponds a molecular gas distributed in substructures, but subexcited. Probably the central region shows a higher CO/FUV ratio because in the spiral arms the molecular gas is less excited than the nucleus.

4.7 Conclusions

The physics of the molecular gas suggested by our observations shows M 81 to be a galaxy that is not only CO-poor in its central region, but that also has molecular clouds with unusual properties, if compared to galaxies with similar distances and morphological type. The absent or very weak molecular gas emission in the nuclear region, the low R_{21} line ratio, and a particularly high X conversion factor value are its main peculiarities. The $N(H_2)/I_{CO}$ conversion factor has a mean value of $X = 3.6 \times 10^{21}$ mol cm^{-2} (K km $s^{-1})^{-1}$, 15.6 times higher than the X value of Strong et al. (1988) derived for our Galaxy.

All unusual results found for the molecular component in the M 81 center are probably due to an excitation process of the gas non-typical for giant spirals in the Local Universe. The spiral arms of this galaxy are CO-poor, and it has been suggested that the FUV surface brightness is too low to heat the molecular gas component. The low CO emission we found in the center

suggests that the gas in the nucleus is also subexcited, with even weaker FUV emission. We concluded that the lack of excitation of the gas, more than the absence of molecular gas, is the cause of the low CO emission there.

4.8 Future perspectives

We are yet interested to explore the CO emission found for the nuclear region of M 81 to understand the reason of this atypical result. To analyze this aspect more in detail, a higher (for instance interferometric) resolution study is needed. Since the excitation of the molecular gas could be perturbed by the low-luminosity AGN, we would map a region relatively far from the center, within the central 1 kpc. To this aim we will plan to observe the region found with IRAM 30 m observations having the major emission, that is in the NE direction far from the nucleus (see Fig. 4.9). With interferometric observations, thanks to a better resolution, we could resolve the substructures of the GMAs already detected and verify if for these structures the condition of the virial equilibrium is valid, and in this case recompute the X ratio. In the literature there are other interferometric studies of M 81, all without an explanation to the problem of the low molecular gas emission, especially for the nuclear area (Sakamoto et al., 2001; Knapen et al., 2006). New interferomeric observations could be compared to other interferometric maps of both galaxies with "normal" behaviour in the gas molecular physics (such as M 51) and with weak CO emission (such as M 31) in order to understand where and why the physical conditions of the molecular gas in M 81 are different.

In addition to the "classical" CO transitions, other ones are very useful to go deeper on the nature of the gas in M 81 central region. The high X ratio that we found can be explained as due not only to very low excitation or very low temperature of the gas. We can suspect that there is a larger than usual clumpiness factor, where small dense clumps, optically thick in CO are spatially diluted in the CO beam. In this last scenario, it is possible that the gas locally collapses, to a much clumpier state than normal ISM conditions, generating regions with higher density than those usually traced by CO. In that case, the true molecular content will be overlooked. Since the CO molecule is not sufficient to study in detail the physics of the molecular gas, it is necessary to explore dense molecular tracers, such as HCN. We also would like to explore the optical thickness in mapping the isotopic molecule ^{13}CO.

Alternatively, the molecular content might be a strong function of the external pressure (P_{ext}), which favors fragmentation of dense clumps, as proposed recently by Blitz & Rosolowsky (2006). However, the external pressure in the center of M 81 is rather high, and the molecular to atomic ratio in this region does not fit in the general correlation involving P_{ext} (see Fig. 4.16). The pressure is essentially depending on the HI gas and on the surface density of the stars, which is comparable to the values of the center of the Milky Way. P_{ext} can be estimated $P_{ext}/k \sim 10^4$-10^5 cm^{-3} K, and so M 81, also considering this aspect, shows an atypical behaviour in this diagram. Observations of HCN and ^{13}CO can bring essential arguments in this interpretation, determining the true molecular surface density, and therefore the true pressure.

Then, the HCN molecule has been shown to be linearly correlated to the FIR emission, since the dense cores are the most relevant for star formation, while the more diffuse CO is a non-linear tracer (Gao & Solomon, 2004b).

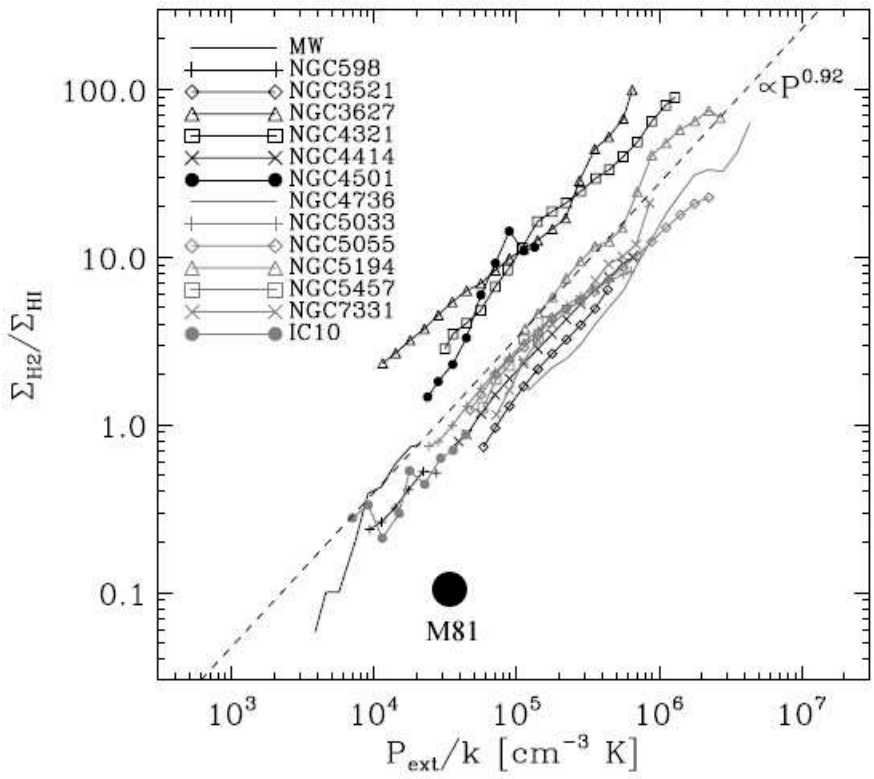

Figure 4.16: This figure, by Blitz & Rosolowsky (2006), shows that all galaxies have a similar scaling between the H_2/HI ratio and the hydrostatic pressure P_{ext}. Following the model of Blitz & Rosolowsky (2006) and assuming an H_2/HI ratio of 0.1 we found that M 81 differs by the behavior of the other galaxies with a rather high pressure.

The HCN/CO emission ratio strongly varies from galaxy to galaxy, and can clearly check our dense clumps scenario. In addition, information on the optical thickness of the CO lines can be derived by the observation of rotational lines of its isotope ^{13}CO, and together with their HCN/CO ratio can test whether the X factor is different from the standard one and varies within the galaxy.

In the literature, some authors (Rickard & Blitz 1985) have found that ^{12}CO/^{13}CO ratio (R) is higher in the central 1 arcmin than in the disks of 6 galaxies, suggesting that X is smaller in galaxy centers, while others, such as Young & Sanders 1986 and Sage & Isbell 1991, have showed that no significant differences between the centers of spiral galaxies and their disks exist. In most cases, the ^{13}CO lines have been studied in detail in gas rich galaxies, such as M 64 (Rosolowsky & Blitz, 2005), and the X factor has been derived similar to that of the Milky Way. But different conclusions are expected from a molecular gas-poor galaxy, such as M 81.

Observations of the HCN and ^{13}CO lines combined with the use of the large velocity gradient (LVG) approximation (Young & Scoville 1984, Sanders et al. 1984) can allow us to determine the optical depth of the molecular gas, identify the filling factor of the diffuse and dense gas, and

derive the fraction of the molecules at high density, to derive its clumpiness. We could be able to test the various possibilities: either a low pressure of the ISM prevents the formation of dense clouds, or on the contrary, the collapse of the molecular gas in small and dense clumps have led us to underestimate the H_2 content, from the CO emission only.

This dense gas study, together with the high resolution CO emission above described, can help us to understand the physical origin of the atypical low CO emission and the consequent high $X = N(H_2/I_{CO})$ conversion factor, much higher that the Galactic value.

Chapter 5

NUGA survey: NGC 3147

Introduction

In this Chapter the study of the small scale physics of the molecular gas in nearby galaxies continues presenting the results obtained for NGC 3147 galaxy, an object of the NUGA survey whose aims and characteristics will be described later. The analysis of interferometric and single-dish observations and the performed modelization for NGC 3147 will soon be published in the paper V. Casasola, F. Combes, S. García-Burillo, L. K. Hunt, S. Léon, and A. Baker, A&A submitted.

5.1 NUGA project

5.1.1 Aims and results already obtained

The study of interstellar gas in the nuclei of galaxies is key for understanding nuclear activity and circumnuclear star formation. Within the central kiloparsec, most of the gas is in the molecular phase, which makes CO lines the optimal tracers of nuclear gas dynamics. The NUclei of GAlaxies-NUGA project (García-Burillo et al., 2003) is a survey of nearby active galaxies whose aim is to map the distribution and dynamics of the molecular gas with the IRAM Plateau de Bure Interferometer (PdBI) in the inner 1 kpc of the nuclei at high spatial resolution ($\sim$0.5″-1″ corresponding to $\sim$50-100 pc), and to study the mechanisms for gas fueling of the different low-luminosity active galactic nuclei (AGNs).

The majority of galaxies possess a central super-massive black-hole, and the gas accretion onto the black hole is the phenomenon usually invoked to explain the nuclear activity in galaxies. However, even if the majority of galaxies have a massive black-hole, the existence of nuclear activity is far from universal. It is not clear whether the main limiting factor is the availability of gas for fueling the AGN or the mechanisms for efficiently removing the gas angular momentum.

The main and non-trivial problem linked to the fueling of AGNs (mass transfer from the $\sim$1 kpc scale to radii of tens of pc) is the removing of the angular momentum from the disk gas. Invoked solutions are associated to non-asymmetric perturbations of external origin, such as galaxy collisions, mergers and mass accretion (Heckman et al., 1986), or of internal origin due to density waves, such as spirals or bars, and their gravity torques (e.g. Sakamoto et al., 1999; Combes, 2001). To understand the origin of these

perturbations is not simple, since the tidal interaction of companions can also trigger bar formation.

Previous (before NUGA) CO single-dish (Heckman et al., 1989; Young et al., 1995; Braine & Combes, 1993; Casoli et al., 1996; Vila-Vilaró et al., 1998) and interferometric (Sakamoto et al., 1999; Regan et al., 2001; Helfer et al., 2003) surveys have mapped the gas in galaxies with insufficient or low spatial resolution (4″-7″). In addition, the majority of these surveys have only included a small number of AGNs in their samples. Therefore, high resolution maps of the molecular gas for the NUGA sample are needed for investigating AGN fueling phenomenon and its link with circumnuclear star formation.

On the modelling side, N-body simulations are performed to analyze the evolution of stellar/gaseous gravitational instabilities in the different study cases. In addition, NUGA has a multiwavelength approach: the sample is defined based on the availability of high quality optical and near infrared images of the galaxies, both from ground-based telescopes and the HST. The long term aim is to complete a supersample of 25-30 objects observed with the IRAM array.

The analysis of the first NUGA data has produced a set of studies of individual galaxies which represent prototypical examples of the large variety of gravitational instabilities unveiled in the maps, including m=1 modes (one-arm spirals, lopsided disks), m=2 perturbations (rings, two arm spirals), and stochastic patterns (non self-gravitating perturbations).

The CO maps of NGC 4826, the first galaxy analyzed of the NUGA sample (García-Burillo et al., 2003), have fully resolved (0.8″-16 pc resolution in the CO(2-1) line) an inner molecular gas disk which is truncated at an outer radius of 700 pc (see Fig. 5.1). The total molecular gas mass is distributed in a lopsided nuclear disk of 40 pc radius, containing 15% of the total gas mass, and two one-arm spirals, which develop at different radii in the disk. The signatures of the streaming motions expected for trailing/leading waves can be analyzed in the framework of the linear density wave theory (Shu et al., 1973). The sign of velocity perturbations changes close to the minor axis when crossing from inside to outside the corotation resonance. A comparison with models may give some insight into the nature of the density waves that may account for the streaming motions observed in CO. García-Burillo et al. (2000) have applied the general formalism to the case of one-arm (m = 1) spirals for two extreme values of the pattern speed (Ω_p) illustrating the "slow" and the "fast" mode solutions. The "slow" solutions are mostly inside corotation of the modes, while the "fast" ones are outside.

The distribution and kinematics of molecular gas in the inner 1 kpc of NGC 4826 show the prevalence of different types of $m = 1$ perturbations in the gas. García-Burillo et al. (2003) have found that the gas kinematics of NGC 4826, even if dominated by rotation, is perturbed by streaming motions related to the $m = 1$ instabilities. The non-circular motions associated with the inner $m = 1$ perturbations (lopsided instability and inner one-arm spiral) agree qualitatively with the pattern expected for a trailing wave developed outside corotation ("fast" wave). In contrast, the streaming motions in the outer $m = 1$ spiral are better explained by a "slow" wave. A paradoxical consequence is that the inner m= 1 perturbations would not favour AGN feeding. An independent confirmation that the AGN is not being generously fueled at present is found in the low values of the gravitational torques exerted by the stellar potential for $R < 530$ pc. The distribution of the star formation in the disk of NGC 4826 is also strongly asymmetrical. The

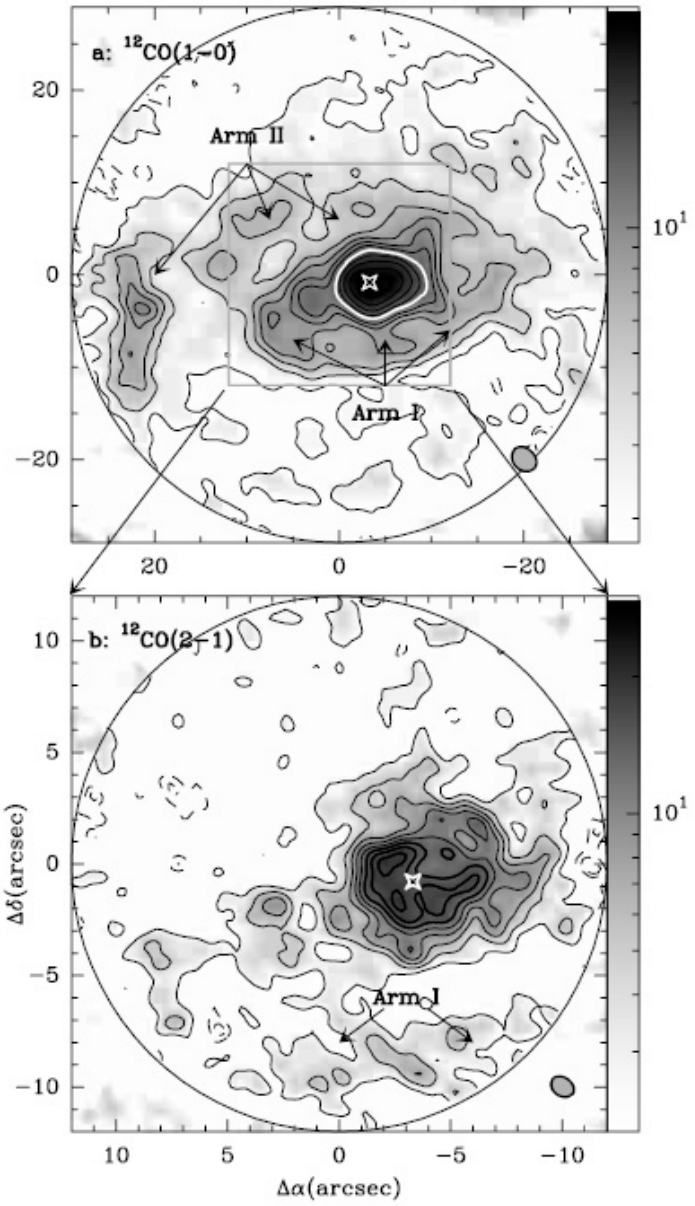

Figure 5.1: a) ^{12}CO(1-0) integrated intensity contours in the inner $\sim 58''$ of NGC 4826 (García-Burillo et al., 2003). Contours beyond the displayed field-of-view have been screened as S/N ration is lower than 3 for $r > 29''$. $\Delta\alpha$ and $\Delta\beta$ are offsets (in arcsec) with respect to the phase tracing center. Contours are -1.75, -0.88, 1.75, 4, 6, 8, 10, 12, 15, 18, 22 to 34 in steps of 5 Jy km s^{-1} beam^{-1}. The dynamical center is indicated by the star marker. The white contour highlights the circumnuclear disk. 1-σ noise = 0.25 Jy km s^{-1} beam^{-1} at the center of the image (1-σ noise = 0.90 Jy km s^{-1} beam^{-1} at the edge of the displayed field-of-view). **b)** Same of **a)** but for the ^{12}CO(2-1) line. The zoomed view shows emission coming from $24''$. Contours beyond the displayed field-of-view have been screened as S/N ratio is lower that 3 for $r > 12''$. Contours are -2.4, -1.4, 2.4 to 19.4 in steps of 2.4 Jy km s^{-1} beam^{-1}. Thick contours inside the circumnuclear disk highlight the asymmetrical pattern. 1-σ noise = 0.36 Jy km s^{-1} beam^{-1} (1-σ noise = 0.80 Jy km s^{-1} beam^{-1} at the edge of the displayed field-of-view). Positions of Arm I and II identified by the authors are indicated. Beam-sizes are represented by filled ellipses.

observed asymmetries, revealed by HST images of the inner disk, follow the scales of the various $m = 1$ perturbations identified in the molecular gas disk (see García-Burillo et al., 2003, for more details). Massive star formation is still vigorous, fed by the significant molecular gas reservoir at $R < 700$ pc. There is supporting evidence for a recent large mass inflow episode in NGC 4826. The onset of $m = 1$ instabilities of the type observed in NGC 4826 may be a consequence of secular evolution of disks with high gas mass contents.

An example of $m = 2$ perturbations in the NUGA sample is the LINER galaxy NGC 7217. With a resolution of $2.4'' \times 1.9''$ and $1.2'' \times 0.8''$ for the lines CO(1-0) and CO(2-1) respectively, Combes et al. (2004) have found that a nuclear ring (at r = $12'' = 0.8$ kpc) dominates the CO maps, and that it has a remarkable sharp surface density gradient at its inner edge (see Fig. 5.2). The latter is the site of the stellar/Hα ring, while the CO emission ring extends farther or is broader (500-600 pc). The morphology of the ring is quite circular, with no evidence of non-circular velocities. In the CO(2-1) map, a central concentration might be associated with the circumnuclear ionized gas detected inside r = $3''$ and interpreted as a polar ring in the literature. The CO(2-1) emission inside $3''$ coincides with a spiral dust lane, clearly seen in the HST $V - I$ color image (see Combes et al., 2004, for more details). Combes et al. (2004) have also performed N-body simulations including gas dissipation and star formation to better understand the nature of the nuclear ring observed. The observed rotation curve of NGC 7217 allowed two possibilities, according to the adopted mass for the disk: (i) either the disk is massive, allowing a strong bar to develop, or (ii) it is dominated in mass by an extended bulge/stellar halo, and supports only a mild oval distortion. The amount of gas also plays an important role in the disk stability, and therefore the initial gas fraction was varied, with star formation reducing the total gas fraction to the observed value. These CO observations have only supported the bulge-dominated model, which is able to account for the nuclear ring in CO and its position relative to the stellar and Hα ring. In this model, the gas content was higher in the recent past (having been consumed via star formation), and the structures formed were more self-gravitating. Only a mild bar formed, which has now vanished, but the stars formed in the highest gas density peaks toward the inner edge of the nuclear ring, which corresponds to the observed thin stellar ring. Combes et al. (2004) did not find evidence for an ongoing fueling of the nucleus; instead, gas inside the ring is presently experiencing an outward flow. To account for the nuclear activity, some gas infall and fueling must have occurred in the recent past (a few Myr ago), since some, albeit very small, CO emission is detected at the very center.

These two galaxies (NGC 4826 and NGC 7217) together the others of the NUGA sample already analyzed reveal a wide range of gravitational instabilities in the central 1 kpc of targets. Most remarkably, $m = 1$ modes appear at different spatial scales in some AGNs, although these modes might not *universally* favour AGN feeding. Point-symmetric $m = 2$ perturbations and stochastic patterns dominate the response in the others. Although general conclusions will have to wait for a global analysis of the 30-galaxy supersample, these results already indicate that the correlation between activity type and nuclear morphology of the host might be weak at scales of ten-to-hundred pc. If confirmed, the lack of a clear evolutionary scenario may reflect a mismatch between the episodic AGN duty cycle, and the larger time-scales needed to build up nuclear gravitational instabilities which are directly involved in fueling AGN.

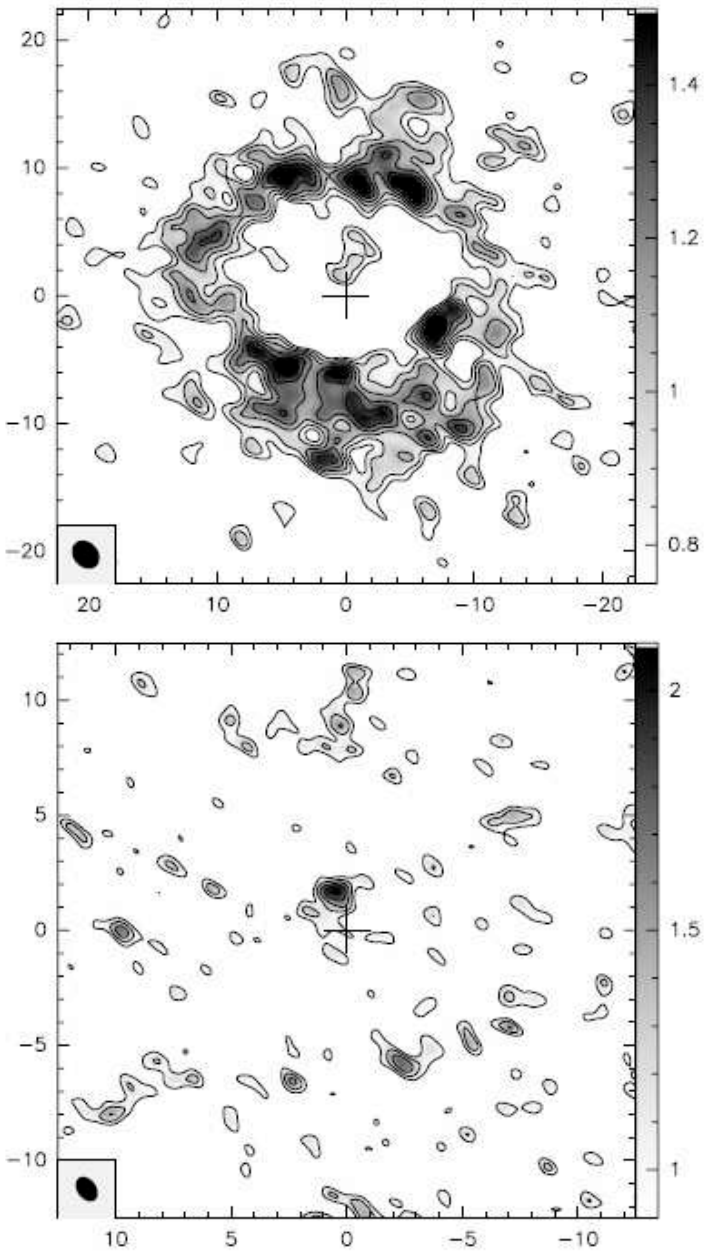

Figure 5.2: *Upper panel*: CO(1-0) integrated intensity contours observed with the IRAM interferometer toward the center of NGC 7217 (Combes et al., 2004). The cross marks the coordinates center. The rms noise is $\sigma = 0.15$ Jy km s^{-1} beam^{-1}. Contour levels are from 5σ to 10σ with 1σ spacing. The beam is plotted at the bottom left. *Bottom panel*: Same as *Upper panel* but for the CO(2-1) integrated intensity (Combes et al., 2004). The rms noise is $\sigma = 0.3$ Jy km s^{-1} beam^{-1}. Contour levels are from 3σ to 10σ with 1σ spacing. The beam is plotted at the bottom left.

Figure 5.3: NGC 3147 galaxy observed with the Palomar 1.5 m telescope, grism 5000-8200 $\mathring{A}$ (NED catalogue, Frei et al., 1996).

In the next sections we will describe the results obtained for NGC 3147 galaxy, the tenth one of the NUGA sample.

5.2 NGC 3147 galaxy

NGC 3147 (D = 40.9 Mpc, for $H_0 = 75$ km s^{-1} Mpc^{-1}) is an isolated (Bettoni et al., 2003) Seyfert 2 galaxy (Ho et al., 1997) of Hubble morphological type SA(rs)bc (see Fig. 5.3).

Both *ROSAT* observations (Roberts & Warwick, 2000) and *Chandra* ones (Terashima & Wilson, 2003) have shown that this galaxy possesses an X-ray point-like source at the position of the nucleus, coincident with the radiosource, where is supposed to be the supermassive black hole. The 0.3-10 keV image of *Chandra* reveals a bright compact source surrounded by very faint, soft, and weak diffuse emission. The 2-10 keV core is clearly detected and restricted to a region of $2''$ in radius. Adopting the known empirical relation between the black hole mass and the bulge stellar velocity dispersion (e.g. Ferrarese & Merritt, 2000; Gebhardt et al., 2000), the black hole mass is estimated to be $\sim 4 \times 10^8$ M$_\odot$ (Ulvestad & Ho, 2001) assuming $\sigma_s = 268$ km s^{-1} (McElroy, 1995). The nuclear bolometric luminosity is $\sim 2 \times 10^{42}$ erg s^{-1}, assuming $L_{bol} = 6.7 \times L_{X(2-10keV)}$ from Ulvestad & Ho (2001), and a ratio $L_{bol}/L_{ed} \simeq 5 \times 10^{-5}$ (Krips et al., 2007a). In other words,

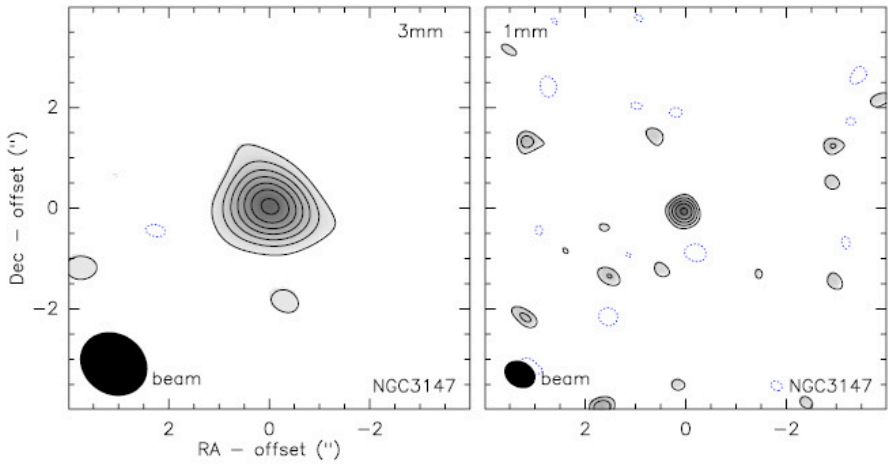

Figure 5.4: Continuum maps of NGC 3147 at 3 mm (*left panel*) and 1 mm (*right panel*) observed with the IRAM PdBI (Krips et al., 2006). Contour levels are from $3\sigma = 0.72$ to 4.8 mJy/beam in steps of 3σ at 3 mm and from $3\sigma = 1.4$ to 3.5 mJy/beam in steps of 1σ at 1 mm. The beam size at both wavelengths is indicated as filled black ellipse in the lower left corner of the maps.

NGC 3147 radiates far below the Eddington rate.

Interferometric observations of the continuum emission at mm wavelengths with MERLIN and the PdBI have also shown a pointlike, non-thermal continuum source at the position of the nucleus of NGC 3147 (Ulvestad & Ho, 2001; Krips et al., 2006, 2007a, see Figs. 5.4 and 5.5).

In addition, very recent optical and X-ray observations of NGC 3147 have investigated the nuclear region of this galaxy (Bianchi et al., 2007). The XMM-Newton spectrum shows that the source is unabsorbed in the X-rays ($N_H < 5 \times 10^{20}$ cm^{-2}), and no broad lines are present in the optical spectrum. The origin of this optical/X-rays misclassification cannot be attributed to variability, since the observations in the two bands are simultaneous. Moreover, a Compton-thick nature of the object can be rejected on the basis of the low equivalent width of the iron K_α line and the large ratio between the 2-10 keV and the [OIII] fluxes. Bianchi et al. (2007) have concluded that NGC 3147 is the first "true" Seyfert 2 because it intrinsically lacks the Broad Line Region (BLR).

5.3 Observations

5.3.1 IRAM single dish CO and HCN observations

We performed IRAM 30 m telescope observations in a 5×5 raster pattern with $7''$ spacing in July 2002 and in June 2004. We used 4 SIS receivers to simultaneously observe at the frequencies of the ^{12}CO(1-0) (115 GHz), the ^{12}CO(2-1) (230 GHz), and the HCN(1-0) (89 GHz) lines. The half power beam widths (HPBW) are $22''$ for CO(1-0), $12''$ for CO(2-1), and $29''$ for HCN(1-0). The typical system temperatures were ∼250 K at 115 GHz, from ∼350 K to ∼700 K at 230 GHz, and ∼120 K at 89 GHz. The line intensity scale is expressed in units of T_{mb}, the beam-averaged radiation temperature,

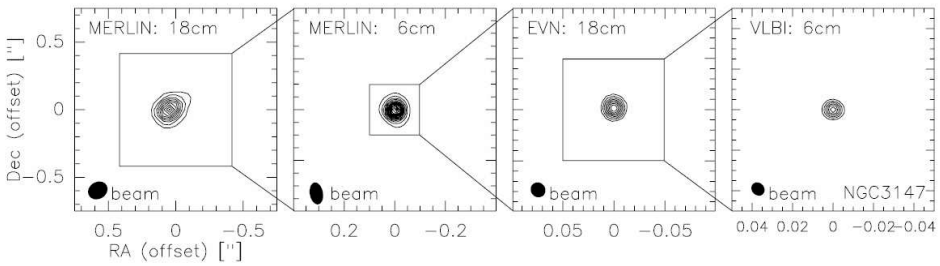

Figure 5.5: MERLIN (*2 left columns*) and EVN/VLBI (*2 right columns*) of the 18 cm and 6 cm continuum emission in NGC 3147 (Krips et al., 2007a). Contour levels are: (5σ=)0.75 to 7.5 mJy/beam in steps of 5σ for MERLIN-18 cm (*left*), (3σ=)0.72 to 10.1 mJy/beam in steps of 5σ for MERLIN-6 cm (*left middle*), (3σ=)0.65 to 5.2 mJy/beam in steps of 5σ for EVN-18 cm (*right middle*), and (5σ=)1.4 to 8.3 mJy/beam in steps of 5σ for EVN-6 cm (*right*).

and the value of T_{mb} is related to T_A^*, by $\eta = T_A^*/T_{mb}$ where η is the telescope main-beam efficiency, as already said in Chapter 4. η is 0.79 at 115 GHz, 0.57 at 230 GHz, and 0.82 at 89 GHz. All observations were performed in "wobbler-switching" mode and the pointing accuracy was $\sim 3''$ rms.

Single dish observations were used to compute short spacings and complete the interferometric measurements (e.g. Combes et al., 2004). In particular, short spacings visibilities are computed from a map built by interpolation of the 30 m beam and multiplied by the PdBI primary beam. We combined 30 m and PdBI data, using the SHORT-SPACE task[1] in the GILDAS software. To find the best compromise between good angular resolution and complete restoration of the missing extended flux the weights attached to the 30 m and PdBI data were varied. We recovered most of the missing flux and end up with an angular resolution of $1.88'' \times 1.63''$ at P.A.[2] of 61.5° for ^{12}CO(1-0) emission and $1.61'' \times 1.4''$ at P.A. of 65.4° for ^{12}CO(2-1) emission. The combined data sets have been written to visibility tables, converted to maps using standard reduction procedures and then deconvolved using the Clark algorithm. The weights are adjusted in order to get the same mean weights in the single-dish data as in the interferometer data in the u-v range of 1.25 D/λ to 2.5 D/λ (D = 15 m). All figures presented in the next sections have been made with short-spacing corrected data.

To estimate the flux filtered out by the interferometric observations, we computed the flux measured by Young et al. (1995), with the 14 m FCRAO telescope (HPBM = $45''$). They have found a CO(1-0) flux toward the center of $I(CO) = 5.75$ K km s^{-1} (in the T_A^* scale) that corresponds to an integrated flux of $S(CO) = 242$ Jy km s^{-1} adopting a conversion factor of 42 Jy/K. In the same region with the PdBI alone we measured 130 Jy km s^{-1} in CO(1-0), so we only recovered about half of the flux in CO(1-0). With short spacings added, we estimated the total flux to 295 Jy km s^{-1}, which is compatible with the FCRAO value within the uncertainties. In CO(2-1), we measured with the 30 m IRAM a total flux of 140 Jy km s^{-1} in a beam

[1]For details on SHORT-SPACE task see Guilloteau & Lucas (2000).

[2]P.A. measured N through E.

Figure 5.6: A view of the IRAM PdBI. Photo by IRAM web site.

of 26″ in diameter, while the PdBI alone indicated 30 Jy km s^{-1}, with a large region with negative flux levels, leading to a missing flux of about 80%. With short spacing the whole flux was recovered.

5.3.2 IRAM interferometer CO observations

We observed the emission of the J = 1-0 and J = 2-1 lines of the ^{12}CO in NGC 3147 using the IRAM Plateau de Bure Interferometer (PdBI) in October 2004 with the configuration ABCD (see Fig. 5.6). The six 15 m antennae were equipped with dual-band SIS receivers yielding SSB receiver temperatures between 40 and 50 K at both frequencies. The water vapor ranged between 4 and 10 mm (i.e., opacities of ∼0.2-0.3) resulting in system temperatures of approximately 200-300 K on average. The spectral correlators were centered at 114.197 GHz (2793.75 km/s) and 228.390 GHz (2793.27 km/s), respectively. The coordinates of the PdBI phase tracking center are given in Table 5.1 and correspond to the nuclear radio (6 cm-VLBA) position of Nagar et al. (2002).

Data cubes with 256″ × 256″ spatial pixels (0.46″/pixel for the CO(1-0) and 0.23″/pixel for the CO(2-1)) were created with 49 velocity planes distant 10 km s^{-1}. The images were reconstructed using the standard IRAM/GAG software (Guilloteau & Lucas , 2000) and restored by 1.8″ x 1.6″ Gaussian-beam (with P.A. = 62°) at 115 GHz and 1.4″ x 1.2″ (with P.A. = 61°) at 230 GHz. In the cleaned maps the rms levels are 2 mJy/beam and 4 mJy/beam for the CO(1-0) and CO(2-1) lines respectively (with a velocity resolution of 10 km s^{-1}). The conversion factors between intensity and brightness temperature are 32 K/(Jy/beam) at 115 Ghz and 14 K/(Jy/beam) at 230 GHz.

A continuum point source was detected both at 3mm and 1.3mm. The continuum flux is 5.2 mJy at 3mm (detected with an rms of 0.2 mJy/beam),

Table 5.1: Fundamental parameters for NGC 3147.

Parameter	Value	Reference
RA (J2000)	$10^h16^m53.6^s$	NED
DEC (J2000)	$73°24'03''$	NED
V_{hel}	2820 km s^{-1}	NED
RC3 Type	SA(rs)bc	NED
t Type	3.88	LEDA
Inclination	29.5°	LEDA
Position angle	150°	LEDA
Distance	40.9 Mpc ($1''$=198 pc)	NED
L_B	4.3 $\times 10^{10}$ $L_\odot$	Bettoni et al. (2003)
M(HI)	8.3 $\times 10^8$ $M_\odot$	Bettoni et al. (2003)
M_{dust}(60 and 100 μm)	1.7 $\times 10^6$ $M_\odot$	Bettoni et al. (2003)
L_{FIR}	3.4 $\times 10^{10}$ $L_\odot$	IRAS

and 2.2 mJy at 1.3mm (with an rms of 0.4 mJy/beam). Both values are consistent with the synchrotron source detected at centimeter wavelengths, with a power-law flux and a slope of -1[3]. All maps presented in the next sections are continuum subtracted.

Both single dish data and interferometric ones were reduced with the GILDAS software. We assumed that NGC 3147 lies at a distance of 40.9 Mpc and so $1'' = 198$ pc.

5.3.3 Near-infrared observations

For modeling the gravitational potential, we used near-infrared images which have the advantage to be relatively free of dust extinction, and more representative of old stellar populations than blue or visible images.

The near-infrared images were obtained in December 1998 at the 3.6 meter Canada-France-Hawaii Telescope (CFHT), using the CFHT Adaptive Optics Bonnette (AOB) and the KIR infrared camera. The AOB, also called PUEO after the sharp-visioned Hawaiian owl, delivers essentially diffraction-limited images at H and K ($0.11''$ and $0.14''$ respectively), and images with FWHM $\sim 0.1''$ at J with guide stars as faint as R=14 (cf Rigaut et al., 1998). Here the Seyfert nucleus of the galaxy was used as a guide. The KIR $1024''$ x $1024''$ HgCdTe array has pixels of $0.035''$ each, providing a field of view of $36'' \times 36''$. The observations were done in excellent conditions of seeing ($\sim 0.6''$ in the V band), with several images taken in a dithering procedure, to correct for camera defects. The total integration time on source was 8 minutes, for each band, J and K$'$, and the total observing time for the two filters was 50 minutes, including sky subtraction and overheads.

[3]The radio spectral index α is defined such as $S_\nu \propto \nu^\alpha$.

5.3.4 Archival observations with *Spitzer* and *GALEX*

We acquired public images of NGC 3147 at other wavelengths to compare our molecular gas observations to other tracers of gas and stars in the ISM.

We used the far-ultraviolet (FUV) image of the *GALEX* satellite, whose band is centered at $\lambda_{eff} = 1516$ Å [4]. This image has been obtained with a total exposure time of 1693 sec and covers a square region on the sky of size $\sim 5500'' \times 5500''$, i.e., much larger than the extent of the optical disk of NGC 3147. The image is available already reduced with the *GALEX* data pipeline, expressed in intensity and is sky-subtracted. The total FUV calibrated magnitude is 14.99 ± 0.01 corresponding to a FUV calibrated flux of 3669.20 ± 17.13 micro-Jansky. We also acquired the 8 μm infrared (IR) image obtained with the *Spitzer/IRAC* telescope [5]. Also in this case the image covers a large region of sky ($\sim 1400'' \times 700''$) which was rotated to canonical orientation (North up, East left) in order to correctly superpose this IR image to the molecular gas map.

5.4 Single dish results

The observations performed with the A and B receivers of the IRAM 30 m telescope in the two CO lines covered the central $\sim 50''$, corresponding to the central ∼10 kpc (in diameter) of the galaxy (Fig. 5.7). The 25 observed positions show that the central region of NGC 3147 presents extended molecular emission in both CO(1-0) and CO(2-1) emissions. The maximum detected T_{mb} is 0.32 K in CO(1-0) and 0.31 K in CO(2-1), in the southeast region corresponding to the offsets (10″,-10″) and (5″,-10″) relative to the galaxy center.

The line ratio $R_{21} = I_{21}/I_{10} = \int T_{mb}(2-1)\mathrm{dv} \,/ \int T_{mb}(1-0)\mathrm{dv}$, indicator of physical properties of the molecular gas (such as excitation temperature and optical depth), has a mean value of 0.8. This value is consistent with the optically thick emission of the molecular gas expected for the central regions of spiral galaxies (Braine & Combes, 1992).

Assuming a H_2-CO conversion factor $X = N(H_2)/I_{CO} = 2.2 \times 10^{20}$ cm^{-2} (K km s^{-1})$^{-1}$ (Solomon & Barrett, 1991), the total H_2 mass derived by these single dish observations is $M_{H_2} = 8.2 \times 10^9$ $M_\odot$, within a radius of 5 kpc.

The HCN(1-0) line has been observed for 9 positions with 7″ spacing covering the central ∼9″ corresponding to the central ∼1.8 kpc (in diameter). The HCN(1-0) emission is detected in some of the 9 observed positions, in particular in the northwest part of the ring. The average spectrum over the center is plotted in Fig. 5.8. The CO(1-0)/HCN(1-0) ratio is equal to 20 on average over the center. Because the observed region contains the AGN, we would expect enhanced HCN emission there. Hence, the observed CO(1-0)/HCN(1-0) ratio is very high. For instance in NGC 1097, this ratio is 3 in the nucleus and 10 in the star-forming ring (Kohno et al., 2003). It is more similar to NGC 6951 (Krips et al., 2007b), where the starburst ring has a ratio of 30, and the nucleus 2.5.

[4] For details on archival *GALEX* images see the web site http://galex.stsci.edu/GR2/.

[5] Archival *Spitzer* images downloaded with Leopard software, see the web site http://ssc.spitzer.caltech.edu/propkit/spot/.

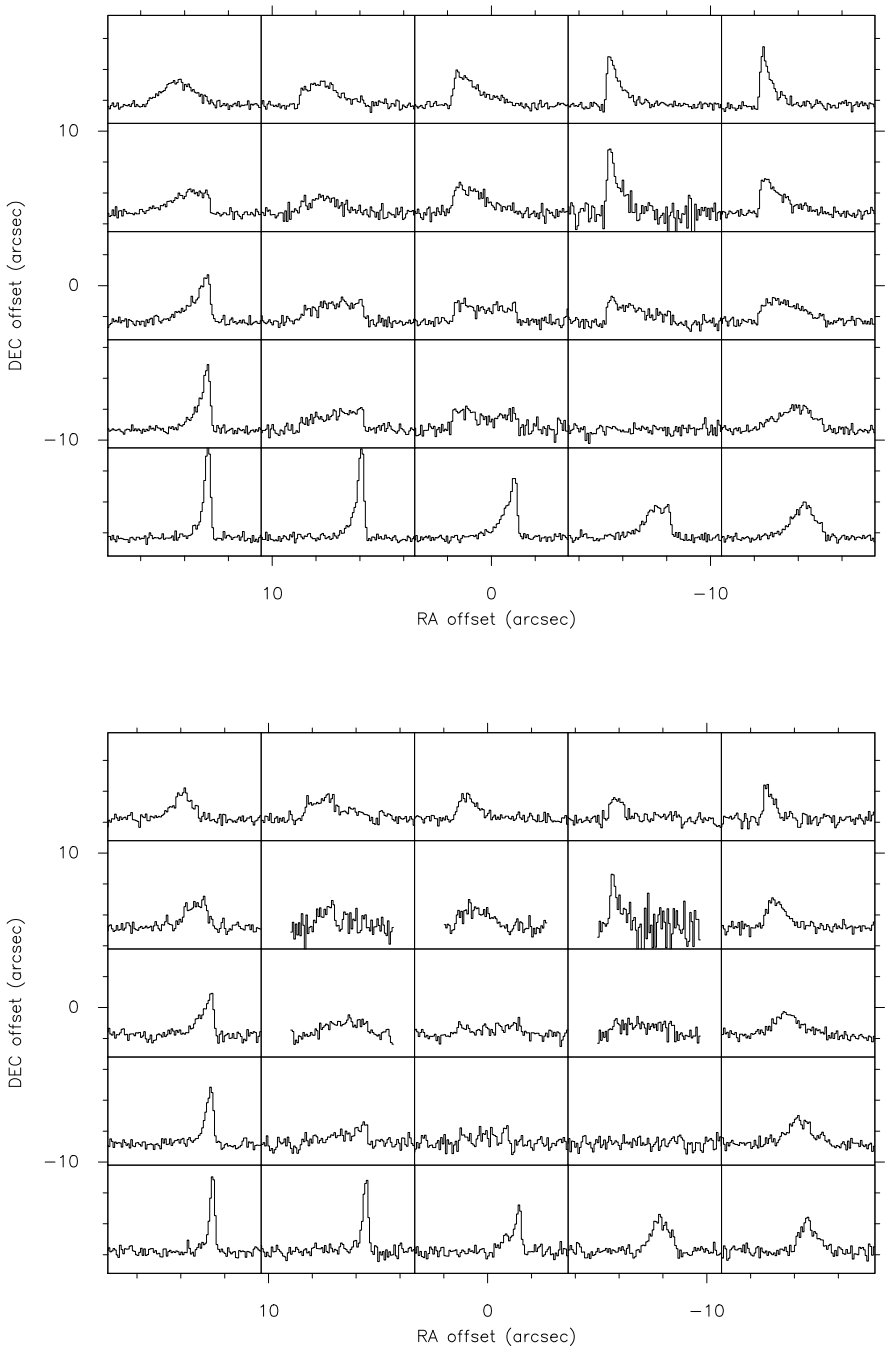

Figure 5.7: Spectra maps of NGC 3147 made with the IRAM 30 m with 7″ spacing in CO(1-0) (top) and CO(2-1) (bottom). The positions are offsets relative to the NGC 3147 center, whose coordinates are listed in Table 5.1. Each spectrum has a velocity scale from -500 to 500 kms^{-1}, and an antenna temperature scale (T_A^*) from -0.05 to 0.25 K for CO(1-0) and 0.20 K for CO(2-1).

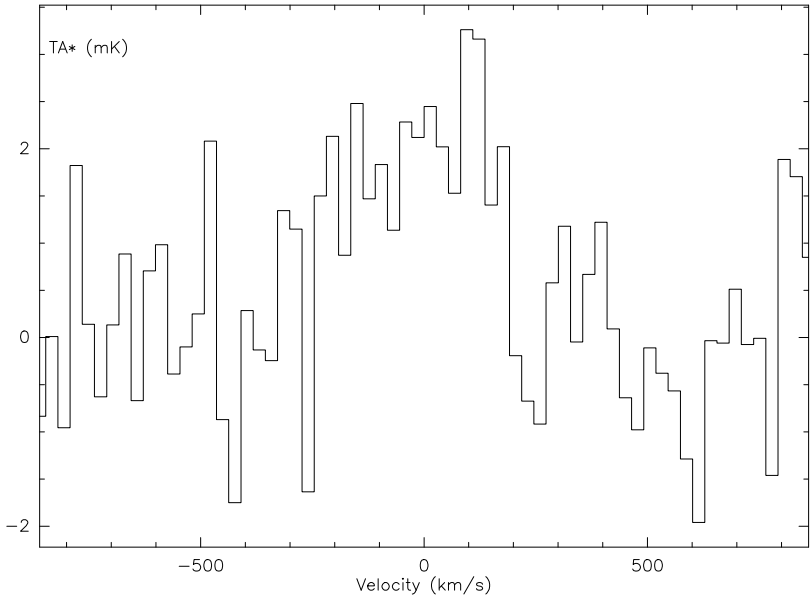

Figure 5.8: Average HCN(1-0) spectrum towards the center of NGC 3147, over the 9-point map made with the IRAM 30 m with 7″ spacing. The HCN is detected, but with a low HCN/CO ratio, of 0.05.

To study the physics and distribution of the molecular gas in detail we need to analyze the interferometric observations, that cover the nuclear region of the galaxy with a better resolution.

5.5 Interferometric results: Molecular gas properties

Fig. 5.9 displays 46 of the channel maps in the CO(1-0) line with a velocity range of 450 km s^{-1}, and a velocity resolution of about 10 km s^{-1}. The velocity field appears regular: the typical spider diagram visible in the channel-map is the signature of a spatially resolved rotating disk (see also Fig. 5.17). The channel maps generated for the CO(2-1) line produce a diagram very similar to that of CO(1-0) emission, at least within the 22″ of its primary beam. All maps are centered on the position of Table 5.1, and the dynamical center coincides with this center, which is also the position of the AGN (the radio continuum source).

5.5.1 Morphology and mass of the CO rings

The CO(1-0) integrated intensity distribution reveals a central peak, a quite symmetric and complete central ring at the distance of about 10″ from the nucleus, and a more external and incomplete ring at the distance of about 20″ from the nucleus (Fig. 5.10). There is a striking depletion between the

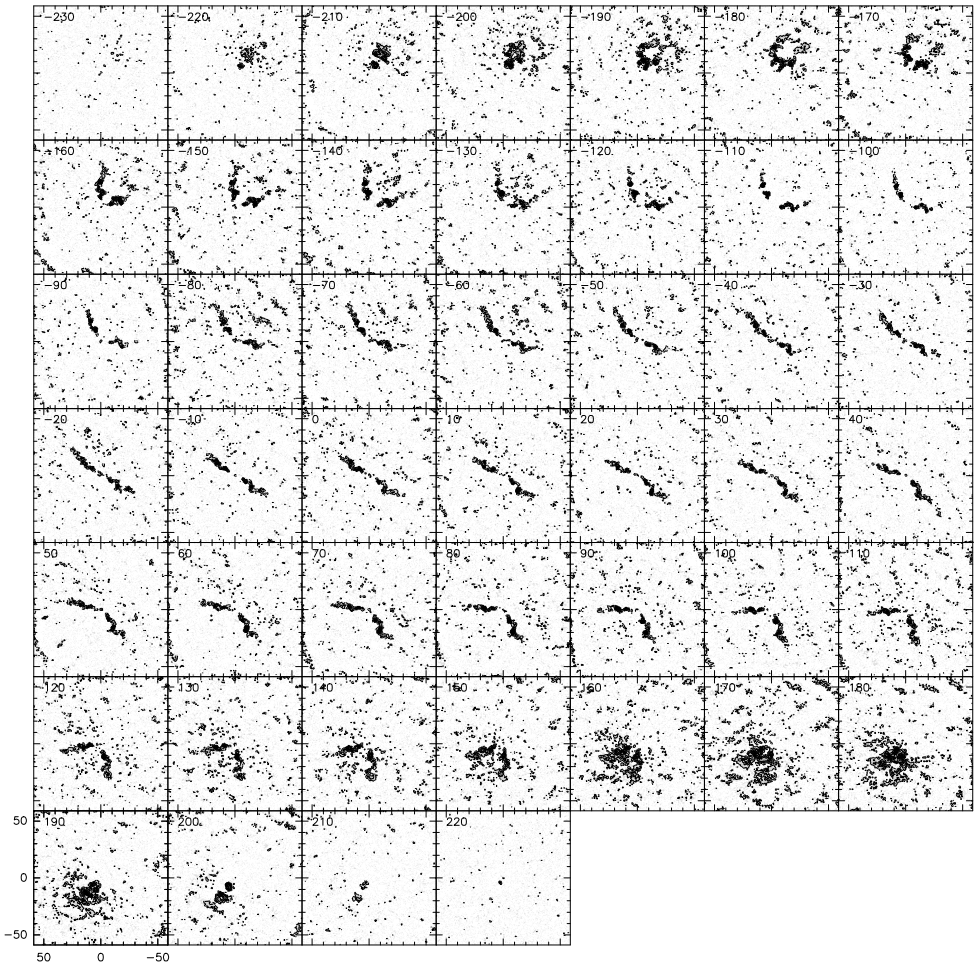

Figure 5.9: CO(1-0) velocity channel maps observed with the IRAM interferometer in the nucleus of NGC 3147 with a spatial resolution of (HPBW) 1.8″ x 1.6″. The center of the observations, given in Table 5.1, is $\alpha_{2000} = 10^h16^m53.6^s$, $\delta_{2000} = 73°24'03''$. Velocity-channels range from v = -230 km s^{-1} to v = 220 km s^{-1} in steps of 10 km s^{-1} relative to V_{hel} = 2813 km s^{-1}. The contours begin at 5 mJy/beam, their spacing is 5 mJy/beam, and the maximum is 50 mJy/beam.

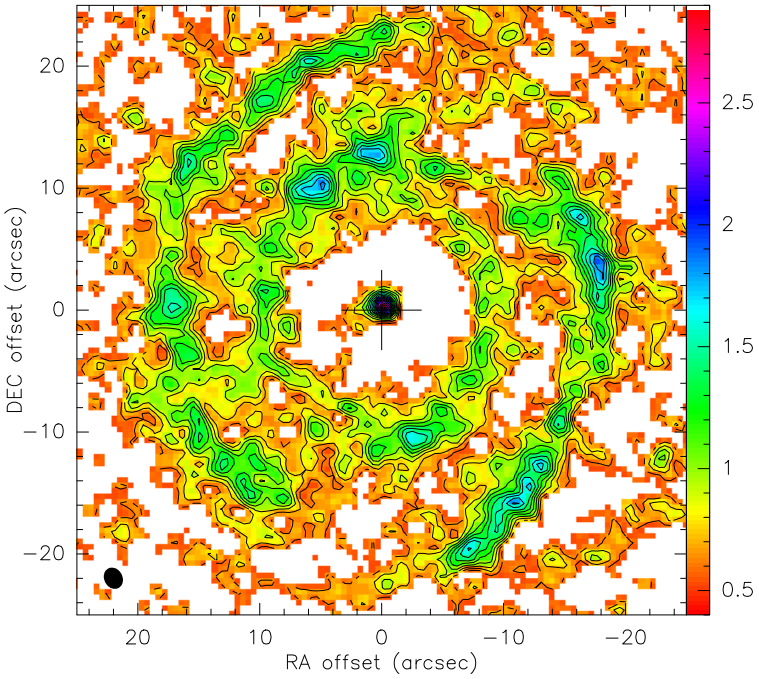

Figure 5.10: ^{12}CO(1-0) integrated intensity contours observed with the IRAM interferometer toward the center of NGC 3147. The cross marks the coordinates of the center as given in Table 5.1 with offsets in arcseconds. The rms noise level is $\sigma = 0.15$ Jy/beam km s^{-1}. The map, derived with 2σ clipping, has not been corrected for primary beam attenuation. Contour levels are from 2σ to 17σ with 1σ spacing. In this map the whole velocity range is used: +/-240 km s^{-1} with 49 channels in steps of 10 km s^{-1}. The beam of 1.8″ x 1.6″ is plotted at the bottom left.

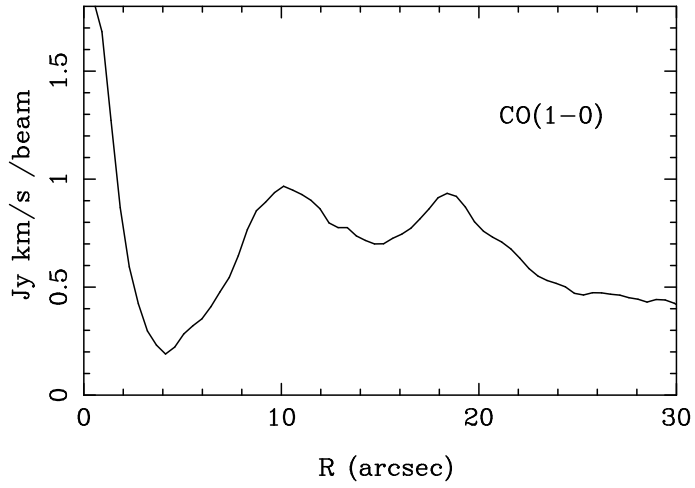

Figure 5.11: Radial distribution (azimuthal average, deprojected to face-on orientation) of the CO(1-0) intensity, shown in Fig. 5.10. This clearly shows the nuclear peak and two CO(1-0) emissions corresponding to the two rings shown in Fig. 5.10.

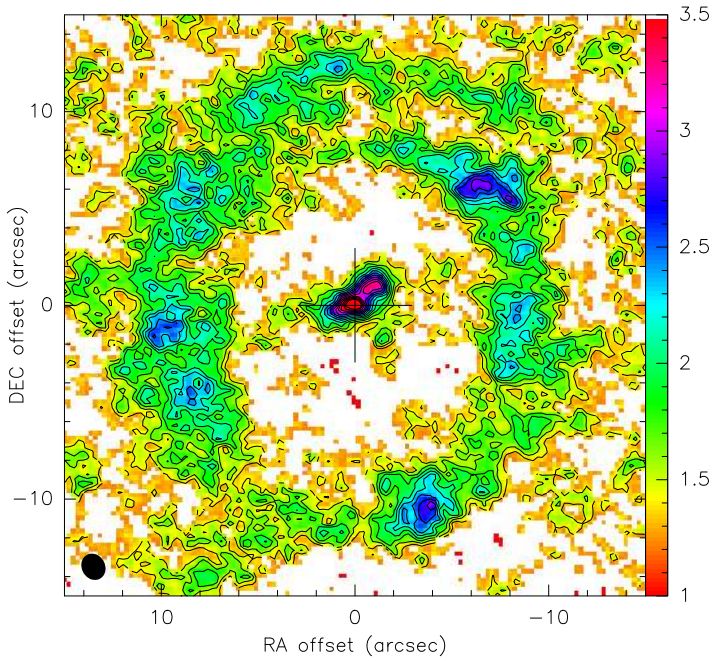

Figure 5.12: ^{12}CO(2-1) integrated intensity contours observed with the IRAM interferometer toward the center of NGC 3147. The cross marks the coordinates of the center as given in Table 5.1 with offsets in arcseconds. The rms noise level is $\sigma = 0.2$ Jy/beam km s^{-1}. The map, derived with 2σ clipping, has not been corrected for primary beam attenuation. Contour levels are from 2σ to 18σ with 1σ spacing. In this map the whole velocity range is used: +/-240 km s^{-1} with 49 channels in steps of 10 km s^{-1}. The beam of 1.4″ x 1.2″ is plotted at the bottom left.

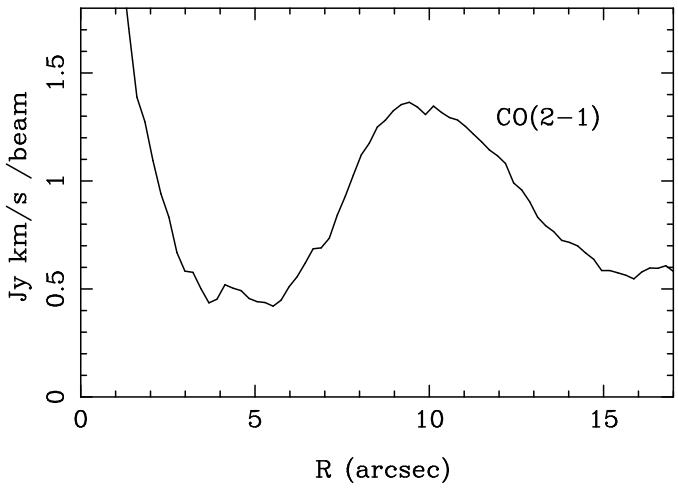

Figure 5.13: Radial distribution (azimuthal average, deprojected to face-on orientation) of the CO(2-1) integrated intensity, shown in Fig. 5.12. This figure clearly shows the central peak and the CO(2-1) emission at ∼10″ corresponding to the inner ring of Fig. 5.12.

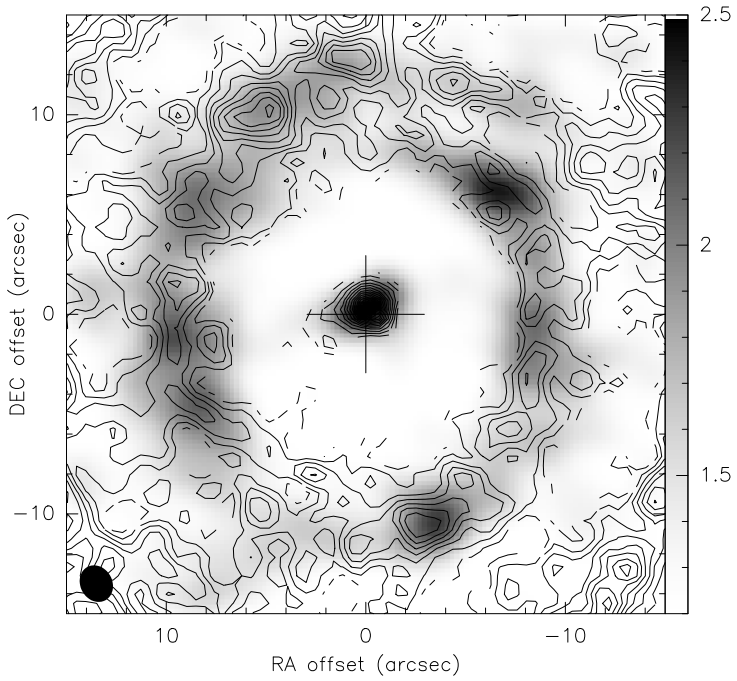

Figure 5.14: Contours of the ^{12}CO(1-0) map, same as Fig. 5.10, superposed with the grey scale ^{12}CO(2-1) map tapered and convolved to the same resolution and corrected for primary beam attenuation, in unit of Jy/beam km s^{-1}. The beam is plotted at the bottom left.

central peak and the inner ring and the outer ring is quite contrasted (see also the radial profile shown in Fig. 5.11).

The two CO(1-0) rings consist of individual giant molecular cloud complexes, each with a mass of a few 10^7 to 10^8 $M_\odot$. The total H_2 mass derived from the interferometer maps, assuming the same H_2-to-CO conversion value used before, is $M_{H_2} = 3.8 \times 10^9$ $M_\odot$. The inner ring alone contributes to more than half of the total mass, $M_{H_2} = 2 \times 10^9$ $M_\odot$, and the two parts of the outer ring have similar mass, the western part has a mass of $M_{H_2} = 9.5 \times 10^8$ $M_\odot$ and the eastern one $M_{H_2} = 8.5 \times 10^8$ $M_\odot$. The total M_{H_2} ($= 3.8 \times 10^9$ $M_\odot$) we find is in good agreement with the estimation of mass derived by Young et al. (1995) for the central offset, $M_{H_2} = 4.4 \times 10^9$ $M_\odot$. Our mass estimation from single dish observations presented in Section 5.4 is larger, since it corresponds to a more extended region.

Because of the restricted field-of-view (FWHM of primary beam of 22″), there is no outer ring detected in CO(2-1) at a radius of 18″. The central concentration is even stronger in CO(2-1) than in CO(1-0), corresponding to a higher density of the molecular gas, and consequently a higher excitation (Fig. 5.12). In Fig. 5.13 the nuclear peak and the 10″-radius ring emission in CO(2-1) are well marked. In addition, Fig. 5.14 shows that when the CO(2-1) data are tapered and convolved to the CO(1-0) resolution, the maxima of the CO(2-1) ring agree quite good with the CO(1-0) ones.

The CO(1-0) distribution we found is in very good agreement with the results obtained by Downes et al. (1991) with IRAM 30 m telescope obser-

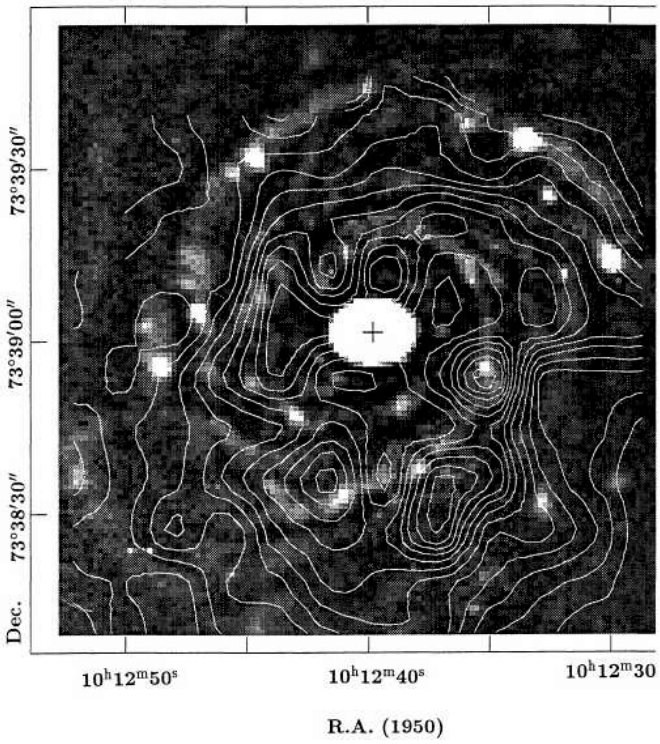

Figure 5.15: CO emission from the galaxy NGC 3147 (Downes et al., 1991), integrated over ± 300 km s^{-1} around the central velocity cz = 2800 km s^{-1}, contour interval = 1 K km s^{-1}, HPBW = 12.5″. The CO contours are superposed on an R-band CCD image made with the 1.2 m telescope of the Observatoire de Haute Provence with low spatial frequencies filtered out the better show the inner spiral arms.

vations of NGC 3147 (see Fig. 5.15). They detected most of the CO in a 10 kpc ring, exactly at the same position of the inner ring in our data. In addition, we found a peak of emission in correspondence of the AGN.

The comparison between the CO maps of the two transitions, at the same resolution and with the same spatial frequency sampling, informs about the excitation conditions of the molecular gas locally, pixel by pixel. The ratio map is shown in Fig. 5.16 where the values are in the range between 0.2 and 1.4. The mean ratio is ∼1 quite consistent with the value found with single dish observations and, also in this case, consistent with the bulk of emission being optically thick, as expected in the nuclei of spiral galaxies. Therefore we will adopt a mean ratio of 1 for NGC 3147. The maximum of 1.4, reached for one of the clumps in the inner ring, probably corresponds to high local density and/or high temperature, may be due to higher local heating.

5.5.2 Kinematics of the CO rings

Studying the kinematics of the molecular gas in detail, we found that there are no significant streaming motions or strong irregularities in the velocity field, in accordance to the two almost circular rings detected in CO(1-0). Fig. 5.17 shows the isovelocity curves of the CO(1-0) emission superposed

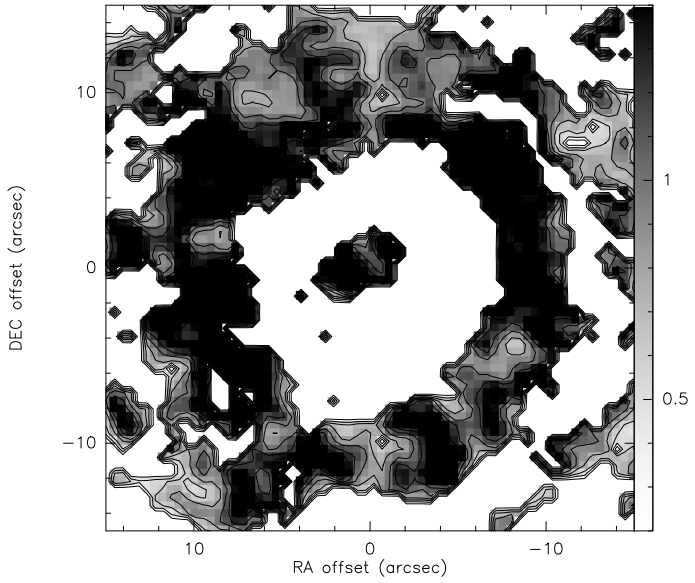

Figure 5.16: Contours and grey scale of the CO(2-1)/CO(1-0) ratio map. Contours are from 0.2 to 2 by 0.1

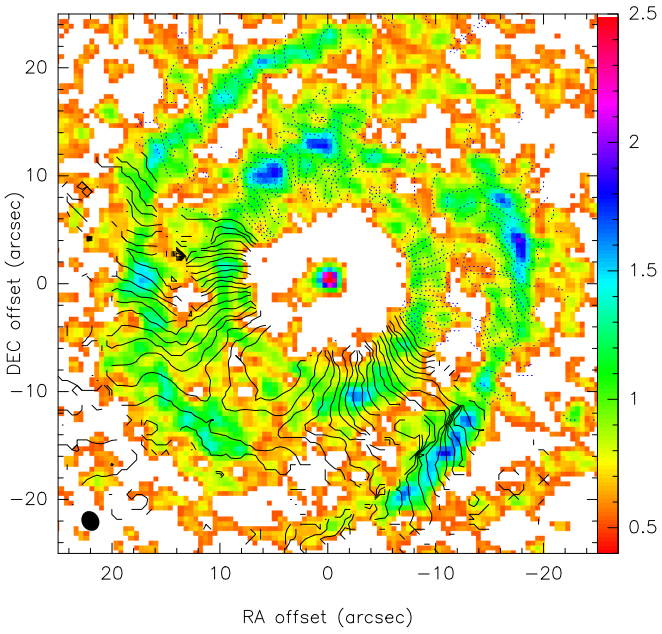

Figure 5.17: Overlay of the integrated ^{12}CO(1-0) emission in grey scale, same as Fig. 5.10, with CO mean-velocity field in contours spanning the range -200 km s^{-1} to +200 km s^{-1} in steps of 10 km s^{-1}. The velocities are referred to V$_{hel}$ = 2820 km s^{-1}. Solid (dashed) lines are used for positive (negative) velocities.

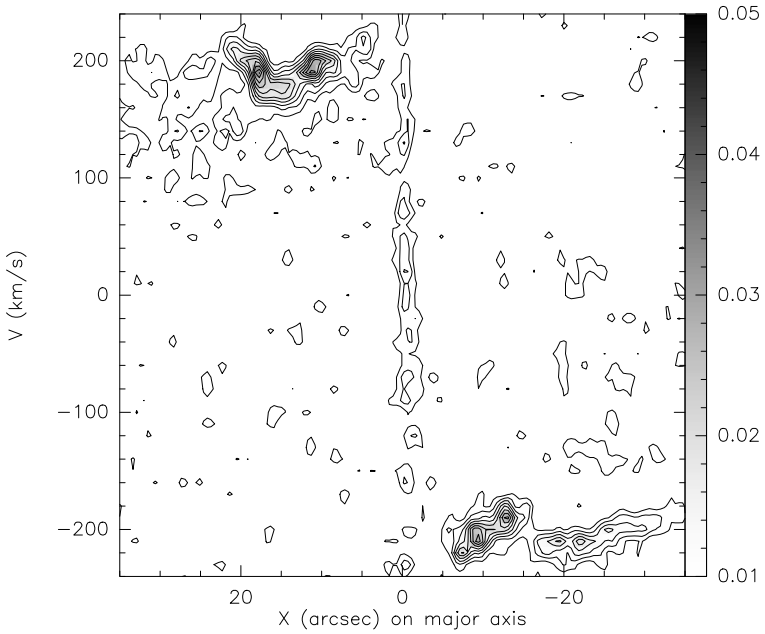

Figure 5.18: CO(1-0) position-velocity (p-v) diagram along the major axis of NGC 3147 using the whole velocity range ±240 km s^{-1} with 49 channels in steps of 10 km s^{-1}. The center (0,0), the heliocentric velocity, and P.A. used are given in Table 5.1. Contour levels are from 0.005 to 0.05 Jy/beam in steps of 0.005 Jy/beam.

on the CO(1-0) emission. There are only some slight wiggles on the isovels, revealing minor streaming motions, which are compatible with t slight gas inflow (see Section 5.8). Also the position-velocity diagram along the major axis in Fig. 5.18 shows the global regularity of the kinematics. This p-v plot has been obtained using the whole velocity range between -240 to 240 km s^{-1} with 49 channels in steps of 10 km s^{-1}.

5.6 Comparison with *Spitzer* and *GALEX*

It is instructive to compare the distribution of the molecular gas in the inner kpc of NGC 3147 with observations at other wavelengths. In particular, molecular clouds are thought to be the birth site of the future generation of stars, and then should be strongly connected to other emissions tracing the star formation, such as the far-ultraviolet and far-infrared emissions.

The FUV image obtained with the *GALEX* satellite shows that NGC 3147 has a quite well defined spiral structure. Observing the central region (see Fig. 5.19) in detail, one can clearly see that there is a compact nucleus with a peak in the center and a sort of ring, incomplete in the northwest direction. Fig. 5.20 shows the superposition of FUV-*GALEX* image with the CO(1-0) contours shown in Fig. 5.10. The cross reported in the figure is at the center of our CO observations and is exactly located in the peak of the FUV emission that is in the center of the galaxy. This agreement suggests that the FUV and CO emission are cospatial in the nuclear region. However

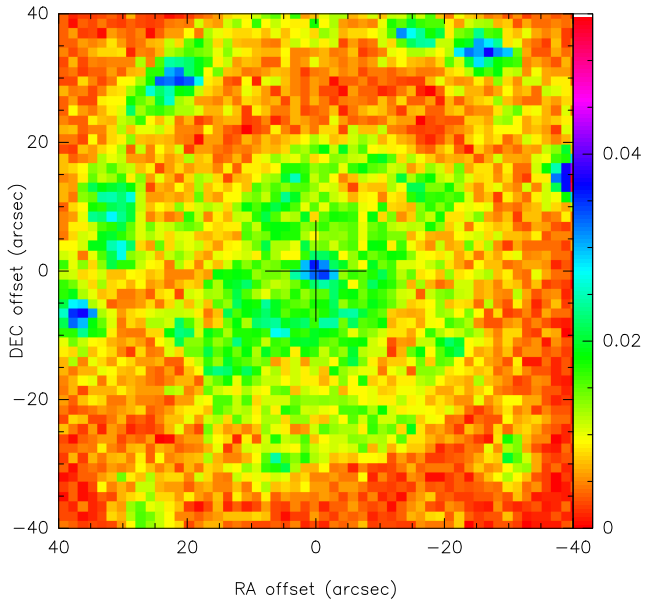

Figure 5.19: FUV*GALEX* sky subtracted image of NGC 3147. The central 80″ of the galaxy are shown. A ring structure around the nucleus, even if incomplete, is evident.

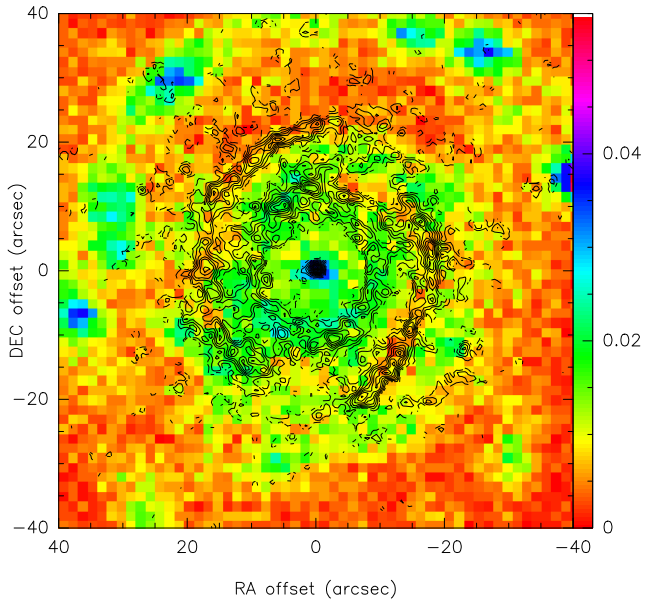

Figure 5.20: Superposition of the CO(1-0) contour levels shown in Fig. 5.10 and the FUV-*GALEX* image shown in Fig. 5.19. The central 80″ are shown. The CO inner ring agrees with the FUV one, the central 10″-radius CO ring is slightly contained in the FUV circular region. But the more external (18″-radius) CO pseudo-ring does not correspond at all with the FUV structures, although there is some overlap with the FUV ring (eastern part). The southwest CO emission appears to fall in the FUV interarm.

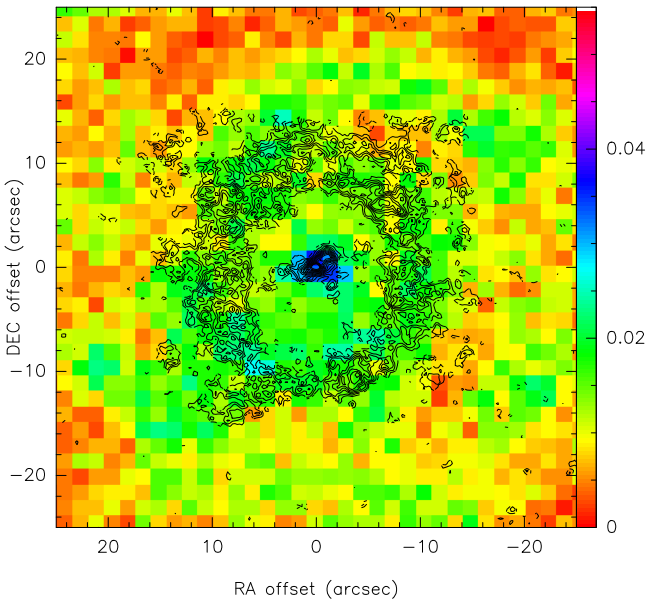

Figure 5.21: Superposition of the CO(2-1) contour levels shown in Fig. 5.12 and the FUV-*GALEX* image shown in Fig. 5.19. The central 50″ are shown. The CO(2-1) nuclear peak agrees with the FUV one, and the CO(2-1) ring is contained in the FUV-*GALEX* inner ring-like structure.

the correspondence is not as good for the rings. The inner 10″-radius CO ring is contained inside the circular region of the FUV emission and the outer CO ring (18″-radius), at least its eastern part, has some overlap with the FUV ring, but there are clear shifts between the two distributions. The CO(2-1) emission (essentially the inner ring) appears to settle also slightly inside the FUV-*GALEX* inner ring-like structure (Fig. 5.21).

We have retrieved the 8 μm *Spitzer/IRAC* image, for the Sbc-type NGC 3147 galaxy, which should represent essentially the emission of warm dust, and in particular the PAH. For late-type the stellar contribution to the 8 μm image is only about 10% (e.g. Pahre et al., 2004). Fig. 5.22 shows this image, dominated by dust, which clearly exhibits a ring structure around the nucleus at about 10″ radius, and a central peak. Such rings are frequently observed in barred galaxies with *Spitzer* (e.g. Regan et al., 2006). The ring visible at 8 μm corresponds both to the CO(1-0) inner ring and the CO(2-1) one (see Figs. 5.23 and 5.24). However the outer CO(1-0) ring is slightly inside the corresponding structures in dust emission. In the southwest region, the CO just falls in the interarm defined by the UV and FIR. The correlation with the inner ring but not the outer one between CO data and UV or FIR ones is a mystery, and we will discuss this result in Section 5.8.

The agreement, where present, between the molecular gas distribution and the ultraviolet and infrared emissions is consistent with on-going star formation within the molecular clouds. We computed the star formation rate (SFR) from both UV and FIR emission for the inner FOV = 45″ from

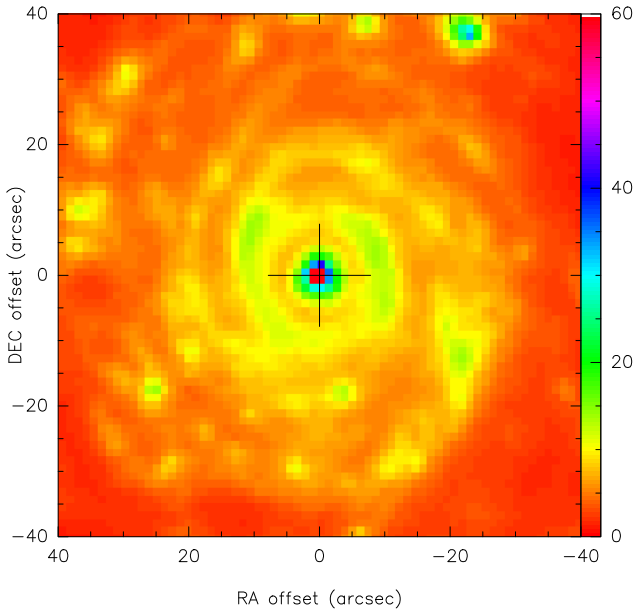

Figure 5.22: 8 μm *Spitzer* image of NGC 3147. The central 80″ of the galaxy are shown. A ring structure around the nucleus is also apparent.

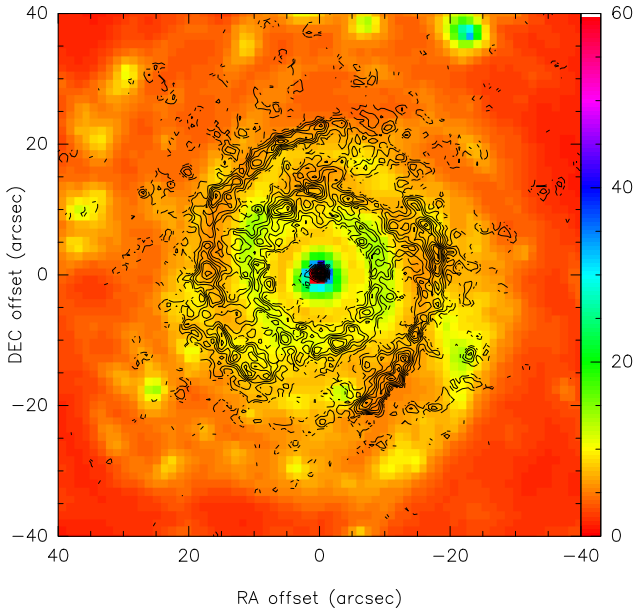

Figure 5.23: Superposition of the CO(1-0) contour levels shown in Fig. 5.10 and the 8 μm *Spitzer/IRAC* image shown in Fig. 5.22. The central 80″ are shown. There is a good agreement between the CO(1-0) and the mid-IR emission in the inner ring, but the external CO(1-0) pseudo-ring does not correspond to the dust emission structures. The CO is found in the dust "interarm" region.

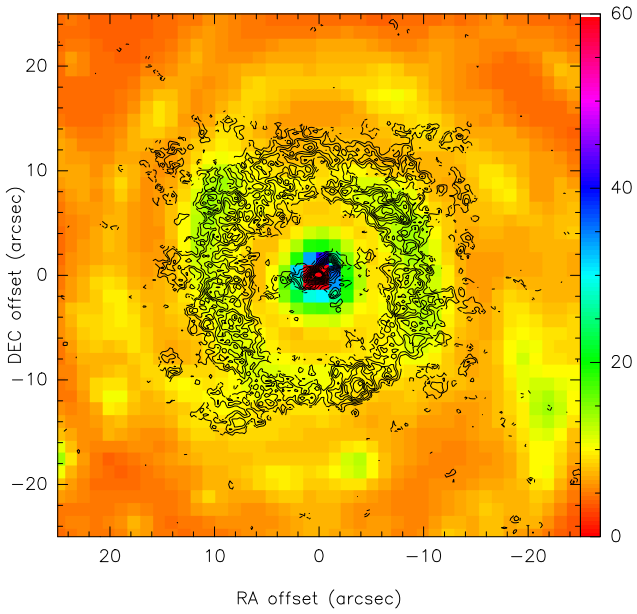

Figure 5.24: Superposition of the CO(2-1) contour levels shown in Fig. 5.12 and the 8 μm *Spitzer/IRAC* image shown in Fig. 5.22. The central 50″ are shown. There is a good agreement between the CO(2-1) ring and nuclear peak and IR ones.

CO(1-0) emission using the calibration given by Kennicutt (1998a):

$$\mathrm{SFR}\,[\mathrm{M}_\odot\,\mathrm{yr}^{-1}] = 1.4 \times 10^{-28}\,\mathrm{L}_\nu \tag{5.1}$$

where L_ν is the UV luminosity in ergs s^{-1} Hz^{-1} over the wavelength range 1500-2800 $\mathring{A}$, and

$$\mathrm{SFR}\,[\mathrm{M}_\odot\,\mathrm{yr}^{-1}] = 4.5 \times 10^{-44}\,\mathrm{L}_{FIR} \tag{5.2}$$

where L_{FIR}, expressed in ergs s^{-1}, refers to the infrared luminosity integrated over the full mid and far-IR spectrum (8-1000 μm). Both in infrared and in ultraviolet emission we find a value for the SFR of about 1 $\mathrm{M}_\odot\,\mathrm{yr}^{-1}$ in the inner FOV = 45″. The total SFR computed using the Eq. 5.2 and L_{FIR} listed in Table 5.1 is about 6 $\mathrm{M}_\odot\,\mathrm{yr}^{-1}$, a value rather low if compared to other star-forming galaxies, such as luminous infrared galaxies (LIRGs, $10^{11}\mathrm{L}_\odot < \mathrm{L}_{IR} \lesssim 10^{12}\mathrm{L}_\odot$) and ultraluminous infrared galaxies (ULIRGs, $\mathrm{L}_{IR} \gtrsim 10^{12}\mathrm{L}_\odot$) where the SFR typically ranges between 10 and 100 $\mathrm{M}_\odot\,\mathrm{yr}^{-1}$ (Gao & Solomon, 2004a; Pasquali et al., 2004).

5.7 Computation of the torques

In this section we describe how the theoretical approach helped us to interpret the molecular gas distribution in the inner region of NGC 3147.

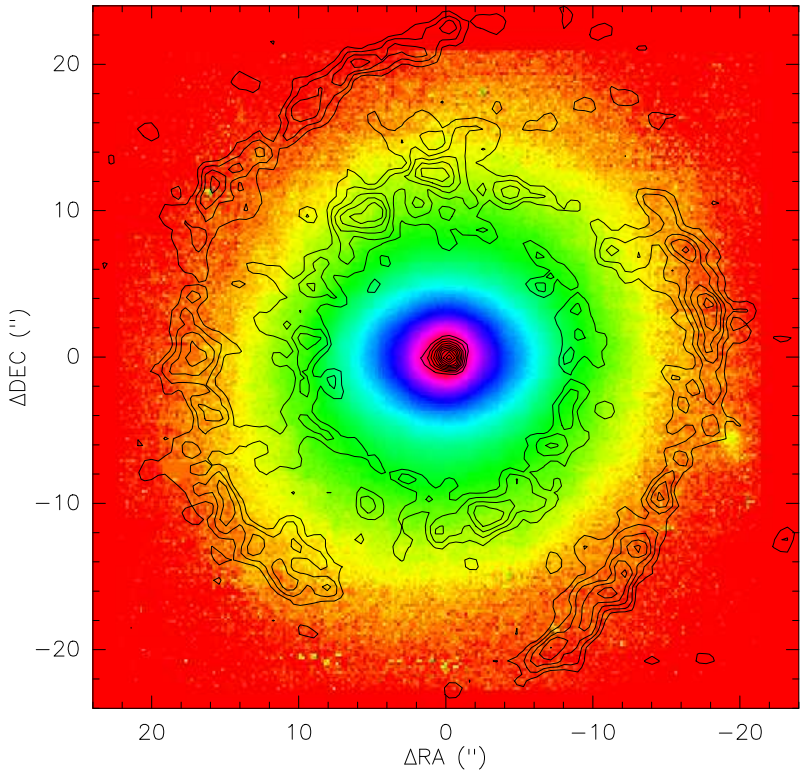

Figure 5.25: CO(1-0) linear contours (0.87 to 2.87 by 0.2 Jy km s^{-1} beam^{-1}) superposed on the near-infrared J image, taken with the CFHT, in logarithmic levels. The nuclear bar of P.A. = 85° lies just inside the nuclear ring in the molecular gas. The major axis of the galaxy is at P.A. = 150°.

5.7.1 Near infrared images

The J image is superposed to the CO contours in Fig. 5.25. It reveals a weak bar feature at a position angle PA = 85°, just contained inside the inner CO ring. Only the near-infrared reveals this bar, since NGC 3147 is not classified as a barred galaxy. It's late type (Sbc) corresponds to a non dominating bulge, and the bar feature is likely not diluted in this bulge. The major axis orientation is 65° from the bar PA, which avoids confusion with projection effects. The high nuclear CO contours show that some gas must have been flowing towards the center. The bar is about 16″ (or 3 kpc) in diameter, while the inner CO ring has a diameter of 20″ (4 kpc).

The bar was not seen in the optical, and NGC 3147 is classified unbarred in the RC3. The bar is only revealed in the near-infrared. Möllenhoff & Heidt (2001) have obtained JHK images with the 2.2 m of Calar Alto observatory with the MAGIC NICMOS3 camera, together with 40 other unbarred and with low inclination. They decomposed the images in bulge and disk components, and noticed that the bulge in NGC 3147 appears at a very different position angle than the disk: PA = 88° instead of PA = 150° for the disk. They concluded that the bulge must be triaxial, which was a rare feature in their sample. Indeed most triaxial bulges appear in the optical because of uneven dust obscuration, and disappear in the NIR. Most bars,

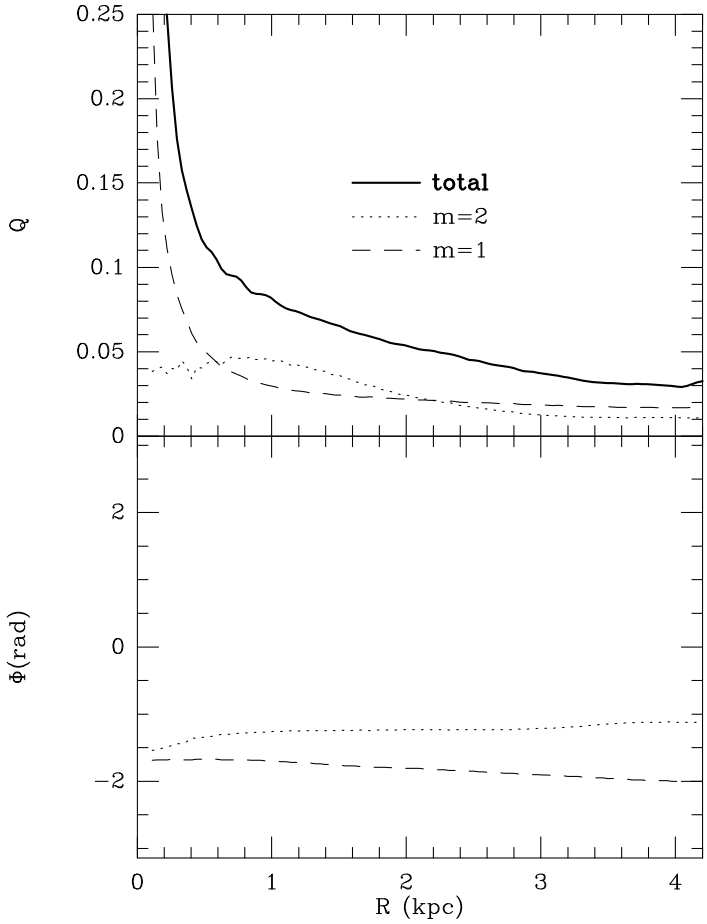

Figure 5.26: Strengths (Q_1, Q_2 and total Q_T) and phases (ϕ_1 and ϕ_2) of the $m = 1$ and $m = 2$ Fourier components of the stellar potential inside a field of $48''$ in diameter (r < 4.6 kpc). The bar strength extends up to 2 kpc in radius, and has a constant phase.

because they are dominated by older stellar populations appear in the NIR, and not in the optical. Hence, we interpret here the elongation at PA = 88° as a weak bar, or oval, rather than a triaxial bulge. We have reduced the MAGIC J and K images and found also the oval seen in the CFH images, although with more noisy isophotes.

5.7.2 Evaluation of the gravitational potential

To evaluate the gravitational potential we assumed that the NIR images can give us the best approximation for the total stellar mass distribution, being less affected by dust extinction or by stellar population biases (see García-Burillo et al., 2005, for more details). Here we recalled the essential definitions and assumptions.

The J image was first deprojected according to the angles PA = 150° and $i = 29.5°$. We have not deprojected the bulge separately, since we do

not know its actual flattening, and because the galaxy is of late type (Sbc), it has not a large contribution. The image is however completed in the vertical dimension by assuming an isothermal plane model with a constant scale height, equal to ∼1/12th of the radial scale-length of the image. The potential is then derived by a Fourier transform method, assuming a constant mass-to-light (M/L) ratio. The M/L value is selected to reproduce the observed CO rotation curve.

For the non-axisymmetric part, the potential $\Phi(R,\theta)$ is then decomposed in the different m-modes:

$$\Phi(R,\theta) = \Phi_0(R) + \sum_m \Phi_m(R)\cos(m\theta - \phi_m(R))$$

where $\Phi_m(R)$ and $\phi_m(R)$ represent the amplitude and phase of the m-mode.

The strength of the m-Fourier component, $Q_m(R)$ is defined as $Q_m(R) = m\Phi_m/R|F_0(R)|$, i.e. by the ratio between tangential and radial forces (e.g. Combes & Sanders, 1981). The strength of the total non-axisymmetric perturbation is defined by:

$$Q_T(R) = \frac{F_T^{max}(R)}{F_0(R)}$$

where $F_T^{max}(R)$ represents the maximum amplitude of the tangential force and $F_0(R)$ is the mean axisymmetric radial force. Fig. 5.26 displays these values as a function of radius for NGC 3147. A bar can be seen clearly, together with an asymmetry towards the center. The lopsideness has a correspondence in the gas morphology described in Section 5.4. The bar is regular in phase, but its strength is relatively modest.

5.7.3 Evaluation of gravity torques

After having calculated the forces per unit mass (F_x and F_y) from the derivatives of $\Phi(R,\theta)$ on each pixel, the torques per unit mass $t(x,y)$ can be computed by:

$$t(x,y) = x\ F_y - y\ F_x \tag{5.3}$$

The torque map is oriented according to the sense of rotation in the plane of the galaxy. The combination of the torque map and the gas density Σ map allows then to derive the net effect on the gas, at each radius. The gravitational torque map weighted by the gas surface density $t(x,y)\times\Sigma(x,y)$, normalized to its maximum value, is shown in Figs. 5.27 and Fig. 5.28 for CO(1–0) and CO(2–1) respectively.

To estimate the radial gas flow induced by the torques, we first computed the torque per unit mass averaged over the azimuth, using $\Sigma(x,y)$ as the actual weighting function, i.e.:

$$t(R) = \frac{\int_\theta \Sigma(x,y)\times(x\ F_y - y\ F_x)}{\int_\theta \Sigma(x,y)} \tag{5.4}$$

By definition, $t(R)$ represents the time derivative of the specific angular momentum L of the gas averaged azimuthally, i.e., $t(R)=dL/dt\ |_\theta$. To derive undimensional quantities, we normalised this variation of angular momentum per unit time, to the angular momentum at this radius, and to the

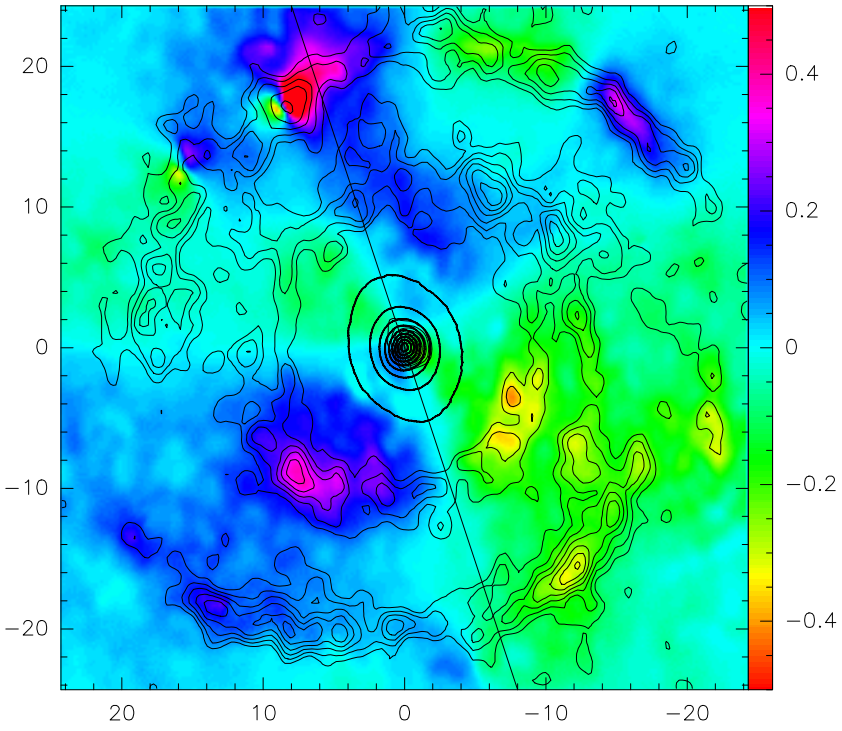

Figure 5.27: The CO(1–0) contours are overlaid onto the gravitational torque map (t(x,y) × Σ(x,y), as defined in text) in the center of NGC 3147. The torque map (grey/color scale) is normalized to the maximum absolute value of the torques. The derived torques change sign as expected in a *butterfly* diagram, delineating four quadrants. The orientation of quadrants follow the bar orientation in NGC 3147. In this deprojected picture, the major axis of the galaxy is oriented parallel to the abscissa Ox. The inclined line reproduces the mean orientation of the bar (P.A. = 20° on the projected image).

rotation period. We then estimate the efficiency of the gas flow with the average fraction of the gas specific angular momentum transferred in one rotation (T_{rot}) by the stellar potential, as a function of radius, i.e., by the function $\Delta L/L$ defined as:

$$\frac{\Delta L}{L} = \frac{dL}{dt}\bigg|_{\theta} \times \frac{1}{L}\bigg|_{\theta} \times T_{rot} = \frac{t(R)}{L_{\theta}} \times T_{rot} \tag{5.5}$$

where L_θ is assumed to be well represented by its axisymmetric estimate, i.e., $L_\theta = R \times v_{rot}$. The $\Delta L/L$ curves for NGC 3147, derived from the CO(1–0) or the CO(2–1) gas are displayed in Figs. 5.29.

Fig. 5.27 shows that the derived torques change sign following a characteristic 2D *butterfly* pattern. The CO contours reveal that for the material in the inner ring of 2 kpc (10″) in radius, part of the gas is trailing the bar, while part of the gas leads the bar. The observed gas distribution is representative of the time spent by a molecular cloud on a typical orbit at this location. The azimuthal average of Fig. 5.29 shows that the torques are predominantly negative inside r = 2.5 kpc, while they become positive outside.

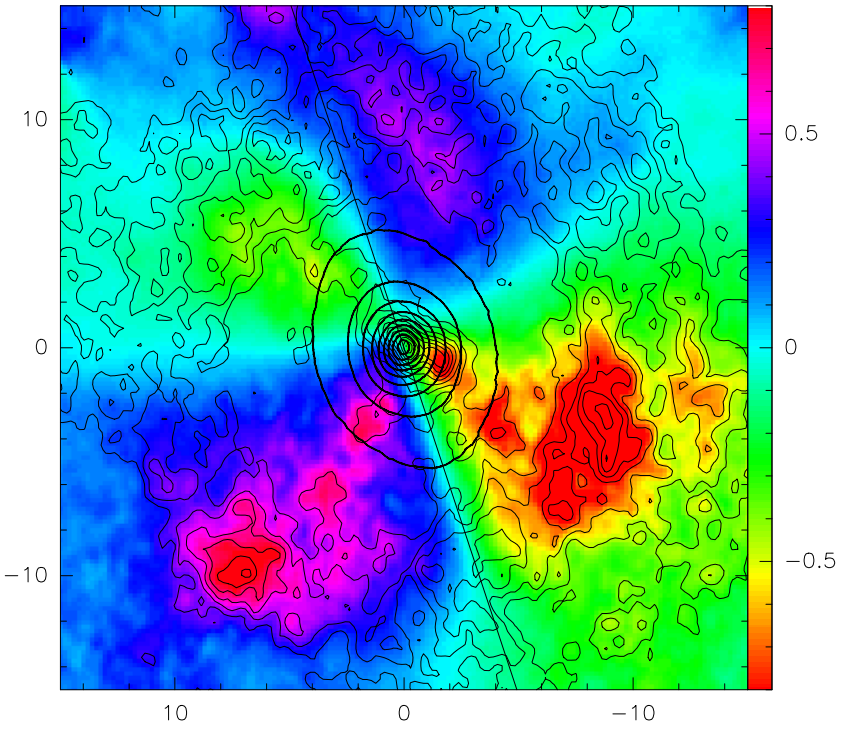

Figure 5.28: Same as Fig. 5.27 for the CO(2–1) emission taken as tracer of gas surface density.

The rotation sense in the galaxy is counterclockwise, and the whole spiral structure is trailing with respect to the rotation, if the near side is the northeast side. In the spiral structure winding into the outer CO(1-0) ring, the torques almost cancel out in average, but are still predominantly positive. Inside the inner ring (r $<$ 2 kpc) however, the dominating torques are negative. The CO(2-1) emission is more clumpy, and our map suffers from less sensitivity; there is relatively more emission in the central part. Although the emission is spread over three quadrants in the center, the negative torques are still predominant there (Fig. 5.28).

5.8 Discussion

We find that two molecular rings, in addition to a central peak of emission, dominate the CO map of the NGC 3147 inner region. The comparison between this distribution and that linked to emission tracing the star formation at various wavelengths shows an apparently mysterious result. While the CO central peak and the inner ring correlate well with the FUV and 8 μm emissions, the outer CO ring does not superpose to the *GALEX* and *Spitzer* distributions but the outer CO spirals appear located inside them. In the southwest region, where this result is more evident, the CO arm falls in the interarm detected by the FUV and FIR emission (see Figs. 5.20 and 5.23). In other words, the correlation between the molecular gas and the tracers of star formation considered here is only revealed for the nuclear peak and the inner ring. This link partially disappears for the outer ring.

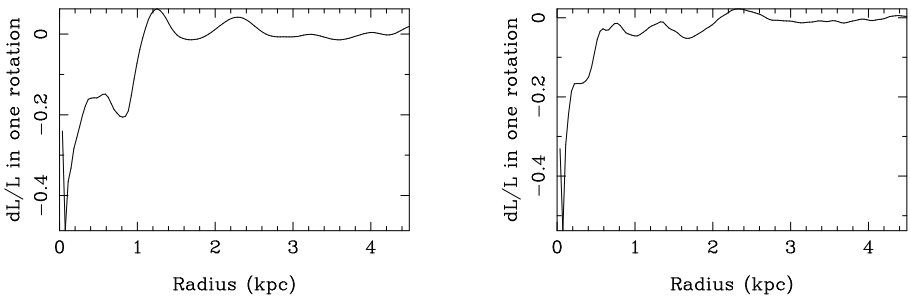

Figure 5.29: The torque, or more precisely the fraction of the angular momentum transferred from/to the gas in one rotation–dL/L–are plotted for CO(1-0) (*left*), and CO(2-1) (*right*). The curve is more noisy for the CO(2-1), because of the clumpiness of the map, but both show negative torques inside 1 kpc in radius, and positive outside.

We think that this result is not due to dust obscuration because the 8 μm-PAH and UV emissions correlate between them but not with CO. A possible explanation is that the CO outer spiral is not a permanent structure but is transient. The gas participates in a spiral wave, forms stars, and then the newly formed stars decouple from the gas component. The young stars heat only the dust present at their location, while the bulk of the gas has moved to another density condensation. The inward migration of the dense gas with respect to the first place of resonance has for instance been discussed by Regan & Teuben (2003). This phenomenon, because it is very transient, is statistically rarely encountered. In this scenario, the CO clouds would not trace stars of the same age of those that have heated the dust observable at 8 μm or of those whose emission is detected in the FUV, but they are the site of the future stellar generation.

There is also a spatial anti-correlation between the CO distribution and the HI one (Viallefond et al., 2008). VLA-HI observations (FV, private communication) show that NGC 3147 has a central hole in HI emission and the molecular gas observed here is entirely contained in this nuclear HI depression, a region where the gas is expected to be denser and so in molecular form.

As for the torques computation, we interpret the results by identifying the resonances with the bar. Let us note that CO resonant rings have already been observed in weakly barred galaxies, where the bar in inconspicuous in the optical (e.g. NGC 5005 Sakamoto et al., 2000). The rotation curve derived from the CO kinematics is rather peaked in the center, and corresponds well to the gravitational model obtained from the near-infrared image. Both are fitted by an axisymmetric mass model, with rotation curve as shown in Fig. 5.30, which allows to derive the proper frequencies.

If the stellar bar ends at about its ultra-harmonic resonance (UHR), as is canonical for bar dynamics, this means that the pattern speed of the bar would be $\Omega_p = 160$ km s^{-1} kpc^{-1}, corresponding to a bar with one or two inner Lindblad resonances, as is common. The presence of these ILRs is not certain however, given the possible non-circular motions in the bar. The inner CO ring would then correspond to the ultra-harmonic resonance (UHR, r = 2 kpc) just inside corotation and the outer CO ring corresponds to the spiral structure getting out of the bar, at the level of its corotation, which is located at 2.2 kpc. The pitch angle of these spiral arms is quite small, as is expected for a weak bar. In this scenario, the gas in the inner

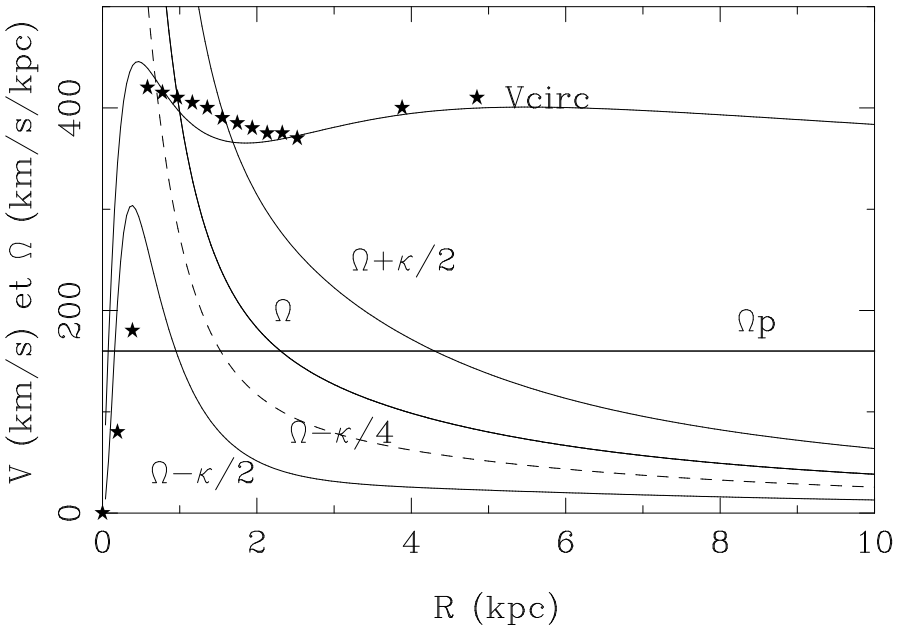

Figure 5.30: Model rotation curve and derived frequencies Ω, $\Omega - \kappa/2$ and $\Omega + \kappa/2$, for NGC 3147. The star symbols are the data derived from the CO kinematics, deprojected with an inclination of i = 29.5°.

CO ring is inside corotation; due to the negative torques there, the gas loses angular momentum and is therefore flowing inwards, fueling the center. Due to the weak bar, the rate of inflow is relatively low, with a time-scale of about 5 rotations (Fig. 5.29).

The amount of gas flowing inwards is sufficient to feed the Seyfert 2 nucleus: the gas surface density there is about 10 $M_\odot\,pc^{-2}$; if the gas at 1 kpc from the center infalls in 5 dynamical time-scale (of 20 Myr) then the feeding rate is about 0.5 $M_\odot\,yr^{-1}$. Assuming a mass-to-energy conversion efficiency of $\epsilon \sim 10\%$ ($L = dM/dtc^2\epsilon$), then a luminosity of the order of 3 $\times 10^{45}$ erg s^{-1} is accounted for, more than enough for this low luminosity AGN.

The spatial resolution of the CO maps are not yet sufficient to determine more precisely whether the gas is actually feeding the AGN, but we can at least conclude that we are seeing the gas inflow fueling the ∼100 pc scale circumnuclear region, a very favorable condition for this feeding.

5.9 Conclusions

The molecular gas in the Seyfert 2 galaxy NGC 3147 has been mapped with high resolution (1.8″ x 1.6″ Gaussian-beam for the CO(1-0) line) inside a radius of 25″ (∼5 kpc). The CO emission shows a central peak and two rings at the distance of 2 kpc and 4 kpc respectively. The observed CO has a mean line intensity ratio I_{21}/I_{10} ∼1, consistent with the optically thick emission expected in nuclei of spiral galaxies, and a regular kinematics without evidence of strong non-circular motions.

Comparing the molecular gas distribution with other tracers of star formation, we find that central emission and the inner CO ring superpose well to the FUV (*GALEX*) and 8 μm emissions (*Spitzer*), while the outer CO ring does not superpose, but is contained inside the second interarm (SW) detected by *GALEX* and *Spitzer*. We interpret this partial disagreement as due to the transient nature of the outer CO ring. It would be a structure in re-condensation that traces the future stellar generation, but decoupled from the recent and ongoing star formation traced by FUV and FIR emissions.

We have identified the presence of a weak bar in NGC 3147, galaxy classified as non-barred in the optical, with a NIR image obtained with the Canada-France-Hawaii Telescope. This stellar bar acting on the gas produces gravity torques. A part of gas present in the inner CO(1-0) ring is trailing the bar, while part of the gas leads the bar. The gravity torques are negative inside a radius of 2.5 kpc, while they become positive outside. In the outer CO(1-0) ring the torques almost cancel out in average, but are positive. In the more clumpy inner CO(2-1) ring, the predominant torques are negative. We interpret these results by identifying the resonances with the bar. The inner CO ring would correspond to the ultra-harmonic resonance (r = 2 kpc) just inside corotation, and the outer CO ring corresponds to the spiral structure getting out of the bar, at the level of its corotation, which is located at 2.2 kpc. In the inner CO ring the gas is inside corotation due to the negative torques there, it loses angular momentum and is flowing inwards, fueling the center.

NGC 3147 is not the first case in the NUGA sample where gas has been found inflowing: NGC 2782 (Hunt et al., 2008), and NGC 6574 (Lindt-Krieg et al., 2008) also show this feature. However, among them, only NGC 2782 has a strong and significant inflow, due to a nuclear bar embedded in the primary one, and with gas aligned with the nuclear bar. The amount of gas inflowing in NGC 3147, quantified from the gravity torques computation, is weak, but yet sufficient to feed the Seyfert 2 nucleus of NGC 3147 with a feeding rate of about 0.5 $M_\odot\,yr^{-1}$. Even if higher spatial resolution is needed to determine whether the gas is actually feeding the AGN, we are observing the gas inflow fueling the $\sim$100 pc central region, a condition that surely favors the fueling of the AGN.

Chapter 6

Conclusions and Future Applications

6.1 Conclusions and obtained results

In this Thesis we studied the small scale physics of the molecular gas in nearby galaxies. The study of the interstellar medium in galaxies, in particular the molecular gas component, is a subject currently in a strong technical and scientific development.

A detailed work on the molecular component of the ISM must be faced studying the spectral energy distribution with observations in a wide range of the galaxy spectrum. Each spectral range (for instance near infrared or microwaves) shows lines produced by different physical conditions. The observation of these lines in nearby galaxies allows to map the distribution of temperature, density and ionisation sources within the galaxy. If peculiar phenomena are present in a galaxy, they can modify the physical conditions and their effect can be also mapped in comparison with normal galaxies. We produced detailed maps of molecular gas in galaxies close enough to separate the single components, such as molecular clouds, diffuse gas, and ionisation sources.

We started with the nearby galaxy Messier 81. We chose this galaxy because considered interesting for its molecular gas content and physics if compared to galaxies with similar distances and morphological type. By previous studies the CO emission of M 81 appears remarkably weak, especially in the central regions, and the molecular content is confined to the HII regions in the spiral arms. The HI profile also reflects a central deficiency in atomic gas: the atomic gas is abundant only in the inner spiral arms of the galaxy and the shapes and the motions observed in HI in the spiral arms quite clearly obey the predictions of the density-wave theory. This strong density wave is attributed to the tidal interaction with the other galaxies of the M 81 group. In addition, interacting galaxies exhibit higher CO luminosity than non-interacting galaxies, but M 81 is different also considering this aspect. Finally, M 81 is also a good candidate for studying the variation of the H_2 to CO conversion ratio in external galaxies. Performing IRAM 30 m observations of the CO molecule in the central region of M 81, we found that it is not only CO-poor, but that also has molecular clouds with non-typical properties for similar galaxies. In addition to the absent or very weak molecular gas emission, we found a low R_{21} (=0.68) line ratio and a particularly high X conversion factor, 15.6 times higher than the standard

X derived for our Galaxy and usually adopted for external galaxies. The low CO emission in the center suggests that the gas is subexcited, with even weaker FUV emission. We concluded that the lack of excitation of the gas, more than the absence of molecular gas, is the cause of the low CO emission in the center of M 81 (Casasola et al., 2007a).

In this Thesis we studied in detail the molecular gas content of another galaxy, the Seyfert 2 NGC 3147, an object of the NUGA survey (García-Burillo et al., 2003; Combes et al., 2004). NUGA was born with the idea to map the distribution and dynamics of the molecular gas with the IRAM Plateau de Bure Interferometer in the inner 1 kpc of the nuclei at high spatial resolution and to study the mechanisms for gas fueling of the different low-luminosity AGNs. Analyzing both interferometric and single-dish observations performed in the central region of NGC 3147, we detected a nuclear emission and two molecular rings or pseudo-rings at r$\sim$10 kpc and r$\sim$20 kpc respectively in the CO(1-0) map, and a nuclear emission and a single central ring at r$\sim$10 kpc in the CO(2-1) map. Comparing the two CO transitions we found a mean line ratio $I_{21}/I_{10} \sim 1$, consistent with the majority of the expected emission optically thick in the nuclei of spiral galaxies. Studying the kinematics we found that the detected rings are quite regular without evidence of non-circular motions. Since molecular clouds are the site of the future generation of stars, we compared the detected CO distribution with observations at wavelengths tracing the star formation, such as the far-ultraviolet and far-infrared emissions. We found that the molecular gas distribution has counterparts in the infrared emission (*Spitzer*) and in the ultraviolet one (*GALEX*). Then, identifying the presence of a bar in NGC 3147 (classified as non-barred galaxy in the optical) by a NIR image, we computed the gravity torques exerted from this stellar bar on the gas. We found that the gas in the main central CO pseudo-ring is subject to a dominant negative torque and loses angular momentum. This condition is expected for gas at ultra-harmonic resonance, just inside the corotation of the stellar bar. On the contrary, the gas outside the corotation, in spiral arms forming the external pseudoring, suffers positive torques and is driven outwards. We concluded that the gas inflow fueling the $\sim$100 pc scale circumnuclear region is active, and that this condition is favorable for the feeding of the low-luminosity Seyfert 2 observed in NGC 3147 (Casasola et al., 2007b).

In combination with these two specific studies on the molecular gas, in this Thesis we also analyzed the relations between different components (also the molecular one) of the ISM for a large sample of galaxies of all the morphologies, activity, and interaction. We found that the known relationship between the CO and the 100 μm fluxes for early-type galaxies is also valid for late-type systems, and that in spiral galaxies the X-ray flux appears linked to B and FIR emissions. On the contrary, the relation between L_X and L_{FIR} for early-type galaxies, both active and non-active, is lacking. We interpreted the observed lack of a direct relation between L_X and L_{FIR} for early-type galaxies like probably due to the different mechanisms producing FIR light in galaxies where the active star formation is no longer active (Galletta et al., 2007). In elliptical galaxies the infrared emission can be no strongly related to the ongoing star formation and to the reprocessing of the radiation in the dense regions where new stars are born. In this picture, the FIR emission comes most likely from circumstellar dusty shells around AGB stars and from an interstellar diffuse medium due to the outflow of dusty gas from AGB and RGB stars. However, it is important also to remember that in the literature it has been considered the opposite scenario, where the

FIR emission and the star formation are linked between them in early-type galaxies similarly to late-type systems (Combes et al., 2007).

6.2 The future: ALMA

Why a Thesis on the molecular gas in external galaxies?
We decided to analyze the small scale physics of the molecular gas in nearby galaxies because submillimeter/millimeter astronomy is entering a period of great discovery. These wavebands are unique in astronomy in containing more than 1000 radio spectral lines of interstellar and circumstellar molecules as well as the thermal continuum spectrum of cold dust in space. They are also the only bands in the electromagnetic spectrum in which we can detect cold dust and molecules far away in young, high-redshift galaxies in the early Universe, and nearby in low-temperature cocoons of protostars in our own Galaxy. They are the only bands that can give us the fine-scale kinematic details in young stellar disks that can potentially form planets, and in old ejected stellar envelopes that are forming dust grains and enriching the interstellar medium with carbon, oxygen and nitrogen. Millimeter bands lie at the crossroads between the radio and infrared/optical wavebands, containing both the synchrotron emission extending from the radio and the thermal emission extending from the optical/infrared. They contain the peak of the microwave background.

On the basis of these considerations it was born the idea of a new telescope for millimeter astronomy: the Atacama Large Millimeter Array - ALMA. Advanced projects of large interferometers were first simultaneously studied in early 1990 in the United States (MMA), Europe (LSA) and Japan (LMSA). It was then decided to merge them in a unique world-wide project with much improved capabilities, ALMA. The latter is currently a joint project between Europe (ESO), North America & Canada (NRAO) and Japan (NAOJ) with the participation of Chile. The ALMA interferometer will be installed in an exceptional site for submillimeter observations, at Chajnantor, Atacama, Chile, at 5010 m elevation. It will include up to 64×12m-dishes, providing a very good coverage in the *uv* interferometric plane (see Figs. 6.1 and 6.2). It will operate in four frequency bands, covering four of the main atmospheric windows between 0.4 mm and 4 mm, and will be equipped with very broad band heterodyne receivers and correlators. Compared to existing facilities, its sensitivity and angular resolution will be increased by almost two orders of magnitude. The construction of ALMA started in 2003 and will be completed in 2012; it will become incrementally operational from 2010 on. ALMA will operate at wavelengths of 0.3 to 9.6 millimeters, where the Earth's atmosphere above a high, dry site is largely transparent, and will provide astronomers unprecedented sensitivity and resolution. The array will have reconfigurable baselines ranging from 150 m to 18 km. Resolutions as fine as $0.005''$ will be achieved at the highest frequencies, a factor of ten better than HST.

ALMA will be a great step for astronomy, and will bring a revolution in millimeter astronomy. ALMA will play a role similar to HST in the optical by opening a completely new range of observational possibilities. There will be no equivalent until ALMA is operational, and it will cover all major topics in astronomy from comets to cosmology, from astrometry to exo-biology, with a special impact in understanding the origins of galaxies, stars, and planets.

This PhD Thesis had the aim to prepare ourselves on a very important

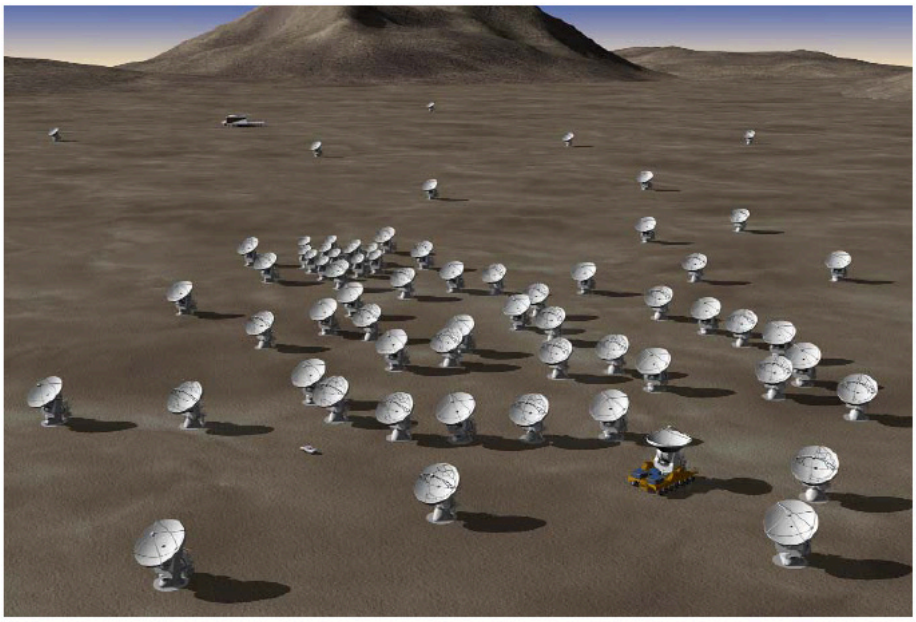

Figure 6.1: Artist's concept of ALMA in a compact configuration.

topic of the ALMA science: molecular gas in galaxies. ALMA will have both the high-resolution and the sensitivity required to map in detail the main dynamical components of spiral galaxies: spiral arms, bars, and also the nuclear embedded bars and resonant rings that will constrain theoretical scenarios of galaxy evolution. In nearby galaxies, the identification of gravitationally bound individual molecular clouds will give insight into the H_2/CO conversion ratio (see M 81 galaxy studied in this Thesis) through virial analysis of all environments (starbursting or quiescent galaxies, with various metallicities). This is of prime importance, since at the present day there are still large uncertainties (order of magnitude) concerning the true molecular content of the galaxies. The ALMA maps will give the information on both parsec and kiloparsec scales needed to explore the relationship between star formation, gas density and gas kinematics, in comparison with other tracers, like the atomic gas, H_α, or radio-continuum. The role of density waves and spiral structure will be addressed in detail. The small scale structure of the molecular component revealed by these high-resolution maps will clarify the mechanisms of starbursts in galaxies, and the associated feedback processes, such as outflows of molecular gas, bubbles and winds. Then, the higher excited CO lines (e.g. CO(6-5)) will be useful to quantify the starbursts that occur sometimes in elliptical galaxies, as the result of external accretion. High spatial resolution is necessary to distinguish the extent of the molecular component, and the origin of the excitation. The radio-galaxies, mostly ellipticals, are suspected to have a dense molecular torus surrounding the AGN, and this particular component could be traced by high-dipole molecules such as HCN or CS.

Another specific topic of ALMA will be the study of the gas in galactic nuclei. The centers of galaxies are often invisible or at least partially obscured at optical wavelengths because of the presence of large amounts

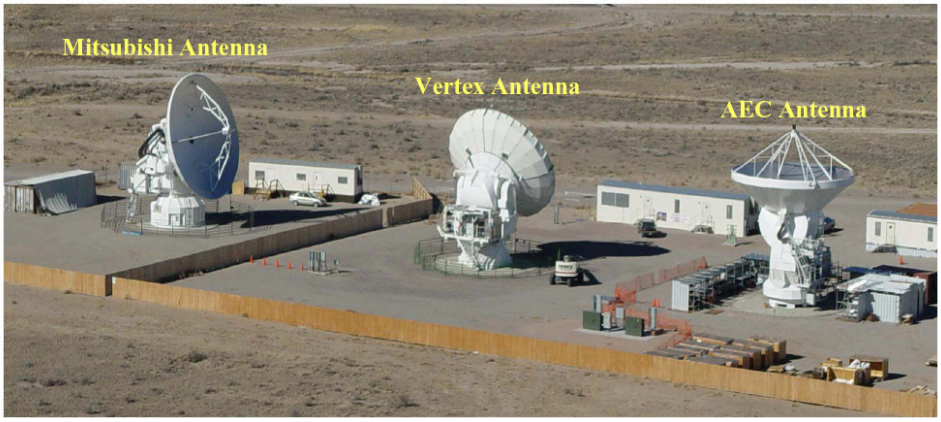

Figure 6.2: ALMA prototype antennas at the Antenna Test Facility (ATF) in New Mexico: the Japanese antenna (*left*), Vertex antenna from North America and Canada (*center*), and the European antenna (*right*).

of dust. With its high spatial resolution, sensitivity and wide frequency coverage, ALMA will offer a unique tool to study both the dust and the gas, which is predominantly molecular in the nuclei of galaxies including the center of our own Galaxy. It will be possible to map at an unmatched level of detail the structure of the nuclei, trace the kinematics of the molecular gas and probe the physical and chemical conditions pertaining deep in the central regions of galaxies from starbursts to AGNs (see NGC 3147 galaxy from NUGA survey studied in this Thesis). Such detailed studies, which will be done for a large number of sources, will address one of the most fundamental problems of the modern astronomy, the nature and evolution of the nuclei of galaxies.

ALMA will also be a privileged instrument to tackle high redshift galaxies, due to the negative K-correction[1] in the millimeter domain (Combes et al., 1999; Combes, 2005). Many dusty star-forming galaxies, invisible in the optical or NIR, will be detected easily through the peak of their emission in the FIR redshifted in the submm between $z = 10$ and $z = 5$. Their mass and dynamics will be determined through the CO lines, together with the efficiency of star formation. Normal intervening galaxies at all z will be studied through absorption lines in front of quasars, exploring the dense tail of the column density spectrum.

6.2.1 Synergy between ALMA and Herschel

The importance of ALMA is also revealed in the synergies with other instruments, such as the Herschel Space Observatory. This and other instruments are considered complementary to ALMA because they have common

[1]The term of K-correction may appear confusing; it has been used for the first time by Wirtz in 1918, for "Kosmologie" to determine the distance-redshift law; Hubble (1929) called also K (after Wirtz's law) his now famous constant, and Oke & Sandage (1968) quantified what they called the K-correction, the combined effect of the changing λ domain (if the spectrum of the object is not flat), and the reduced λ-interval observed at high redshift, given a photometry band.

Figure 6.3: Image of the Herschel Space Observatory.

scientific projects, such as the stars and planets formation, the spectral line surveys (nearby spirals, dwarf galaxies, low surface brightness galaxies-LSBGs, and local AGNs), and the primordial Universe (Cosmic Microwave Background-CMB and Dark Energy).

Herschel (Fig. 6.3), that it will be the largest ever infrared space (programme launch: End 2008), will observe at wavelengths that have never previously been explored (60-670 μm). Why observe in the infrared range? Large parts of the Universe are too cold to radiate in the visible wavelength range or at shorter wavelengths. The study of these cooler objects is only possible by observing in the infrared spectrum or at even longer (submillimetre) wavelengths. Bodies with temperatures between five and fifty Kelvin have radiative emission peaks in the wavelength range observed by Herschel, and gas with temperatures between ten and a few hundred Kelvin exhibit their brightest molecular and atomic emission lines at these wavelengths. Additionally, many objects of great interest for the astronomers are concealed within or behind clouds of gas and dust. In the early stages of their formation, stars and planets are surrounded by the gas and dust clouds from which they are being created. Galactic cores and most of the remnants of the early Universe are also hidden from view by dust clouds. The dust particles in these clouds are comparable in size to the wavelength of visible light and are therefore efficient at scattering or absorbing radiation at these wavelengths. Infrared radiation is less affected by these clouds, the longer the wavelength, the thicker the dust cloud that it can penetrate.

Chapter 7

Candidate's list of papers

- **Casasola, V.**, Bettoni, D., & Galletta, G. 2004, VizieR Online Data Catalog, 342, 20941
- **Casasola, V.**, Bettoni, D., & Galletta, G. 2004, A&A, 422, 941
- **Casasola, V.**, Piovan, L., Galletta, G., Bettoni, D., & Merlin, E. 2006, Proceedings of the Conference "From Stars to Galaxies: Building the Pieces to Build Up the Universe", Vallenari et al. eds., ASP Conf. Series, arXiv:astro-ph/0612131
- Galletta, G., **Casasola, V.**, Piovan, L., Merlin, E., & Bettoni, D. 2007, A&A, 462, 495
- **Casasola, V.**, Combes, F., Bettoni, D., Pohlen, M., Galletta, G., & Tenaglia, F. 2007, Astrophysics and Space Science (Apss), special issue of "Science with ALMA: a new era for Astrophysics" Conference, ed. Dr. Bachiller, arXiv:astro-ph/0702018
- **Casasola, V.**, Combes, F., Galletta, G., & Bettoni, D. 2007, Proceedings of the Conference "Pathways through an eclectic Universe", J. H. Knapen, T. J. Mahoney, and A. Vazdekis (Eds.), ASP Conf. Ser., 2007, arXiv:0706.3769
- **Casasola, V.**, Combes, F., Bettoni, D., & Galletta, G. 2007, A&A, 473, 771
- **Casasola, V.**, Combes, F, García-Burillo, S., Hunt, L. K., Léon, S., Baker, A. J. 2007, Proceedings of the Conference "Formation and Evolution of galaxy disks", J. G. Funes, and E. M. Corsini eds., ASP Conf. Series, arXiv:astro-ph/0712.0294
- **Casasola, V.**, Combes, F, García-Burillo, S., Hunt, L., Léon, S., Baker, A. J. 2008, A&A submitted

Bibliography

Allen, R. J., & Lequeux, J. 1993, ApJL, 410, L15

Allen, R. J., Knapen, J. H., Bohlin, R., & Stecher, T. P. 1997, ApJ, 487, 171

Allen, R. J., Heaton, H. I., & Kaufman, M. J. 2004, ApJ, 608, 314

Arimoto, N., Sofue, Y., & Tsujimoto, T. 1996, PASJ, 48, 275

Arp, H. 1966, Atlas of peculiar galaxies, Pasadena: California Inst. Technology, 1966

Arp, H. C., & Madore, B., A catalogue of southern peculiar galaxies and associations, New York : Cambridge University Press, 1987

Bally, J., Stark, A. A., Wilson, R. W., & Langer, W. D. 1987, ApJL, 312, L45

Barvainis, R., Antonucci, R., & Coleman, P. 1992, ApJL, 399, L19

Barvainis, R., Tacconi, L., Antonucci, R., Alloin, D., & Coleman, P. 1994, Nature, 371, 586

Beck, R., Krause, M., & Klein, U. 1985, A&A, 152, 237

Beck, R. 2000, Astronomy, physics and chemistry of H_3^+, 358, 777

Beck, R. 2001, Space Science Reviews, 99, 243

Beck, R., & Krause, M. 2005, Astronomische Nachrichten, 326, 414

Beelen, A., et al. 2004, A&A, 423, 441

Benson, P. J., & Myers, P. C. 1989, ApJS, 71, 89

Bertoldi, F., & McKee, C. F. 1992, ApJ, 395, 140

Bettoni, D., Galletta, G., García-Burillo, S., & Rodríguez-Franco, A. 2001, A&A, 374, 421

Bettoni, D., Galletta, G., & García-Burillo, S. 2003, A&A, 405, 5

Beuing, J., Dobereiner, S., Bohringer, H., & Bender, R. 1999, MNRAS, 302, 209

Bianchi, S., Corral, A., Panessa, F., Barcons, X., Matt, G., Bassani, L., Carrera, F. J., & Jimenez-Bailon, E. 2007, ArXiv e-prints, 710, arXiv:0710.4226

Bietenholz, M. F., et al. 1996, ApJ, 457, 604

Binney, J., & Merrifield, M. 1998, Galactic astronomy / James Binney and Michael Merrifield. Princeton, NJ : Princeton University Press, 1998. (Princeton series in astrophysics) QB857 .B522 1998 ($35.00)

Biskamp, D. 2003, Magnetohydrodynamic Turbulence, by Dieter Biskamp, pp. 310. ISBN 0521810116. Cambridge, UK: Cambridge University Press, September 2003.

Blitz, L., & Shu, F. H. 1980, ApJ, 238, 148

Blitz, L., Magnani, L., & Mundy, L. 1984, ApJL, 282, L9

Blitz, L., & Stark, A. A. 1986, ApJL, 300, L89

Blitz, L. 1990, The Evolution of the Interstellar Medium, 12, 273

Blitz, L. 1993, Back to the Galaxy, 278, 98

Blitz, L., & Rosolowsky, E. 2006, ApJ 650, 933

Bonnell, I. A., Bate, M. R., Clarke, C. J., & Pringle, J. E. 1997, MNRAS, 285, 201

Boselli, A., Lequeux, J., & Gavazzi, G. 2002, A&A, 384, 33

Boselli, A., Lequeux, J., & Gavazzi, G. 2002, Ap&SS, 281, 127

Bot, C., Boulanger, F., Rubio, M., & Rantakyro, F. 2007, A&A, 471, 103

Bregman, J. N., Hogg, D. E., & Roberts, M. S. 1992, ApJ, 387, 484

Braine, J., & Combes, F. 1992, A&A, 264, 433

Braine, J., & Combes, F. 1993, A&A, 269, 7

Braine, J., Lisenfeld, U., Duc, P.-A., & Leon, S. 2000, Nature, 403, 867

Brouillet, N., Baudry, A., & Combes, F. 1988, A&A, 196, L17

Brouillet, N., Baudry, A., Combes, F., Kaufman, M., & Bash, F. 1991, A&A, 242, 35

Brouillet, N., Kaufman, M., Combes, F., Baudry, A., & Bash, F. 1998, A&A, 333, 92

Brown, R. L., & Vanden Bout, P. A. 1991, AJ, 102, 1956

Brown, R. L., & Vanden Bout, P. A. 1992, ApJL, 397, L19

Boulares, A., & Cox, D. P. 1990, ApJ, 365, 544

Burbidge, G. R. 1956, ApJ, 124, 416

Burstein, D., Jones, C., Forman, W., Marston, A. P., & Marzke, R. O. 1997, ApJS, 111, 163

Calzetti, D., Kinney, A. L., & Storchi-Bergmann, T. 1994, ApJ, 429, 582

Calzetti, D. 2001, PASP, 113, 1449

Calzetti, D., et al. 2005, ApJ, 633, 871

Carilli, C. L., et al. 2001, ApJ, 555, 625

Carlstrom, J. E., & Kronberg, P. P. 1991, ApJ, 366, 422

Carpenter, J. M., Snell, R. L., & Schloerb, F. P. 1995, ApJ, 445, 246

Casasola, V., Bettoni, D., & Galletta, G. 2004, A&A, 422, 941

Casasola, V., Combes, F., Bettoni, D., & Galletta, G. 2007, A&A, 473, 771

Casasola, V., Combes, F., García-Burillo, S., Hunt, L. K., Léon, S., & and Baker, A., A&A submitted

Casoli, F., Clausset, F., Combes, F., Viallefond, F., & Boulanger, F. 1990, A&A, 233, 357

Casoli, F., Dickey, J., Kazes, I., Boselli, A., Gavazzi, G., & Jore, K. 1996, A&APS, 116, 193

Casoli, F., et al. 1998, A&A, 331, 451

Chabrier, G. 2003, PASP, 115, 763

Charlot, S., & Fall, S. M. 2000, ApJ, 539, 718

Charmandaris, V., Combes, F., & van der Hulst, J. M. 2000, A&A, 356, L1

Chi, X., & Wolfendale, A. W. 1993, Nature, 362, 610

Chi, S., & Park, Y.-S. 2006, Journal of Korean Astronomical Society, 39, 9

Chini, R., Kreysa, E., Kruegel, E., & Mezger, P. G. 1986, A&A, 166, L8

Ciotti, L., Pellegrini, S., Renzini, A., & D'Ercole, A. 1991, ApJ, 376, 380

Clemens, D. P., & Barvainis, R. 1988, ApJS, 68, 257

Cohen, R. S., Cong, H., Dame, T. M., & Thaddeus, P. 1980, ApJL, 239, L53

Combes, F., Encrenaz, P. J., Lucas, R., & Weliachew, L. 1977, A&A, 55, 311

Combes, F., & Sanders, R. H. 1981, A&A, 96, 164

Combes, F., Prugniel, P., Rampazzo, R., & Sulentic, J. W. 1994, A&A, 281, 725

Combes, F., & Becquaert, J.-F. 1997, A&A, 326, 554

Combes, F., Maoli, R., & Omont, A. 1999, A&A, 345, 369

Combes, F. 2001, Advanced Lectures on the Starburst-AGN, 223

Combes, F., et al. 2004, A&A, 414, 857

Combes, F. 2005, SF2A-2005: Semaine de l'Astrophysique Française, 697

Combes, F., Young, L. M., & Bureau, M. 2007, MNRAS, 377, 1795

Condon, J. J., & Yin, Q. F. 1990, ApJ, 357, 97

Condon, J. J. 1992, ARA&A, 30, 575

Cox, P., Deharveng, L., & Leene, A. 1990, A&A, 230, 181

Cram, L., Hopkins, A., Mobasher, B., & Rowan-Robinson, M. 1998, ApJ, 507, 155

Crutcher, R. M., Mouschovias, T. C., Troland, T. H., & Ciolek, G. E. 1994, ApJ, 427, 839

Crutcher, R. M. 1999, ApJ, 520, 706

Dame, T. M., Elmegreen, B. G., Cohen, R. S., & Thaddeus, P. 1986, ApJ, 305, 892

David, L. P., Jones, C., & Forman, W. 1992, ApJ, 388, 82

Devereux, N. A., & Young, J. S. 1991, ApJ, 371, 515

Dickman, R. L., Snell, R. L., & Schloerb, F. P. 1986, ApJ, 309, 326

Digel, S. W., Lyder, D. A., Philbrick, A. J., Puche, D., & Thaddeus, P. 1996, ApJ, 458, 561

Downes, D., Radford, S. J. E., & Solomon, P. M. 1991, Dynamics of Galaxies and Their Molecular Cloud Distributions, 146, 295

Draine, B. T. 1978, ApJS, 36, 595

Duc, P.-A., & Mirabel, I. F. 1998, A&A, 333, 813

Eckart, A., Downes, D., Genzel, R., Harris, A. I., Jaffe, D. T., & Wild, W. 1990, ApJ, 348, 434

Elmegreen, B. G., & Lada, C. J. 1977, ApJ, 214, 725

Elmegreen, B. G. 1985, Protostars and Planets II, 33

Elmegreen, B. G. 1993, ApJ, 411, 170

Fabbiano, G. 1989, ARA&A, 27, 87

Fabbiano, G., Kim, D.-W., & Trinchieri, G. 1992, ApJS, 80, 531

Ferrarese, L., & Merritt, D. 2000, ApJL, 539, L9

Frei, Z., Guhathakurta, P., Gunn, J. E., & Tyson, J. A. 1996, AJ, 111, 174

Galletta, G., Casasola, V., Piovan, L., Merlin, E., & Bettoni, D. 2007, A&A, 462, 495

Gao, Y., & Solomon, P. M. 2004a, Apj, 606, 271

Gao, & Solomon, 2004b, ApJS, 152, 63G

García-Burillo, S., Guélin, M., & Cernicharo, J. 1993, A&A, 274, 123

García-Burillo, S., Sempere, M. J., Combes, F., Hunt, L. K., & Neri, R. 2000, A&A, 363, 869

García-Burillo, S., et al. 2003, A&A, 407, 485

García-Burillo, S., Combes, F., Schinnerer, E., Boone, F., & Hunt, L. K. 2005, A&A, 441, 1011

Gebhardt, K., et al. 2000, ApJL, 539, L13

Graciá-Carpio, J., García-Burillo, S., Planesas, P., & Colina, L. 2006, ApJL, 640, L135

Graham, J. A. 1998, ApJ, 502, 245

Graham, J. A. 1999, Bulletin of the American Astronomical Society, 31, 950

Greve, T. R., et al. 2005, MNRAS, 359, 1165

Griffiths, R. E., & Padovani, P. 1990, ApJ, 360, 483

Gioia, I. M., Gregorini, L., & Klein, U. 1982, A&A, 116, 164

Gordon, K. D., Calzetti, D., & Witt, A. N. 1997, ApJ, 487, 625

Gordon, K. D., et al. 2004, ApJS, 154, 215

Guilloteau, S., & Lucas, R. 2000, in Imaging at Radio through Submillimeter Wavelengths, ed. J. G. Mangum, S. J. Radford (San Francisco: ASP), 299

Heckman, T. M., Smith, E. P., Baum, S. A., et al.: 1986, ApJ, 311, 526

Heckman, T. M., Blitz, L., Wilson, A. S., Armus, L., & Miley, G. K. 1989, ApJ, 342, 735

Heiles, C. 1996, ApJ, 462, 316

Helfer, T. T., Thornley, M. D., Regan, M. W., Wong, T., Sheth, K., Vogel, S. N., Blitz, L., & Bock, D. C.-J. 2003, ApJS, 145, 259

Henkel, C., Chin, Y.-N., Mauersberger, R., & Whiteoak, J. B. 1998, A&A, 329, 443

Heyer, M. H., Carpenter, J. M., & Ladd, E. F. 1996, ApJ, 463, 630

Heyer, M. H., & Terebey, S. 1998, ApJ, 502, 265

Hildebrand, R. H. 1983, QJRAS, 24, 267

Ho, L. C., Filippenko, A. V., & Sargent, W. L. W. 1996, ApJ, 462, 183

Ho, L. C., Filippenko, A. V., & Sargent, W. L. W. 1997, ApJS, 112, 315

Horellou, C., & Booth, R. 1997, A&AS, 126, 3

Hunt L., Combes F., García-Burillo S. et al., A&A, submitted

Impey, C., & Gregorini, L. 1993, AJ, 105, 853

Iono, D., et al. 2006, PASJ 58, 957

Iono, D., et al. 2007, ApJ, 659, 283

Israel, F. P., & Baas, F. 1999, A&A, 351, 10

Kamphuis, J., & Briggs, F. 1992, A&A, 253, 335

Kaufman, M., Bash, F. N., Hine, B., Rots, A. H., Elmegreen, D. M., & Hodge, P. W. 1989, ApJ, 345, 674

Kaufman, M. J., Wolfire, M. G., Hollenbach, D. J., & Luhman, M. L. 1999, ApJ, 527, 795

Kenney, J. D. P., Wilson, C. D., Scoville, N. Z., Devereux, N. A., & Young, J. S. 1992, ApJL, 395, L79

Kennicutt, R. C., Jr. 1998a, The Stellar Initial Mass Function (38th Herstmonceux Conference), 142, 1

Kennicutt, R. C., Jr., et al. 1998b, ApJ, 498, 181

Kennicutt, R. C., Jr. 1998c, ApJ, 498, 541

Kim, D.-W., & Fabbiano, G. 2004, ApJ, 611, 846

Klein, U., Wielebinski, R., & Morsi, H. W. 1988, A&A, 190, 41

Knapen, J. H., Allen, R. J., Heaton, H. I., Kuno, N., & Nakai, N. 2006, A&A, 455, 897

Knapp, G. R., Turner, E. L., & Cunniffe, P. E. 1985, AJ, 90, 454

Knapp, G. R., Guhathakurta, P., Kim, D.-W., & Jura, M. A. 1989, ApJS, 70, 329

Kneib, J.-P., Neri, R., Smail, I., Blain, A., Sheth, K., van der Werf, P., & Knudsen, K. K. 2005, A&A, 434, 819

Knudsen, K. K., Walter, F., Weiss, A., Bolatto, A., Riechers, D. A., & Menten, K. 2007, ApJ, 666, 156

Kohno, K., Kawabe, R., & Vila-Vilaró, B. 1999, ApJ, 511, 157

Kohno, K., Ishizuki, S., Matsushita, S., Vila-Vilaro, B., Kawabe, R.: 2003, PASJ, 55, L1

Kong, X., et al. 2000, AJ, 119, 2745

Kong, X., Charlot, S., Brinchmann, J., & Fall, S. M. 2004, MNRAS, 349, 769

Kramer, C., Stutzki, J., Rohrig, R., & Corneliussen, U. 1998, A&A, 329, 249

Krips, M., Eckart, A., Neri, R., Schödel, R., Leon, S., Downes, D., García-Burillo, S., & Combes, F. 2006, A&A, 446, 113

Krips, M., Eckart A., Krichbaum T.P. et al. 2007, A&A, 464, 553

Krips, M., Neri R., García-Burillo, S.,: 2007b, A&A 468, L63

Kroupa, P., Tout, C. A., & Gilmore, G. 1993, MNRAS, 262, 545

Lada, C. J. 1991, NATO ASIC Proc. 342: The Physics of Star Formation and Early Stellar Evolution, 329

Lada, E. A. 1992, ApJL, 393, L25

Lada, C. J., Lada, E. A., Clemens, D. P., & Bally, J. 1994, ApJ, 429, 694

Laird, E. S., Nandra, K., Adelberger, K. L., Steidel, C. C., & Reddy, N. A. 2005, MNRAS, 359, 47

Larson, R. B. 1981, MNRAS, 194, 809

Leisawitz, D., & Hauser, M. G. 1988, ApJ, 332, 954

Lisenfeld, U., & Völk, H. J. 2000, A&A, 354, 423

Lees, J. F., Knapp, G. R., Rupen, M. P., & Phillips, T. G. 1991, ApJ, 379, 177

Leger, A., & Puget, J. L. 1984, A&A, 137, L5

Lindt-Krieg, E., Eckart, A., Neri, R., Krips, M., Pott, J. -., Garcia-Burillo, S., & Combes, F. 2008, arXiv:0712.3133, A&A accepted

Loinard, L., Dame, T. M., Koper, E., Lequeux, J., Thaddeus, P., & Young, J. S. 1996, ApJL, 469, L101

Loiseau, N., Nakai, N., Sofue, Y., Wielebinski, R., Reuter, H.-P., & Klein, U. 1990, A&A, 228, 331

McElroy, D. B. 1995, ApJS, 100, 105

Merlin, E., & Chiosi, C. 2006, A&A, 457, 437

McMahon, R. G., Omont, A., Bergeron, J., Kreysa, E., & Haslam, C. G. T. 1994, MNRAS, 267, L9

Maddalena, R. J., & Thaddeus, P. 1985, ApJ, 294, 231

Magnani, L., Caillault, J.-P., Buchalter, A., & Beichman, C. A. 1995, ApJS, 96, 159

Maloney, P., & Black, J. H. 1988, ApJ, 325, 389

Mauersberger, R., Henkel, C., Weiß, A., Peck, A. B., & Hagiwara, Y. 2003, A&A, 403, 561

McKee, C. F. 1989, ApJ, 345, 782

McLaughlin, D. E., & Pudritz, R. E. 1996, ApJ, 469, 194

McKee, C. F., & Zweibel, E. G. 1992, ApJ, 399, 551

McKee, C. F., Zweibel, E. G., Goodman, A. A., & Heiles, C. 1993, Protostars and Planets III, 327

Möllenhoff, C., & Heidt, J. 2001, A&A, 368, 16

Morganti, R., et al. 2006, MNRAS, 371, 157

Moriarty-Schieven, G. H., Andersson, B.-G., & Wannier, P. G. 1997, ApJ, 475, 642

Motte, F., Andre, P., & Neri, R. 1998, A&A, 336, 150

Myers, P. C., & Benson, P. J. 1983, ApJ, 266, 309

Nagar, N. M., Falcke, H., Wilson, A. S., & Ulvestad, J. S. 2002, A&A, 392, 53

Nakanishi, K., Okumura, S. K., Kohno, K., Kawabe, R., & Nakagawa, T. 2005, PASJ, 57, 575

Nakai, N., & Kuno, N. 1995, PASJ, 47, 761

Neri, R., et al. 2003, ApJL, 597, L113

Oke, J. B., & Sandage, A. 1968, Apj, 154, 21

Omont, A., McMahon, R. G., Cox, P., Kreysa, E., Bergeron, J., Pajot, F., & Storrie-Lombardi, L. J. 1996, A&A, 315, 1

Omont, A., Cox, P., Bertoldi, F., McMahon, R. G., Carilli, C., & Isaak, K. G. 2001, A&A, 374, 371

Omont, A., Beelen, A., Bertoldi, F., Cox, P., Carilli, C. L., Priddey, R. S., McMahon, R. G., & Isaak, K. G. 2003, A&A, 398, 857

Pahre, M. A., Ashby, M. L. N., Fazio, G. G., & Willner, S. P. 2004, ApJS, 154, 235

Papadopoulos, P. P. 2007, ApJ, 656, 792

Pasquali, A., Gallagher, J. S., & de Grijs, R. 2004, A&A, 415, 103

Patel, N. A., Goldsmith, P. F., Snell, R. L., Hezel, T., & Xie, T. 1995, ApJ, 447, 721

Paturel, G., et al. 1997, A&AS, 124, 109

Peletier, R. F., et al. 2001, New Astronomy Review, 45, 83

Pellegrini, S., Cappi, M., Bassani, L., Malaguti, G., Palumbo, G. G. C., & Persic, M. 2000, A&A, 353, 447

Petitpas, G. R., & Wilson, C. D. 1998, ApJ, 503, 219

Phillips, T. G., Wannier, P. G., Scoville, N. Z., & Huggins, P. J. 1979, ApJ, 231, 720

Phillips, M. M., Jenkins, C. R., Dopita, M. A., Sadler, E. M., & Binette, L. 1986, AJ, 91, 1062

Piovan, L., Tantalo, R., & Chiosi, C. 2006, MNRAS, 370, 1454

Popescu, C. C., Misiriotis, A., Kylafis, N. D., Tuffs, R. J., & Fischera, J. 2000, A&A, 362, 138

Popescu, C. C., Tuffs, R. J., Völk, H. J., Pierini, D., & Madore, B. F. 2002, ApJ, 567, 221

Quinn, P. J. 1984, ApJ, 279, 596

Ranalli, P., Comastri, A., & Setti, G. 2003, A&A, 399, 39

Rand, R. J., & Kulkarni, S. R. 1990, ApJL, 349, L43

Rand, R. J. 1993, ApJ, 410, 68

Rand, R. J. 1995, AJ, 109, 2444

Regan, M. W., Thornley, M. D., Helfer, T. T., Sheth, K., Wong, T., Vogel, S. N., Blitz, L., & Bock, D. C.-J. 2001, ApJ, 561, 218

Regan, M. W., Teuben P., ApJ, 582, 723

Regan, M. W., Thornley, M. D., Vogel S.N., et al., 2006, ApJ, 652, 1112

Reuter, H.-P., Krause, M., Wielebinski, R., & Lesch, H. 1991, A&A, 248, 12

Rieke, G. H., Lebofsky, M. J., Thompson, R. I., Low, F. J., & Tokunaga, A. T. 1980, ApJ, 238, 24

Rigaut, F., Salmon, D., Arsenault, R. et al. 1998, PASP, 110, 152

Roberts, M. S., Hogg, D. E., Bregman, J. N., Forman, W. R., & Jones, C. 1991, ApJS, 75, 751

Roberts, T. P., & Warwick, R. S. 2000, MNRAS, 315, 98

Rohlfs, K., & Wilson, T. L. 1996, Tools of Radio Astronomy, XVI, 423 pp. 127 figs., 20 tabs.. Springer-Verlag Berlin Heidelberg New York. Also Astronomy and Astrophysics Library

Romano, D., Chiappini, C., Matteucci, F., & Tosi, M. 2005, A&A, 430, 491

Rosolowsky, E., & Blitz, L. 2005, ApJ, 623, 826

Rosolowsky, E., & Leroy, A. 2006, PASP, 118, 590

Rubio, M., Lequeux, J., & Boulanger, F. 1993, A&A, 271, 9

Sadler, E. M. 1987, Structure and Dynamics of Elliptical Galaxies, 127, 125

Sage, L. J., & Westpfahl, D. J. 1991, A&A, 242, 371

Sakamoto, K., Okumura, S. K., Ishizuki, S., & Scoville, N. Z. 1999, ApJS, 124, 403

Sakamoto, K., Baker A.J., Scoville N.Z., 2000, ApJ, 533, 149

Sakamoto, K., Fukuda, H., Wada, K., & Habe, A. 2001, AJ, 122, 1319

Salpeter, E. E. 1955, ApJ, 121, 161

Sanders, D. B., Solomon, P. M., & Scoville, N. Z. 1984, ApJ, 276, 182

Sanders, D. B., Scoville, N. Z., & Solomon, P. M. 1985, ApJ, 289, 373

Sanders, D. B., & Mirabel, I. F. 1985, ApJL, 298, L31

Sanders, D. B., Scoville, N. Z., Young, J. S., Soifer, B. T., Schloerb, F. P., Rice, W. L., & Danielson, G. E. 1986, ApJL, 305, L45

Scalo, J. M. 1986, Fundamentals of Cosmic Physics, 11, 1

Scalo, J. 1990, Physical Processes in Fragmentation and Star Formation, 162, 151

Scalo, J. 1998, The Stellar Initial Mass Function (38th Herstmonceux Conference), 142, 201

Schinnerer, E., Eckart, A., Tacconi, L. J., Genzel, R., & Downes, D. 2000, ApJ, 533, 850

Schmidt, M. 1959, ApJ, 129, 243

Schiminovich, D., van Gorkom, J. H., van der Hulst, J. M., & Kasow, S. 1994, ApJL, 423, L101

Schneider, N., Stutzki, J., Winnewisser, G., & Blitz, L. 1996, ApJL, 468, L119

Schuster, K.-F., et al. 2004, A&A, 423, 1171

Schweizer, F., & Seitzer, P. 1992, AJ, 104, 1039

Shu, F. H., Milione, V., & Roberts, W. W., Jr. 1973, ApJ, 183, 819

Shu, F. H., Lizano, S., & Adams, F. C. 1987, Star Forming Regions, 115, 417

Smith, D. A., Allen, R. J., Bohlin, R. C., Nicholson, N., & Stecher, T. P. 2000, ApJ, 538, 608

Sheth, K., Vogel, S. N., Regan, M. W., Teuben, P. J., Harris, A. I., & Thornley, M. D. 2002, AJ, 124, 2581

Sheth, K., Vogel, S. N., Wilson, C. D., & Dame, T.M., AJ accepted, arXiv:astro-ph/07104559

Solomon, P. M., & de Zafra, R. 1975, ApJL, 199, L79

Solomon, P. M., Rivolo, A. R., Barrett, J., & Yahil, A. 1987, ApJ, 319, 730

Solomon, P. M., & Sage, L. J. 1988, ApJ, 334, 613

Solomon, P. M., & Rivolo, A. R. 1989, ApJ, 339, 919

Solomon, P. M., & Barrett, J. W. 1991, Dynamics of Galaxies and Their Molecular Cloud Distributions, 146, 235

Solomon, P. M., Radford, S. J. E., & Downes, D. 1992, Nature, 356, 318

Solomon, P. M., & Vanden Bout, P. A. 2005, ARA&A, 43, 677

Spitzer, L. 1978, New York Wiley-Interscience, 1978, 333,

Strong, A. W., et al. 1988, A&A, 207, 1

Strong, A. W., Moskalenko, I. V., & Reimer, O. 2000, ApJ, 537, 763

Stutzki, J., & Guesten, R. 1990, ApJ, 356, 513

Sullivan, M., Mobasher, B., Chan, B., Cram, L., Ellis, R., Treyer, M., & Hopkins, A. 2001, ApJ, 558, 72

Tacconi, L. J., et al. 2006, ApJ, 640, 228

Taylor, C. L., Kobulnicky, H. A., & Skillman, E. D. 1998, AJ, 116, 2746

Taylor, C. L., & Wilson, C. D. 1998, ApJ, 494, 581

Telesco, C. M., & Harper, D. A. 1980, ApJ, 235, 392

Tenjes, P. 1994, Baltic Astronomy, 3, 180

Terashima, Y., & Wilson, A. S. 2003, ApJ, 583, 145

Testi, L., & Sargent, A. I. 1998, ApJL, 508, L91

Thornley, M., et al. 1999, Ap&SS, 269, 391

Thronson, H. A., Jr., & Telesco, C. M. 1986, ApJ, 311, 98

Tinsley, B. M. 1980, Fundamentals of Cosmic Physics, 5, 287

Tuffs, R. J., & Popescu, C. C. 2003, Exploiting the ISO Data Archive. Infrared Astronomy in the Internet Age, 511, 239

Ulvestad, J. S., & Ho, L. C. 2001, ApJL, 562, L133

van Dishoeck, E. F., & Black, J. H. 1988, ApJ, 334, 771

van Gorkom, J., & Schiminovich, D. 1997, The Nature of Elliptical Galaxies; 2nd Stromlo Symposium, 116, 310

Véron-Cetty, M.-P., & Véron, P. 2003, A&A, 412, 399

Viallefond, F., et al., 2008, in preparation

Vila-Vilaró, B., Taniguchi, Y., & Nakai, N. 1998, AJ, 116, 1553

Visser, H. C. D. 1980, A&A, 88, 159

Vogel, S. N., Kulkarni, S. R., & Scoville, N. Z. 1988, Nature, 334, 402

Vorontsov-Velyaminov, B. A. 1959, Atlas and catalog of interacting galaxies (1959)

Weil, M. L., & Hernquist, L. 1993, ApJ, 405, 142

Wiklind, T., Combes, F., & Henkel, C. 1995, A&A, 297, 643

Wild, W. 1999, The 30 m Manual-IRAM, Granada

Williams, J. P., de Geus, E. J., & Blitz, L. 1994, ApJ, 428, 693

Williams, J. P., Blitz, L., & Stark, A. A. 1995, ApJ, 451, 252

Williams, J. P., & Maddalena, R. J. 1996, ApJ, 464, 247

Williams, J. P., & Blitz, L. 1998, ApJ, 494, 657

Wilson, C. D., & Scoville, N. 1990, ApJ, 363, 435

Wilson, C. D., & Scoville, N. 1992, ApJ, 385, 512

Wilson, C. D. 1995, ApJL, 448, L97

Williams, J. P., Blitz, L., & McKee, C. F. 2000, Protostars and Planets IV, 97

Willott, C. J., Martínez-Sansigre, A., & Rawlings, S. 2007, AJ, 133, 564

Wood, D. O. S., Myers, P. C., & Daugherty, D. A. 1994, ApJS, 95, 457

Young, J. S., & Scoville, N. 1982, ApJL, 260, L41

Young, J. S., & Scoville, N. Z. 1984, ApJ, 287, 153

Young, J. S., & Knezek, P. M. 1989, ApJL, 347, L55

Young, J. S., & Scoville, N. Z. 1991, ARA&A, 29, 581

Young, J. S., et al. 1995, ApJS, 98, 219

Zaritsky, D., Harris, J., Thompson, I. B., & Grebel, E. K. 2004, AJ, 128, 1606

Acknowledgements

The work presented in this Thesis has been carried out thanks to the logistic and financial support of:

- Padova University, Astronomy Department;
- Paris Observatory-LERMA;
- Pierre et Marie Curie University, Paris 6;
- Italian-France University;
- Grant Vinci for my stay in Paris, February-July 2006;
- European Association For Research In Astronomy (EARA) agreement for my stay in Paris, January-July 2007;
- RadioNet Networking Activities-Travel Funds.

This Thesis was developed at the Padova Astronomy Department and Paris Observatoy-LERMA. I wish to thank all the people whom I collaborated with during these three years of PhD studies. Special thanks go to:

- my supervisors, Prof. Giuseppe Galletta and Prof. Françoise Combes. Giuseppe encouraged me to have my French experience, giving me the change to know and work together with Françoise, astronomer of international renown. Thanks to Françoise I worked at a very high scientific level and in a stimulating environment. My gratefulness towards Françoise is enormous;
- Prof. Loretta Gregorini, the referee of this Thesis, for her very helpful suggestions and for reading the whole Thesis;
- Prof. Eduardo Battaner and Prof. Werner W. Zeilinger, the referees of this Thesis for the Doctor Europeaus degree;
- Dr. Leslie Kipp Hunt, Dr. Santiago García-Burillo, Dr. Andrew Baker, and Dr. Stéphane Léon for their teaching and collaboration in the NUGA project;
- Dr. Daniela Bettoni, for her constant support;
- Prof. Cesare Chiosi and Dr. Lorenzo Piovan, for the useful discussions especially concerning theoretical models of galaxies;

- Jacopo Fritz and Giulia Rodighiero, for their friendship and for all the interesting and useful discussions;

- Paola Di Matteo, for her friendship, hospitality in Paris and Rome, and for interesting discussions especially concerning interacting galaxies, LaTeX style, but also concerning Boulangeries, Brasseries and Crêperies in Paris;

- Chiara Ferrari, for her constant availability and for the personal and professional suggestions;

- PhD Students of the XX Cycle in Padova, especially Elena Ricciardelli and Carlo Giocoli;

- Anna Romano, Alessia Moretti, Sara Magrin, Mattia Vaccari, and all the friends of the Padova Astronomy Department and Observatory for their friendship and availability.

A very special thank goes to my family, Benito, Carmen, Simone and Micia, and to my friends (Cristina, Roberto, Rosso, Maba, Guido, Elena, Martina, ...)

Many friends I met during these years and you are all in my mind!